

JNCASR
620.5 P08



5836

5836

5836

**Contributions to the Synthesis,
Characterization, Modification and Properties
of Nanomaterials**

5836

A THESIS SUBMITTED IN FULFILMENT
OF THE DEGREE OF
DOCTOR OF PHILOSOPHY
AS A PART OF THE INTEGRATED Ph.D. PROGRAMME

by

S. R. C. Vivek Chand



CHEMISTRY AND PHYSICS OF MATERIALS UNIT
JAWAHARLAL NEHRU CENTRE FOR ADVANCED SCIENTIFIC
RESEARCH

Bangalore – 560 064

OCTOBER 2008


620.5
POE

Dedicated to my parents

DECLARATION

I hereby declare that the matter embodied in the thesis entitled "**Contributions to the Synthesis, Characterization, Modification and Properties of Nanomaterials**" is the result of investigations carried out by me at the Chemistry and Physics of Materials Unit, Jawaharlal Nehru Centre for Advanced Scientific Research, Bangalore, India under the supervision of Prof. C. N. R. Rao and that it has not been submitted elsewhere for the award of any degree or diploma.

In keeping with the general practice in reporting scientific observations, due acknowledgement has been made whenever the work described is based on the findings of other investigators.



S. R. C. Vivek Chand

CERTIFICATE

I hereby certify that the matter embodied in this thesis entitled "**Contributions to the Synthesis, Characterization, Modification and Properties of Nanomaterials**" has been carried out by Mr. S. R. C. Vivek Chand at the Chemistry and Physics of Materials Unit, Jawaharlal Nehru Centre for Advanced Scientific Research, Bangalore, India under my supervision and that it has not been submitted elsewhere for the award of any degree or diploma.



Prof. C. N. R. Rao
(Research Supervisor)

Acknowledgements

- ◊ I express my sincere gratitude to Prof. C. N. R. Rao, F.R.S. for suggesting the interesting research problems, invaluable guidance, constant encouragement and moral support. His enthusiasm and passion for doing science has inspired me in taking up experimental research. I am extremely fortunate to work with him. He has not just been a research supervisor, but a real father figure for me. I am extremely grateful to him for his keen interest in my academic and personal welfare.
- ◊ It is has been a great pleasure working with Dr. Govindaraj. I am extremely grateful to him for teaching me the various aspects of experimental research and for his constant encouragement throughout the project work.
- ◊ I thank Anil, Basavaraj, Srinath, Srinivas, Vasu, Selvi, Srinivasa Rao and Usha madam for their help in various measurements. I also thank Kavitha, Motin and Dr. Chandrabhas for the Raman spectroscopic measurement. I would like to thank Dr. Raju for his immense help during the NSP work. I also thank Dr. Ramamurthy of IISc for his help and discussions in the study of mechanical properties of inorganic nanowire reinforced polymer nanocomposites
- ◊ I thank my collaborators Drs. Sudheendra, Deepak and Gundiah as well as Jayakanth, Gomathi, Pal, Cele for their invaluable help.
- ◊ I thank my teachers both in IISc and JNC especially Profs. K. L. Sebastian, T. N. Guru Row, J. Gopalakrishnan, P. K. Das, A. G. Samuelson, S. Chandraskharan, P. Balaram, S. Yashonath, M. S. Hegde, A.

Umarji, A. R. Chakravarthy, S. Narasimhan and G. U. Kulkarni for their informative courses.

- ◇ I would like to thank my lab mates, Drs. Gautam, Deepak and Nath, Kalyani, Chandu, Bhat, Neenu, Leela, Kanishka, Subrahmanyam for their fruitful discussions and wonderful work atmosphere.
- ◇ I also thank Lakshmi, Divya, Gautam, Leonard, Meenakshi, Neena, Neenu, Reji, Ujjal, Deepak, Pritesh, Rakesh, Sudheendra, Vinod, Kalyani, John, Pushpa, Thiru, Claudy, Raju, Jyoti, Gomathi, Sandeep, Ramakrishna, Dash, Kabra, Kapoor, Rinki, Ved, Arun, for all their help and affection. Also my batchmate Ayan.
- ◇ I also thank my seniors Dr. Anupama and Dr. Vaidhyanathan for their help and suggestions during course-work.
- ◇ I thank past and present Computer lab staff for the excellent Computer facilities provided.
- ◇ I would like to thank Mrs. Rao and Mr. Sanjay for their love and care towards me.
- ◇ Finally, I would like express by deepest regards to my parents and sister for their love, patience, understanding and motivation.

Preface

The thesis consists of eight chapters, of which the first chapter presents a brief overview of the synthesis, properties and potential application of nanomaterials. The other seven chapters deal with various aspects of nanomaterials including their synthesis, modification and properties.

Chapter 2 describes the use of nebulized spray pyrolysis of precursor to obtain carbon nanotubes and metal nanowires. Purification of carbon nanotubes by a new method employing high temperature hydrogen treatment is described in Chapter 3. A new method of generating chemically bonded ceramic oxide coatings on carbon nanotubes and inorganic nanowires are described in Chapter 4. Functionalization and solubilization of metal oxide nanowires and BN nanotubes are covered in Chapter 5.

Chapter 6 deals with electrical properties of nanocomposites formed by carbon nanotubes and inorganic nanowires with conducting polymers. Mechanical properties of composites of inorganic nanowire with polymers are described in Chapter 7. Electrochemical supercapacitors employing carbon nanotube, graphenes and polyaniline-SWNT nanocomposites are dealt within Chapter 8.

Contents

Acknowledgements	v
Preface	vii
1 Nanomaterials: A brief overview	1
1.1 Introduction	1
1.2 Carbon Nanotubes	4
1.2.1 Synthesis	5
1.2.2 Structure and Characterization	10
1.2.3 Chemistry of carbon nanotubes	16
1.2.4 Properties and Application	23
1.3 Graphene	28
1.4 Inorganic Nanotubes and Fullerenes	32
1.5 Inorganic Nanowires	34
1.5.1 Synthesis	34
1.5.2 Properties and Applications	38
1.6 References	45
2 Synthesis of carbon nanotubes and metal nanowires by nebulized spray pyrolysis	57
2.1 Introduction	58
2.2 Nebulized Spray Pyrolysis	60
2.3 Experimental details	63
2.4 Results and Discussion	65
2.4.1 Carbon Nanotubes	65
2.4.2 Metal Nanowires	77
2.5 Conclusions	85

2.6	References	87
3	A new method of purification of carbon nanotubes using hydrogen treatment	91
3.1	Introduction	91
3.2	Experimental details	93
3.3	Results and Discussions	95
3.4	Protocol for the purification of SWNTs	103
3.5	Conclusions	109
3.6	References	110
4	Chemically-bonded ceramic coatings on carbon nanotubes and inorganic nanowires	113
4.1	Introduction	113
4.2	Experimental details	115
4.3	Results and Discussion	117
4.4	Conclusions	121
4.5	References	122
5	Functionalization and Solubilization of inorganic nanowires and Boron Nitride nanotubes	123
5.1	Introduction	123
5.2	Experimental Details	125
5.3	Results and Discussion	127
5.3.1	Metal oxide nanowires	127
5.3.2	Boron Nitride nanotubes	133
5.4	Conclusions	137
5.5	References	138
6	Electrical properties of nanocomposites of carbon nanotubes and inorganic nanowires with conducting polymers	141

6.1	Introduction	142
6.2	Experimental Details	144
6.3	Results and Discussion	147
6.3.1	Carbon Nanotubes	147
6.3.2	Inorganic nanowires	154
6.4	Conclusions	163
6.5	References	164
7	Mechanical properties of nanocomposites of inorganic nanowires with polymers	167
7.1	Introduction	167
7.2	Experimental details	168
7.3	Results and Discussion	170
7.4	Conclusions	184
7.5	References	186
8	Electrochemical Supercapacitors based on Carbon nanostruc- tures	187
8.1	Introduction	187
8.2	Experimental Details	193
8.3	Results and Discussion	195
8.3.1	Carbon Nanotubes and Graphenes	195
8.3.2	Polyaniline-SWNT nanocomposites	201
8.4	Conclusions	203
8.5	References	204

Chapter 1

NANOMATERIALS: A BRIEF OVERVIEW

1.1 Introduction

Understanding the properties of nanometer sized objects is one of the important scientific challenges of the recent past [1,2]. Accordingly, there has been tremendous interest in the synthesis and properties of nanomaterials with different sizes and shapes. Initial efforts towards this goal started with Michael Faraday in the 19th century [3]. Faraday studied colloids of gold and termed them as ‘divided metals’, now popularly known as nanocrystals. Individual nanostructures include clusters, quantum dots, nanocrystals, nanowires, and nanotubes, while collections of nanostructures involve arrays, assemblies, and superlattices of the individual nanostructures. Nanostructures constitute a bridge between molecules and infinite bulk systems. The physical and chemical properties of nanomaterials can differ significantly from those of the atomic-molecular or the bulk materials of the same composition.

These unique properties which are quite different from that of bulk arise as there are more atoms on the surface, i.e. large surface/volume ratio as evident from Figure 1.1 (A). The effects determined by size pertain to the evolution of structural, thermodynamic, electronic, spectroscopic, and chemical features of these finite systems with increasing size. Size effects are of two types: one is concerned with specific size effects (e.g., magic numbers of atoms in metal clusters, quantum mechanical effects at small sizes) and the other with size-scaling applicable to relatively larger nanostructures. For example, as the size of gold nanoparticles decreases one observe a decrease in their melting

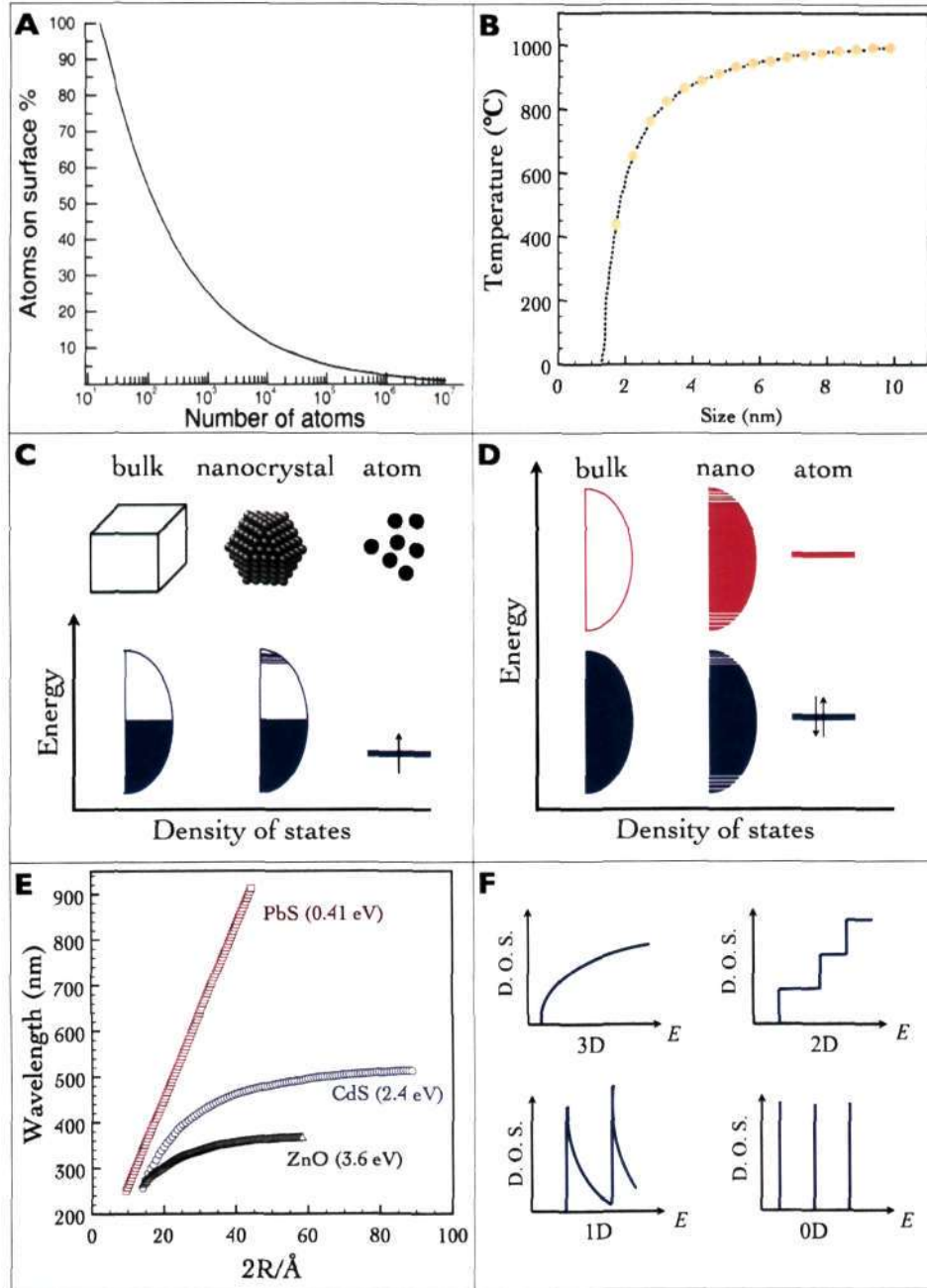


Figure 1.1: (A) Variation of the atoms on the surface as a function of total atoms in a nanocrystal, (B) Melting point of gold nanocrystals as a function of size, (C) Effect of size of metal nanocrystals, (D) Effect of size of semiconductors, (E) Variation of bandgap of semiconductor nanoparticles as a function of their diameter and (F) Change in the density of states as a function of shape (from bulk to 2D, 1D and 0D).

point (Figure 1.1 (B)). In the case of metal nanocrystals, gaps open in their density of states and below a critical diameter they're are no longer metallic (Figure 1.1 (C)). In the case of semiconductors, one observes an increase in the bandgap as the diameter of the nanoparticle decreases (Figure 1.1 (D)). The variation of bandgap of different semiconductor nanocrystals as a function of diameter is shown in Figure 1.1 (E). Very small nanoparticles (or clusters) behave like molecules with discrete energy levels. The properties of a nanosystem can also be modified by changing the shape.

The effect of dimension on the electronic structure of a material is illustrated in Figure 1.1 (F). Nanoparticles are zero-dimensional and exhibit molecule-like behavior. Two-dimensional nanomaterials such as thin films exhibit steps in their electronic density of states (DOS) while van Hove singularities (sharp spikes) are observed in the case of one-dimensional analogues.

It is generally accepted that quantum confinement of electrons by the potential wells of nanometer-sized structures may provide one of the most powerful means to control electrical, optical, magnetic and thermoelectric properties of solid state functional materials. The ability to tune the properties by controlling the size and shape makes them attractive for potential application in new devices and technologies. The themes underlying nanoscience and nanotechnology are twofold: one is the bottom-up approach, that is, the miniaturization of the components, as articulated by Feynman, who stated in the 1959 lecture that there is plenty of room at the bottom [4] and the other is the approach of the self-assembly of molecular components, where each nanostructured component becomes part of a suprastructure. The latter approach is akin to that of Jean-Marie Lehn [5].

In this chapter, a brief summary of the current understanding on the various synthetic methodologies, properties and phenomena associated with

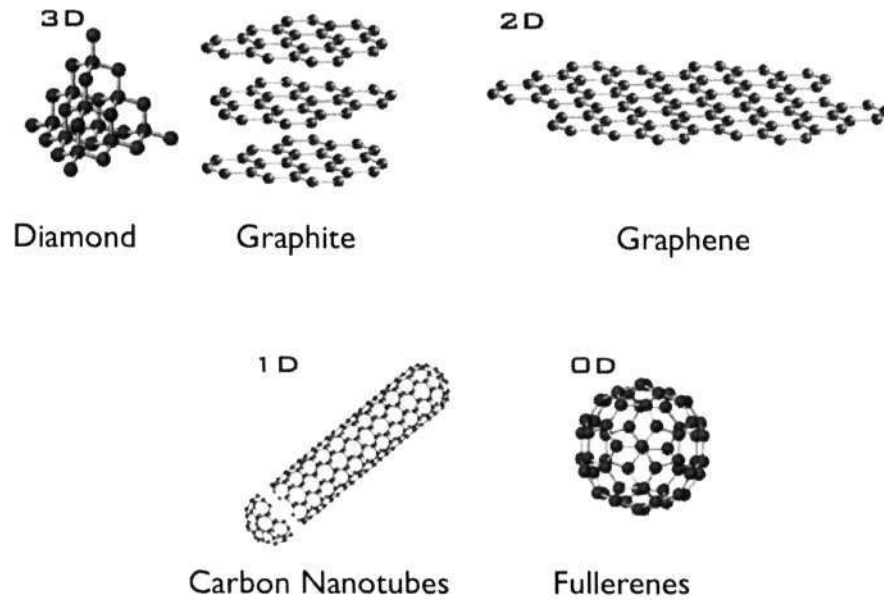


Figure 1.2: Different allotropes of carbon: diamond, graphite, graphene, carbon nanotubes and fullerene (C₆₀).

nanomaterials such as carbon nanotubes, graphenes as well as inorganic nanotubes and nanowires are described.

1.2 Carbon Nanotubes

The well-known crystalline allotropes of carbon are diamond and graphite. Diamond has tetrahedral sp^3 bonding while graphite has planar sp^2 bonding. The other recently discovered allotropes are: graphene, carbon nanotubes and fullerenes (see Figure 1.2). Graphene can be obtained by pulling out a single-layer of graphite. Carbon nanotubes can be obtained by rolling graphene sheet to form a cylinder. Fullerenes are a clusters of carbon with three coordinate carbon atoms tiling the spherical or nearly spherical surfaces, the best known example, C₆₀, with a truncated icosahedral structure formed by twelve pentagonal rings and twenty hexagonal rings. The coordination at every carbon atom is not planar, slightly pyramidalized, with some sp^3 character present in the essentially sp^2 carbons. The curvature needed

for the formation of closed structure is due to the presence of five-member rings.

Ever since the discovery of fullerenes in 1985 by Kroto *et al.* [6], there has been an enormous interest in the synthesis and properties of carbon nanomaterials. Fullerenes can be produced in large quantities by the arc-evaporation of graphite [7]. Carbon nanotubes, the nearly one-dimensional analogue of fullerenes were discovered by Iijima [8]. Nanotubes can be multi-walled with a central tubule surrounded by graphitic layers separated at approximately 3.4 Å. A single-walled carbon nanotube (SWNTs) unlike multi-walled carbon nanotubes (MWNTs) consist of a single tubule without additional graphitic layers. Graphene has been recently discovered by Geim and co-workers at the University of Manchester [9, 10]. Aspects related to carbon nanotubes will be covered in this section, while graphene will be covered in the next section.

1.2.1 Synthesis

MWNTs have been traditionally prepared by the arc-evaporation of graphite [8]. A schematic diagram of the arc-discharge chamber is shown in Figure 1.3 (a). In this method, an electric arc is struck between two graphite electrodes, with a current of 60-100 A across a potential of 20-30 V in a helium atmosphere (approximately 500 torr). Carbon evaporates from the anode and gets deposited at the cathode, thereby yielding a cathodic stub. The cathodic stub contains a high yield of MWNTs. Carbon nanotubes can be prepared in large quantities using plasma arc-jets, by optimizing the quenching process in an arc between a graphite anode and a cooled copper electrode [11]. SWNTs were first synthesized by metal-catalyzed dc-arcing of graphite electrodes [12, 13]. The graphite anode is normally filled with metal powders such as Fe, Co or Ni and pure graphite is used as the cathode. Large

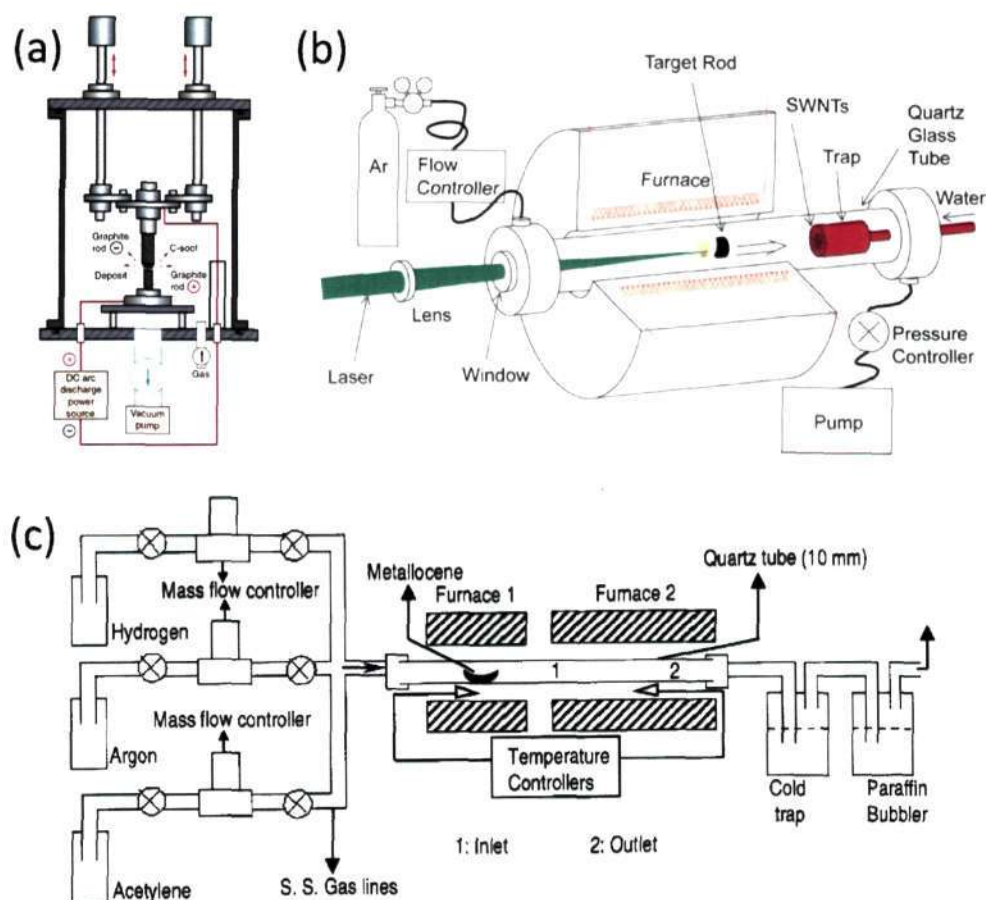


Figure 1.3: Schematic diagrams of (a) arc-discharge chamber, (b) high-temperature laser ablation and (c) organometallic pyrolysis experimental set-ups.

quantities of SWNTs as seen in Figure 1.4 (a) can be obtained by using a mixture of 1 at.% of Y and 4.2 at.% of Ni [14]. SWNTs have also been synthesized by the condensation of a laser-vaporized carbon-nickel-cobalt mixture at 1200°C [15]. A sketch of the laser-ablation set-up is shown in Fig 1.3 (b). Nanotubes have also been prepared under electrochemical [16] and hydrothermal conditions [17].

The decomposition of hydrocarbons over small metal catalyst has been the focus area of research in the synthesis of carbon nanotubes due to their scalability and ease of synthesis [18–20]. MWNTs have been obtained by the decomposition of acetylene under inert conditions over Fe or Co/graphite

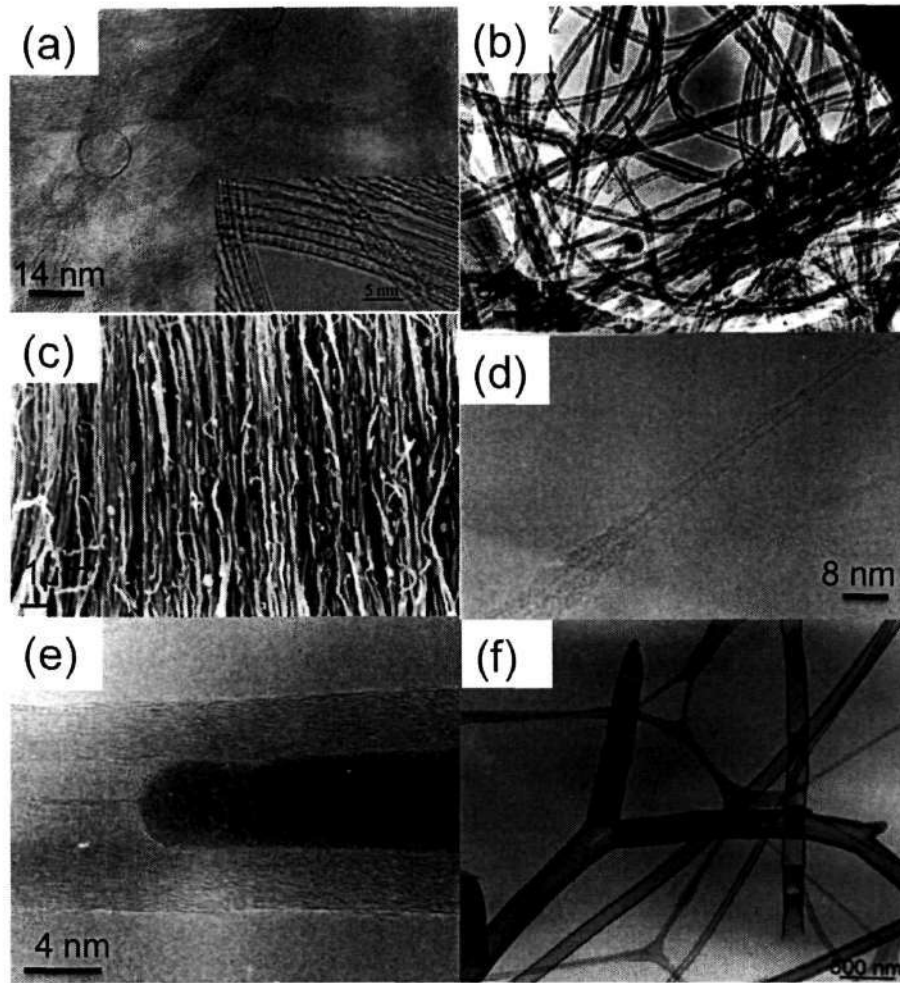


Figure 1.4: Electron microscope images of (a) SWNTs prepared by arc-discharge process, (b) MWNTs, (c) aligned MWNT bundles, (d) SWNTs, (e) Fe-filled MWNTs and (f) Y-junction carbon nanotubes prepared by organometallic route respectively. Inset in (a) shows C_{60} filled SWNTs, carbon “peapods”.

[21, 22] and Fe/SiO₂ [23]. The presence of transition metal catalyst is essential for the formation of nanotubes and the diameter of the nanotube is determined by the size of the metal particles [24]. Aligned MWNT bundles have been obtained by chemical vapor deposition over transition metal catalyst embedded in the pores of mesoporous silica or in the channels of alumina membranes [25, 26]. Plasma-enhanced chemical vapor deposition on nickel-coated glass using acetylene and ammonia has been employed by Ren *et al.* [27] to obtain aligned MWNT bundles.

Pyrolysis of organometallic compounds such as ferrocene, cobaltocene, nickel or iron phthalocyanine in a two stage furnace provides a straight forward procedure to prepare carbon nanotubes [28–35]. The organometallic compound acts as a source of carbon and metal catalyst nanoparticles. In a typical synthesis, a metallocene is slowly sublimed from Furnace 1 to Furnace 2 placed at a higher temperature in an inert atmosphere (see Figure 1.3 (c)). Additional hydrocarbons such as acetylene, methane, etc can also be used as secondary carbon sources. The parameters that can be varied in these pyrolysis reactions are sublimation rate of the organometallic precursor, flow rate of the carrier gas and the pyrolysis temperature. This method has yielded MWNTs [28–30], aligned MWNT bundles [31,36], aligned metal-filled MWNTs [32], Y-junction MWNTs [33,34] as well as SWNTs [35,37] under various experimental conditions. Aligned MWNT bundles have been obtained when the catalyst precursor was rapidly sublimed and SWNTs are obtained under dilute catalyst and hydrocarbon conditions. Electron microscope images of various types of nanotubes obtained by the pyrolysis route is shown in Figures 1.4 (b)-(f). The advantage of the precursor method is that the aligned bundles are produced in one step, at a relatively low cost, without need of substrates. Y-junction nanotubes can be obtained when an additional carbon source containing sulphur is incorporated [33,34].

Dai *et al.* [38] have prepared SWNTs by the disproportionation of CO over Mo particles of few nanometer dispersed in a fumed alumina matrix at 1200°C. Flahaut *et al.* [39] have synthesized SWNTs by passing a H₂-CH₄ mixture over transition metal containing oxide spinels, obtained by the combustion route.

Several models for the growth of carbon nanotubes have been proposed. Endo and Kroto [40], based on the observation of C₂ ejection from the C₆₀ in the mass spectrometry, suggest that tube formation process is a consequence

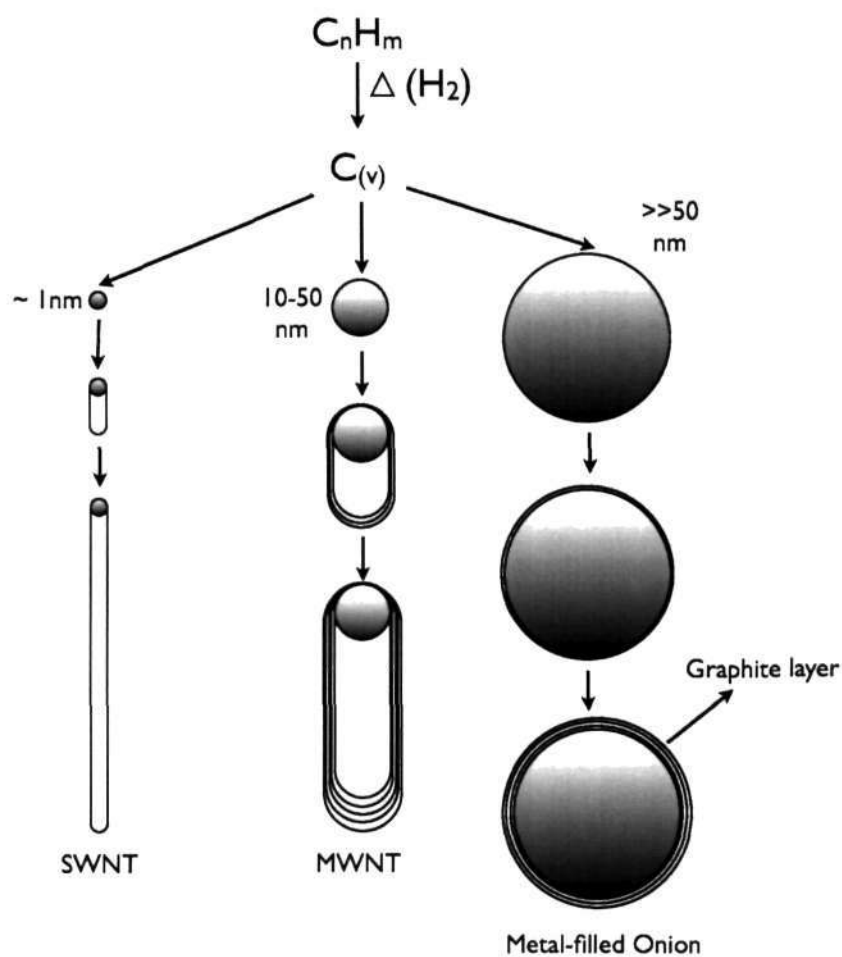


Figure 1.5: Schematic representation of the dependence of carbon nanostructure obtained by hydrocarbon pyrolysis on the diameter of the catalyst particle.

of the formation of fullerenes. Isotope scrambling experiments show that under the conditions of formation, the plasma has vaporized atoms of carbon. Given the right conditions the tip opens and the nanotube grows [41]. Iijima *et al.* [42] have presented evidence based on electron microscopy for the open-ended growth of carbon nanotubes. Rao and co-workers [19] have suggested that nanotubes prepared by the pyrolysis of hydrocarbon over metal nanoparticles grow in four steps. The hydrocarbon decomposes on the metal surface to release hydrogen and carbon, which dissolves in the metal in the first step (see the illustration in Figure 1.5). The second step involves the

diffusion of carbon through the metal particle and its precipitation on the rear face to form the body of the filament. The supply of carbon onto the front face is faster than the diffusion through the bulk, causing accumulation of carbon on the front face, which would lead to the physical blocking of the active surface. Surface diffusion of carbon prevents this problem. In the last step, over-coating and deactivation of the catalyst particle leads to the termination of the growth. Oberlin *et al.* [43] have proposed a mechanism where bulk diffusion is insignificant and the carbon is transported by surface diffusion. A “yarmulke” mechanism based on the formation of a hemispherical graphene cap on the catalyst particle by Dai *et al.* [38]. Here the nanotubes grow from such a yarmulke (skull cap) and the diameter of the nanotube is controlled by the size of the nanometer-sized catalyst particles yielding SWNTs. A salient feature of this model is the absence of the possibility of dangling bond creation at all stages of growth. SWNTs produced by the arc-discharge and laser ablation process may also be formed by this yarmulke process.

Purification is an important problem faced in the use of carbon nanotubes for various purposes. As-synthesized SWNTs prepared by processes such as arc-discharge, laser-ablation, HiPco and pyrolysis of hydrocarbon or organometallic precursors, contain carbonaceous impurities, typically amorphous carbon and graphite nanoparticles, as well as particles of the transition metal catalyst. More details regarding carbon nanotube purification can be found in Chapter 3.

1.2.2 Structure and Characterization

A SWNT can be visualized by cutting C_{60} across the middle and adding a cylinder of graphene of the same diameter. If the C_{60} is bisected normal to a five-fold axis, an armchair tube is obtained and if it is bisected normal to a

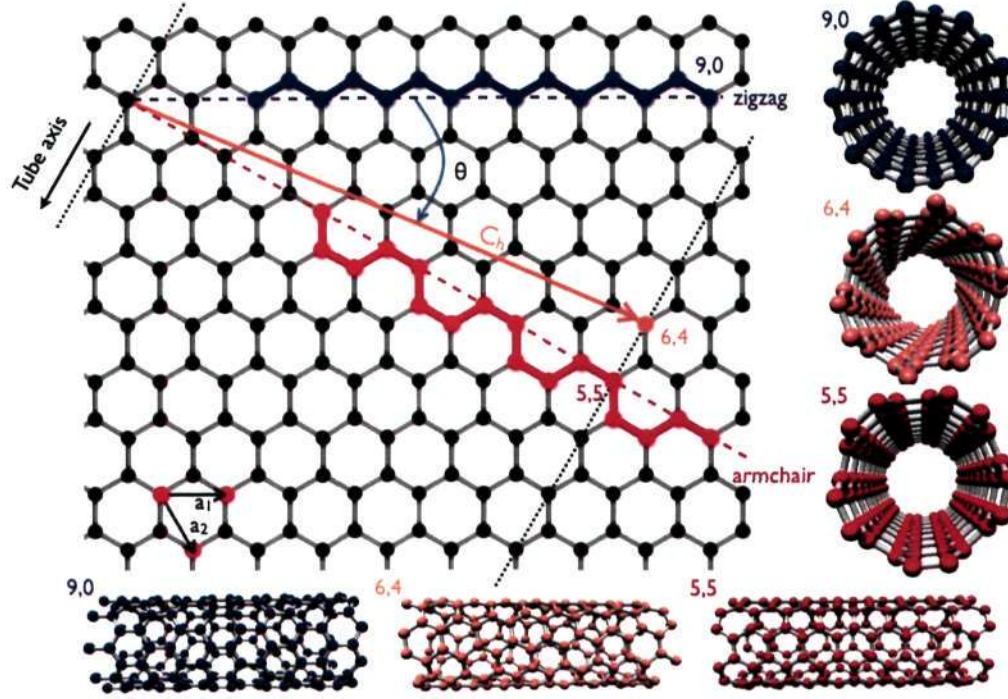


Figure 1.6: A two-dimensional graphene sheet showing zigzag and armchair directions along with chiral vector \vec{C}_h (in orange) and chiral angle θ . Computer generated models of 20 Å sections and cross-sections of zigzag (9,0), chiral (6,4) and armchair (5,5) nanotubes.

three fold axis, a zigzag tube is formed. In addition, a variety of chiral tubes can be obtained with the screw axis along the axis of the tube (armchair and zigzag nanotubes are achiral). Nanotubes can be defined by a chiral angle θ and a chiral vector \vec{C}_h given by equation (1.1) where \vec{a}_1 and \vec{a}_2 are unit vectors in a 2D graphene lattice (see Figure 1.6), while n and m are integers.

$$\vec{C}_h = n\vec{a}_1 + m\vec{a}_2 \quad (1.1)$$

The vector \vec{C}_h connects two crystallographically equivalent sites on a 2D graphene sheet while the chiral angle is the angle it makes with respect to the zigzag direction (Figure 1.6). A tube is formed by rolling up the graphene sheet such that the two points connected by the chiral vector coincide. The nanotube can be specified by the pair of integers (n,m) , which have a wide

range of values. For the armchair nanotubes, $n = m \neq 0$ while $n \neq 0, m = 0$ for the zigzag nanotubes. For a nanotube defined by the index (n, m) , the diameter, d , and chiral angle, θ , are given by the equations (1.2) and (1.3), where $a = 1.42 \text{ \AA}$ and $0 \leq \theta \leq 30^\circ$.

$$d = a \cdot (m^2 + m \cdot n + n^2)^{1/2} / \pi \quad (1.2)$$

$$\theta = \arctan(-(\sqrt{3})^{1/2} \cdot m) / (2n + m) \quad (1.3)$$

The MWNTs consist of capped concentric cylinders separated by 3.45 \AA , which is close to the separation between the (002) planes in graphite. The carbon nanotubes are capped by dome-shaped hemispherical fullerene-type units. The capping unit consists of pentagons and hexagons. SWNTs have defects like bends, which are due the presence of pentagons and heptagons on opposite side of the tube [44].

The electronic structure of SWNTs is closely related to its structure. The basic electronic band structure of SWNTs can be derived from a graphene sheet while neglecting hybridization effects due to the finite curvature of the tube structure. Graphene is a semi-metal with valence and conduction bands degenerate only at six corners (K_B) of the hexagonal first Brillouin zone (see Figure 1.7 (a)). The Fermi surface of the graphene sheet is thus reduced to these six points. In SWNTs, the wavevector k is quantized along the circumferential direction due to periodic boundary condition, $k \cdot \vec{C}_h = 2\pi q$, where q is any integer. Therefore, only a particular set of states, which are parallel to the corresponding tube axis with a spacing of $2/d$, are allowed as evident from Figure 1.7 (b). On the basis of this simple scheme, if one of the allowed wavevectors passes through a Fermi K_B of the graphene sheet, the SWNT should be metallic, and otherwise it should be semiconducting [45–47]. SWNTs are metallic when $(n - m)/3$ is an integer, and otherwise they are semiconductors. Low-temperature scanning tunneling microscopy

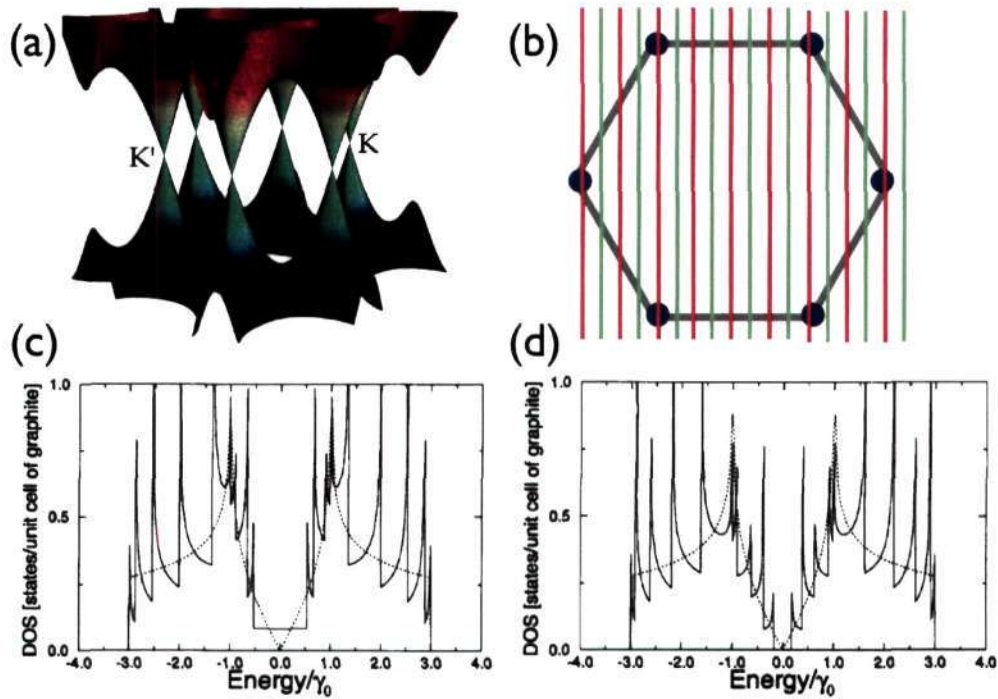


Figure 1.7: (a) Three-dimensional plot of the π and π^* graphene energy bands and (b) a 2D projection with the allowed 1D wavevectors k for a metallic (red) and semiconducting (green) SWNTs. The hexagon defines the first Brillouin zone of a graphene sheet, and the black dots in the corners are the K_B points. (c) and (d) density of states plot for metallic and semiconducting SWNTs respectively.

(STM) and scanning tunneling spectroscopy (STS) studies of SWNTs have shown the size-specific transport properties in agreement with theoretical predictions [48, 49].

Optical absorption and fluorescence spectroscopy has also been used to study SWNTs. All the optical spectroscopic processes in semiconducting SWNTs and most in metallic SWNTs are attributed to transitions between corresponding van Hove singularities. The presence of energy gaps is induced by features such as doping, curvature and bundling. A small energy gap at the Fermi level opens up in the case of metallic nanotubes due to the curvature of the graphene sheet [50]. A typical optical absorption spectra of SWNTs is shown in Figure 1.8 (b). The near-infrared transitions designated at S_{11} and S_{22} arise from the inter-van Hove energy levels in semiconducting

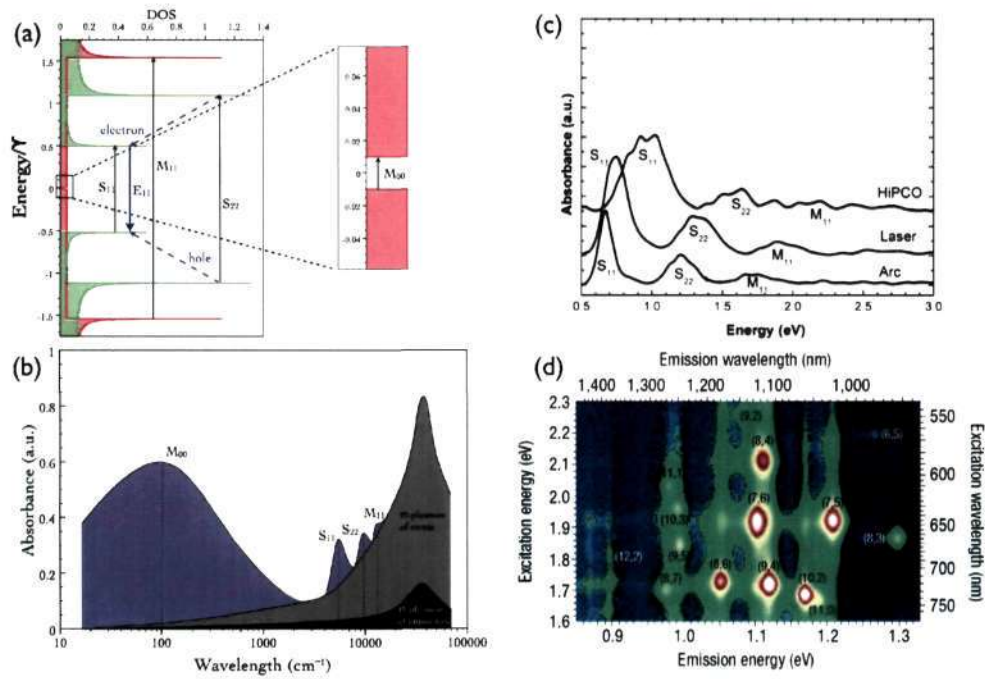


Figure 1.8: (a) Scheme of the electronic transitions occurring in SWNTs, (b) schematic absorption spectra of SWNTs, (c) optical absorption spectra of SWNTs prepared by the arc-discharge, laser ablation and HiPco processes, and (d) 2D photoluminescence map of HiPco SWNTs.

SWNTs while metallic SWNTs exhibit absorption bands (M_{11}) in the visible region. Metallic SWNTs show a band (M_{00}) in the infrared spectrum (100 cm^{-1}) which arises due to the small gap near the Fermi level (attributed to effects of finite curvature and broken symmetry). The absorption spectra of SWNTs show a blue shifted as the diameter of the nanotube decreases as seen in Figure 1.8 (c).

Bundled SWNTs do not exhibit photoluminescence as the electron-hole pair non-radiatively decay due to the presence of metallic SWNTs in the bundles. Photoluminescence is only observed when the nanotubes are individualized and the process occurs in three steps: (a) an absorption of light at S_{22} followed by (b) a relaxation from S_{11} using a phonon-electron interaction, and (c) a spontaneous emission at E_{11} . The photoluminescence emission is

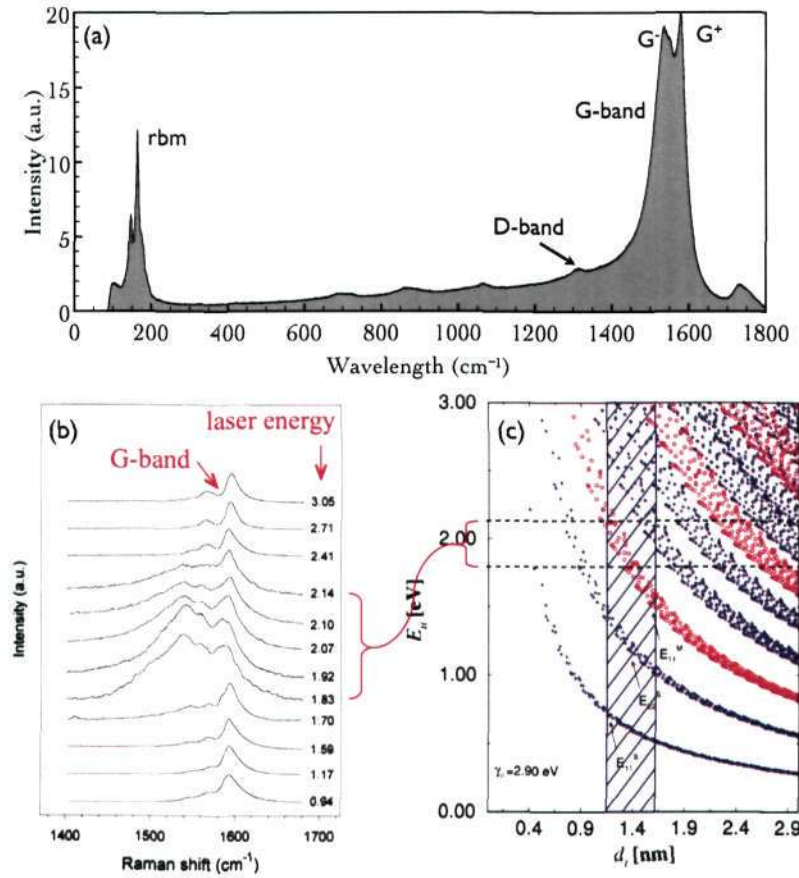


Figure 1.9: (a) Typical Raman spectra of arc-discharge SWNTs obtained using 632 nm Ar laser, (b) Resonant Raman spectra of the tangential G-band modes of SWNT bundles measured with several different laser lines, on a sample with (c) Resonant transition energies E_{ii} vs diameter. The dashed area indicates the diameter distribution of the sample. Blue crosses are for S-SWNTs and red open circles for M-SWNTs.

possible with the S_{11} transition while a wide range of wavelengths are useful for excitation. As the energy of the van Hove singularities maxima are mainly dependent on the nanotube chirality, the (n,m) values of the different nanotubes present in a sample can be characterized using two-dimensional photoluminescence mapping. A typical photoluminescence map of HiPco SWNTs is shown in Figure 1.8 (d).

Raman spectroscopy is an essential tool in the study of carbon nanotubes as it gives important insights into the structure and electronic properties of nanotubes. The primary Raman bands observed in SWNTs are: the G-band

(1540-1600 cm^{-1}), the D-band (1340 cm^{-1}) and the radial breathing modes (100-300 cm^{-1}) as seen in Figure 1.9 (a). The G-band in SWNTs arise from the longitudinal optical (LO) and transverse optical (TO) modes [51]. The G bands in semiconducting tubes are termed as G^+ (1590 cm^{-1}) and G^- (1567 cm^{-1}), are due to LO (axial) and TO (circumferential) modes, respectively. In metallic tubes, G^+ (1580 cm^{-1}) and G^- (1540 cm^{-1}) peaks are due to TO (circumferential) and LO (axial) modes, the opposite of the semiconducting case. Because of the electron-phonon coupling interaction the G linewidth in metallic tubes is usually broader (60 cm^{-1}) than that in semiconducting tubes (10 cm^{-1}). The frequency of the radial breathing mode is related to the diameter of the SWNT ($d = 248/\omega$). Diameter selective resonance behavior of SWNTs were observed by Rao *et al.* [52]. The Raman scattering process in nanotubes is resonant in nature. Whenever the energy of the incident photons matches an optical transition energy, one expects to find resonant enhancement of the corresponding photophysical process. Thus, isolated single nanotubes have been studied using resonant Raman spectroscopy and (n, m) indices have been determined [53]. Diffraction methods have also been used to probe the structure and properties of carbon nanotubes. Electron diffraction studies establish the presence of helicity [54]. The XRD pattern of MWNTs show only the $(hk0)$ and $(00l)$ reflections but no (hkl) reflections [55].

1.2.3 Chemistry of carbon nanotubes

Functionalization and solubilization is an important area in the study of carbon nanotubes [56–58]. In Figure 1.10, we show the different types of chemical modification strategies employed to functionalize SWNTs. Good dispersion of nanotubes are required for various applications, such as in the preparation of composites. Using specific interaction, it is also possible to

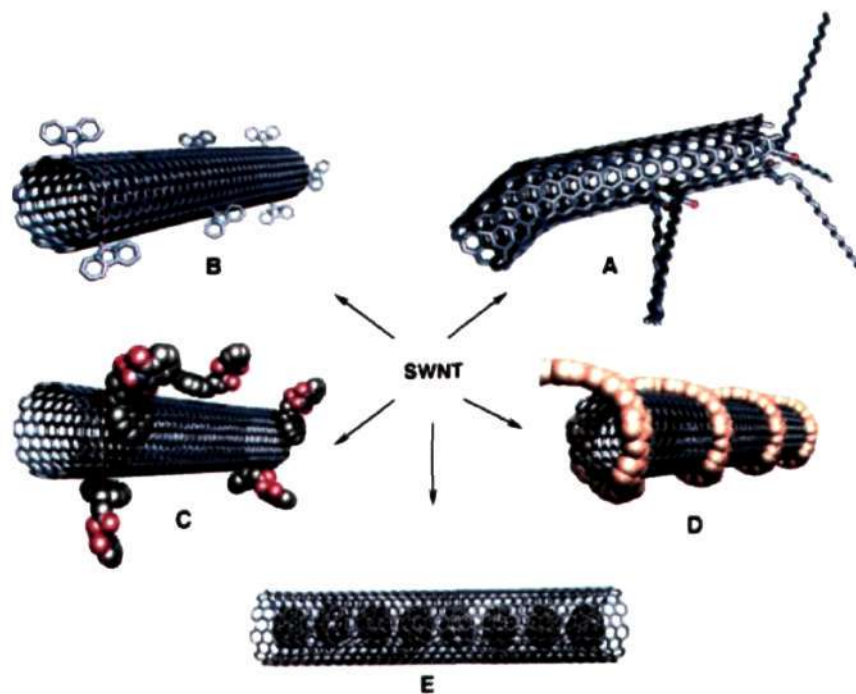


Figure 1.10: Functionalization possibilities for SWNTs: (a) defect-group functionalization, (b) covalent sidewall functionalization, (c) non-covalent exohedral functionalization with aromatic molecules, (d) noncovalent exohedral functionalization with polymers, and (e) endohedral functionalization with, for example, C_{60} . (From ref. [56])

separate metallic and semi-conducting SWNTs. The chemistry of carbon nanotubes is broadly classified into two, covalent and non-covalent functionalization respectively.

Covalent Functionalization

In covalent functionalization, covalent bonding is used to attach functional groups to the nanotube walls or endcaps. The ends of the tubes are often closed by catalyst nanoparticles in the crude material. These catalyst particles are removed in the oxidative work-up, for example, with HNO_3 , which results in ends largely decorated with carboxyl groups. Some defects of the six-membered-ring carbon structure of the nanotubes, such as the inclusion of five- or seven membered rings in the carbon network, stem from the initial

formation of the tubes. The defects in the sidewalls can also be introduced under drastic conditions such as refluxing for long periods in concentrated HNO_3 . The appearance of carboxyl groups in these positions [59,60] can only be explained by the tube structure breaking open. Defects in SWNTs are important in the covalent chemistry of the tubes because they can either serve as anchor groups for further functionalization, or be created by the covalent attachment of functional groups. The evidence collected to date indicates that nanotubes can tolerate a limited number of defects before a macroscopic sample loses its special electronic and mechanical properties [61–63]. Defects are therefore a promising starting point for the development of the covalent chemistry of SWNTs.

It is well-known in fullerene chemistry that the reactivity in addition reactions depends very strongly on the curvature of the fullerene [64]. Normally, SWNTs bear no caps at their ends, and instead consist of graphitic sidewalls, usually with defects. Thus, there are no strongly curved regions that could serve as reactive targets for direct additions. As the typical diameter of a SWNT (1-2 nm) is larger than that of a fullerene, its relative reactivity is even less than that of the flat regions in fullerenes. Further problems in reactions with SWNTs are their low solubility or dispersability, and their occurrence in bundles. Therefore, functionalization of the sidewalls by covalent-bond formation will only be successful if a highly reactive reagent is used. SWNTs can be reacted with elemental fluorine between 150 – 600 °C to obtain fluorinated-SWNTs with a degree of fluorination was 0.1-1 [65,66]. This method can be used for the further derivatization of SWNTs with tri-alkyl amines. [67]. The fluorinated SWNTs can be dissolved in alcohols by ultrasonication [68,69] and hence become available for transformations using wet chemistry. The fluorine atoms in fluorinated SWNTs can be substituted for alkyl groups by treatment with alkyl lithium or Grignard compounds [70],

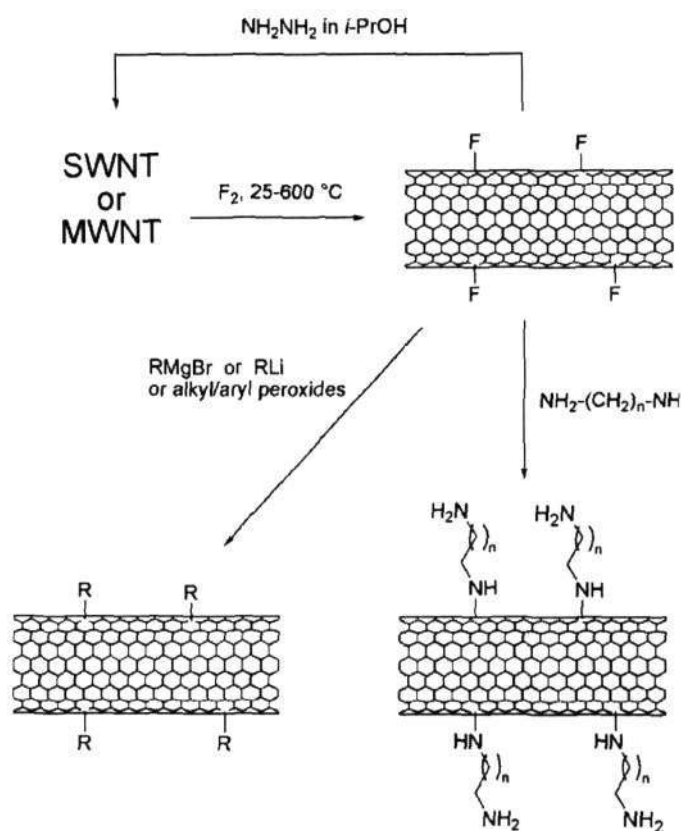


Figure 1.11: Reaction scheme for fluorination of nanotubes, defunctionalization, and further derivatization. (From ref. [57])

resulting derivatized nanotubes are soluble, for example, in chloroform and exhibit a degree of alkylation of about 0.1 (see Figure 1.11).

Non-covalent Functionalization

The formation of noncovalent aggregates with surfactants or wrapping with polymers are suitable methods for the preparation of functional SWNTs as shown in Figure 1.10 (c) and (d). It is believed that the nanotubes are in the hydrophobic interiors of the corresponding micelles, which results in stable dispersions. When the hydrophobic part of the amphiphile contains an aromatic group, an especially strong interaction results, because effective π - π stacking interactions can then form with the graphitic sidewalls

of the SWNTs. This effect was demonstrated in the aggregation with N-succinimidyl-1-pyrenebutanoate [71]. Polymers have also been used in the formation of supramolecular complexes of SWNTs [72]. Thus, the suspension of purified tubes in the presence of polymers such as poly(m-phenylene-co-2,5-dioctoxy-p-phenylenevinylene) (PmPV), in organic solvents such as CHCl_3 , leads to the polymer wrapping around the tubes (Figure 1.10 (d)). The properties of these supramolecular compounds are markedly different from those of the individual components. For example, the SWNT/PmPV complex exhibits a conductivity eight-times higher than that of the pure polymer, without any restriction of its luminescence properties.

Separation of metallic and semiconducting SWNTs

As-produced SWNTs typically consists of metallic (33%) and semiconducting SWNTs (67%). To date there is no synthetic strategy that produces one kind of SWNTs specifically. Thus, several physical as well as chemical methods have been developed in the literature for the separation of metallic and semiconducting SWNTs after synthesis. The physical methods include ultracentrifugation, chromatography and dielectrophoresis. Dielectrophoresis sorts SWNTs according to their dielectric constant in the presence of an a.c. electric field [73, 74]. Owing to differences in the dielectric constants of metallic and semiconducting SWNTs, effective electronic type sorting can be achieved. Consequently, recent work has focused on attempts to scale-up dielectrophoresis using larger electrodes [75] or dielectrophoretic field-flow fractionation [76]. In addition to electronic type separation, the latter approach also has shown evidence for diameter sorting among semiconducting SWNTs. Metallic SWNTs with small diameters can be removed selectively by treatment with nitric and sulfuric acid mixtures [78]. Large-scale separation of

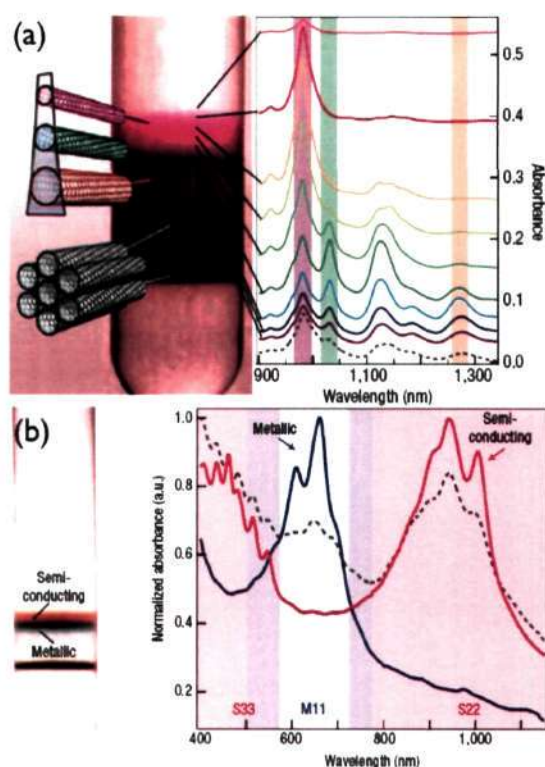


Figure 1.12: Sorting SWNTs using density gradient ultracentrifugation (DGU): Photographs and optical spectra of each layer for (a) Small-diameter (0.7-1.1 nm) SWNTs encapsulated with sodium cholate and (b) Large-diameter (1.1-1.6 nm) SWNTs encapsulated with a co-surfactant mixture of sodium cholate and sodium dodecyl sulphate. (From ref. [77])

metallic and semi-conducting SWNTs has been achieved using a dispersion-centrifugation process using long chain alkyl amines [79]. In this process, HiPco nanotubes are dispersed in a solution of 1-octylamine in THF wherein the amine strongly adsorbs on the metallic nanotubes and centrifugation is used to selectively enrich of the metallic nanotubes. Metallic and semiconducting SWNTs can be separated by the selective functionalization using azomethine ylides [80]. Metallic SWNTs are also preferentially destroyed by laser irradiation [81]. Optical absorption of metallic SWNTs are less affected by bundling effects compared to the semiconducting SWNTs resulting in an enhanced absorption ratio of metallic and semiconducting SWNTs [82]. Density gradient ultracentrifugation (DGU) has been used to sort SWNTs

according to their buoyant density [83]. Experimentally, the DGU approach was first used to sort DNA-SWNT hybrids by diameter [84]. However, the DNA encapsulation chemistry possessed several disadvantages including irreversible wrapping, high cost and inability to disperse large-diameter (>1.2 nm) SWNTs. Consequently, subsequent work focused on surfactant encapsulated SWNTs [77]. Sodium cholate encapsulation led to clear diameter sorting by DGU as evidenced by the visibly distinguishable colored bands shown in Figure 1.12. When using co-surfactant mixtures of sodium cholate and sodium dodecyl sulphate, electronic-type sorting by DGU was achieved as seen in Figure 1.12. The latter sorting was attributed to inequivalent binding of the two surfactants as a function of the SWNT polarizability, which produced differences in the density of the SWNT-surfactant hybrid depending on SWNT electronic type. Following iterative application of the DGU technique, purities approaching 99% have been achieved.

Coatings, fillings and decoration of metal nanoparticles

Metal nanoparticle coated nanotubes have attracted a lot of interest due to their potential application in catalysis and fuel cells. Rao and co-workers were one of the first to coat MWNTs with various metal nanoparticles [85]. Metals such as Au and Pt have been filled in SWNTs and the metals form nanowires [86]. Green and co-workers have investigated the crystal growth behavior of solid phase halides encapsulated within single walled carbon nanotubes [87]. 1D crystals with completely novel structures can form inside SWNTs. Where the encapsulated crystal has a structure recognizably related to that of the bulk material, crystals are formed with lower surface coordination and all exhibit substantial lattice distortions as a result of this reduced coordination and/or van der Waals constriction effects. Luzzi and co-workers [88] have filled C_{60} into SWNTs to yield to “peapods”.

1.2.4 Properties and Application

Carbon nanotubes exhibit a wide range of interesting properties [19]. Due to their nearly one-dimensional electronic structure, electron transport in metallic SWNTs and MWNTs occurs ballistically over long nanotube lengths, enabling them to carry high currents with essentially no heating [89]. Carbon nanotubes also behave as field effect transistors (FETs) and have potential application in nanoelectronics [90, 91]. Typical FET designs used in the literature are shown in Figure 1.13. Complex three-point nanotube junctions have been proposed as the building blocks of nanoelectronics by Menon and Srivastava [92]. The Y- and T-type junctions appear to defy the conventional models in favor of an equal number of five- and seven-membered rings to create nanotube junctions. It has been suggested that Y junctions can be created with an equal number of five- and eight-membered rings [92]. Y-junction MWNTs obtained by the pyrolysis route show asymmetry in the I-V curve at the junction [33] and have potential application in nano-circuits based on carbon nanotubes. Novel electrical switching behavior and logic in carbon nanotube Y-junctions has been recently reported [93]. Three-terminal transistor-like operations of Y-junction CNT devices showing differential current amplification have been reported [94]. Y-junction SWNT based FETs has been fabricated and the device exhibits an on/off ratio of 10^5 with a low off-state leakage current of 10-13 A [95]. A floating-potential dielectrophoresis method has been used to achieve controlled alignment of individual semiconducting or metallic SWNTs between two electrical contacts with high repeatability [96]. Carbon nanotube FETs with sub-20 nm short channels and on/off current ratios of $>10^6$ have been demonstrated [97]. These nanotube transistors display on-currents in excess of $15 \mu\text{A}$ for a drain-source bias of 0.4 V. Improvement in the performance of the CNT-FETs has been achieved by chemical optimization/tuning of the nanotube/substrate

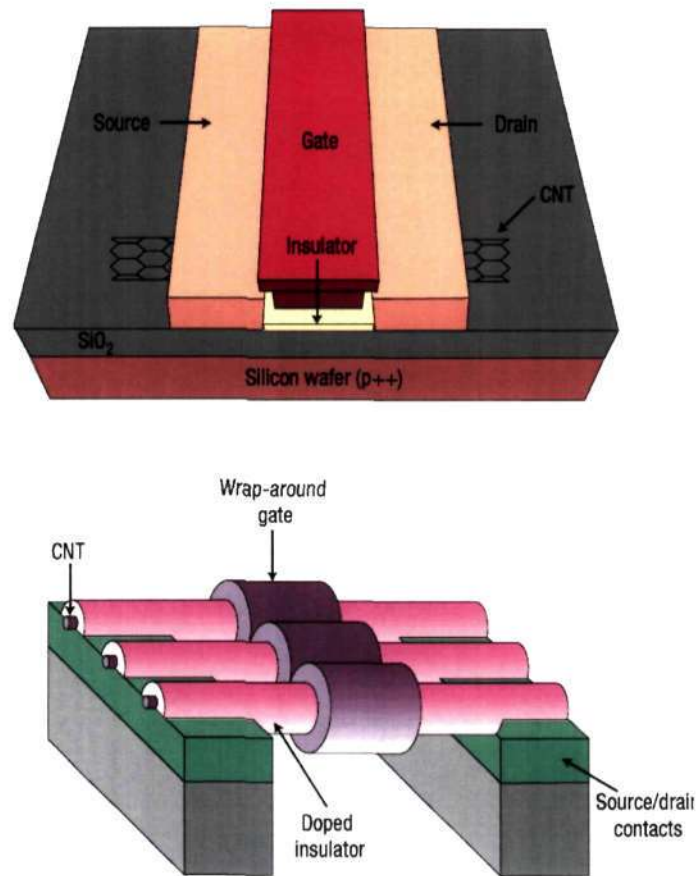


Figure 1.13: Designs of carbon nanotube field-effect transistors: (a) schematic of a top-gated carbon nanotube field-effect transistor and (b) schematic of an array of nanotube transistors with wrap-around gates and doped gate extensions (From ref. [91])

and nanotube/electrode interfaces [98]. This method of selective placement of individual SWNTs by patterned aminosilane monolayer was used for the fabrication of self-assembled carbon nanotube transistors. The aminosilane monolayer reactivity can be used to improve carrier injection and the doping level of the SWNTs. These chemical treatments reduce the Schottky barrier height at the nanotube/metal interface down to that of an almost ohmic contact. Such self-assembled FETs open new prospects for gas sensors as demonstrated for the 20 ppb of triethylamine. The possibility of using CNTs

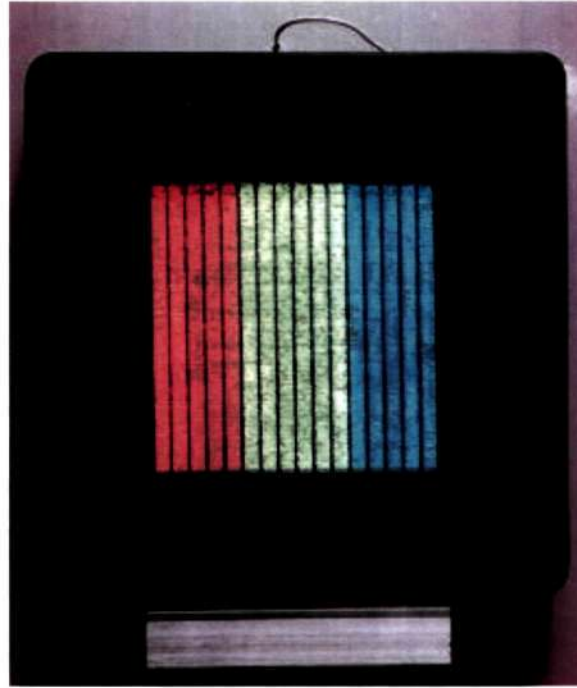


Figure 1.14: Image of a fully sealed 4.5" SWNT-based field emission display.

as potential devices to improve neural signal transfer while supporting dendrite elongation and cell adhesion has been demonstrated [99]. These results strongly suggest that the growth of neuronal circuits on a CNT grid is accompanied by a significant increase in the network activity. The increase in the efficacy of the neural signal transmission may be related to the specific properties of CNTs.

SWNTs exhibit large thermoelectric power at high temperatures. The large thermoelectric power indicates the breaking of electron-hole symmetry due to the self-assembly of nanotubes into crystalline lattices [100]. Phonons also propagate easily along the nanotube. The measured room temperature thermal conductivity for an individual MWNT (> 3000 W/mK) is greater than that of natural diamond and the basal plane of graphite (both 2000 W/mK) Field emission properties of carbon nanotubes have direct application in vacuum microelectronic devices. Carbon nanotubes are ideal as field emission (FE) sources due to their small diameter, high chemical stability,

high mechanical strength and low carbon mobility [101, 102]. Carbon nanotube based FE devices such as displays, x-ray generators, gas discharge tube protectors and microwave amplifiers have been made. Shown in Figure 1.14 is a 4.5" color field emission display based on SWNTs cold cathodes fabricated at Samsung [103]. Carbon nanotubes based FE devices can be operated at room temperature which eliminates heating of cathode as in conventional FE sources. The possibility of miniaturization of devices, high current density, narrow energy distribution and quick start could lead to the commercialization of CNT based FE devices. Carbon nanotubes, produced by ferrocene pyrolysis deposited on a tungsten tip exhibits high emission current densities with good performance characteristics [104]. The optical limiting properties of the carbon nanotubes are considered important for applications involving high power lasers. The optical limiting behavior of visible nanosecond laser pulses in the SWNT suspensions occurs mainly due to nonlinear scattering [105].

Graphite, carbonaceous materials and carbon fibre electrodes are commonly used in fuel cells, batteries and other electrochemical applications. There have been several investigations for the use of carbon nanotubes for energy storage. The small dimensions, smooth topology, hollow cavity and perfect surface specificity make carbon nanotubes suitable for energy storage. The high electrochemically accessible surface area of porous nanotube arrays, combined with their high electronic conductivity and useful mechanical properties, makes them attractive as electrodes for devices employing electrochemical double-layer charge injection. Examples include supercapacitors with giant capacitances in comparison with those of ordinary dielectric-based capacitors [106, 107], and electromechanical actuators that may be useful in robots [108]. Hydrogen and lithium have been electrochemically stored in carbon nanotubes. Functionalized carbon nanotubes treated with pyrrole

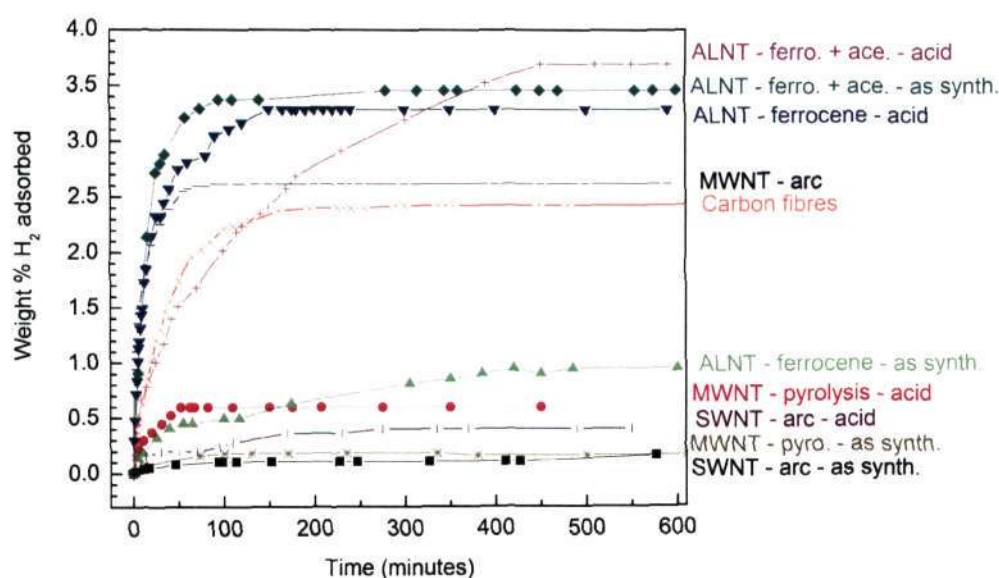


Figure 1.15: Amount of hydrogen adsorbed in wt% as a function of time for the various carbon nanostructures. (From ref. [117])

have been employed as electrode materials in supercapacitors [109]. A capacitance of 350 F/g with power and energy densities of 4.8 kW/kg and 3.3 KJ/kg respectively, were obtained for these electrodes in 6 M KOH with a double layer capacity of 154 $\mu\text{F}/\text{cm}^2$. Aligned MWNTs-RuO₂ nanocomposites have been investigated for use as supercapacitors [110]. A composite with pseudocapacitance properties and high electrical conductivity has been obtained by the pyrolysis of carbon nanotube/polyacrylonitrile blends [111]. Thin films formed by MWNTs with high packing density and alignment yield high power density supercapacitors [112]. Stacked-cup carbon nanotubes have been used in photochemical solar cells [113]. SWNTs can be used as integrated building blocks for solar energy conversion [114]. In this study, SWNTs have been combined with porphyrin to prepared nanostructured devices. SWNT-CdSe nanocomposites may be useful for light harvesting and photoinduced charge transfer [115]. Early reports that carbon nanotubes can store considerable amounts of hydrogen created high expectations [116]. Gundiah *et al.* [117] have systematically measured H₂ adsorption on well-characterized samples of

SWNTs, MWNTs, aligned multi-walled nanotube bundles as well as carbon fibres. Figure 1.14, shows that hydrogen storage does not exceed 3.7 wt %. Clearly, carbon nanotubes fall short of expectations for use in automobile industry.

1.3 Graphene

Graphene is the name given to a flat monolayer of carbon atoms tightly packed into a two-dimensional (2D) honeycomb lattice, and is a basic building block for graphitic materials of all other dimensionalities [118]. Theoretically, graphene has been studied for sixty years and is widely used for describing properties of various carbon-based materials. Graphene was an academic material as it was widely believed that 2-D crystals are unstable. Geim and co-workers [9] in 2005 showed that a single layer of graphene is indeed stable, thus opening a new area of fascinating physics and chemistry.

Preparation

Single- or few-layer graphene has been grown on metal substrates epitaxially by chemical vapor deposition of hydrocarbons [119, 120] and by thermal decomposition of SiC [121–124]. Although, graphite flakes with 20-100 layers thick can be obtained easily by micromechanical cleavage of graphite, only recently Geim and co-workers [9] have successfully detected the presence of single-layer as well as bilayer graphene. The critical ingredient to their success was the observation that graphene becomes visible in an optical microscope if placed on top of a Si wafer with a carefully chosen thickness of SiO₂, owing to a feeble interference-like contrast with respect to an empty wafer. Even a small change in SiO₂ thickness (say only a 5% difference, 315 nm instead of the current standard of 300 nm) can make single-layer graphene completely invisible. In Figure 1.16, typical AFM and TEM images of graphene

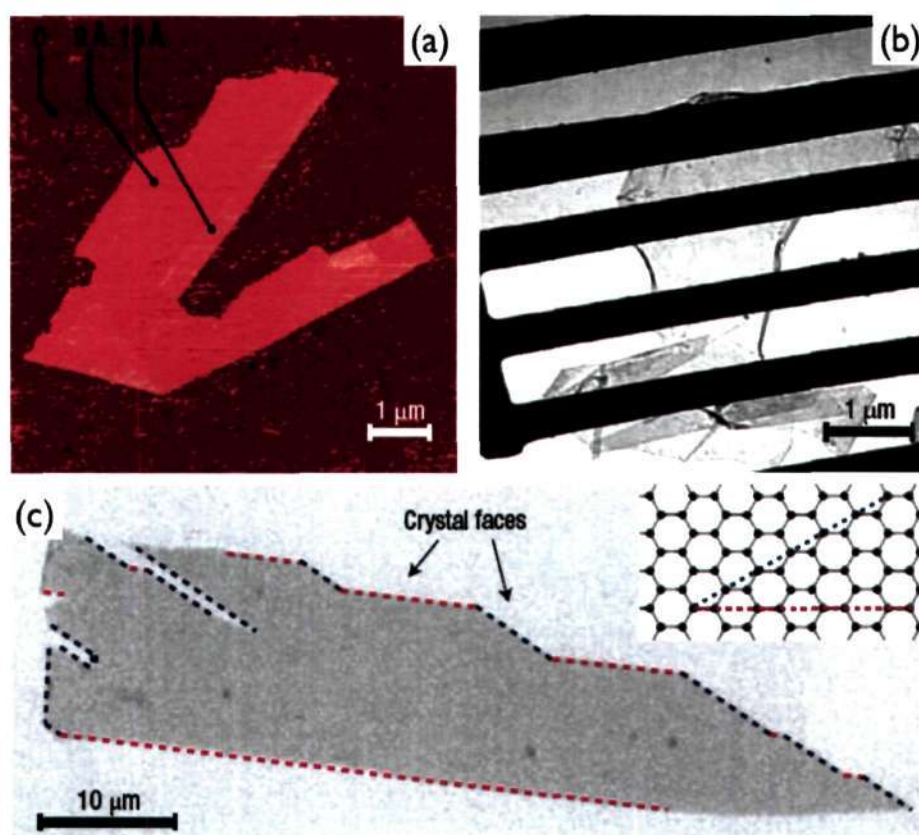


Figure 1.16: (a) Graphene visualized by atomic force microscopy, (b) A graphene sheet freely suspended on a micrometer-size metallic scaffold and (c) SEM image of a relatively large graphene crystal, which shows that most of the crystals faces are zigzag and armchair edges as indicated by blue and red lines and illustrated in the inset. (From ref [118])

are shown. The folded region exhibiting a relative height of $\sim 4 \text{ \AA}$, clearly indicates that it is a single layer. Single-layer graphene has a tendency to fold at the edges.

The large-scale synthesis of graphenes (with mass of grams or kilograms) for applications such as mechanical reinforcement, gas adsorption, electrochemistry still remains a challenge. Chemical methods are necessary and there has been some interest in this area. Graphene has been prepared using methods such as (a) pyrolysis of camphor under reducing conditions, (b) exfoliation of graphitic oxide and (c) thermal conversion of nanodiamond.

Somani *et al.* [125] have prepared graphene (with > 15 layers) by the pyrolysis of camphor over nickel particles under a reducing atmosphere. The reaction was carried out in a two-stage furnace and camphor was slowly sublimed (170°C) by heating from the first furnace to the second furnace held at 770°C where the micron sized nickel particles were placed. There have been several efforts in the preparation of graphene from graphitic oxide. Ruoff and co-workers [126, 127] have carried out exfoliation by reducing graphite oxide with hydrazine under intense ultrasonication. Aksay and co-workers [128] have carried out thermal exfoliation of graphite oxide prepared by the oxidation of graphite with nitric acid, sulphuric acid and potassium chlorate. Enoki and co-workers [129] have prepared graphene by the thermal conversion of nanodiamond. In this method, commercially obtained nanodiamond is heated in an inert atmosphere at high temperatures ($1500 - 2200^\circ\text{C}$).

Properties

Graphene exhibits a pronounced ambipolar electric field effect such that charge carriers can be tuned continuously between electrons and holes in concentrations n as high as 10^{13} cm^{-2} and their mobilities μ can exceed $15,000 \text{ cm}^2 \text{ V}^{-1} \text{ s}^{-1}$ even under ambient conditions. In graphene, μ remains high even at high n ($>10^{12} \text{ cm}^{-2}$) in both electrically and chemically doped devices [130], which translates into ballistic transport on the submicrometer scale (currently up to $\sim 0.3 \mu\text{m}$ at 300 K). A further indication of the systems extreme electronic quality is the quantum Hall effect (QHE) that can be observed in graphene even at room temperature, extending the previous temperature range for the QHE by a factor of 10. In Figure 1.17, a SEM image of a graphene hall bar is shown along with the energy levels for graphene obtained from Schrodinger and Dirac equations and the actual Hall measurements. An equally important reason for the interest in graphene is a

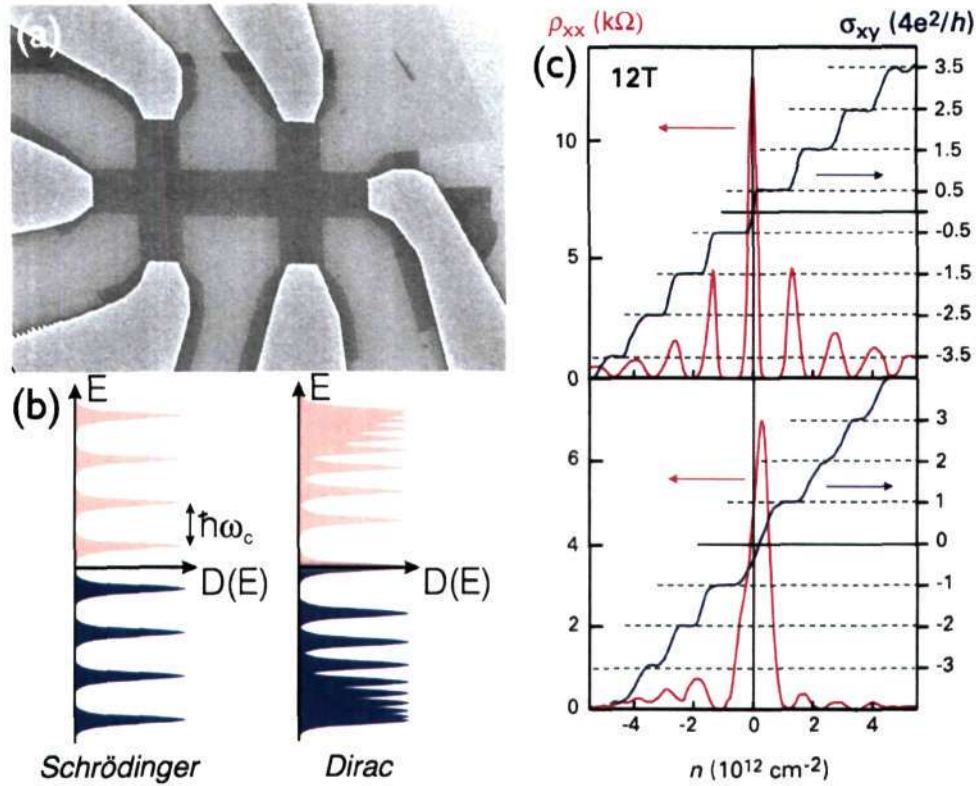


Figure 1.17: (a) SEM image of a graphene hall device with channel width of $1 \mu\text{m}$, (b) Landau levels for Schrodinger electrons with two parabolic bands touching each other at zero energy and for Dirac electrons and (c) Resistivity (red) and Hall conductivity (blue) as a function of carrier concentration in graphene (top) and bilayer graphene (bottom). (From ref. [118])

particular unique nature of its charge carriers. The Schrodinger equation is generally used in condensed matter physics to describe electronic properties of materials. Graphene is an exception, its charge carriers mimic relativistic particles and are more easily and naturally described starting with the Dirac equation rather than the Schrodinger equation. Single gas molecules can be detected using graphene based Hall devices [130].

Field effect transistors using graphene nanoribbons prepared by exfoliation of graphite oxide have been fabricated [131]. All sub 10 nm graphene nanoribbons give semiconducting FETs with on/off ratios up to 10^6 and on-state current density as high as $2000 \mu\text{A}/\mu\text{m}$.

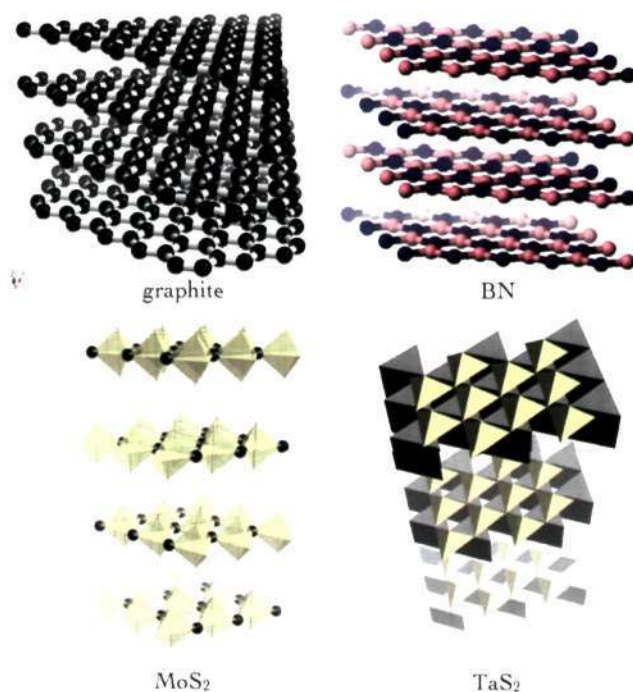


Figure 1.18: Comparison of the structures of (a) graphite and inorganic layered compounds such as (b) BN; (c) MoS₂; (d) NbS₂/TaS₂. In the layered dichalcogenides, the metal is in trigonal prismatic (TaS₂) or octahedral coordination (MoS₂).

1.4 Inorganic Nanotubes and Fullerenes

Since the discovery of carbon nanotubes, there has been tremendous interest in the preparation of nanotubes of other layered inorganic materials such as boron nitride and metal chalcogenides [132]. These materials possess a layer structure similar to that of graphite as seen in Figure 1.18. Boron nitride (BN) crystallizes in a graphite-like structure and can be simply viewed as replacing a C-C pair in the graphene sheet with the iso-electronic B-N pair. Pure BN nanotubes have been generated by employing several procedures, yielding nanotubes with varying wall thickness and morphology. Nanotubes of boron nitride were first prepared by Chopra *et al.* [133] by a carbon-free plasma discharge between a BN packed tungsten rod and a cooled copper electrode. BN nanotubes have been prepared by the carbothermal reduction

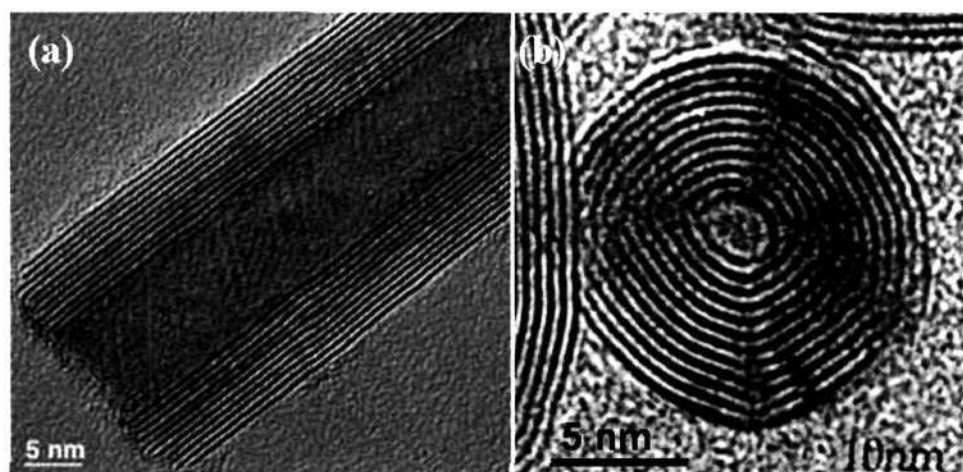


Figure 1.19: HREM images of (a) MoS₂ nanotubes and (b) WS₂ fullerene.

of ultradisperse amorphous boron oxide and B₄C in the presence of nitrogen between 1100 and 1450 °C [134], and by thermal annealing of ball-milled boron powder in an ammonia atmosphere [135]. Carbon nanotubes have been used to prepare BN nanotubes by the reaction with B₂O₃ in a nitrogenous atmosphere. Thus, Golberg *et al.* [136] have synthesized multi-walled BN nanotube ropes by carrying out the reaction of a mixture of B₂O₃ and MWNTs at 1500 °C in a nitrogen atmosphere in the presence of a MoO₃ catalyst.

The metal dichalcogenides, MX₂ (M = Mo, W, Nb, Hf; X = S, Se) contain a metal layer sandwiched between two chalcogen layers with the metal in a trigonal pyramidal or octahedral coordination mode. Tenne *et al.* [137,138] first demonstrated that Mo and W dichalcogenides are capable of forming nanotubes. Closed fullerene-type structures (inorganic fullerenes) also formed along with the nanotubes. The dichalcogenide structures contain concentrically nested fullerene cylinders, with a less regular structure than in the carbon nanotubes. Rao and co-workers [139] have showed that amorphous MX₃ is an intermediate product obtained in the reaction and inorganic nanotubes and fullerenes can be directly obtained from MX₃ under

reductive conditions. Using this method they have synthesized nanotubes of MoS_2 , MoSe_2 , WS_2 , WSe_2 , NbS_2 , NbSe_2 , etc [139–144]. Typical TEM images of inorganic nanotubes and nanowires are shown in Figure 1.19. Transition metal chalcogenides possess a wide range of interesting physical properties. They are widely used in catalysis and as lubricants. They have both semi-conducting and superconducting properties. The quasi-spherical shape of the fullerene-like WS_2 and MoS_2 nanoparticles and their inert sulphur-terminated surface suggested that they could serve as superior solid lubricants in the form of additives to lubrication fluids, greases and for self-lubricating coatings.

1.5 Inorganic Nanowires

One-dimensional nanostructures such as wires, belts and rods of important inorganic materials have been synthesized in the last few years [145, 146]. Nanowires are expected to play an important role as both interconnects and functional units in fabricating electronic, optoelectronic, electrochemical and electromechanical devices.

1.5.1 Synthesis

One-dimensional nanowires can be prepared by a variety of physical methods which include lithography techniques such as electron-beam (e-beam) or focused ion beam writing, proximal probe patterning and extreme UV or x-ray photolithography. An important aspect of the one-dimensional structures relates to their crystallization, wherein the evolution of a solid from a vapor, a liquid, or a solid phase involves nucleation and growth (Figure 1.20 (b)). As the concentration of the building blocks (atoms, ions or molecules) of a solid becomes sufficiently high, they aggregate into small nuclei (clusters) through homogeneous nucleation [147]. These clusters serve as seeds for the further growth to form larger clusters. Several chemical methods have been

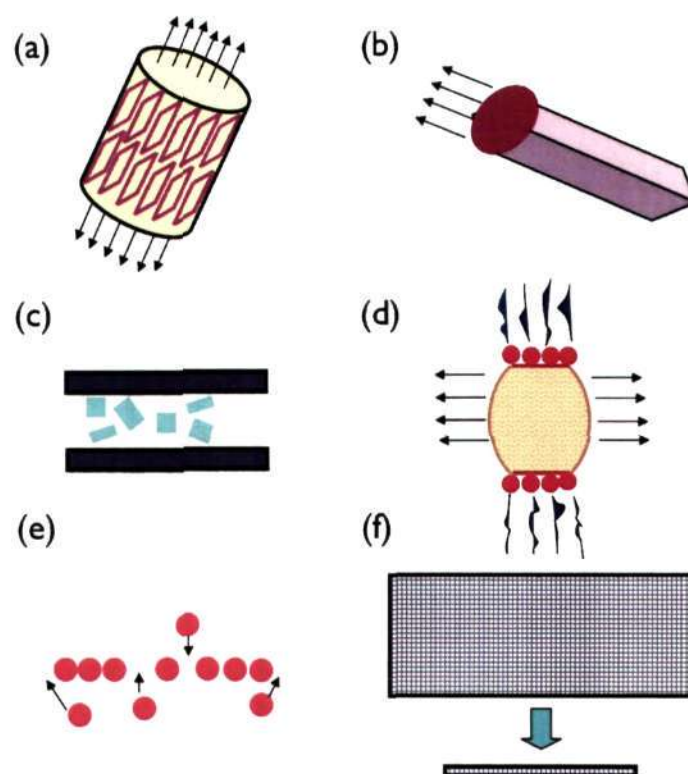


Figure 1.20: Schematic illustration of six strategies that have been demonstrated for achieving 1D growth.

developed for the synthesis of nanowires. In Figure 1.20, we illustrate the six commonly used strategies for the preparation of nanowires. They are:

- ◇ Use of intrinsically anisotropic crystallographic structure of a solid to obtain 1-D nanostructures. Se [148–150], Te as well as molybdenum chalcogenides have been prepared.
- ◇ Growth from vapor phase involving either the vapor-solid (VS) or the vapor-liquid-solid (VLS) mechanism. Several classes of nanowires have been prepared employing this approach.
- ◇ Use of various templates which include porous membranes such as anodic alumina (AAO) membranes and track-etched polymer membranes. Existing one-dimensional structures such carbon nanotubes and nanowires have been used as templates for the synthesis of nanowires

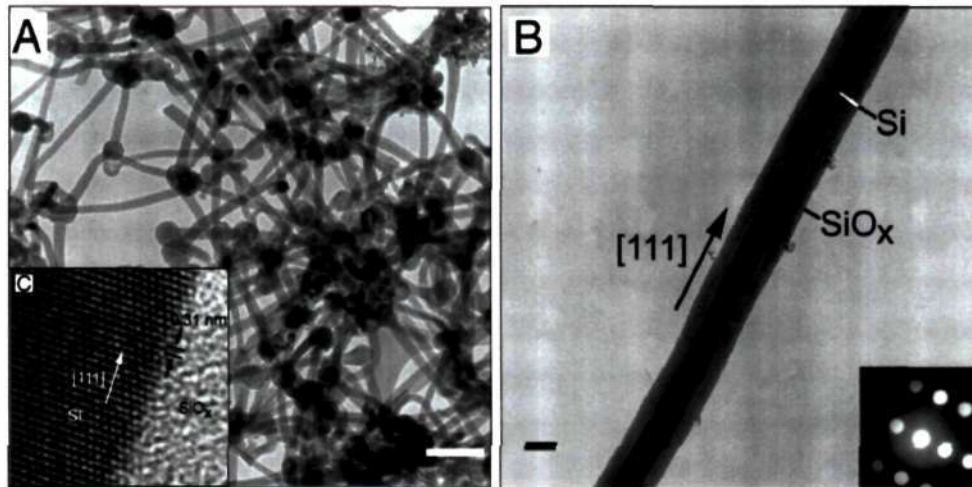


Figure 1.21: Silicon nanowires obtained by the VLS mechanism using the laser ablation process. (From ref. [151])

as well as nanotubes.

- ◇ Appropriate capping agents have been used to kinetically control the growth rates at various facets of the seed.
- ◇ Self assembly of zero dimensional nanostructures to one-dimensional nanostructures by oriented attachment.
- ◇ Use of supersaturation to control and modify the growth habitat of the seed.

In 1960s, Wigner [147] proposed the VLS mechanism for the growth of large single-crystalline silicon whiskers. According to the mechanism, the anisotropic growth is promoted by the presence of the liquid alloy/solid interface. Nanowires of Si, Ge and binary semiconductors such as GaAs, ZnO etc. have been prepared using this route. Laser ablation of appropriate targets [151, 152] and thermal evaporation [153] of appropriate precursor has been used for the synthesis of nanowires by this method. Si nanowires prepared by the laser ablation route is shown in Figure 1.21 Until recently, the only evidence for the growth of nanowires by the VLS mechanism is

the presence of droplets at the end of the nanowires. Wu *et al.* [154] have reported real-time observation of Ge nanowire growth in an *in-situ* high-temperature TEM, which demonstrates the validity of the VLS mechanism. The experimental observations suggest that there are three stages in the growth: metal alloying, crystal nucleation and axial growth. Lee and co-workers [155, 156] have proposed an oxide assisted growth mechanism for the growth of Si nanowires in the absence of catalyst. In the presence of SiO₂, the yield of the Si nanowires increases. Si_xO (x > 1) vapors are generated by the thermal evaporation or laser ablation which decomposes to give Si nanowires. One-dimensional nanostructures can be obtained by the VS process if one can control the nucleation and growth process. Nanowires of several oxide like ZnO, SnO₂, etc. have been synthesized by the process. Carbothermal route is a simple route for the synthesis of several classes of nanowires. The process involves the heating a mixture of the precursor (generally oxide) with carbon (activated carbon or carbon nanotubes) in a suitable atmosphere [157]. The first step normally involves the formation of a volatile metal suboxide by the reaction with carbon. Oxide, nitride or carbide nanowires are obtained when the suboxide is heated in the presence of O₂, NH₃, N₂ or C.

Solution based approaches utilize the anisotropic growth dictated by the crystallographic structure of the solid material, or confined and directed by templates, or kinetically controlled by supersaturation, or by the use of appropriate capping agent. Buhro and coworkers [158] have developed a low-temperature solution-liquid-solid (SLS) method for the synthesis of crystalline nanowires of III-V semiconductors. A metal with a low melting point is used a catalyst and the desired material material generated through the decomposition of organometallic precursor. Korgel *et al.* [159] have extended this strategy for the synthesis of Si and Ge nanowires in supercritical fluids.

1.5.2 Properties and Applications

Various properties and applications of nanowires of different materials have been investigated widely in the literature. Due to their high surface area, the nanowires exhibit significantly lower melting point which is inversely proportional to the diameter of the nanowire [160]. Surface plasmon properties of gold and silver nanorods have been investigated by El-Sayed and coworkers [161]. One-dimensional nanostructures exhibit two surface plasmon corresponding to the transverse and longitudinal plasmon resonances. Absorption and scattering properties of gold nanoparticles of different size, shape, and composition have been calculated using Mie theory and discrete dipole approximation method [162]. Absorption and scattering efficiencies and optical resonance wavelengths have been calculated for three commonly used classes of nanoparticles: gold nanospheres, silica-gold nanoshells, and gold nanorods. The calculated spectra clearly reflect the well-known dependence of the optical properties (viz. the resonance wavelength, the extinction cross-section, and the ratio of scattering to absorption), on the nanoparticle dimensions. Gold nanorods show optical cross-sections comparable to nanospheres and nanoshells, however, at much smaller effective size. To compare the effectiveness of nanoparticles of different sizes for real biomedical applications, size-normalized optical cross-sections or per micron coefficients are calculated. Gold nanorods show per micron absorption and scattering coefficients that are an order of magnitude higher than those for nanoshells and nanospheres. Multiple higher-order plasmon resonances in colloidal cylindrical gold nanorods electrochemically deposited in anodic aluminum oxide templates (AAO) have been studied [163]. Homogeneous suspensions of nanorods with an average diameter of 85 nm and with varying lengths have been used. The AAO template provided a synthetic route that resulted in a homogeneous suspension of rods with the proper dimensions to

observe these modes. The experimental optical spectra agree with discrete dipole approximation calculations (DDA) that have been modeled from the dimensions of the gold nanorods. As in the lithographically generated patterns, both the even and odd modes were detected up to the seventh order and were in good agreement with DDA. Fabrication of a self-organized photosensitive gold nanoparticle chain encapsulated in a dielectric nanowire has been achieved by using a microreactor approach [164]. Such a hybrid nanowire shows pronounced surface plasmon resonance (SPR) absorption. More remarkably, a strong wavelength-dependent and reversible photoreponse has been demonstrated in a two-terminal device using an ensemble of gold nanopod silica nanowires under illumination, whereas no photoreponse was observed for the plain silica nanowires. These results show the potential of using gold nanopodded silica nanowires as wavelength-controlled optical nanoswitches.

Nanowires have recently been explored as building blocks to fabricate nanoscale electronic devices through self-assembly. Nanowire based field-effect transistors (FETs), p-n junctions, bipolar junction transistors, complementary inverters and resonant tunneling diodes have been fabricated [165,166]. Nanowires with very short lengths (usually few atoms across) also exhibit ballistic transport (conductance quantization in units of $2 e^2 h^{-1}$). Self-assembly of nanowires has been used by Huang *et al.* [167] for the fabrication of OR, AND, and NOR logic-gate structures. Field-effect transistors of ZnO nanowires have been fabricated and studied in vacuum and in a variety of ambient gases [168]. Field-effect transistors based on the self-assembly of colloidal ZnO nanorods have also been examined [169]. ZnO nanowire field-effect transistors composed of individual ZnO nanowires can be made using a self-assembled superlattice as the gate insulator, a device of possible

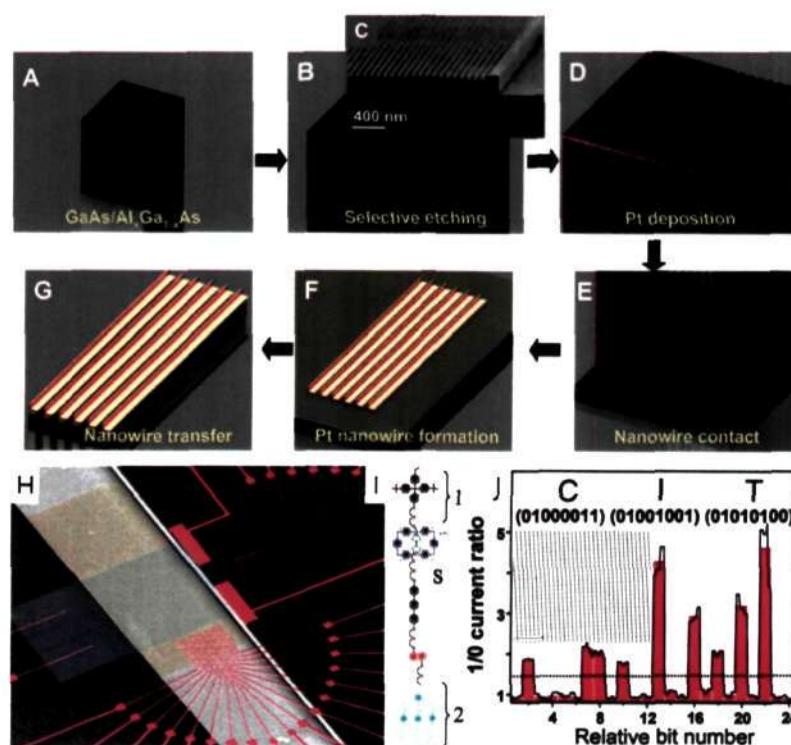


Figure 1.22: (A)-(G) The SNAP process of fabricating nanowires on substrates using GaAs/Al_xGa_{1-x}As superlattice as the master. (H) False-color SEM micrograph of the 160 kilo-bit memory is shown at left. (I) The bistable, electrochemically switchable, amphiphilic [2]-rotaxane molecule (J) ASCII character read and write memory demonstration. (From ref. [172])

use in flexible display and logic technologies [170]. Piezoelectric nanogenerators based on ZnO nanowire arrays have been shown to convert nanoscale mechanical energy into electrical energy with the efficiency of the power generation of 17 to 30% [171]. The coupling of piezoelectric and semiconducting properties of zinc oxide creates a strain field and charge separation across the nanowire as a result of its bending. The rectifying characteristic of the Schottky barrier formed between the metal tip and the nanowire leads to electrical current generation. Heath and co-workers [172] have fabricated a nanowire-based memory with a high storage density. The nanowires were fabricated using a “Superlattice nanowire pattern transfer” (SNAP) process and is shown schematically in Figure 1.22. In contrast to quantum dots, the light emitted from nanowires is highly polarized along their longitudinal axes and

polarization sensitive nanoscale photodetectors have been fabricated [173]. The longitudinal resonance energy is inversely proportional to the nanowire length. Room temperature UV-lasing from ZnO nanowire arrays have been observed [174]. Aligned CdS nanowires are shown to exhibit optical waveguide behavior on continuous-wave laser excitation [175]. Optically pumped room-temperature lasing in GaN nanowires with low lasing thresholds has been reported [176]. Nanoscale light-emitting diodes with colors ranging from ultraviolet to near-infrared have been prepared using a solution-based approach in which electron-doped semiconductors are assembled with hole-doped silicon nanowires in crossed nanowire architecture [177].

Light induced insulator to conductor transition has been observed in ZnO nanowires by Kind *et al.* [178], which could be used as UV detectors and photo-switches. Single-crystal ZnO nanowires can be used as ultraviolet photodetectors [179]. A ZnO nanowire photodetector with a fast photoresponse time was fabricated by a simple method of growing ZnO nanowires by bridging the gap of two patterned zinc electrodes [180]. The nanowire growth is self-catalytic, involving the direct heating of patterned Zn electrodes at 700 °C in an O₂/Ar gas flow for 3 h. The fabricated photodetector demonstrated fast response of shorter than 0.4 ms to UV illumination in air, which could be attributed to the adsorption, desorption, and diffusion of water molecules in the air onto the nanowire significantly influencing the photoresponse.

As the dimension of the nanowire is reduced the phonon mean free path and the thermal conductivity are reduced due to the scattering by the boundaries. The reduced thermal conductivity is desirable for applications such as thermoelectric cooling and power generation. The thermoelectric figure of merit (Z) could be substantially enhanced for thin nanowires by carefully controlling their diameter, composition and carrier concentrations

[181,182]. Dresselhaus and coworkers [183] observe a semi-metal to semiconductor transition in Bi nanowire arrays when the diameter is 52 nm. Size-dependent transport and thermoelectric properties of individual polycrystalline Bi nanowires has been reported [184]. The combination of nanofabrication methods and device architecture has allowed four-point electric, thermoelectric, magnetic-field and electric-field-effect measurements on individual Bi nanowires. No clear semimetal-to-semiconductor transition or enhancement in thermoelectric power has been observed, probably due to the polycrystalline nature of Bi nanowires.

Single crystalline one-dimensional nanostructures are supposed to have significantly superior mechanical properties than their counterparts that have larger dimensions. SiC nanorods pinned at one end of the solid surface (see Figure 1.23) have a Young's modulus of 610-660 GPa in good agreement with theoretical predications [185]. Gold nanowires show an Youngs modulus which is independent of diameter whereas the yield strength is largest for the smallest diameter nanowires [186]. The elastic modulus of (0001) ZnO nanowires grown on a sapphire surface has been measured (29 ± 8 GPa) using atomic force microscopy [187]. ZnS nanobelts exhibit 79% increase in hardness and 52% decrease in elastic modulus compared to bulk ZnS [188].

A high-throughput procedure is reported for lithographically processing one-dimensional nanowires [189]. This procedure has been called on-wire lithography. ZnO nanorods, nanowires and nanotubes prepared by different procedures including prepared by electrochemical deposition in alumina membranes have been investigated for hydrogen and ethanol sensing characteristics [190]. The sensing characteristics of these nanostructures were also investigated after impregnating them with 1% Pt. The nanowires exhibit excellent hydrogen sensing characteristics at relatively low temperatures ($< 150^\circ\text{C}$). One type of nanorods shows a dependence of the sensitivity on the

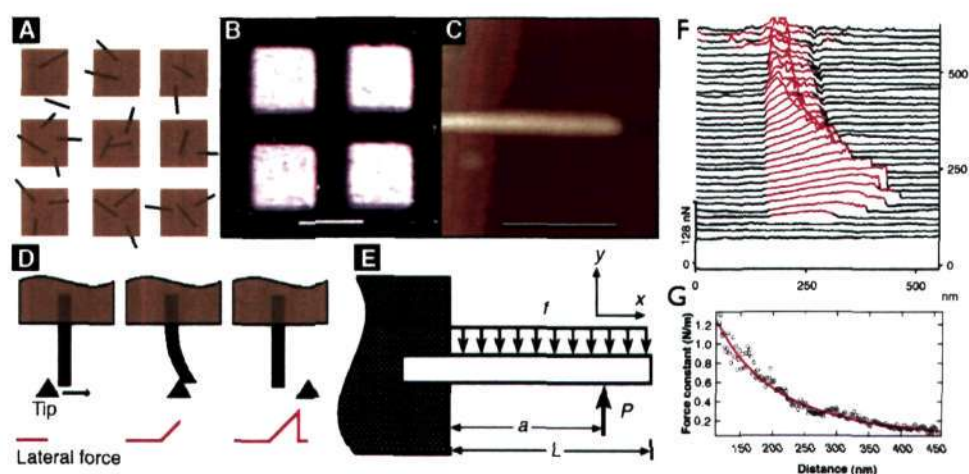


Figure 1.23: (A) SiC NRs deposited on a cleaved MoS₂ substrate, and then pinned by deposition of a grid of square SiO pads. (B) Optical micrograph of a sample showing the SiO pads (white) and the MoS₂ substrate (blue). (C) An AFM image of a 35.3 nm diameter SiC NR protruding from a SiO pad (scale bar is 500 nm). (D) Schematic of beam bending with an AFM tip. (E) Schematic of a pinned beam with a free end. (F) F-d response of a 23.0 nm diameter SiC NR recorded with a normal load of 7.7 nN. (G) Dependence of the force constant $k(x)$ on position x along the axis of the same NR. (From ref. [185])

hydrogen concentration, along with short recovery and response times. The nanorods and nanowires impregnated with Pt show high sensitivity for 1000 ppm of ethanol at or below 150 °C, with short recovery and response times. Both nanorods and nanowires exhibit good sensing characteristics for 1000 ppm of ethanol at or below 423 K, where as Pt impregnated nanorods and nanowires show better sensitivity for both hydrogen and ethanol.

There has been tremendous interest in the use of nanomaterials in energy storage and generation. Intercalation of lithium ions in TiO₂-B nanowires has been carried out without any structural degradation or loss of nanowire morphology [191]. Photovoltaic applications of aligned silicon nanowire arrays have been explored [192]. Dye-sensitized solar cells incorporating ZnO nanowires have been assembled [193, 194]. Dye-sensitized solar cells using TiO₂ single-crystalline nanorod electrodes provide efficient photocurrent generation in a quasi-solid-state, with a conversion efficiency of 6.2% under 100

mW/cm² [195]. A method based on template synthesis has been used for the construction of an array of coplanar fuel cells wherein each cell is 200 nm in diameter [196]. An array of nano fuel cells is produced by utilizing two arrays of porous Pt electrodes in between a polymer electrolyte membrane or an electrolyte support matrix sandwiched. Electrodeposition of Pt-Cu nanowires inside a porous AAO membrane and the subsequent treatment with fuming HNO₃ acid gives rise to an array of porous platinum electrodes. This method of producing an array of coplanar fuel cells allows for the series connection of fuel cells outside the array and eliminates the need for fuel and air manifolds, thereby reducing the overall system complexity. Initial prototypes utilizing an aqueous solution of NaBH₄ as a fuel have produced power densities of around 1 mW/cm².

It has been demonstrated how light force, irrespective of the polarization of the light, can be used to run a simple nanorotor [197]. While the gradient force of a single beam optical trap is used to hold an asymmetric nanorod, the utilization of the scattering force generates a torque on the nanorod, making it rotate about the optic axis. The inherent textural irregularities or morphological asymmetries of the nanorods give rise to the torque under the radiation pressure. Even a small surface irregularity with non-zero chirality is sufficient to produce enough torque for moderate rotational speed. Self-powered synthetic nanorotors have been prepared from bar-coded gold-nickel nanorods having the gold end anchored to the surface of a silicon wafer. Constant velocity circular movements are observed when hydrogen peroxide is catalytically decomposed to oxygen at the unattached nickel end of the nanorod [198].

1.6 References

1. C. N. R. Rao, A. Muller, and A. K. Cheetham, *The Chemistry of Nanomaterials* (WILEY-VCH, Weinheim, 2004).
2. C. N. R. Rao and A. Govindaraj, *Nanotubes and Nanowires* (Royal Society of Chemistry, London, 2005).
3. M. Faraday, *Philos. Trans. R. Soc. London.* **147**, 145 (1857).
4. R. Feynman, *Miniaturization* (Reinhold, New York, 1961).
5. J. Lehn, *Supramolecular Chemistry* (VCH, Weinheim, 1995).
6. H. W. Kroto, J. R. Heath, S. C. O'Brien, R. Curl, and R. E. Smalley, *Nature* **318**, 162 (1985).
7. W. Kratschmer, L. Lamb, K. Fostiropoulos, and D. Huffman, *Nature* **347**, 354 (1990).
8. S. Iijima, *Nature* **354**, 56 (1991).
9. K. S. Novoselov, D. Jiang, F. Schedin, T. J. Booth, V. V. Khotkevich, S. V. Morozov, and A. K. Geim, *Proc. Natl. Acad. Sci. U.S.A.* **102**, 10451 (2005).
10. K. S. Novoselov, A. K. Geim, S. V. Morozov, D. Jiang, M. I. Katsnelson, I. V. Grigorieva, S. V. Dubonos, and A. A. Firsov, *Nature* **438**, 197 (2005).
11. D. T. Colbert, J. Zhang, S. M. McClure, P. Nikolaev, Z. Chen, J. H. Hafner, D. W. Owens, P. G. Kotula, C. B. Carter, J. H. Weaver, A. G. Rinzler, and R. E. Smalley, *Science* **266**, 1218 (1994).
12. D. S. Bethune, C. H. Kiang, M. S. De Vries, G. Gorman, R. Savoy, J. Vazquez, and R. Beyers, *Nature* **363**, 605 (1993).
13. S. Iijima and T. Ichihashi, *Nature* **363**, 603 (1993).
14. C. Journet, W. K. Maser, P. Bernier, A. Loiseau, M. Lamy de la Chapelle, S. Lefrant, P. Deniard, R. Lee, and J. E. Fischer, *Nature* **388**, 756 (1997).
15. A. Thess, R. Lee, P. Nikolaev, H. Dai, P. Petit, J. Robert, C. Xu, Y. H. Lee, S. G. Kim, A. G. Rinzler, D. T. Colbert, G. E. Scuseria, D. Tománek, J. E. Fischer, and R. E. Smalley, *Science* **273**, 483 (1996).
16. W. K. Hsu, J. P. Hare, M. Terrones, H. W. Kroto, D. R. M. Walton, and P. J. F. Harris, *Nature* **377**, 687 (1995).
17. Y. Gogotsi, J. A. Libera, and M. Yoshimura, *J. Mater. Res.* **15**, 2591 (2000).

18. C. N. R. Rao, A. Govindaraj, R. Sen, and B. C. Satishkumar, *Mater. Res. Inno.* **2**, 128 (1998).
19. C. N. R. Rao, B. C. Satishkumar, A. Govindaraj, and M. Nath, *Chem-PhysChem* **2**, 78 (2001).
20. C. N. R. Rao and A. Govindaraj, *Acc. Chem. Res.* **35**, 998 (2002).
21. M. J. Yacaman, M. M. Yoshida, L. Rendón, and T. Santiesteban, *Appl. Phys. Lett.* **62**, 202 (1993).
22. V. Ivanov, J. B. Nagy, P. Lambin, A. Lucas, Z. B. Zhang, D. Bernaerts, G. V. Tendeloo, A. Amelinckx, and J. V. Landuyt, *Chem. Phys. Lett.* **223**, 329 (1994).
23. K. Hernadi, A. Fonseca, J. B. Nagy, D. Bernaerts, J. Riga, and A. Lucas, *Synth. Met.* **77**, 31 (1996).
24. N. M. Rodriguez, *J. Mater. Res.* **8**, 3233 (1993).
25. W. Z. Li, S. S. Xie, L. X. Qian, B. H. Chang, B. S. Zou, W. Y. Zhou, R. A. Zhao, and G. Wang, *Science* **274**, 1701 (1996).
26. G. Che, B. B. Lakshmi, C. R. Martin, E. R. Fisher, and R. S. Ruoff, *Chem. Mater.* **10**, 260 (1998).
27. Z. F. Ren and Z. P. Huang, *Science* **282**, 1105 (1998).
28. R. Sen, A. Govindaraj, and C. N. R. Rao, *Chem. Phys. Lett.* **267**, 276 (1997).
29. R. Sen, B. C. Satishkumar, A. Govindaraj, K. R. Harikumar, M. K. Renganathan, and C. N. R. Rao, *J. Mater. Chem.* **7**, 2335 (1997).
30. M. Yudasaka, R. Kikuchi, Y. Ohki, and S. Yoshimura, *Carbon* **35**, 195 (1997).
31. B. C. Satishkumar, A. Govindaraj, and C. N. R. Rao, *Chem. Phys. Lett.* **307**, 158 (1999).
32. B. C. Satishkumar, A. Govindaraj, P. V. Vanitha, A. K. Raychaudhuri, and C. N. R. Rao, *Chem. Phys. Lett.* **362**, 301 (2002).
33. B. C. Satishkumar, P. J. Thomas, A. Govindaraj, and C. N. R. Rao, *Appl. Phys. Lett.* **77**, 2530 (2000).
34. F. L. Deepak, A. Govindaraj, and C. N. R. Rao, *Chem. Phys. Lett.* **345**, 5 (2001).
35. B. C. Satishkumar, A. Govindaraj, R. Sen, and C. N. R. Rao, *Chem. Phys. Lett.* **293**, 47 (1998).

36. C. N. R. Rao, R. Sen, B. C. Satishkumar, and A. Govindaraj, *Chem. Commun.* 1525 (1998).
37. H. M. Cheng, F. Li, G. Su, H. Y. Pan, L. L. He, X. Sun, and M. S. Dresselhaus, *Appl. Phys. Lett.* **72**, 3282 (1998).
38. H. Dai, A. G. Rinzler, P. Nikolaev, A. Thess, D. T. Colbert, and R. E. Smalley, *Chem. Phys. Lett.* **260**, 471 (1996).
39. E. Flahaut, A. Govindaraj, A. Peigney, C. Laurent, A. Rousset, and C. N. R. Rao, *Chem. Phys. Lett.* **300**, 236 (1999).
40. M. Endo and H. W. Kroto, *J. Phys. Chem.* **96**, 6491 (1992).
41. T. W. Ebbesen, J. Tabuchi, and K. Tanigaki, *Chem. Phys. Lett.* **1991**, 336 (1992).
42. S. Iijima, P. M. Ajayan, and T. Ichihashi, *Phys. Rev. Lett.* **69**, 3100 (1992).
43. A. Oberlin, M. Endo, and T. Koyama, *J. Crys. Growth* **32**, 335 (1976).
44. S. Iijima, *MRS Bulletin* **19**, 43 (1994).
45. J. W. Mintmire, B. I. Dunlap, and C. T. White, *Phys. Rev. Lett.* **68**, 631 (1992).
46. N. Hamada, S. Sawada, and A. Yoshiyama, *Phys. Rev. Lett.* **68**, 1579 (1992).
47. R. Saito, M. Jujita, G. Dresselhaus, and M. S. Dresselhaus, *Appl. Phys. Lett.* **60**, 2204 (1992).
48. J. W. G. Wildöer, L. C. Venema, A. G. Rinzler, R. E. Smalley, and C. Dekker, *Nature* **391**, 59 (1998).
49. T. W. Odom, J. Huang, P. Kim, and C. M. Lieber, *Nature* **391**, 62 (1998).
50. M. Ouyang, J. L. Huang, and C. M. Lieber, *Acc. Chem. Res.* **35**, 1018 (2002).
51. A. Das, A. K. Sood, A. Govindaraj, A. M. Saitta, M. Lazzeri, F. Mauri, and C. Rao, *Phys. Rev. Lett.* **99**, 136803 (2007).
52. A. M. Rao, E. Richter, S. Bandow, B. Chase, P. C. Eklund, K. A. Williams, S. Fang, K. R. Subbaswamy, M. Menon, A. Thess, R. E. Smalley, G. Dresselhaus, and M. S. Dresselhaus, *Science* **275**, 187 (1997).
53. M. S. Dresselhaus, G. Dresselhaus, A. Jorio, A. G. Souza Filho, M. A. Pimenta, and R. Saito, *Acc. Chem. Res.* **35**, 1070 (2002).

54. S. Amelinckx, A. Lucas, and P. Lambin, *Rep. Prog. Phys.* **62**, 1471 (1999).
55. R. Seshadri, A. Govindaraj, H. Aiyer, R. Sen, G. N. Subbanna, A. Raju, and C. Rao, *Current Sci.* **66**, 839 (1994).
56. A. Hirsch, *Angew. Chem. Inter. Ed.* **41**, 1853 (2002).
57. D. Tasis, N. Tagmatarchis, A. Bianco, and M. Prato, *Chem. Rev.* **106**, 1105 (2006).
58. E. Joselevich, *ChemPhysChem* **5**, 619 (2004).
59. M. A. Hamon, H. Hu, P. Bhowmik, S. Niyogi, B. Zhao, M. E. Itkis, and R. C. Haddon, *Chem. Phys. Lett.* **347**, 8 (2001).
60. D. B. Mawhinney, V. Naumenko, A. Kuznetsova, J. T. Yates, J. Liu, and R. E. Smalley, *Chem. Phys. Lett.* **324**, 213 (2001).
61. M. A. Hamon, J. Chen, H. Hu, Y. Chen, M. E. Itkis, A. M. Rao, P. C. Eklund, and R. C. Haddon, *Adv. Mater.* **11**, 834 (1999).
62. J. Chen, A. M. Rao, S. Lyuksyutov, M. E. Itkis, M. A. Hamon, H. Hu, R. W. Cohn, P. C. Eklund, D. T. Colbert, R. E. Smalley, and R. C. Haddon, *J. Phys. Chem. B* **105**, 2525 (2001).
63. A. Kukovecz, C. Kramberger, M. Holzinger, H. Kuzmany, J. Schalko, M. Mannsberger, and A. Hirsch, *J. Phys. Chem. B* **106**, 6374 (2002).
64. A. Hirsch, *Top. Curr. Chem.* **199**, 1 (1999).
65. A. Hamwi, H. Alvergnat, S. Bonnamy, and F. Béguin, *Carbon* **35**, 723 (1997).
66. E. T. Mickelson, C. B. Huffman, A. G. Rinzler, R. E. Smalley, R. H. Hauge, and J. L. Margrave, *Chem. Phys. Lett.* **296**, 188 (1998).
67. J. L. Stevens, A. Y. Huang, H. Peng, I. W. Chiang, V. N. Khabashesku, and J. L. Margrave, *Nano Lett.* **3**, 331 (2003).
68. K. F. Kelly, I. W. Chiang, E. T. Mickelson, R. H. Hauge, J. L. Margrave, X. Wang, G. E. Scuseria, C. Radloff, and N. J. Halas, *Chem. Phys. Lett.* **313**, 445 (1999).
69. E. T. Mickelson, I. W. Chiang, J. L. Zimmerman, P. J. Boul, J. Lozano, J. Liu, R. E. Smalley, R. H. Hauge, and J. L. Margrave, *J. Phys. Chem. B* **103**, 4318 (1999).
70. P. J. Boul, J. Liu, E. T. Mickelson, C. B. Huffman, L. M. Ericson, I. W. Chiang, K. A. Smith, D. T. Colbert, R. H. Hauge, J. L. Margrave, and R. E. Smalley, *Chem. Phys. Lett.* **310**, 367 (1999).

71. R. J. Chen, Y. Zhang, D. Wang, and H. Dai, *J. Am. Chem. Soc.* **123**, 3838 (2001).
72. S. A. Curran, P. M. Ajayan, W. J. Blau, D. L. Carroll, J. N. Coleman, A. B. Dalton, A. P. Davey, A. Drury, B. McCarthy, S. Maier, and A. Strevens, *Adv. Mater.* **10**, 1091 (1998).
73. R. Krupke, F. Hennrich, H. V. Löhneysen, and M. M. Kappes, *Science* **301**, 344 (2003).
74. R. Krupke, S. Linden, M. Rapp, and F. Hennrich, *Adv. Mater.* **18**, 1468 (2006).
75. T. Lutz and K. J. Donovan, *Carbon* **43**, 2508 (2005).
76. H. Peng, N. T. Alvarez, C. Kittrell, R. H. Hauge, and H. K. Schmidt, *J. Am. Chem. Soc.* **128**, 8396 (2006).
77. M. S. Arnold, A. A. Green, J. Hulvat, S. I. Stupp, and M. C. Hersam, *Nature Nanotech.* **1**, 60 (2006).
78. C. Yang, J. S. Park, K. H. An, S. C. Lim, K. Seo, B. Kim, K. A. Park, S. Han, C. Y. Park, and Y. H. Lee, *J. Phys. Chem. B* **109**, 19242 (2005).
79. Y. Maeda, S. Kimura, M. Kanda, Y. Hirashima, T. Hasegawa, T. Wakahara, Y. Lian, T. Nakahodo, T. Tsuchiya, T. Akasaka, J. Lu, X. Zhang, Z. Gao, Y. Yu, S. Nagase, S. Kazaoui, N. Minam, T. Shimizu, H. Tokumoto, and R. Saito, *J. Am. Chem. Soc.* **127**, 10287 (2005), cited By (since 1996): 46.
80. C. Ménard-Moyon, N. Izard, E. Doris, and C. Mioskowski, *J. Am. Chem. Soc.* **128**, 6552 (2006).
81. H. Huang, R. Maruyama, K. Noda, H. Kajiura, and K. Kadono, *J. Phys. Chem. B* **110**, 7316 (2006).
82. H. Huang, H. Kajiura, R. Maruyama, K. Kadono, and K. Noda, *J. Phys. Chem. B* **110**, 4686 (2006).
83. A. A. Green and M. C. Hersam, *Mater. Today* **10**, 59 (2007).
84. M. S. Arnold, S. I. Stupp, and M. C. Hersam, *Nano Lett.* **5**, 713 (2005).
85. B. C. Satishkumar, E. M. Vogl, A. Govindaraj, and C. N. R. Rao, *J. Phys. D* **29**, 3173 (1996).
86. A. Govindaraj, B. C. Satishkumar, M. Nath, and C. N. R. Rao, *Chem. Mater.* **12**, 202 (2000).
87. J. Sloan, A. I. Kirkland, J. L. Hutchison, and M. L. H. Green, *Chem. Commun.* 1319 (2002).

88. B. W. Smith, M. Monthieux, and D. E. Luzzi, *Nature* **396**, 323 (1998).
89. W. Liang, M. Bockrath, D. Bozovic, J. H. Hafner, M. Tinkham, and H. Park, *Nature* **411**, 665 (2001).
90. S. J. Tans, A. R. M. Verschueren, and C. Dekker, *Nature* **393**, 49 (1998).
91. P. Avouris, Z. Chen, and V. Perebeinos, *Nature Nanotech.* **2**, 605 (2007).
92. M. Menon and D. Srivastava, *Phys. Rev. Lett.* **79**, 4453 (1997).
93. P. R. Bandaru, C. Daraio, S. Jin, and A. M. Rao, *Nat. Mater.* **4**, 663 (2005).
94. B. R. Perkins, D. P. Wang, D. Soltman, A. J. Yin, J. M. Xu, and Zaslavsky, *Appl. Phys. Lett.* **87**, 123504 (2005).
95. D. H. Kim, J. Huang, B. K. Rao, and W. Choi, *J. Appl. Phys.* **99**, 056106 (2006).
96. L. Dong, V. Chirayos, J. Bush, J. Jiao, V. M. Dubin, R. V. Chebrian, Y. Ono, J. F. Conley Jr, and U. B. D., *J. Phys. Chem. B* **109**, 13148 (2005).
97. R. V. Seidel, A. P. Graham, J. Kretz, B. Rajasekharan, G. S. Duesberg, M. Liebau, E. Unger, F. Kreupl, and W. Hoenlein, *Nano Lett.* **5**, 147 (2005).
98. S. Auvray, V. Derycke, M. Golfman, A. Filoramo, O. Jost, and J. P. Bourgoin, *Nano Lett.* **5**, 451 (2005).
99. V. Lovat, D. Pantarotto, L. Lagostena, B. Cacciari, M. Grandolfo, M. Righi, Spalluto, M. Prato, and L. Ballerini, *Nano Lett.* **5**, 1107 (2005).
100. J. Hone, I. Ellwood, M. Munro, A. Mizel, M. L. Cohen, A. Zettl, A. G. Rinzler, and R. E. Smalley, *Phys. Rev. Lett.* **80**, 1042 (1998).
101. Y. Saito, K. Hamaguchi, S. Uemura, K. Uchida, Y. Tasaka, F. Ikazaki, M. Yumura, A. Kasuya, and Y. Nishina, *Appl. Phys. A* **67**, 95 (1998).
102. Y. Saito and S. Uemura, *Carbon* **38**, 169 (2000).
103. W. B. Choi, D. S. Chung, J. H. Kang, H. Y. Kim, Y. W. Jin, I. T. Han, Y. H. Lee, J. E. Jung, N. S. Lee, G. S. Park, and J. M. Kim, *Appl. Phys. Lett.* **75**, 3129 (1999).
104. R. B. Sharma, V. N. Tondare, D. S. Joag, A. Govindaraj, and C. N. R. Rao, *Chem. Phys. Lett.* **344**, 283 (2001).

105. S. R. Mishra, H. S. Rawat, S. C. Mehendale, K. C. Rustagi, A. K. Sood, R. Bandyopadhyay, A. Govindaraj, and C. N. R. Rao, *Chem. Phys. Lett.* **317**, 510 (2000).
106. K. H. An, W. S. Kim, Y. S. Park, J. Moon, D. J. Bae, S. C. Lim, Y. S. Lee, and Y. H. Lee, *Adv. Funt. Mater.* **11**, 387 (2001).
107. C. Niu, E. K. Sichel, R. Hoch, D. Moy, and H. Tennent, *Appl. Phys. Lett.* **70**, 1480 (1997).
108. R. H. Baughman, C. Cui, A. A. Zakhidov, Z. Iqbal, J. N. Barisci, G. M. Spinks, G. G. Wallace, A. Mazzoldi, D. De Rossi, A. G. Rinzler, O. Jaschinski, S. Roth, and M. Kertesz, *Science* **284**, 1340 (1999).
109. C. Zhou, S. Kumar, C. D. Doyle, and J. M. Tour, *Chem. Mater.* **17**, 1997 (2005).
110. J. S. Ye, H. F. Cui, X. Liu, T. M. Lim, W. D. Zhang, and F. S. Sheu, *Small* **1**, 560 (2005).
111. F. Beguin, K. Szostak, G. Lota, and E. Frackowiak, *Adv. Mater.* **17**, 2380 (2005).
112. C. Du, J. Yeh, and N. Pan, *Nanotechnology* **16**, 350 (2005).
113. T. Hasobe, S. Fukuzumi, and P. V. Kamat, *Angew. Chem. Inter. Ed.* **45**, 755 (2006).
114. D. M. Guldi, G. M. A. Rahman, M. Prato, N. Jux, S. Qin, and W. Ford, *Angew. Chem. Inter. Ed.* **44**, 2015 (2005).
115. I. Robel, B. A. Bunker, and P. V. Kamat, *Adv. Mater.* **17**, 2458 (2005).
116. A. C. Dillon, K. M. Jones, T. A. Bekkedahl, C. H. Kiang, D. S. Bethune, and M. J. Heben, *Nature* **386**, 377 (1997).
117. G. Gundiah, A. Govindaraj, N. Rajalakshmi, K. S. Dhathathreyan, and C. N. R. Rao, *J. Mater. Chem.* **13**, 209 (2003).
118. A. K. Geim and K. S. Novoselov, *Nat. Mater.* **6**, 183 (2007).
119. T. A. Land, T. Michely, R. J. Behm, J. C. Hemminger, and G. Comsa, *Surf. Sci.* **264**, 261 (1992).
120. A. Nagashima, K. Nuka, H. Itoh, T. Ichinokawa, C. Oshima, and S. Otani, *Surf. Sci.* **291**, 93 (1993).
121. A. J. van Bommel, J. E. Crombeen, and A. van Tooren, *Surf. Sci.* **48**, 463 (1975).

122. C. Berger, Z. Song, T. Li, X. Li, A. Y. Ogbazghi, R. Feng, Z. Dai, N. Alexei, M. E. H. Conrad, P. N. First, and W. A. De Heer, *J. Phys. Chem. B* **108**, 19912 (2004).
123. C. Berger, Z. Song, X. Li, X. Wu, N. Brown, C. Naud, D. Mayou, T. Li, J. Hass, A. N. Marchenkov, E. H. Conrad, P. N. First, and W. A. De Heer, *Science* **312**, 1191 (2006).
124. T. Ohta, A. Bostwick, T. Seyller, K. Horn, and E. Rotenberg, *Science* **313**, 951 (2006).
125. P. R. Somani, S. P. Somani, and M. Umeno, *Chem. Phys. Lett.* **430**, 56 (2006).
126. S. Stankovich, D. A. Dikin, G. H. B. Dommett, K. M. Kohlhaas, E. J. Zimney, E. A. Stach, R. D. Piner, S. T. Nguyen, and R. S. Ruoff, *Nature* **442**, 282 (2006).
127. S. Stankovich, R. D. Piner, X. Q. Chen, N. Q. Wu, S. T. Nguyen, and R. S. Ruoff, *J. Mater. Chem.* **16**, 155 (2006).
128. H. C. Schniepp, J. L. Li, M. J. McAllister, H. Sai, M. H. Alonso, D. H. Adamson, R. K. Prud'homme, R. Car, D. A. Saville, and I. A. Aksay, *J. Phys. Chem. B* **110**, 8535 (2006).
129. O. Andersson, B. L. V. Prasad, H. Sato, T. Enoki, Y. Hishiyama, Y. Kaburagi, M. Yoshikawa, and S. Bandow, *Phys. Rev. B* **58**, 16387 (1998).
130. F. Schedin, A. K. Geim, S. V. Morozov, E. W. Hill, P. Blake, M. I. Katsnelson, and K. S. Novoselov, *Nat. Mater.* **6**, 652 (2007).
131. X. Wang, Y. Ouyang, X. Li, H. Wang, J. Guo, and H. Dai, *Phys. Rev. Lett.* **100**, 206803 (2008).
132. C. N. R. Rao and M. Nath, *Dalton Trans.* **1** (2003).
133. N. G. Chopra, R. J. Luyken, K. Cherrey, V. H. Crespi, M. L. Cohen, S. G. Louse, and A. Zettl, *Science* **269**, 966 (1995).
134. V. V. Pokropivny, V. V. Shorokod, G. S. Oleinik, A. V. Kurdyumov, T. S. Bartnitskaya, A. V. Pokropivny, A. G. Sisonyuk, and D. M. Sheichenko, *J. Solid State Chem.* **154**, 214 (2000).
135. Y. Chen, J. F. Gerald, J. S. Williams, and S. Bulcock, *Chem. Phys. Lett.* **299**, 260 (1999).
136. D. Goldberg, Y. Bando, K. Karashima, and T. Sato, *Chem. Phys. Lett.* **323**, 185 (2000).
137. R. Tenne, L. Margulis, M. Genut, and G. Hodes, *Nature* **360**, 444 (1992).

138. Y. Feldman, E. Wasserman, D. J. Srolovitz, and R. Tenne, *Science* **267**, 222 (1995).
139. M. Nath, A. Govindaraj, and C. N. R. Rao, *Adv. Mater.* **13**, 283 (2001).
140. M. Nath and C. N. R. Rao, *Chem. Commun.* 2236 (2001).
141. M. Nath and C. N. R. Rao, *J. Am. Chem. Soc.* **123**, 4841 (2001).
142. M. Nath, K. Mukhopadhyay, and C. N. R. Rao, *Chem. Phys. Lett.* **352**, 163 (2002).
143. M. Nath and C. N. R. Rao, *Angew. Chem. Inter. Ed.* **41**, 3451 (2002).
144. M. Nath, S. Kar, A. K. Raychaudhuri, and C. N. R. Rao, *Chem. Phys. Lett.* **368**, 690 (2003).
145. Y. Xia, P. Yang, Y. Sun, Y. Wu, B. Mayers, B. Gates, Y. Yin, F. Kim, and H. Yan, *Adv. Mater.* **15**, 353 (2003).
146. C. N. R. Rao, F. L. Deepak, G. Gundiah, and A. Govindaraj, *Prog. Solid State Chem.* **31**, 5 (2003).
147. R. S. Wigner and W. C. Ellis, *Appl. Phys. Lett.* **4**, 89 (1964).
148. Y. Xia, B. Gates, B. Mayers, and A. Grossman, *Adv. Mater.* **14**, 1749 (2002).
149. U. K. Gautam, M. Nath, and C. N. R. Rao, *J. Mater. Chem.* **13**, 2845 (2003).
150. U. K. Gautam and C. N. R. Rao, *J. Mater. Chem.* **14**, 2530 (2004).
151. A. M. Morales and C. M. Lieber, *Science* **279**, 208 (1998).
152. X. Duan and C. M. Lieber, *Adv. Mater.* **12**, 298 (2000).
153. Z. W. Pan, Z. R. Dai, and Z. L. Wang, *Science* **291**, 1947 (2001).
154. Y. Wu and Y. P., *J. Am. Chem. Soc.* **123**, 3165 (2001).
155. S. T. Lee, N. Wang, Y. F. Zhang, and Y. H. Tang, *MRS Bulletin* **24**, 36 (1999).
156. N. Wang, Y. H. Tang, Y. F. Zhang, C. S. Lee, and S. T. Lee, *Phys. Rev. B* **58**, R16024 (1998).
157. C. N. R. Rao, G. Gundiah, F. L. Deepak, A. Govindaraj, and A. K. Cheetham, *J. Mater. Chem.* **14**, 440 (2004).
158. T. J. Trentler, K. M. Hickman, G. S. C., A. M. Viano, P. C. Gibbons, and W. E. Buhro, *Science* **270**, 1791 (1995).

159. J. D. Holmes, K. P. Johnston, R. C. Doty, and B. A. Korgel, *Science* **287**, 1471 (2000).
160. Y. Wu and Y. P., *Adv. Mater.* **13**, 520 (2001).
161. M. A. El-Sayed, *Acc. Chem. Res.* **34**, 257 (2001).
162. P. K. Jain, K. S. Lee, I. H. El-Sayed, and M. A. El-Sayed, *J. Phys. Chem. B* **110**, 7238 (2006).
163. E. K. Payne, K. L. Shuford, S. Park, G. C. Schatz, and C. A. Mirkin, *J. Phys. Chem. B* **110**, 2150 (2006).
164. M. S. Hu, H. L. Chen, C. H. Shen, L. S. Hong, B. R. Huang, K. H. Chen, and L. C. Chen, *Nat. Mater.* **5**, 102 (2006).
165. X. Duan, Y. Huang, Y. Cui, J. Wang, and C. M. Lieber, *Nature* **409**, 66 (2001).
166. Y. H. Huang, X. Duan, Y. Cui, L. J. Lauhon, K. H. Kim, and C. M. Lieber, *Science* **294**, 1313 (2001).
167. Y. Huang, X. Duan, Q. Wie, and C. M. Lieber, *Science* **291**, 630 (2001).
168. J. Goldberger, D. J. Sirbuly, M. Law, and P. Yang, *J. Phys. Chem. B* **109**, 9 (2005).
169. B. Sun and H. Sirringhaus, *Nano Lett.* **5**, 2408 (2005).
170. S. Ju, K. Lee, D. B. Janes, M. H. Yoon, A. Facchetti, and T. J. Marks, *Nano Lett.* **5**, 2281 (2005).
171. Z. L. Wang and J. Song, *Science* **312**, 242 (2006).
172. J. E. Green, J. Wook Choi, A. Boukai, Y. Bunimovich, E. Johnston-Halperin, E. Deionno, Y. Luo, B. A. Sheriff, K. Xu, Y. Shik Shin, H. Tseng, J. F. Stoddart, and J. R. Heath, *Nature* **445**, 414 (2007).
173. J. F. Wang, M. S. Gudiksen, X. Duan, Y. Cui, and C. M. Lieber, *Science* **293**, 1455 (2001).
174. M. Huang, S. Mao, H. Fieck, H. Yan, Y. Wu, H. Kind, E. Weber, R. Russo, and P. Yang, *Science* **292**, 1857 (2001).
175. A. Pan, R. Liu, Q. Yang, Y. Zhu, G. Yang, B. Zou, and K. Chen, *J. Phys. Chem. B* **109**, 24268 (2005).
176. S. Gradecak, F. Qian, Y. Li, H. G. Park, and C. M. Lieber, *Appl. Phys. Lett.* **87**, 173111 (2005).
177. Y. Huang, X. Duan, and C. M. Lieber, *Small* **1**, 142 (2005).
178. H. Kind, H. Yan, M. Law, B. Messer, and P. Yang, *Adv. Mater.* **14**, 158 (2003).

179. C. L. Hsu, S. J. Chang, Y. R. Lin, P. C. Li, T. S. Lin, S. Y. Tsai, T. Lu, and I. C. Chen, *Chem. Phys. Lett.* **416**, 7568 (2005).
180. J. B. K. Law and J. T. L. Thong, *Appl. Phys. Lett.* **88**, 133114 (2006).
181. L. D. Hicks and M. S. Dresselhaus, *Phys. Rev. B* **47**, 16631 (1993).
182. Y. M. Lin, S. B. Cronin, J. Y. Ying, M. S. Dresselhaus, and J. P. Hermans, *Appl. Phys. Lett.* **76**, 3944 (2000).
183. Z. Zhang, X. Sun, M. S. Dresselhaus, and J. Y. Ying, *Phys. Rev. B* **61**, 4850 (2000).
184. A. Boukai, K. Xu, and J. R. Heath, *Adv. Mater.* **18**, 864 (2006).
185. E. W. Wong, P. E. Sheehan, and C. M. Lieber, *Science* **277**, 1971 (1997).
186. B. Wu, A. Heidelberg, and B. J. Bolan, *Nat. Mater.* **4**, 525 (2005).
187. J. Song, X. Wang, E. Riedo, and Z. L. Zang, *Nano Lett.* **5**, 1954 (2005).
188. X. Li, X. Wang, Q. Xiong, and P. C. Eklund, *Nano Lett.* **5**, 1982 (2005).
189. L. Qian, S. Park, L. Huang, and C. A. Mirkin, *Science* **309**, 113 (2005).
190. C. S. Rout, S. H. Krishna, S. R. C. Vivekchand, A. Govindaraj, and C. Rao, *Chem. Phys. Lett.* **418**, 586 (2006).
191. A. R. Armstrong, A. Armstrong, J. Canales, R. Garcia, and P. G. Bruce, *Adv. Mater.* **17**, 862 (2005).
192. K. Peng, Y. Xu, Y. Wu, Y. Yan, and S. T. Lee, *Small* **1**, 1062 (2005).
193. M. Law, L. E. Greene, J. C. Johnson, R. Saykally, and P. Yang, *Nat. Mater.* **4**, 455 (2005).
194. J. B. Baxter and E. S. Aydil, *Appl. Phys. Lett.* **86**, 053114 (2005).
195. M. Y. Song, Y. R. Ahn, S. M. Jho, D. Y. Kim, and J. P. Ahn, *Appl. Phys. Lett.* **87**, 113113 (2005).
196. K. W. Lux and K. J. Rodriguez, *Nano Lett.* **6**, 288 (2006).
197. M. Khan, A. K. Sood, F. L. Deepak, and C. N. R. Rao, *Nanotechnology* **17**, S287 (2006).
198. S. F. Bidoz, A. C. Arsenault, I. Manners, and O. G. A., *Chem. Commun.* 441 (2005).

Chapter 2

SYNTHESIS OF CARBON NANOTUBES AND METAL NANOWIRES BY NEBULIZED SPRAY PYROLYSIS

Summary¹

In this chapter, we describe the use of nebulized spray pyrolysis (NSP) for the synthesis of carbon nanotubes and metal nanowires. Multi-walled carbon nanotubes (MWNTs) with fairly uniform diameter as well as aligned MWNT bundles have been prepared by the NSP of organometallic precursors such as ferrocene dissolved in hydrocarbon solvents such as benzene and toluene. Well-graphitized MWNTs were obtained with a solution of ferrocene in xylene. Single-walled nanotubes (SWNTs) were obtained when NSP was carried out with cobaltocene or nickelocene in admixture with toluene. $\text{Fe}(\text{CO})_5$ in mixture with acetylene also yielded aligned MWNT bundles.

Metal nanowires could be obtained by the nebulized spray pyrolysis of metal acetate precursors. This method has been employed for the synthesis of zinc, cadmium and lead nanowires. The nanowires are single-crystalline. Nanonecklaces were obtained in the case of cobalt by using cobalt acetate as the precursor.

Oxidation of zinc and cadmium nanowires gives one-dimensional oxidic nanostructures. In the case of zinc metal, tubular ZnO was obtained.

NSP can be employed for large-scale production of carbon nanotubes and other one-dimensional nanomaterials.

¹Papers based on this study have appeared in *Chem. Phys. Lett.* (2004), *Adv. Mater.* (2004) and *J. Nanosci. Nanotech* (2007)

2.1 Introduction

Carbon nanotubes and metal nanowires constitute an important class of one-dimensional nanomaterials, which provide models to study the relationship between electrical transport, optical and other properties with dimensionality and size confinement. In recent years, several methods have been employed for the synthesis of carbon nanotubes as well as metal nanowires and have been described in detail in Chapter 1. Carbon nanotubes have been traditionally prepared by the arc-evaporation of graphite [1]. A current of 60-100 amperes is passed between two graphite electrodes in a helium atmosphere (approximately 500 torr) which leads to the evaporation of carbon from the anode and is deposited on the cathode (also known as the cathodic stub). The stub contains a high yield of multi-walled carbon nanotubes. Single-walled carbon nanotubes (SWNTs) were first synthesized by metal-catalyzed dc-arcing of graphite electrodes [2, 3]. The graphite anode is normally filled with metal powders such as Fe, Co or Ni and pure graphite is used as the cathode. However, several carbon nanotube synthesis methods have been developed, particularly the decomposition of hydrocarbons over small metal catalyst has been the focus area of research, due to their scalability and ease of synthesis [4, 5]. Aligned MWNT bundles have been obtained by chemical vapor deposition over transition metal catalyst embedded in the pores of mesoporous silica or the channels of alumina membranes [6, 7]. Plasma-enhanced chemical vapor deposition on nickel-coated glass using acetylene and ammonia has been employed by Ren and Huang [8] to obtain aligned MWNT bundles.

Pyrolysis of metallocenes such as ferrocene and other organometallic compounds like nickel and iron phthalocyanine in a two stage furnace provides a straight forward procedure to prepare carbon nanotubes [9]. The parameters that can be varied in these pyrolysis reactions are sublimation rate

of the catalyst precursor, flow rate of the carrier gas, the use of additional carbon sources such as acetylene and the pyrolysis temperature. Using this method, MWNTs [10–12], aligned MWNT bundles [13, 14], aligned metal-filled MWNTs [15], Y-junction MWNTs [16, 17] as well as single-walled carbon nanotubes (SWNTs) [18, 19] have been prepared employing different experimental conditions. Aligned MWNT bundles are obtained when the catalyst was rapidly sublimed and SWNTs under dilute catalyst and hydrocarbon conditions. Y-junction nanotubes can be obtained when an additional carbon source containing sulphur was incorporated. The advantage of the precursor method is that the aligned bundles are produced in one step, at a relatively low cost, without prior preparation of substrates. Glerup *et al.* [27, 28] have modified this two stage furnace method and have used aerosol method for carrying the catalyst and carbon source for the synthesis of MWNTs and nitrogen doped MWNTs. Ajayan and co-workers have synthesized long strands of SWNTs by the pyrolysis of a spray containing ferrocene, thiophene and n-hexane [29].

General methods for the synthesis of metal nanowires include vapor-solid or vapor-liquid-solid growth and the use of templates such as anodic alumina membranes (AAO) [20, 21], carbon nanotubes [22], etc. Nanowires of metals such as Au and Ag have been synthesized by a seed-mediated approach as well as by solution-based methods [23–25]. Laser ablation has been employed to obtain nanowires of Si and Ge [26].

In this chapter, we have systematically investigated the use of nebulized spray pyrolysis for the synthesis of carbon nanotubes and metal nanowires. For carbon nanotube synthesis, we have used organometallics such as ferrocene, nickelocene, cobaltocene, $\text{Fe}(\text{CO})_5$, etc. We have also extended this method for the preparation of metal nanowires starting from simple metal precursors. The method is simple, template-free and in-expensive. Nebulized

spray pyrolysis has been employed earlier for the preparation of sub-micron sized particles [30] and epitaxial thin films [31–33] of complex metal oxides. The advantage of using nebulized spray is the large number of parameters that can be utilized to control the pyrolysis reaction and it can be easily scaled into an industrial scale process, as the reactants are fed into the furnace continuously. We have been able to control the diameter distribution and quality of the nanotubes by adjusting the various available parameters like pyrolysis temperature, carrier gas flow rate, catalyst precursor concentration, various hydrocarbon sources and various catalyst precursors. We have characterized the nanotubes obtained by various experiments by electron microscopy and X-ray diffraction. The versatility of this method is demonstrated by the synthesis of single-crystalline nanowires of zinc, cadmium and lead. It is noteworthy that there are very few reports in the literature on the synthesis of zinc and lead nanowires, and no report on cadmium nanowires. For example, zinc nanobelts have been obtained by the carbothermal reduction of ZnS [34], while nanowires are prepared by the reduction of ZnO with graphite in an NH₃ atmosphere [35]. Single-crystalline lead nanowires have been synthesized by the decomposition of lead acetate in ethylene glycol [36]. In the NSP process, we have employed methanolic solutions of metal acetate to produce nanowires of zinc, cadmium and lead. We have also briefly examined the effect of oxidation on the morphology of zinc and cadmium nanowires.

2.2 Nebulized Spray Pyrolysis

Nebulized spray is a spray generated by an ultrasonic atomizer [37]. When a high frequency (100 kHz-10 MHz range) ultrasonic beam is directed to a gas-liquid interface, a geyser forms at the surface. The height of the geyser is proportional to the acoustic intensity. The formation of the geyser is

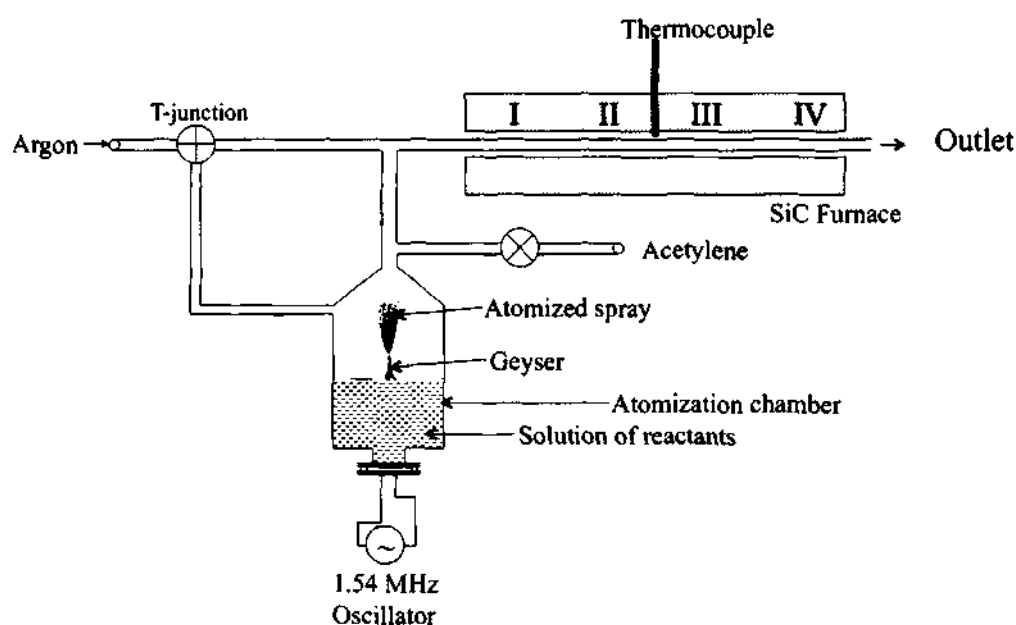


Figure 2.1: Schematic representation of the experimental set-up used for the synthesis of carbon nanotubes.

accompanied by the generation of a spray, resulting from the vibrations at the liquid surface and cavitation at the gas-liquid interface. The quantity of the spray produced is also a function of the acoustic intensity and of certain physical properties of the liquid (vapor pressure, viscosity and surface tension).

In Figure 2.1, we show the schematic diagram of the experimental set-up. A piezoelectric transducer (made of PZT) is at the base of the atomization chamber. The transducer is connected to a high frequency voltage generator. The frequency of the voltage generator is fixed at a value close to the resonance frequency of the transducer. By varying the voltage, the acoustic intensity can be varied. During the atomization process, the liquid is heated close to $100\text{ }^{\circ}\text{C}$, hence, some of the atomized liquid may change into the vapor state which is detrimental to the spray homogeneity. To avoid this problem, the nozzle carrying the mist from the atomization chamber should be narrow and long. A very narrow and long nozzle leads to collisions of droplets and

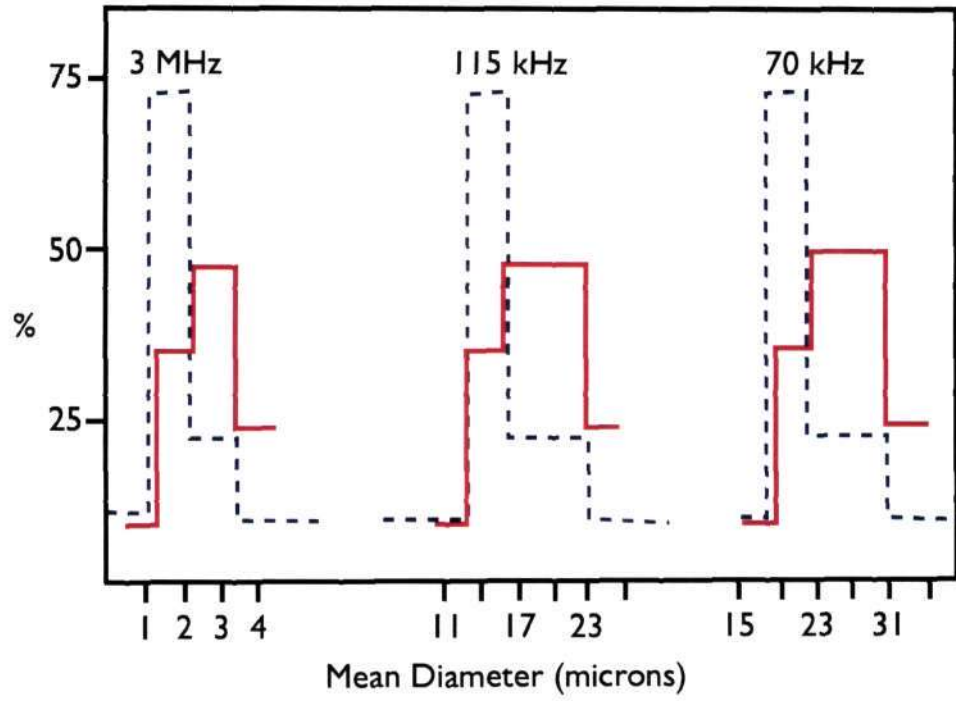


Figure 2.2: Variation of droplet size and distribution for water with frequency.

there is change in the size distribution of the droplets. The relationship between the capillary wavelength (C) at the liquid surface and mean diameter of the atomized droplets (D) is given as below:

$$D = a \cdot C \quad (2.1)$$

where a is constant. From the Kelvin's equation, the capillary wavelength can be written as a function of surface tension of the liquid (s), density (r) and ultrasonic excitation frequency (f):

$$C = (8 \cdot \pi \cdot s / r \cdot c^2)^{1/3} \quad (2.2)$$

a has been experimentally determined to be 0.34. Therefore,

$$D = 0.34(8 \cdot \pi \cdot s / r \cdot f^2)^{1/3} \cdot (ps / r f^2)^{1/3} \quad (2.3)$$

The frequency dependence of the D leads to a very narrow distribution in the droplet size. The variation of droplet size and distribution for water as a function of frequency is shown in Figure 2.2. It has been shown that, at constant ultrasonic power level and gas flow rate, the amount of material transported (r):

$$r = ps/s \cdot h \quad (2.4)$$

where ps is the saturated vapor pressure of the liquid, s its surface tension and h its dynamic viscosity.

2.3 Experimental details

The solution of the reactants was nebulized using a 1.54 MHz ultrasonic beam as shown in the Figure 2.1. In all the experiments, ultra high pure argon was used as the carrier gas and the gas flow rate was controlled using UNIT mass flow controllers. The average droplet size for the various solvents for 1.54 MHz frequency is approximately 2.2 μm . In all experiments, the atomized spray was carried into a 25 mm quartz tube that was placed in a SiC furnace which was held at a particular temperature (pyrolysis temperature). In the case of carbon nanotubes, ferrocene, nickelocene, cobaltocene and iron pentacarbonyl were used as both catalyst and carbon sources. Benzene, toluene, xylene, mesitylene and n-hexane were used as solvents for the catalyst and also act as carbon sources. We have also used acetylene as an additional carbon source in some of the pyrolysis experiments.

Silicon substrates were placed in the regions I, II, III and IV of the reactor to collect the product as shown in Figure 2.1. The quartz tube and the nebulization chamber are purged and oxygen is removed before the experiment. In a typical nebulized spray reaction, a solution of metallocene was nebulized and passed into the furnace using 1000 sccm of argon for 30 min.

After the reaction, the flow rate was reduced to 20 sccm and the furnace was allowed to cool. The products were collected after the tube cooled to room temperature. In the case of $\text{Fe}(\text{CO})_5$, it was nebulized for 5 minutes and the atomized droplets were carried into the furnace by a mixture of 100 sccm of acetylene and 1000 sccm of argon. The acetylene was stopped after 25 min. Pyrolysis of the atomized spray yielded MWNTs primarily in regions II and III while primarily carbon spheres were obtained in region IV in the case of ferrocene. We observed SWNTs in region IV when cobaltocene and nickelocene were used as catalyst precursors. We have changed the droplet size by increasing the ultrasonic excitation frequency to 2.6 MHz, the average droplet size decreases to $1.55 \mu\text{m}$. To compare the quality of the MWNTs produced by nebulized spray pyrolysis, we prepared arc-discharge MWNTs by striking an arc between two graphite electrodes in a helium atmosphere. The cathodic deposit was collected, powdered and sonicated in ethanol for 2 h to separate the turbostratic graphite from the MWNTs.

In the case of metal nanowires, a methanolic solution of the acetate of zinc, cadmium or lead was prepared with a concentration of 40 g/l. This solution was nebulized and the spray carried into a quartz tube kept in a pre-heated silicon carbide furnace maintained between 800 and 900 °C using Ar as a carrier gas. Typical flow rates of Ar used were between 500-1000 sccm. All experiments were performed using a quartz tube with an inner diameter of 25 mm. The reaction was typically carried out for 30 min. The shiny deposits obtained at the outlet was used for further analysis.

The powder X-ray diffraction (XRD) patterns were recorded using a Seifert XRD 3000 TT instrument. The scanning electron microscope (SEM) images were obtained with a Leica S-440I microscope. Transmission electron microscope (TEM) images were obtained with a JEOL JEM 3010 instrument operating at an accelerating voltage of 300 kV.

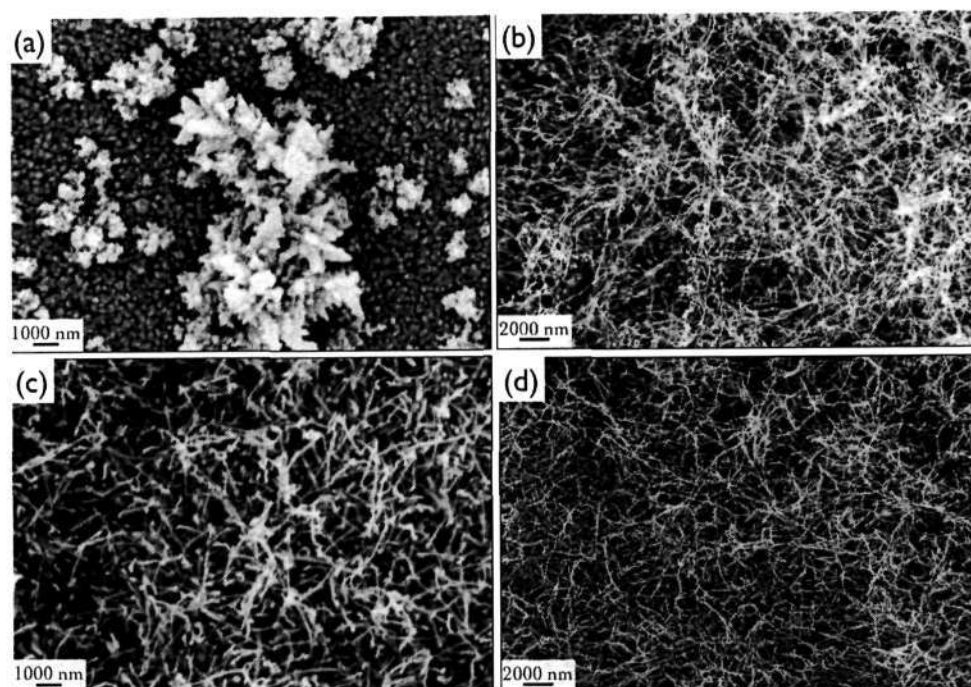


Figure 2.3: (a) and (b)-SEM images of products obtained in region II and region III by pyrolysis of nebulized spray of 20 g/l solution of ferrocene in toluene at 840 °C. (c) and (d) SEM images of products obtained by pyrolysis at 900 °C.

2.4 Results and Discussion

2.4.1 Carbon Nanotubes

Nebulized spray pyrolysis of a solution of ferrocene in toluene (20 g/l) gave a good yield of MWNTs in regions II and III as shown in Figure 2.3. The formation of the MWNTs was found to be sensitive to temperature. At lower temperatures, the yield of the MWNTs decreased and catalyst metal particles were obtained as seen in the SEM image in Figures 2.3 (a) and (b). The optimum temperature for the growth of MWNTs was found to be 900 °C with a large yield of MWNTs in both region II and III (See Figures 2.3 (c) and (d)). The nanotubes are approximately 40 nm in diameter and tens of micron long as revealed by the SEM images. At higher temperatures the yield of nanotubes decreased and was accompanied by the formation of

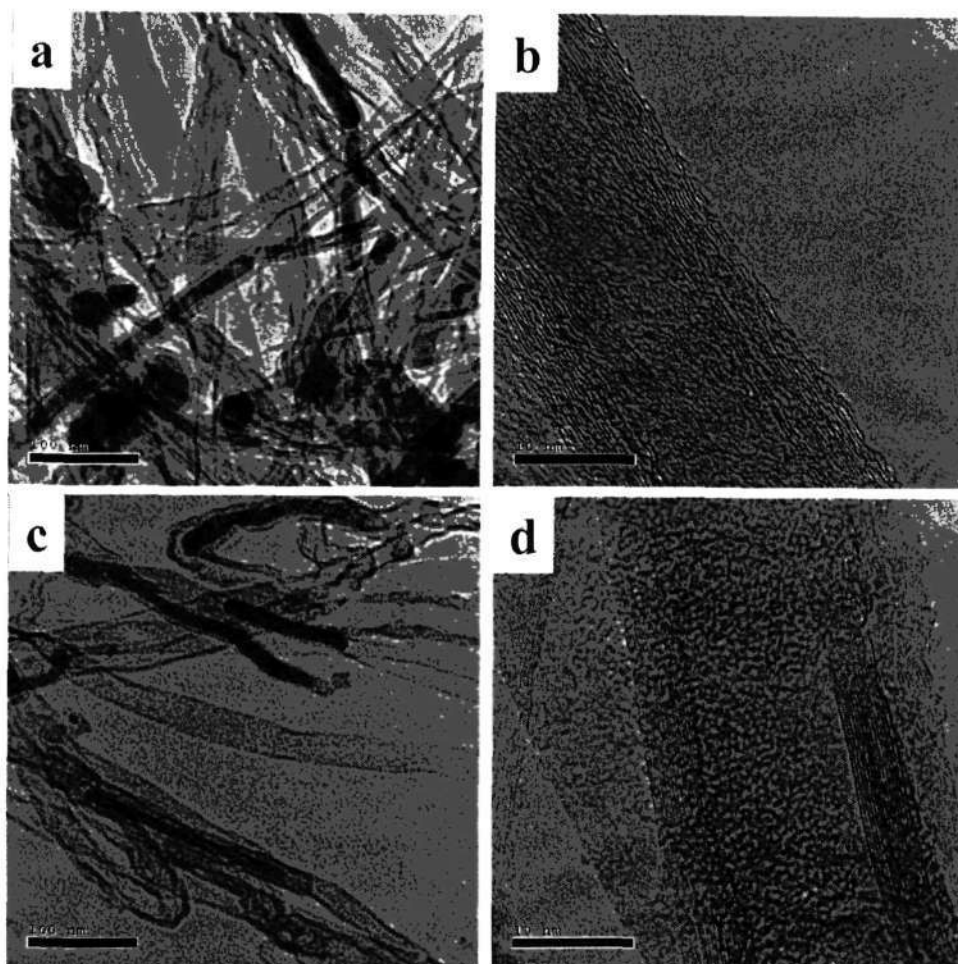


Figure 2.4: (a) and (b) TEM images of products obtained in region II and region III by pyrolysis of nebulized spray of 20 g/l solution of ferrocene in toluene at 840 °C. (c) and (d) TEM images of products obtained by pyrolysis at 900 °C.

shiny carbon films on the walls of the quartz tube. The auto-pyrolysis of toluene and other solvents increases as the temperature increases and larger quantities of carbon spheres were obtained in region IV. In Figure 2.4, TEM images of MWNTs obtained by the nebulized spray pyrolysis of a solution of ferrocene in toluene (20 g/l) shows that many of the MWNTs are metal filled. The average diameter of MWNTs were estimated as 36 nm (diameter range of 36 ± 16 nm). From high-resolution electron microscopy (HREM), we found that the crystallinity of MWNTs increases with the increase in the pyrolysis temperature as seen in Figures 2.4 (b) and (d).

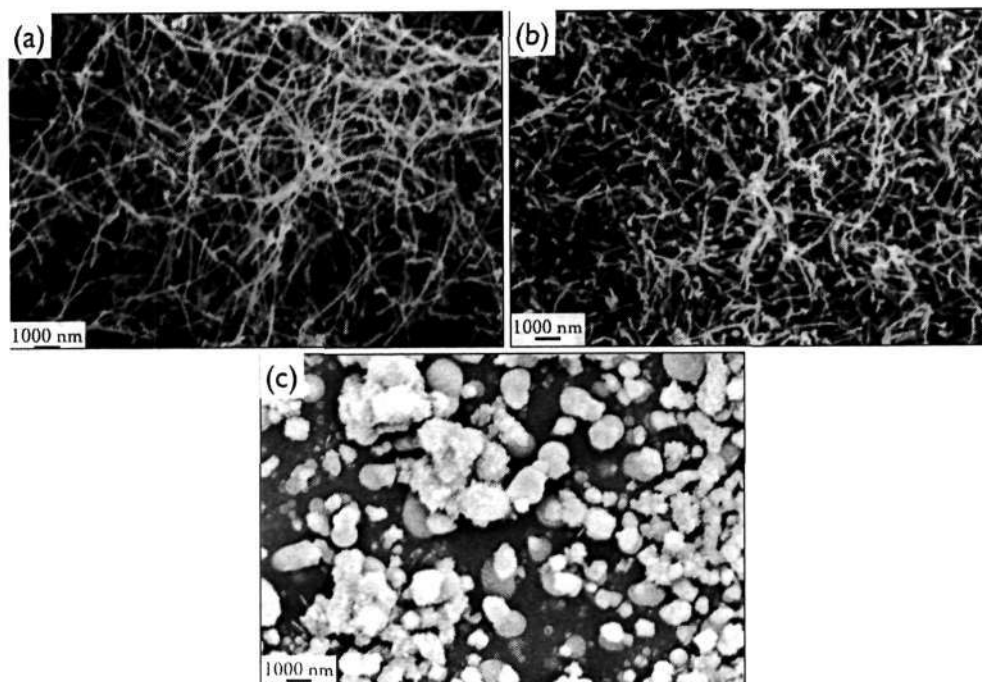


Figure 2.5: SEM images of MWNTs obtained by the pyrolysis of a toluene solution of ferrocene (20 g/l) at 900 °C with a Argon flow rate of (a) 500 sccm (b) 1000 sccm and (c) 2000 sccm.

The quantity of the reactants carried inside the furnace is directly proportional to the Ar flow rate. The flow rate of the carrier gas also affects the yield and quality of the MWNTs. At low flow rate of 200 sccm of argon, yield of MWNTs was negligible as little reactant was carried. Very short MWNTs and large particles were obtained at a high flow rate of 2000 sccm of argon. A flow rate of 1000 sccm of argon was found to be ideal for the growth of MWNTs. In Figure 2.5 (a), we show MWNTs obtained in region II when 500 sccm of argon was used and Figure 2.5 (b) shows the large particles when the argon flow rate was 2000 sccm.

The concentration of ferrocene in toluene was found to be crucial in determining the yield of the MWNTs. Bulbs of MWNTs were obtained when the concentration of ferrocene was increased to 80 g/l (saturated solution) as revealed by the SEM image in Figure 2.6 (a). These bulbs indeed contain thousands of MWNT as seen in Figure 2.5 (b). As the concentration

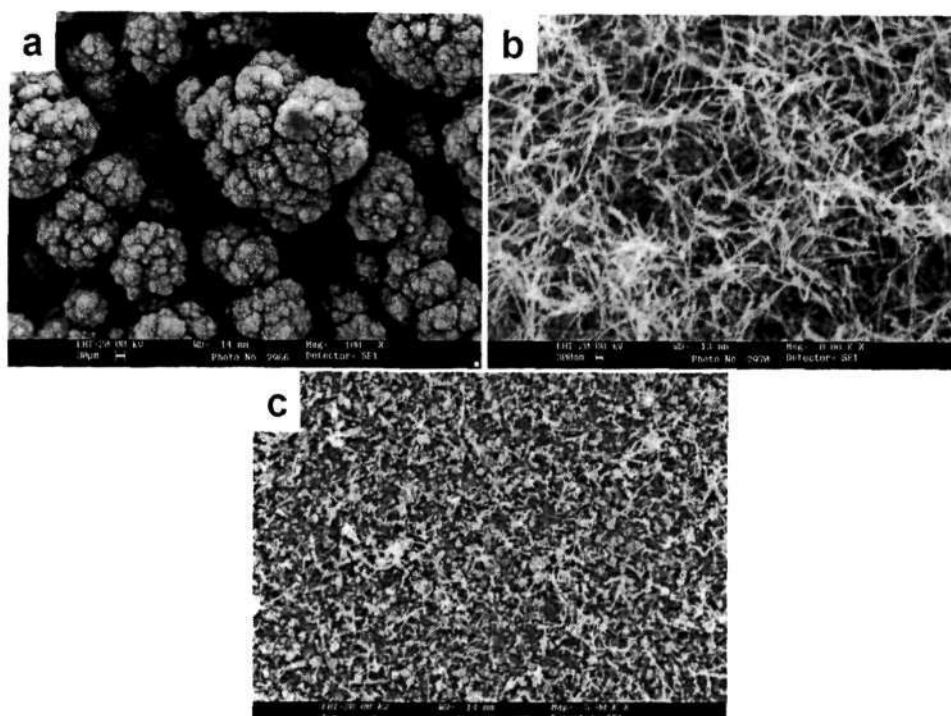


Figure 2.6: (a) and (b) SEM image of the MWNTs pyrolysis of toluene solution of ferrocene (80 g/l) at 900 °C in region II and (c) SEM image of particles obtained in region III in the same reaction.

of ferrocene was increased the yield of MWNTs also increased. A concentration of 20 g/l was found out to be ideal as MWNTs were obtained in both regions II and III while at higher concentration catalyst particles were obtained in region III as seen in Figure 2.6 (c). The average diameter of the MWNTs decreased to 23 nm and the distribution narrowed down to 23 ± 11 nm. In the absence of ferrocene only carbon spheres were obtained which is in agreement with our earlier observations in the laboratory [38]. Glerup *et al.* [27,28] observe that the diameter of the MWNTs are proportional to the concentration of the catalyst. The concentration and droplet size in our experiments are different from their values. The larger droplet size and higher concentration indicates that there are multiple nucleation centers within the droplet. Even though there is multiple nucleation, the diameter distribution of MWNTs obtained from any particular region of the furnace was

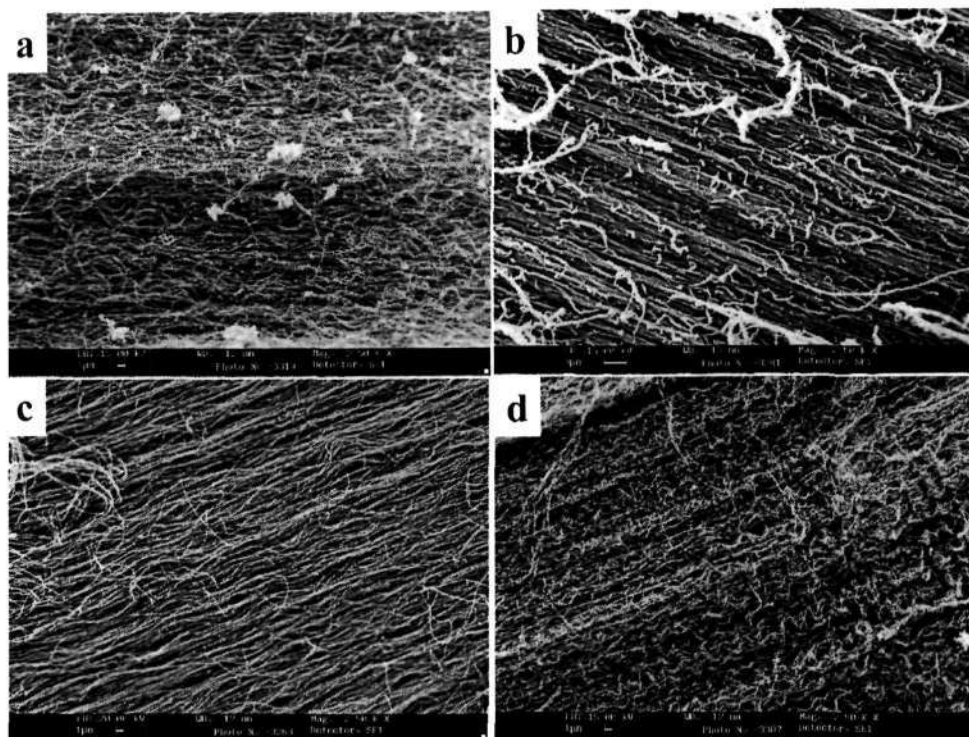


Figure 2.7: SEM images of MWNTs obtained by the pyrolysis of ferrocene in (a) benzene, (b) xylene, (c) mesitylene (d) n-hexane at 900 °C with an argon flow rate of 1000 sccm.

found to be narrow. Further, the bulbs of MWNTs are also an additional evidence for the formation of multiple nucleation within the droplet. We did not observe any significant changes when the droplet size was decreased to 1.55 μm . Aligned MWNT bundles were obtained when other hydrocarbon like benzene, xylene, mesitylene and n-hexane were used instead toluene as seen in Figures 2.7. The choice of the solvent for the catalyst precursor is important to determine to nature of the final product as indicated by the above observation. The aligned MWNT bundles had lengths greater than 100 micrometer and homogenous throughout the silicon substrate. The SEM images indicate aligned MWNTs without impurities such as nanoparticles and amorphous carbon can be obtained when mesitylene is used as a carbon source. The density of aligned MWNTs increases as we move from xylene to n-hexane with n-hexane solutions of ferrocene yielding the highest



Figure 2.8: Photograph of aligned MWNT obtained by nebulized spray pyrolysis of toluene solution of ferrocene (80 g/l) at 900 °C with 100 sccm of acetylene as additional carbon source.

density of aligned MWNTs as seen in Figure 2.7. Large quantities of aligned MWNT can be obtained by our route as indicated by Figure 2.8. The diameter distribution plots for the MWNTs obtained with various carbon sources under similar reaction conditions is given in Figure 2.9. The nebulized spray pyrolysis of ferrocene in benzene yielded aligned MWNTs with an average diameter of 59 nm (diameter distribution: 59 ± 26 nm) as seen in Figure 2.9 (a). Large quantities of graphite sheathed metal nanoparticles were also observed in addition to the MWNTs. In Figure 2.10 (a), we show a typical TEM image of MWNTs and graphite sheathed metal nanoparticles when benzene was used a carbon source. Large and well-graphitized MWNTs were obtained when xylene and mesitylene (average diameters 100 nm) were used as a carbon source as seen in Figures 2.10 (b) and (c). Only aligned carbon nanotubes were observed when mesitylene and n-hexane were used as carbon sources. We consider n-hexane and mesitylene as ideal sources of carbon for the synthesis of aligned MWNTs as they yield copious quantities of MWNTs.

Aligned MWNT bundles can be obtained with toluene when acetylene was added as additional carbon source. When 100 sccm of acetylene was

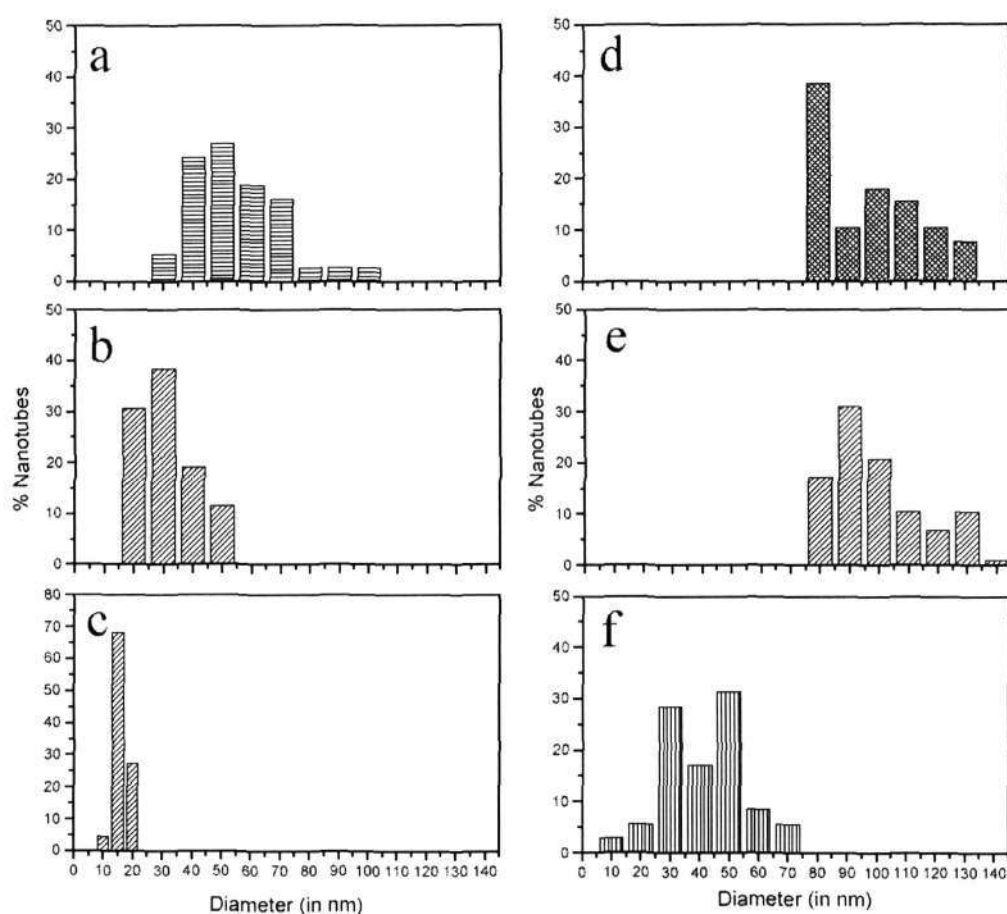


Figure 2.9: Diameter distribution plots of MWNTs obtained by the pyrolysis of ferrocene solution of (a) benzene, (b) toluene, (c) toluene with inclusion of 100 sccm of acetylene, (d) xylene (e) mesitylene and (f) n-hexane at 900 °C with an argon flow rate of 1000 sccm. The diameters were calculated from TEM micrographs.

included to the atomized spray of ferrocene in toluene, multi-layer aligned MWNT bundles were obtained as seen in Figure 2.11 (a). A single layer of aligned MWNTs was obtained by reducing the nebulization time from 30 min to 5 min, while the acetylene flow was continued for the remaining 25 min. The SEM image in Figure 2.11 (b) shows 1 mm long MWNTs obtained by the method as described above. The density of aligned MWNTs depended on the flow rate of acetylene and concentration of ferrocene as seen in Figures 2.11 (c) and (d) respectively. By increasing concentration of ferrocene, we were able to obtain highly dense aligned MWNT bundles

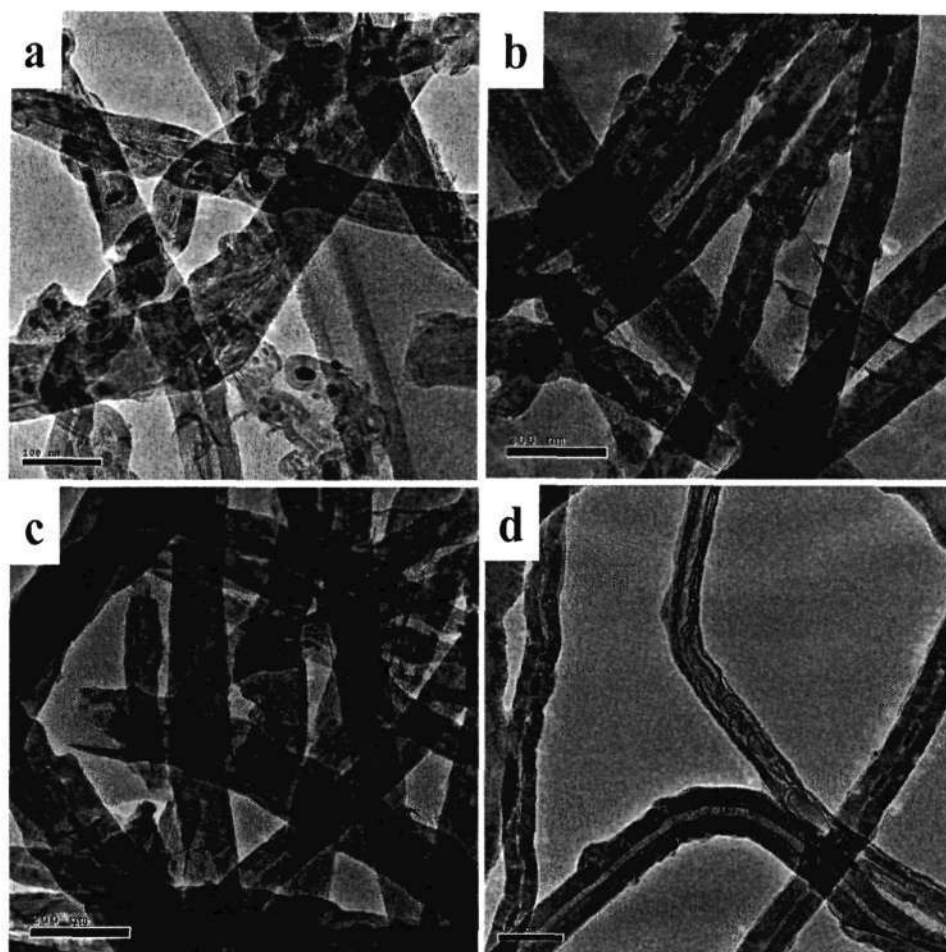


Figure 2.10: TEM images of MWNTs obtained by the pyrolysis of ferrocene in (a) benzene, (b) xylene, (c) mesitylene (d) n-hexane at 900 °C with an argon flow rate of 1000 sccm.

with MWNTs of larger diameters. When the concentration of ferrocene was decreased to 10 g/l MWNTs with no alignment were obtained indicating the presence of a critical concentration for the synthesis of aligned MWNT bundles by this approach. As the flow rate of acetylene was decreased to 50 sccm the density of the aligned MWNTs decreased (see Figure 2.11 (c)). Figure 2.12 shows the TEM images of aligned MWNTs obtained by this approach. The diameter distribution of the MWNTs decreases drastically when the nebulization time is reduced to 5 min, here MWNTs with an average diameter of 18 nm (diameter distribution 18 ± 4.5 nm) were obtained in the

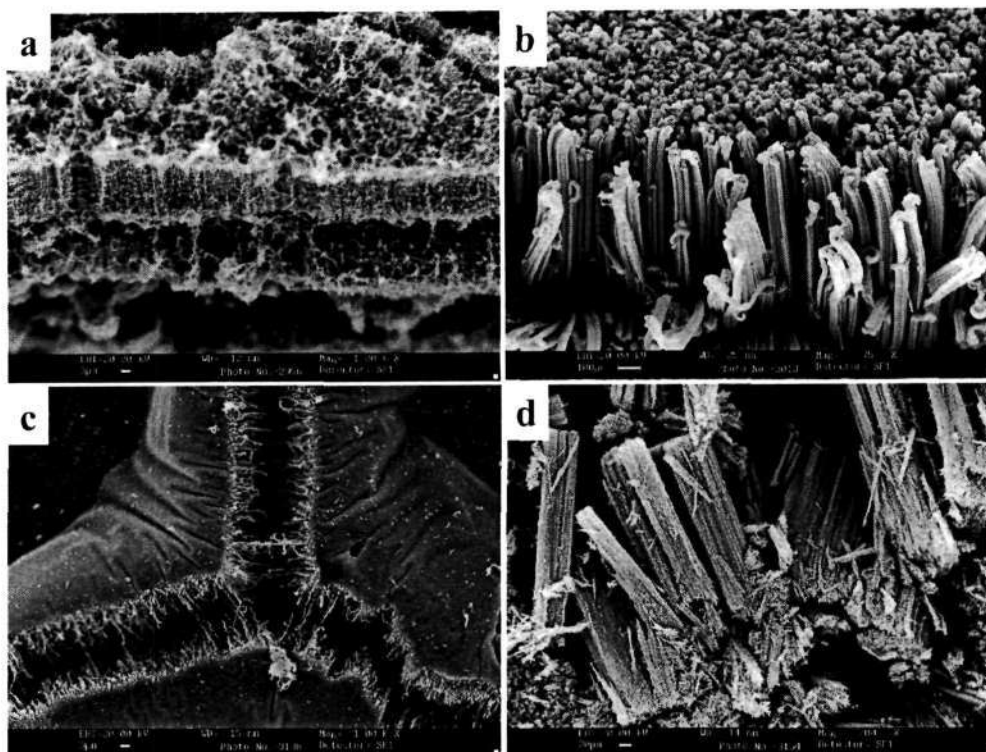


Figure 2.11: (a) SEM image of aligned MWNTs obtained by the pyrolysis of a solution of Ferrocene in toluene (20 g/l) along with 100 sccm Acetylene for 30m. (b) SEM image of aligned MWNTs obtained by the pyrolysis of toluene solution of ferrocene (20 g/l) for 5 min and acetylene flow of 100 sccm for a duration of 30 min. (c) SEM image of aligned MWNTs obtained at a lower flow rate of 50 sccm. (d) SEM image of highly dense aligned MWNTs obtained by the pyrolysis higher concentration of ferrocene in toluene (80 g/l). The pyrolysis temperature in all the above is 900 °C.

region II as seen Figure 2.9 (c). The MWNTs obtained by the inclusion of acetylene are more graphitized than the MWNTs obtained under similar conditions in the absence of acetylene (see inset of Figure 2.12 (b)) indicating acetylene is a good carbon source. Decreasing the pyrolysis temperature did not decrease the crystallinity of MWNTs as seen in the inset of Figure 2.12 (c). The number of graphitic layer increased as the concentration of ferrocene was increased as seen in Figure 2.12 (d) indicating the increase in the size of the catalyst particle. We also carried out pyrolysis reactions with other metallocenes like cobaltocene and nickelocene. The solubility of cobaltocene in toluene was a limiting factor and the solubility was found out

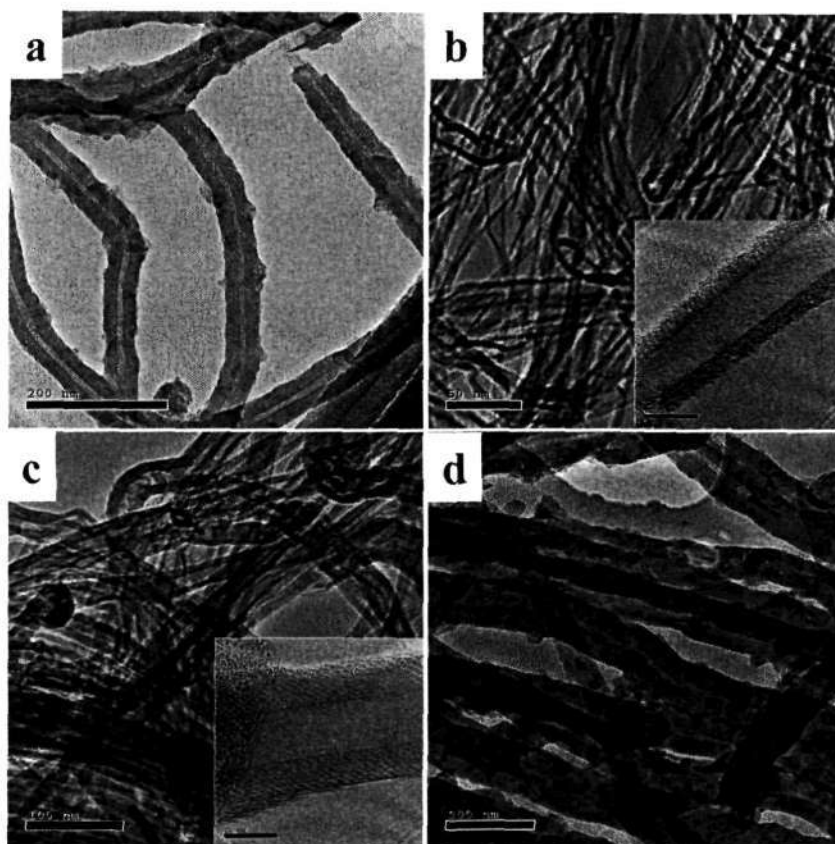


Figure 2.12: (a) TEM image of aligned MWNTs obtained by the pyrolysis of a solution of Ferrocene in toluene (20 g/l) along with 100 sccm Acetylene for 30m. (b) TEM image of aligned MWNTs obtained by the pyrolysis of toluene solution of ferrocene (20 g/l) for 5 min and acetylene flow of 100 sccm for 30 min., inset shows the HRTEM image for the same sample. (c) TEM image of aligned MWNTs obtained at a lower temperature of 840 °C. (d) TEM image of highly dense aligned MWNTs obtained by the pyrolysis of ferrocene solution (80 g/l).

to be close to 10 g/l. In Figures 2.13 (a)-(c), we show the TEM images of the nanotubes obtained by the nebulized spray pyrolysis of a saturated solution of cobaltocene in toluene. MWNTs with smaller diameters were obtained in region II (diameter ranging between 5-25 nm). We observed few isolated SWNTs in region IV along with a large amount of amorphous carbon covered metal nanoparticles. In Figure 2.13 (d), we show a typical TEM image of MWNTs obtained by the nebulized spray pyrolysis of a 20.0 g/l solution of nickelocene in toluene.

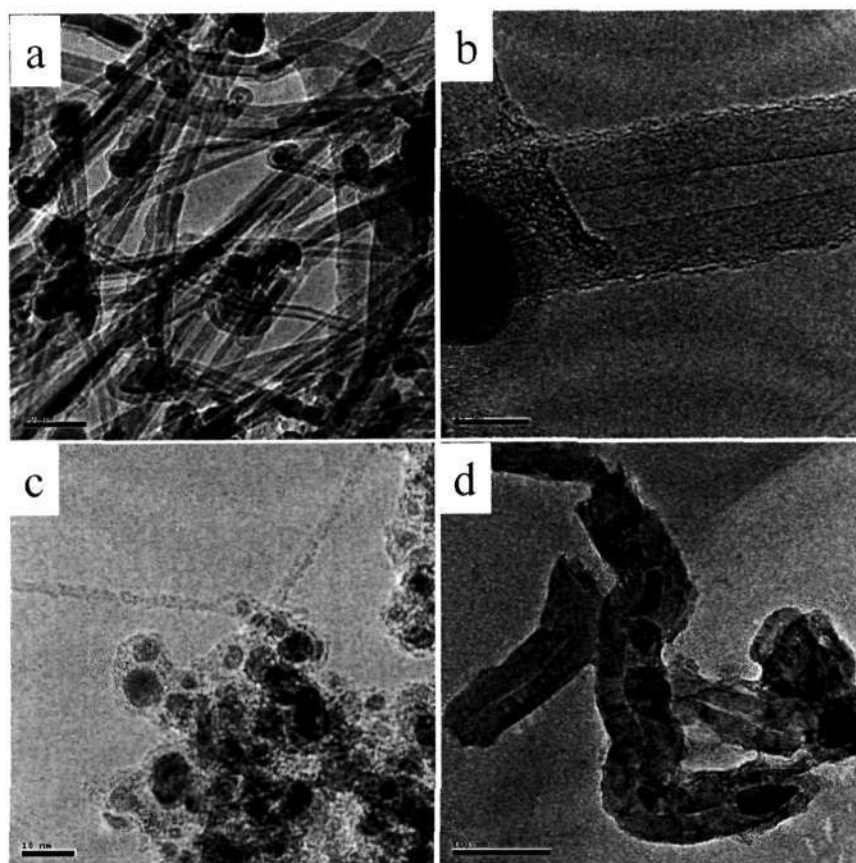


Figure 2.13: (a) TEM image of MWNTs obtained in Region II by the nebulized spray pyrolysis of cobaltocene in toluene (saturated), (b) HREM image of the same as in (a), (c) TEM image of SWNTs in Region IV by the nebulized spray pyrolysis of cobaltocene in toluene and (d) TEM image of MWNTs obtained by the nebulized spray pyrolysis of nickelocene in toluene (20.0 g/l).

We also used $\text{Fe}(\text{CO})_5$ as a metal source and it can be used without any addition of solvent. Nebulized spray pyrolysis of $\text{Fe}(\text{CO})_5$ alone yields bead like connected structures in regions I and IV of the furnace. The addition of acetylene yields aligned MWNTs in regions II and III while carbon coated metal particles (5-15 nm in diameter) were obtained in region IV. In Figure 2.14 (a), we show a typical SEM image of aligned MWNTs obtained by the pyrolysis of a nebulized spray of $\text{Fe}(\text{CO})_5$ at 900 °C with a flow 100 sccm of acetylene and 1000 sccm of argon. The TEM image in Figure 2.14 (b), shows that the aligned MWNTs have an average diameter of 33 nm. The MWNTs

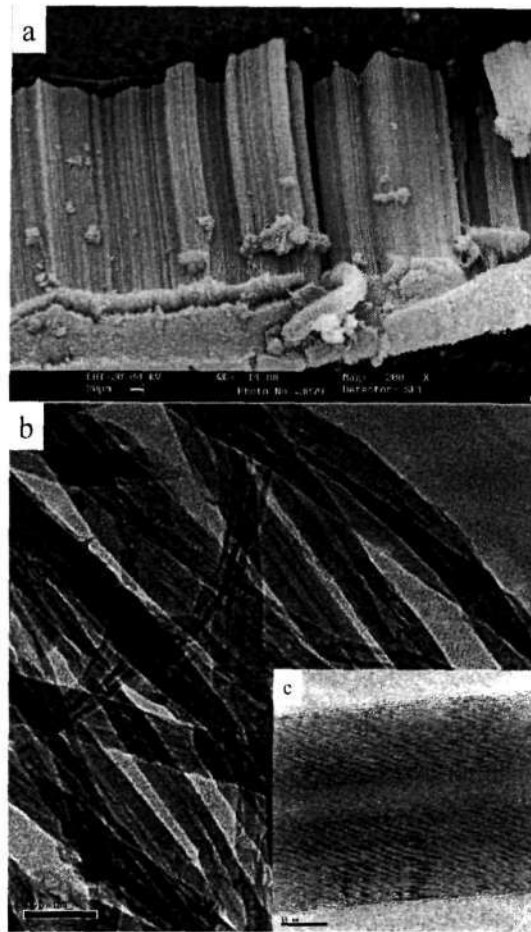


Figure 2.14: (a) SEM image of aligned MWNTs obtained by the nebulization of $\text{Fe}(\text{CO})_5$ in the presence of 100 sccm acetylene. (b) TEM image of the aligned MWNTs. (c) HREM image of a MWNT.

obtained by this route are well graphitized as seen in Figure 2.14 (c). The only disadvantage in using $\text{Fe}(\text{CO})_5$ is the corrosion of the atomizer electrode as $\text{Fe}(\text{CO})_5$ is very reactive.

MWNTs exhibit squared Lorentzian (001) and saw-tooth (hk0) in their X-ray diffraction pattern [39]. We have used X-ray diffraction to obtain the crystallinity of the nanotubes. In Figure 2.15, we compare the powder X-ray diffraction patterns of the MWNTs obtained by the various routes to that of the arc discharge MWNTs. It seems that xylene is the best hydrocarbon source for the synthesis of well graphitized MWNTs by nebulized spray pyrolysis from X-ray diffraction results.

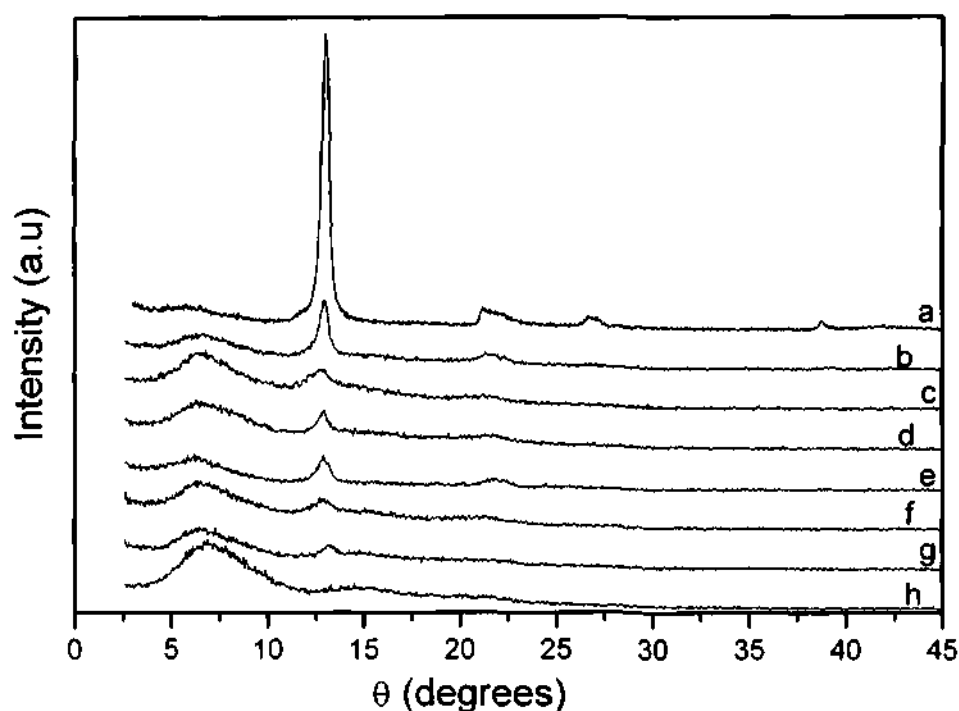


Figure 2.15: Powder X-ray diffraction pattern of (a) arc-discharge MWNTs, (b)-(h) MWNTs obtained in region III when xylene, toluene with acetylene, mesitylene, benzene, $\text{Fe}(\text{CO})_5$ -acetylene, n-hexane and toluene were used as the carbon sources.

2.4.2 Metal Nanowires

Solutions of metal acetates in methanol were carried by a suitable carrier gas (Ar) into a preheated furnace to obtain nanowires of the corresponding metals. The product gets deposited in the cooler regions of the quartz tube (near the outlet), where the temperature is in the 200 – 300 °C range. Zinc nanowires were obtained in copious quantities as a gray, shiny deposit when the pyrolysis of zinc acetate in methanol was carried out at 800 – 1000 °C. The scanning electron microscope (SEM) images of the nanowires reveal the length of the nanowires are in the order of several tens of microns (Figure 2.16). The XRD pattern shown in Figure 2.17 (a), is characteristic of the hexagonal structure of zinc (JCPDS card: No. 04-0831, $a = 2.67 \text{ \AA}$, $c = 4.95 \text{ \AA}$). Low-magnification transmission electron microscope (TEM) images

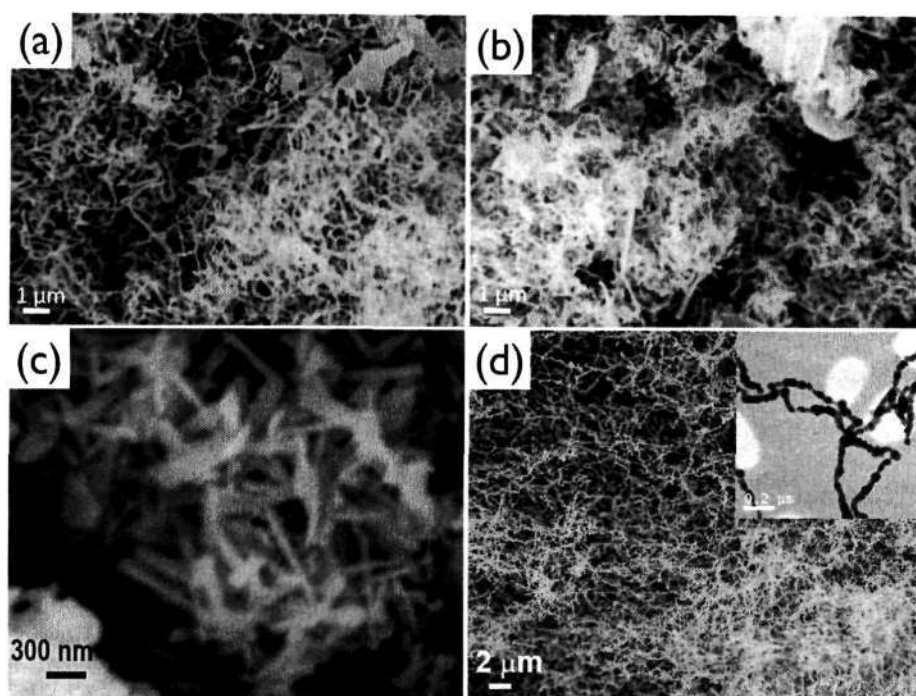


Figure 2.16: SEM image of products obtained by the nebulized spray pyrolysis of methanolic solution of respective precursors: (a) Zinc nanowires at 800 °C, (b) Cadmium nanowires at 800 °C, (c) Lead nanowires at 1000 °C and (d) Cobalt nanonecklaces at 1000 °C. Inset in (d) show TEM image of the nanonecklaces.

in Figure 2.18 (a) illustrates that nanowires have a diameters in the 50-100 nm range. The nanowires appear to have a zigzag morphology but there are no catalyst droplets at the wire ends. A few nanosheets of zinc were also occasionally observed (Figure 2.18 (b)). The selected area electron diffraction pattern (SAED) of a nanowire is shown in Figure 2.18 (c), shows reflections due to the (102), (100) and (110) planes of zinc, confirming the nanowires to be single-crystalline. The high-resolution electron microscope (HREM) image of a single nanowire in Figure 2.18 (d) has lattice spacing of 0.208 nm, corresponding to the (101) planes of zinc.

We have extended the synthetic procedure to obtain cadmium nanowires, which do not seem to have been reported hitherto. A gray deposit was obtained at the outlet by using cadmium acetate as the metal source. SEM

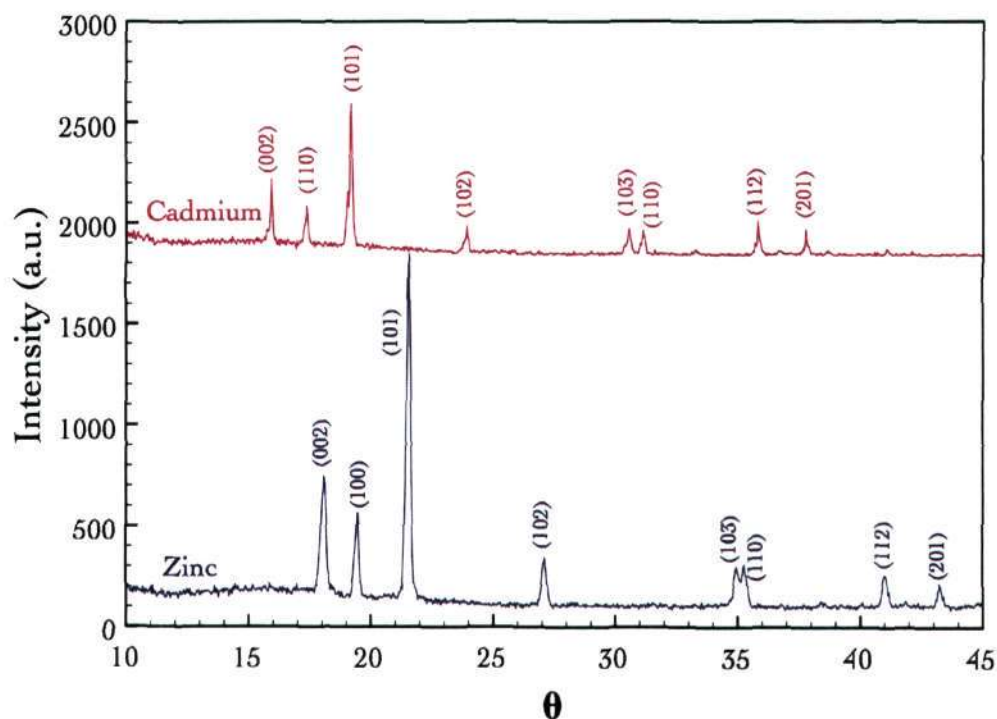


Figure 2.17: X-ray diffraction pattern of zinc nanowires and cadmium nanowires obtained by the nebulized spray pyrolysis.

images in Figure 2.16 (b) reveals the high yield of nanowires obtained. The nanowires were 60-150 nm in diameter and tens of microns in length. The XRD pattern of the nanowires is consistent with the hexagonal structure of cadmium (JCPDS card: No. 05-0674, P6/mmc, $a = 2.97 \text{ \AA}$, $c = 5.62 \text{ \AA}$) as shown in Figure 2.17. The presence of cadmium nanowires is illustrated by the TEM images in Figure 2.19. The ends of the nanowires do not show the presence of any droplet as in the case of zinc nanowires. On increasing the temperature of the reaction from 800 to 1000 °C, the diameters of the nanowires obtained increased to approximately 700 nm. The HREM image of a single nanowire in Figure 2.19 (c) shows a lattice spacing of 0.257 nm, corresponding to the (100) lattice planes of cadmium.

The single-crystalline nature of the nanowires is also borne out by the

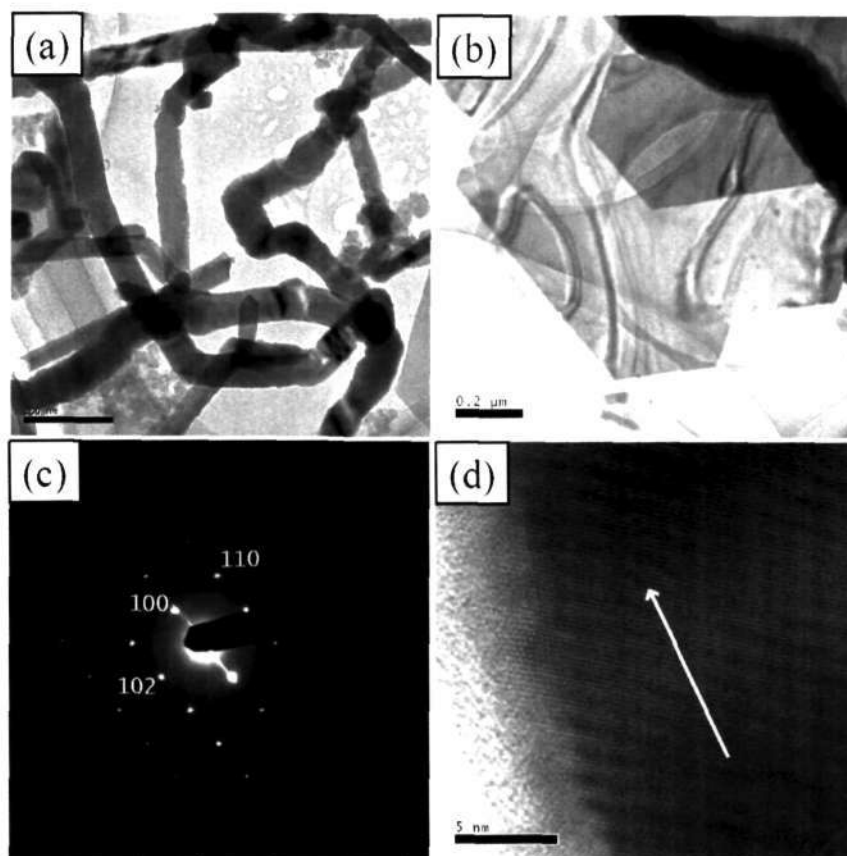


Figure 2.18: (a) and (b) low-magnification TEM images of zinc nanowires and nanosheets obtained by the NSP of methanolic solution of zinc acetate, (c) SAED pattern of a single zinc nanowire and (d) HREM image of a zinc nanowire. The arrow in (d) indicates the growth direction.

SAED pattern of a nanowire given as an inset in Figure 2.19 (c), the reflections corresponding to the (101) and (002) planes. Preliminary experiments show that it is possible to synthesize lead nanowires as shown by the SEM image in Figure 2.16 (c). The nanowires have diameters between 50-100 nm with lengths of a few microns. The formation of metal nanowires by nebulized spray pyrolysis of methanolic solutions of metal acetates can be understood as follows. The spray contains tiny droplets with diameters of 1-2 microns, which are transported by the carrier gas into the furnace maintained at 800 – 1000 °C. At this temperature, the melting and decomposition of the acetates into metal vapor occurs, probably aided by the

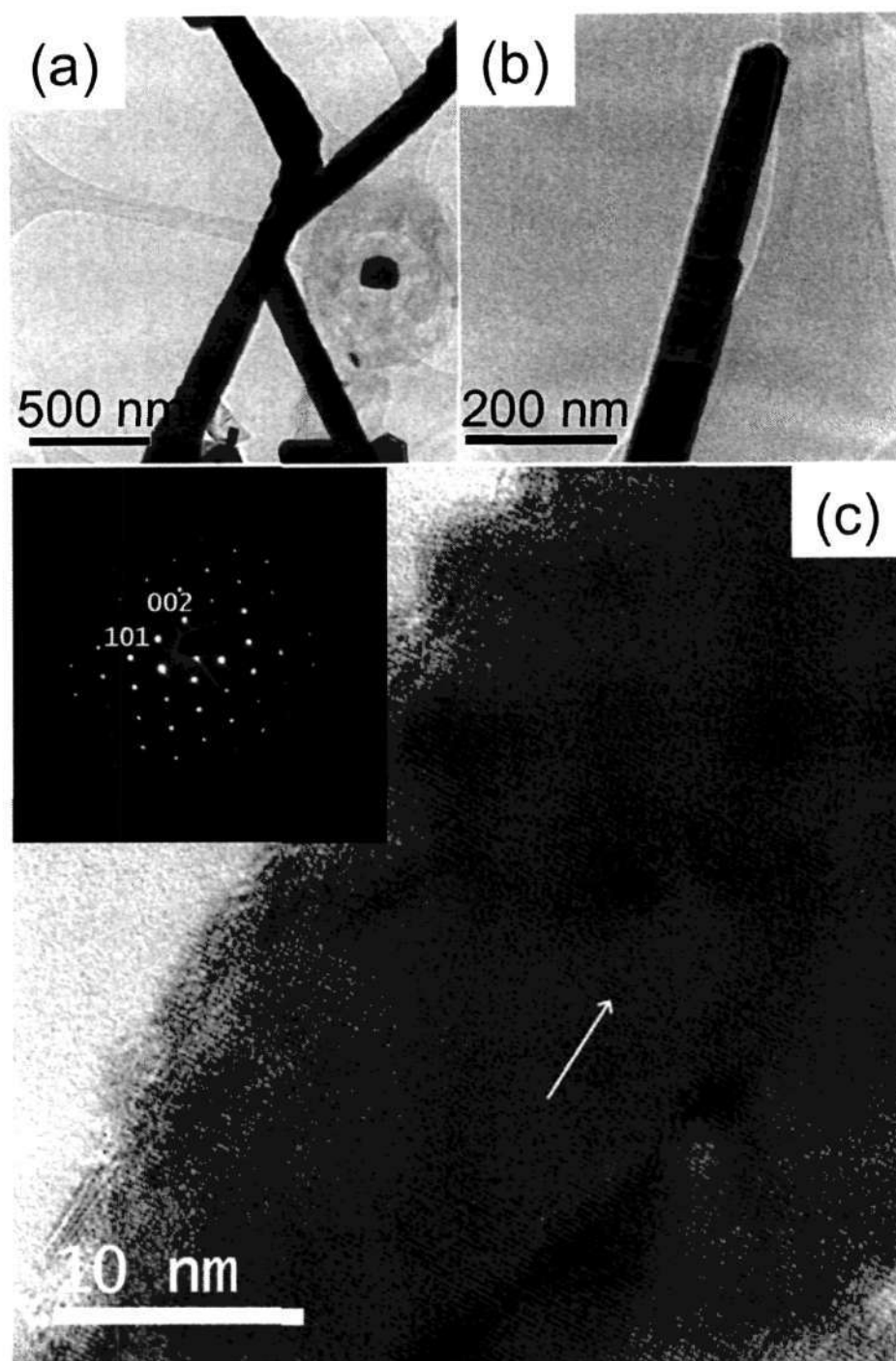


Figure 2.19: (a) and (b) TEM images of cadmium nanowires obtained by the NSP of cadmium acetate in methanol at 800°C. (c) HREM of a cadmium nanowire. The arrow shows the growth direction. SAED of the nanowire is shown as inset.

hydrogen gas formed by the decomposition of methanol into hydrogen and carbon monoxide. No metal oxide impurity occurs due to the strong reducing atmosphere. The metal vapor condenses in the cooler regions on the quartz tube to form nanowires. The absence of metal droplets at the ends of the nanowires strongly suggests that the nanowires grow by the vapor-solid mechanism.

Conversion of a nanowire to another nanostructure is of interest. Gates *et al.* [40] converted Se nanowires into Ag_2Se nanowires by using a soft chemistry. We have examined the oxidation of zinc and cadmium nanowires. The zinc nanowires were heated in air at 450°C at a rate of $5^\circ\text{C}/\text{min}$ for 4 h to yield ZnO as indicated by the XRD pattern in the inset of Figure 2.20 (JCPDS card: No. 36-1451, $P6_3mc$, $a = 3.25 \text{ \AA}$, $c = 5.21 \text{ \AA}$). There was no impurity corresponding to zinc indicating the complete oxidation of the nanowires. The SEM images in Figures 2.21 (a) and (b) reveal the nanostructures to be tubular in nature, although the dimensions are similar to those of the starting zinc.

We show TEM images in Figures 2.21 (c) and (d) to demonstrate the hollow nature of the ZnO nanotubes, with diameters in the 60-100 nm range. The nanotubes are made-up of crystallites with a size of 10 to 20 nm, wherein each crystallite is single-crystalline. The SAED pattern shown in the inset of Figure 2.21 (e) confirms that the nanotubes are made of such crystallites. The HREM image of a part of ZnO nanotube in Figure 2.21 (f) shows a lattice spacing of 0.26 nm, corresponding to the (002) lattice planes of ZnO. The photoluminescence spectrum shown in Figure 2.22, shows bands at 382 nm, 435 nm and 485 nm. The 382 nm band is due to the band-edge emission while the 435 nm and 485 nm bands are defect related. ZnO is a wide bandgap (3.37 eV) semiconductor and has been extensively investigated for short wavelength light-emission, transparent conducting and piezoelectric

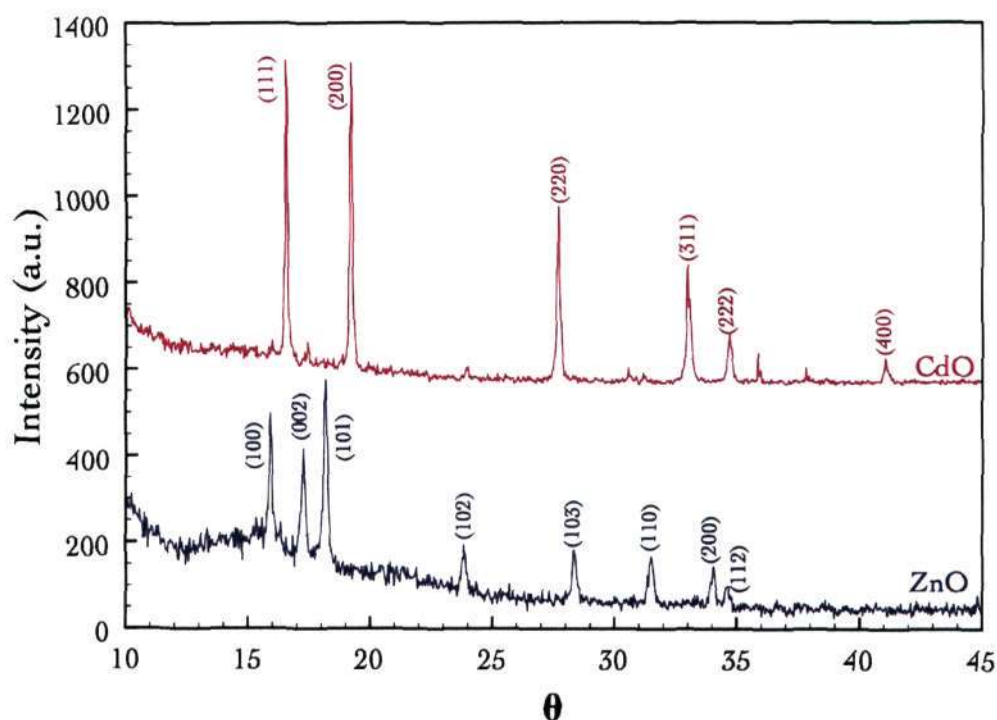


Figure 2.20: XRD patterns of ZnO and CdO obtained by the oxidation of zinc and cadmium nanowires respectively.

material. Though there have been several reports on the synthesis of ZnO nanowires [41], there have been relatively few on ZnO nanotubes [42].

We also carried out oxidation of cadmium nanowires under similar conditions. The XRD pattern in Figure 2.20 reveals the conversion of hexagonal cadmium into cubic CdO (JCPDS card:No. 05-0640, $Fm\bar{3}m$, $a = 4.70 \text{ \AA}$). Most of the nanowires melt before they oxidized leading to the loss in morphology (Figure 2.21 (g)). TEM images show the presence of necklace-like nanostructures (Figure 2.21 (h)).

Thermogravimetric analysis of zinc nanowires and cadmium nanowires in flowing O_2 gas is shown in Figure 2.23. It reveals that the oxidation begins at roughly 300°C in the case of zinc, presumably at the surfaces of the nanowires, followed by the diffusion of metal from the center of the nanowire towards the surface. In the case of zinc, the metal gets oxidized into the oxide giving hollow ZnO nanotubes. The cadmium nanowires melt (m.p.

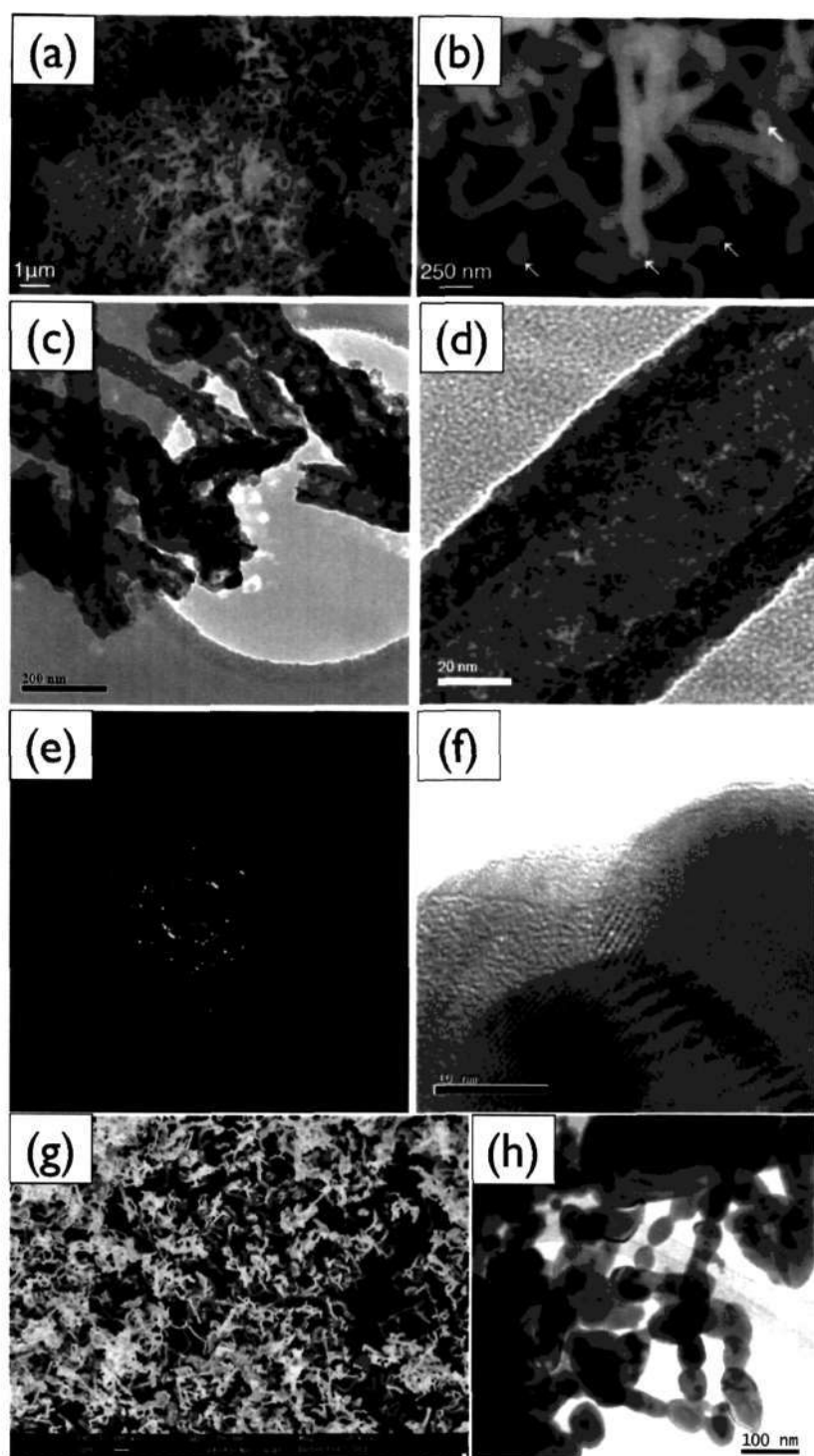


Figure 2.21: (a) and (b) SEM images of ZnO obtained by the oxidation of zinc nanowires at 450 °C. (c) and (d) TEM images of ZnO nanotubes, (e) SAED pattern of a ZnO nanotube, (f) HREM image of a part of ZnO nanotube, (g) and (h) SEM and TEM images of CdO nanostructures obtained by the oxidation of cadmium nanowires.

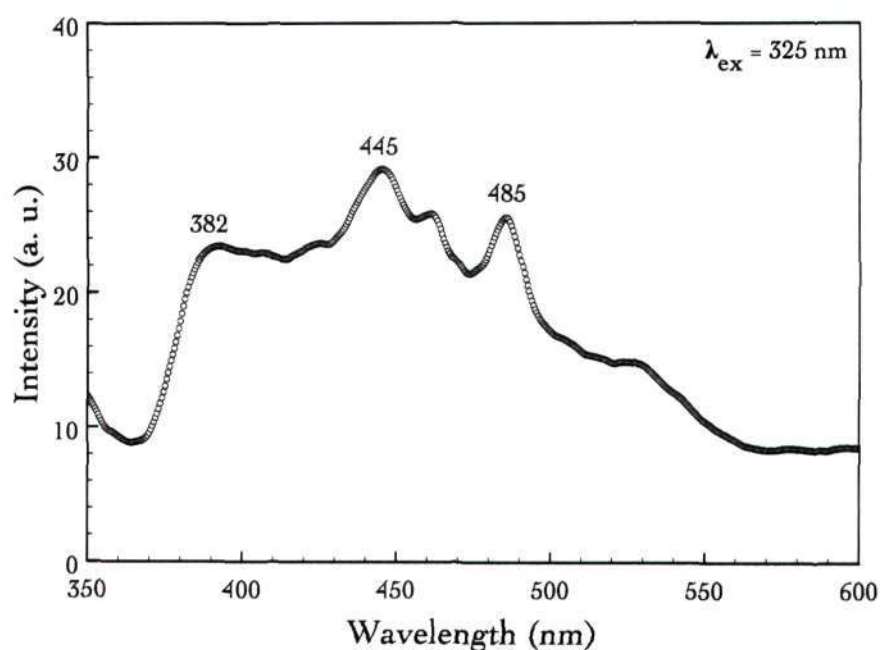


Figure 2.22: Photoluminescence spectrum of ZnO nanotubes obtained the oxidation of zinc nanowires at 450 °C.

of cadmium is 320.9 °C) before they get oxidized (350 °C) while zinc gets oxidized before it can melt (m.p. of zinc is 419 °C).

2.5 Conclusions

Nebulized spray pyrolysis can be conveniently used for the continuous production of MWNTs. The quality of the product is dependent on the pyrolysis temperature, carrier gas flow rate, carbon source used and catalyst precursor concentration. Many of the hydrocarbons yield aligned MWNT bundles. SWNTs were also obtained in certain instances. The inclusion of acetylene to an atomized spray of ferrocene in toluene yields aligned MWNT bundles with a narrow diameter distribution. Nebulized spray pyrolysis of iron pentacarbonyl in the presence of acetylene also yields aligned MWNT bundles. Well-graphitized MWNTs were obtained when xylene was used as the additional carbon source.

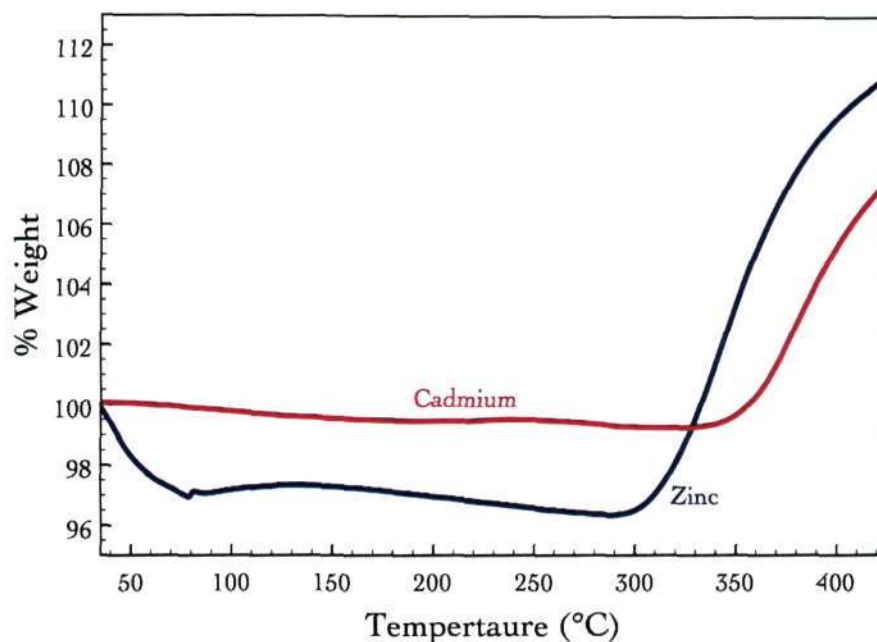


Figure 2.23: TGA plot of (a) Zn and (b) Cd nanowires in flowing oxygen at a heating rate of 10°C per minute.

We have also demonstrated the synthesis of nanowires of four metals by the technique of nebulized spray pyrolysis. This can be extended to synthesize nanowires of other metals, elemental materials and alloys. An advantage of this method is that the nanowires obtained are in high yields and single-crystalline. Though we have used metal acetates as precursors, we believe that other metal salts soluble in methanol can also be used to obtain metal nanowires by the nebulized spray pyrolysis route. It is noteworthy that we obtain nanotubes of oxides by the oxidation of the metal nanowires.

2.6 References

1. S. Iijima, *Nature* **354**, 56 (1991).
2. S. Iijima and T. Ichihashi, *Nature* **363**, 603 (1993).
3. D. S. Bethune, C. H. Kiang, M. S. De Vries, G. Gorman, R. Savoy, J. Vazquez, and R. Beyers, *Nature* **363**, 605 (1993).
4. C. N. R. Rao, B. C. Satishkumar, A. Govindaraj, and M. Nath, *Chem-PhysChem* **2**, 78 (2001).
5. C. N. R. Rao, A. Govindaraj, R. Sen, and B. C. Satishkumar, *Mater. Res. Inno.* **2**, 128 (1998).
6. G. Che, B. B. Lakshmi, C. R. Martin, E. R. Fisher, and R. S. Ruoff, *Chem. Mater.* **10**, 260 (1998).
7. W. Z. Li, S. S. Xie, L. X. Qian, B. H. Chang, B. S. Zou, W. Y. Zhou, R. A. Zhao, and G. Wang, *Science* **274**, 1701 (1996).
8. Z. F. Ren and Z. P. Huang, *Science* **282**, 1105 (1998).
9. C. N. R. Rao and A. Govindaraj, *Acc. Chem. Res.* **35**, 998 (2002).
10. R. Sen, A. Govindaraj, and C. N. R. Rao, *Chem. Phys. Lett.* **267**, 276 (1997).
11. R. Sen, A. Govindaraj, and C. N. R. Rao, *Chem. Mater.* **9**, 2078 (1997).
12. M. Yudasaka, R. Kikuchi, Y. Ohki, and S. Yoshimura, *Carbon* **35**, 195 (1997).
13. C. N. R. Rao, R. Sen, B. C. Satishkumar, and A. Govindaraj, *Chem. Commun.* 1525 (1998).
14. B. C. Satishkumar, A. Govindaraj, and C. N. R. Rao, *Chem. Phys. Lett.* **307**, 158 (1999).
15. B. C. Satishkumar, A. Govindaraj, P. V. Vanitha, A. K. Raychaudhuri, and C. N. R. Rao, *Chem. Phys. Lett.* **362**, 301 (2002).
16. B. C. Satishkumar, P. J. Thomas, A. Govindaraj, and C. N. R. Rao, *Appl. Phys. Lett.* **77**, 2530 (2000).
17. F. L. Deepak, A. Govindaraj, and C. N. R. Rao, *Chem. Phys. Lett.* **345**, 5 (2001).
18. B. C. Satishkumar, A. Govindaraj, R. Sen, and C. N. R. Rao, *Chem. Phys. Lett.* **293**, 47 (1998).

19. H. M. Cheng, F. Li, G. Su, H. Y. Pan, L. L. He, X. Sun, and M. S. Dresselhaus, *Appl. Phys. Lett.* **72**, 3282 (1998).
20. D. Al-Mawlawi, C. Z. Liu, and M. Moskovits, *J. Mater. Res.* **9**, 1014 (1994).
21. K. Nielsch, F. Müller, A. Li, and U. Gösele, *Adv. Mater.* **12**, 582 (2000).
22. A. Govindaraj, B. C. Satishkumar, M. Nath, and C. N. R. Rao, *Chem. Mater.* **12**, 202 (2000).
23. B. D. Busbee, S. O. Obare, and C. J. Murphy, *Adv. Mater.* **15**, 414 (2003).
24. Y. Sun, B. Gates, B. Mayers, and Y. Xia, *Nano Lett.* **2**, 165 (2002).
25. K. Soulantica, A. Maisonnat, F. Senocq, M. Fromen, M. Casanove, and B. Chaudret, *Angew. Chem. Inter. Ed.* **40**, 2984 (2001).
26. A. M. Morales and C. M. Lieber, *Science* **279**, 208 (1998).
27. M. Glerup, M. Castignolles, M. Holzinger, G. Hug, A. Loiseau, and P. Bernier, *Chem. Commun.* **9**, 2542 (2003).
28. M. Glerup, H. Kanzow, R. Almairac, M. Castignolles, and P. Bernier, *Chem. Phys. Lett.* **377**, 293 (2003).
29. H. W. Zhu, C. L. Xu, D. H. Wu, B. Q. Wei, R. Vajtai, and P. M. Ajayan, *Science* **296**, 884 (2002).
30. P. Murugavel, M. Kalaiselvam, A. R. Raju, and C. N. R. Rao, *J. Mater. Chem.* **7**, 1433 (1997).
31. A. R. Raju, H. N. Aiyer, and C. N. R. Rao, *Chem. Mater.* **7**, 225 (1995).
32. A. R. Raju, H. N. Aiyer, B. V. Nagaraju, R. Mahendiren, A. K. Raychaudhuri, and C. N. R. Rao, *J. Phys. D* **30**, L71 (1997).
33. H. N. Aiyer, A. R. Raju, G. N. Subbanna, and C. N. R. Rao, *Chem. Mater.* **9**, 755 (1997).
34. Y. Wang, L. Zhang, G. Meng, C. Liang, G. Wang, and S. Sun, *Chem. Commun.* 2632 (2001).
35. Y. Yan, P. Liu, M. J. Romero, and M. M. Al-Jassim, *J. Appl. Phys.* **93**, 4807 (2003).
36. Y. Wang, T. Herricks, and Y. Xia, *Nano Lett.* **3**, 1163 (2003).

37. M. Langlet and J. C. Joubert, in Chemistry of Advanced Materials- A 'chemistry for the 21st century' (IUPAC monograph) Edited by C.N.R. Rao, Blackwell Scientific publishers, 1993, 55.
38. A. Govindaraj, R. Sen, B. V. Nagaraju, and C. N. R. Rao, *Phil. Mag. Lett.* **76**, 363 (1997).
39. R. Seshadri, A. Govindaraj, H. Aiyer, R. Sen, G. N. Subbanna, A. Raju, and C. Rao, *Current Sci.* **66**, 839 (1994).
40. B. Gates, B. Mayers, Y. Wu, Y. Sun, B. Cattle, P. Yang, and Y. Xia, *Adv. Funct. Mater.* **12**, 679 (2002).
41. M. H. Huang, Y. Wu, H. Feick, N. Tran, E. Weber, and P. Yang, *Adv. Mater.* **13**, 113 (2001).
42. G. Gundiah, S. Mukhopadhyay, U. G. Tumkurkar, A. Govindaraj, U. Maitra, and C. N. R. Rao, *J. Mater. Chem.* **13**, 2118 (2003).

Chapter 3

A NEW METHOD OF PURIFICATION OF CARBON NANOTUBES USING HYDROGEN TREATMENT

Summary¹

In this chapter, we describe the purification of carbon nanotubes by a new method involving high-temperature hydrogen treatment. The method involves acid washing followed by hydrogen treatment in the 700 – 1200 °C range. While acid washing dissolves the metal particles, the hydrogen treatment removes amorphous carbon as well as the carbon coating on the metal nanoparticles. The high quality of the nanotubes obtained after purification has been verified by thermogravimetry, transmission electron microscopy, X-ray diffraction and spectroscopic methods. A protocol for the purification of SWNTs prepared by the arc-discharge method is described.

3.1 Introduction

Multi-walled carbon nanotubes (MWNTs) are generally synthesized by the arc-evaporation of graphite or by the pyrolysis of hydrocarbons over metal nanoparticles. Single-walled carbon nanotubes (SWNTs) have been produced by arc-evaporation as well as by laser ablation of metal-impregnated graphite rods. MWNTs, SWNTs and aligned carbon nanotube bundles are

¹Papers based on this study have appeared in *Proc. Ind. Acad. Sci.* (2003), *J. Phys. Chem. B* (2004) and *Small* (2005).

obtained in a single step by the pyrolysis of organometallic precursors (Chapter 1 for more details). The as-synthesized nanotubes usually contain impurities such as amorphous carbon and metal nanoparticles, the latter being specially prominent when metal catalysts are employed. As-synthesized SWNTs prepared by processes such as arc-discharge, laser-ablation, HiPco and pyrolysis of hydrocarbon or organometallic precursors, contain carbonaceous impurities, typically amorphous carbon and graphite nanoparticles, as well as particles of the transition metal catalyst. Often these metal catalyst nanoparticles are coated with graphitic layers. Thus, purification is an important problem faced in the use of single-walled carbon nanotubes (SWNTs) for various studies and applications. An early purification strategy for arc-discharge multi-walled carbon nanotubes was the use of high temperature oxidation in air [1], but this is not entirely satisfactory for use with SWNTs. The problem lies with the catalyst metal particles present in the material. In the presence of oxygen and other oxidizing gases, the metal particles catalyze the low-temperature oxidation of the nanotubes. Some of the purification methods for SWNTs reported in the literature employ a combination of the following steps: gas- or vapor-phase oxidation, wet chemical oxidation/treatment, centrifugation or filtration (including chromatography techniques) [2–11]. Bandow *et al.* [2] used microfiltration to rid SWNTs of contaminants such as carbon nanospheres, metal nanoparticles, polycyclic aromatic carbons and fullerenes. Dujardin *et al.* [3,4] used acid refluxing for the purification of SWNTs obtained by laser-ablation. Strong oxidation and acid refluxing, however, affect the structure of the nanotubes and acid digestion of impurities also gives rise to functional groups on the nanotube surface. High-temperature vacuum annealing of the purified samples is carried out in some of the procedures to remove the surface functional groups [5,6]. Hydrothermal treatment has been used to remove amorphous carbon from the

nanotube surface [7, 8]. The amorphous carbon present in the nanotubes is generally burnt away by heating in air or oxygen around 300 – 400 °C [3, 4]. Chiang *et al.* [9,10] have used wet oxygen (20 % O₂ in argon passed through a water-filled bubbler) to remove carbonaceous shells encapsulating the metal particles, which were subsequently dissolved in conc. HCl. Martinez *et al.* [11] employed a combination of air oxidation and microwave acid digestion to purify arc-discharge SWNTs. Sen *et al.* [12] have recently examined the effect of oxidation conditions on the purity of the SWNTs synthesized by the arc-discharge process and found a 3-fold improvement in purity on repeated reactions with oxygen at 265 – 315 °C. CO₂-treatment at 800 – 1000 °C has been suggested for the removal of carbon covering over the metal nanoparticles by Gilbert *et al.* [13]. Xu *et al.* [14] have outlined a controlled and scalable multi-step purification method to remove carbonaceous and metallic impurities from raw HiPco SWNTs. In this study, the carbon-coated iron nanoparticles were exposed and oxidized by multi-step oxidation at increasing temperatures, with the oxidized iron nanoparticles being deactivated by using either C₂H₂F₄ or SF₆.

Due to the importance of purification in nanotube research, we have explored an alternative method involving high-temperature hydrogen treatment. The method has been most effective in purifying both SWNTs by arc-discharge, laser ablation, HiPco as well as MWNTs.

3.2 Experimental details

Arc discharge SWNTs (arc SWNTs) were synthesized by the method as reported by Journet *et al.* [15] using a composite rod containing Y (1 at.%) and Ni (4.2 at.%) as the anode and a graphite rod as the cathode, under a helium pressure of 660 torr with a current of 100 A and 30 V. The nanotubes were heated in air at 300 °C for 12 h and then stirred in conc. HNO₃ at 60 °C

for 24 h in order to dissolve the metal nanoparticles. The product was washed with distilled water, dried, dispersed in ethanol under sonication, and filtered using Millipore ($0.3 \mu\text{m}$) filter paper. The filtered product was dried in an oven at 100°C for 2 h. The sample was heated to 1000°C in a furnace at a rate of 3°C per minute, in flowing hydrogen at 100 sccm and held at that temperature for 2 h. The resulting sample was again stirred in conc. HNO_3 at 60°C for 3 h and finally heated in a furnace at 1000°C for 2 h in flowing hydrogen (100 sccm). A similar procedure was employed for the purification of SWNTs obtained by laser ablation (laser SWNTs). A CS_2 extraction was carried out on the laser SWNTs and subsequently treated with 3 N HCl at 60°C for 24 h to dissolve the metal nanoparticles. The nanotubes were heated in flowing hydrogen (100 sccm) at 1000°C for 2 h and the product was again stirred with 3 N HCl at 60°C for 3 h and finally heated at 1000°C for 2 h in flowing hydrogen (100 sccm). A similar procedure was employed for HiPco SWNTs. Suspensions of SWNTs for recording Visible-NIR spectroscopy were prepared as reported by O'Connell *et al.* [16]. We used H_2O instead of D_2O to obtain a SDS dispersion of SWNTs.

Arc-discharge MWNTs were prepared by striking an arc between two graphite electrodes in a He atmosphere. The cathodic deposit was collected, powdered and sonicated in ethanol to separate the nanotubes from the heavier turbostatic graphite. The nanotubes were then refluxed in a 2:1 mixture of conc. HNO_3 and conc. H_2SO_4 (acid treated MWNTs) for 20 h. The acid treated MWNTs were hydrogen treated at 1100°C for 2 h. Aligned MWNT bundles were obtained by ferrocene pyrolysis (see chapter 2) and were subjected to acid treatment before they were heated in hydrogen at 1100°C .

The nanotubes were characterized at each stage by powder X-ray diffraction, scanning electron microscopy (SEM), transmission electron microscopy (TEM) and Raman spectroscopy. The powder X-ray diffraction patterns

were recorded using a Seifert XRD 3000 TT instrument. The SEM images were obtained with a Leica S-440I microscope and TEM images with a JEOL JEM 3010 instrument operating at an accelerating voltage of 300 kV. Raman measurements were performed in a 90° geometry using a Jobin Yvon TRIAX 550 triple grating spectrometer equipped with a cryogenic charge-coupled device camera, using diode-pumped frequency doubled solid state Nd:YAG laser of 532 nm (Model DPSS 532-400, Coherent Inc. USA).

3.3 Results and Discussions

The as-synthesized arc SWNTs contain a lot of impurities as seen in the SEM image in Figure 3.1 (a). TEM images reveal the presence of amorphous carbon and metal nanoparticles apart from SWNT bundles (Figure 3.1 (c)). The image also reveals that the SWNTs bundles have a diameter 10-30 nm. Most of the metal nanoparticles got dissolved in the ensuing acid washing, but the nanotubes are covered with amorphous carbon as seen in TEM image in Figure 3.1 (d). In Figure 3.1 (e), we show the TEM image after the hydrogen treatment. The absence of amorphous carbon is clearly evident and the bundles grow in size and have diameters in the 20-50 nm range. The small metal nanoparticles melt and agglomerate into larger particles. It is well known that the melting points of small clusters are much lower than the bulk. Inset in Figure 3.1 (e) shows a TEM image of an agglomerated metal particle. In bulk, nickel (m.p. 1726 K) and yttrium (m.p. 1795 K) melt above the temperatures employed in our purification procedure. Melting and agglomeration of the metal nanoparticles occurs in the 750 – 850 °C range. These metal nanoparticles are removed in the second acid washing, carried out for a shorter duration.

The second acid treatment is followed by the high temperature hydrogen treatment at 1000 °C to obtain pure SWNTs. A TEM image of the purified

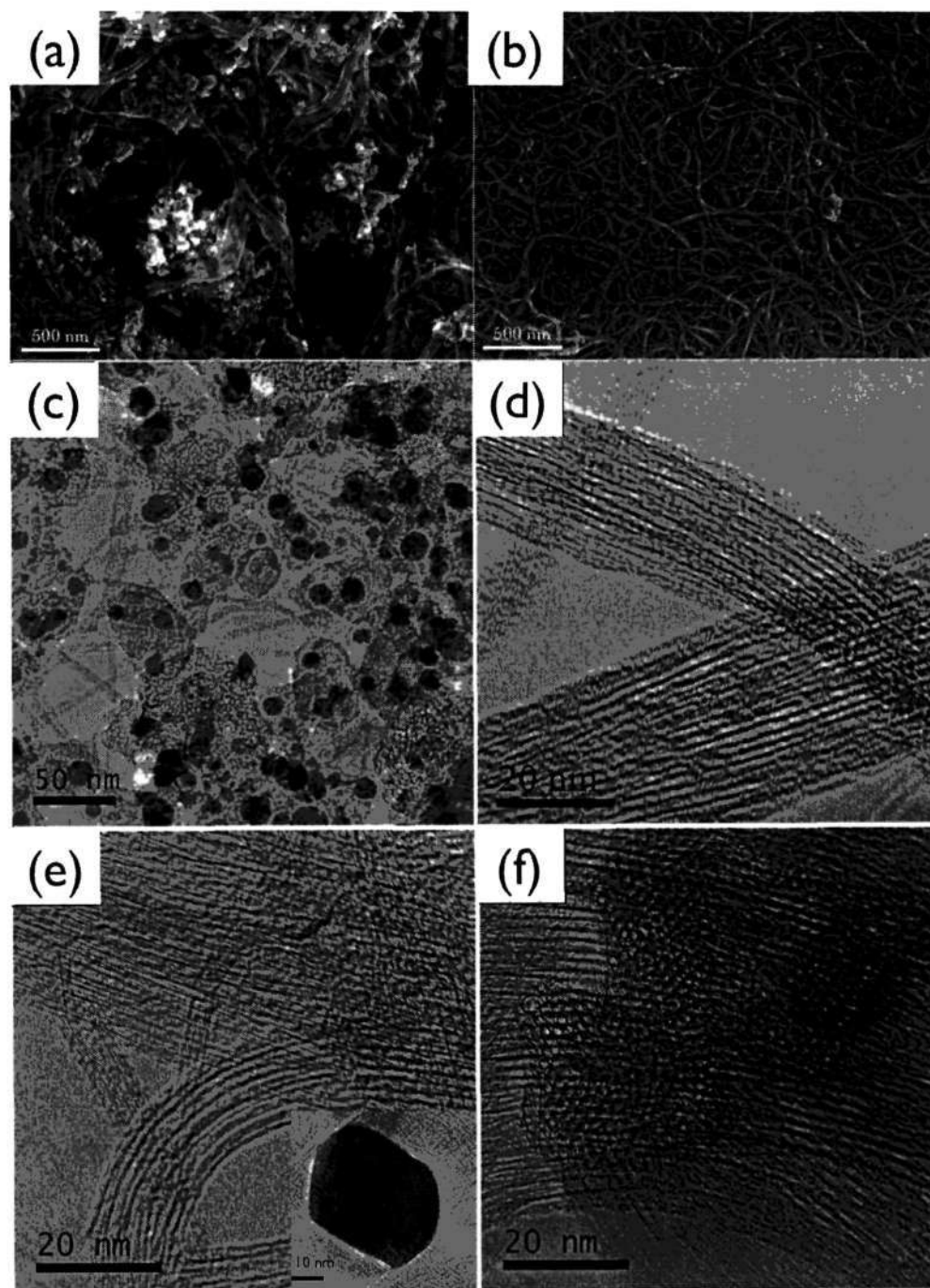


Figure 3.1: (a) and (b) FESEM images of as-prepared SWNTs and hydrogen purified SWNTs respectively. TEM images of (c) as-synthesized arc SWNTs, (d) after first acid washing, (e) after first hydrogen treatment and (f) after second hydrogen treatment. Inset in (e) shows a TEM image of a large metal nanoparticle after first hydrogen treatment.

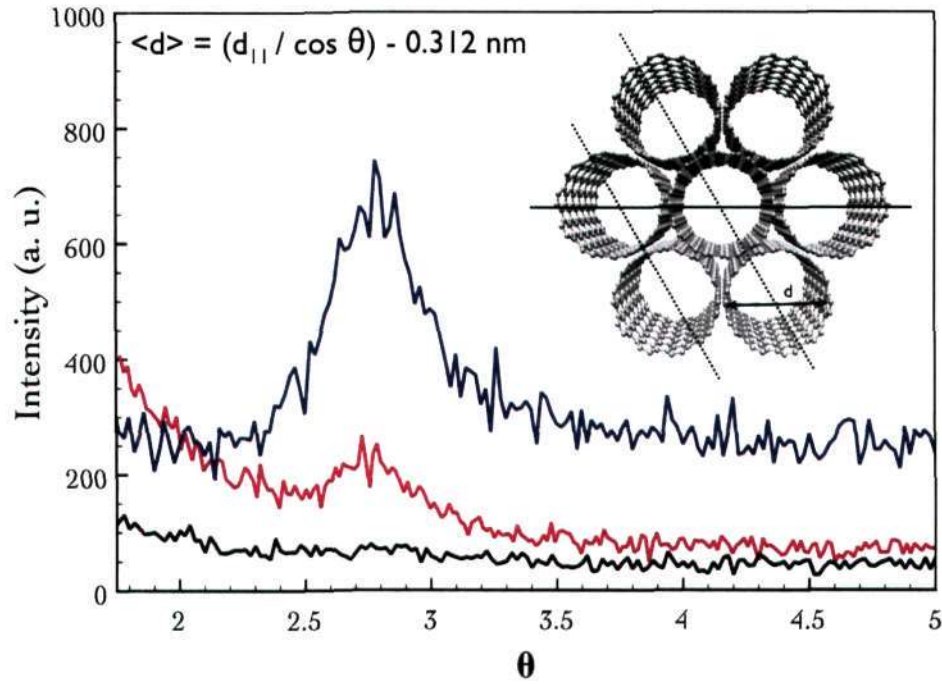


Figure 3.2: XRD pattern of (a) as-synthesized arc SWNTs, (b) after first acid washing and (c) after the second hydrogen treatment.

SWNTs is shown in Figure 3.1 (f). The corresponding SEM image of purified SWNTs is shown in Figure 3.1 (b). We do not observe any hollow onion-like structures often found in SWNTs purified by other methods [7, 8], indicating thereby that carbon covering on the metal particles is etched away by hydrogen.

SWNTs form a triangular lattice and give a distinctive low angle reflection in the X-ray diffraction pattern [17]. In Figure 3.2, we show the low-angle XRD patterns of the as-synthesized and acid-treated SWNTs as well as those obtained after second hydrogen treatment. The (1,0) diffraction line is not observed in the case of as-synthesized SWNTs and appears as a small hump in acid treated SWNTs. This line is seen as an intense peak in the case of second hydrogen-treated sample. The mean diameter D_{mean} given in nanometers can be calculated using the following relationship:

$$D_{mean} = (d_{11} / \cos(\theta)) - 0.312 \quad (3.1)$$

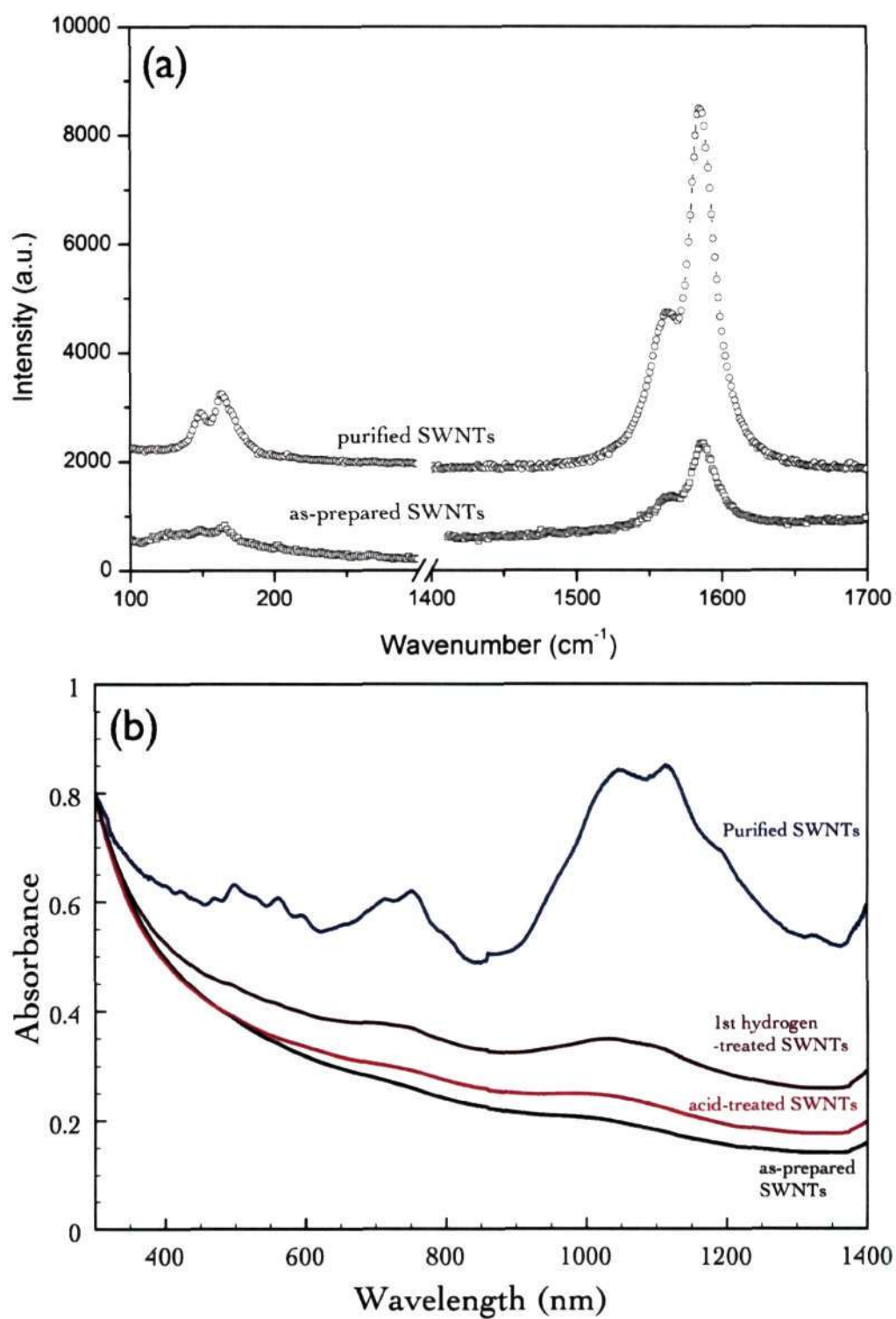


Figure 3.3: (a) Raman spectra of arc SWNTs of as-synthesized and purified SWNTs after second hydrogen treatment. (b) Visible-NIR spectra of arc SWNTs: as-synthesized, after first acid washing, after first hydrogen treatment and after second hydrogen treatment.

The mean diameter of the purified SWNTs is estimated to be 1.52 nm from the (1,0) diffraction line.

The G-band and the radial-breathing modes of SWNTs in the Raman spectra are strong in intensity while the other Raman modes are weak. The Raman spectra of the as-synthesized and purified arc SWNTs are shown in Figure 3.3 (a). The as-synthesized sample (curve (a)) shows a G-band which is split into two bands at 1562 cm^{-1} and 1586 cm^{-1} . The D-band appears as a broad peak centered at 1343 cm^{-1} indicating that the sample contains amorphous carbon. The second order Raman bands appear as weak peaks centered at 941 cm^{-1} and 1075 cm^{-1} . The purified sample shows an intense split G-band (1563 cm^{-1} and 1585 cm^{-1}) and strong radial-breathing modes. The D-band is considerably weaker after hydrogen treatment. The radial breathing modes show the diameters lie in the 1.32-1.89 nm range, in agreement with the calculated diameter distribution obtained from TEM images and low-angle x-ray diffraction. The Visible-NIR spectra of the arc SWNTs at various stages of purification is shown in Figure 3.3 (b). Due to their one-dimensional nature, carbon nanotubes exhibit van Hove singularities in the electronic density of states. Visible NIR spectroscopy provides additional evidence to the one-dimensional nature. The peak centered at 1100 nm is due to the S_{22} transition in semiconducting SWNTs and the second set of peaks near 700 nm due to the M_{11} of metallic nanotubes. The intensity of the two bands progressively increase with each step of purification and markedly after the second hydrogen treatment.

We have also carried out hydrogen treatment of SWNTs obtained by laser ablation. The TEM images in Figure 3.4, show the laser SWNTs at various stages of purification. Fullerenes, metal nanoparticles, amorphous carbon and SWNT bundles are present in the as-synthesized laser SWNTs (Figure 3.4 (a)). The fullerenes were removed by CS_2 extraction and the

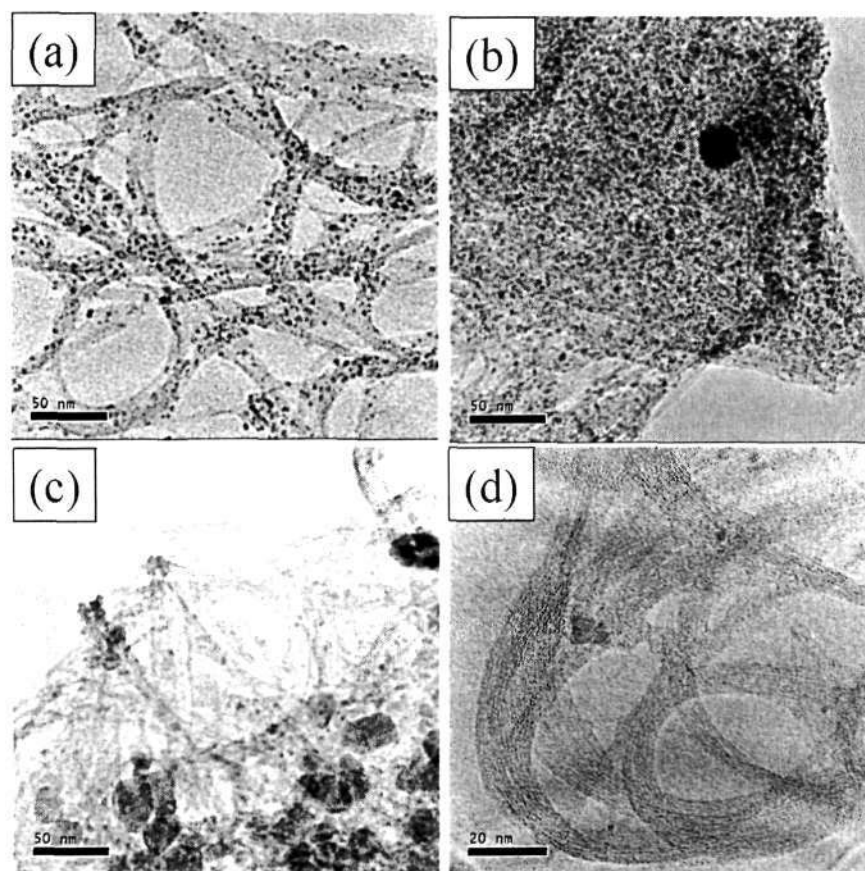


Figure 3.4: TEM images of laser SWNTs- (a) as-synthesized, (b) after first acid washing, (c) after first hydrogen treatment and (d) after second hydrogen treatment.

metal nanoparticles were partly dissolved in acid. After the acid washing, amorphous carbon continues to cover the SWNTs (Figure 3.4 (b)). This amorphous carbon was removed by a hydrogen treatment at 1000 °C as can be seen in Figure 3.4 (c). Similar to the arc SWNTs, we observe an agglomeration of the undissolved metal nanoparticles, which could be removed by the subsequent acid treatment. The nanotubes heated again in hydrogen at 1000 °C were indeed of high purity (Figure 3.4 (d)). The purity of the nanotubes was also revealed in the Raman and visible-NIR spectra. In Figure 3.5 (a), we show the Raman spectra of the as-prepared laser SWNTs and that after the second hydrogen treatment. The intensity of the G-band increases

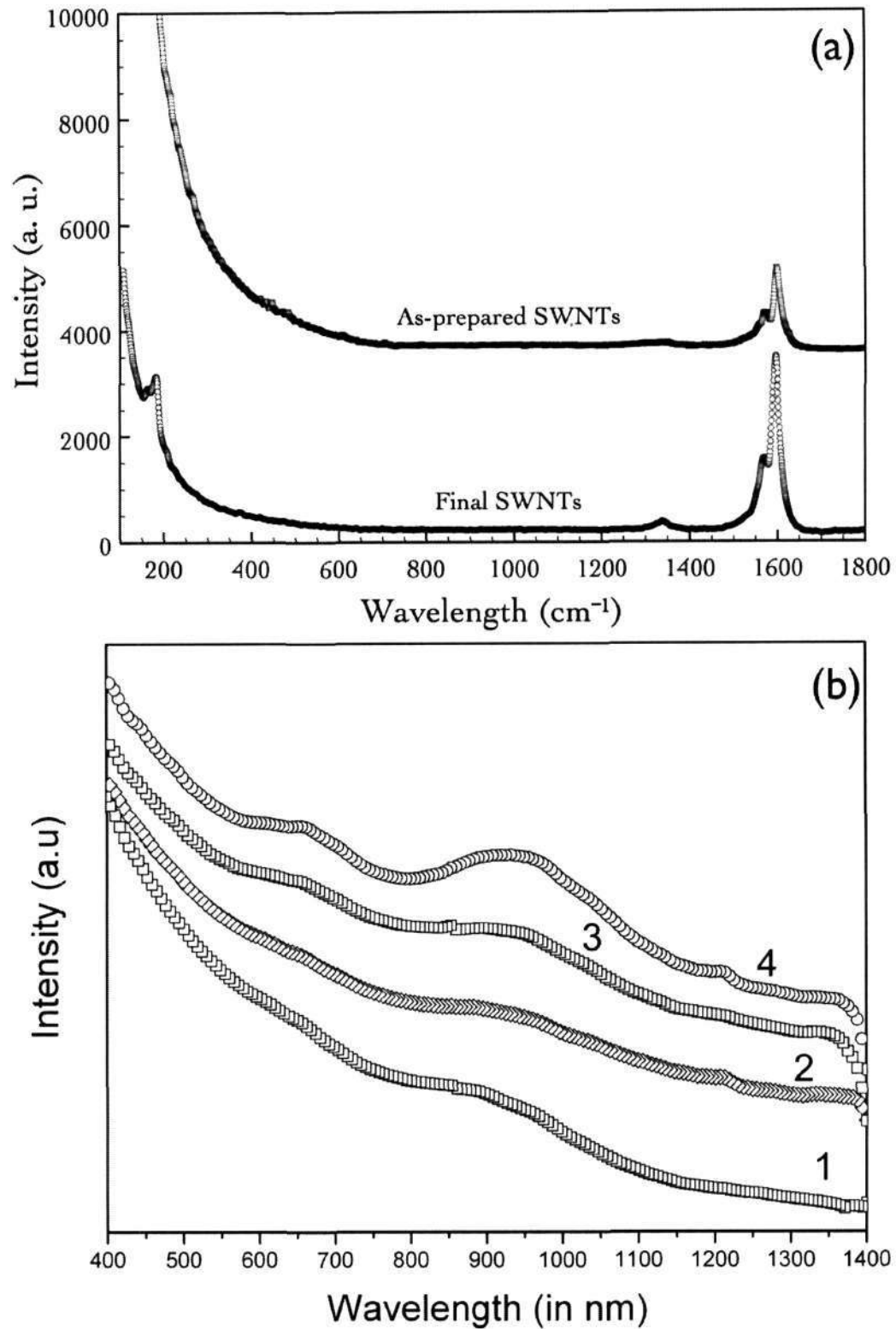


Figure 3.5: (a) Raman spectra of as-prepared laser SWNTs and second hydrogen treatment. (b) Visible-NIR spectra of laser SWNTs: (1) as-synthesized, (2) after first acid washing, (3) after first hydrogen treatment and (4) after second hydrogen treatment.

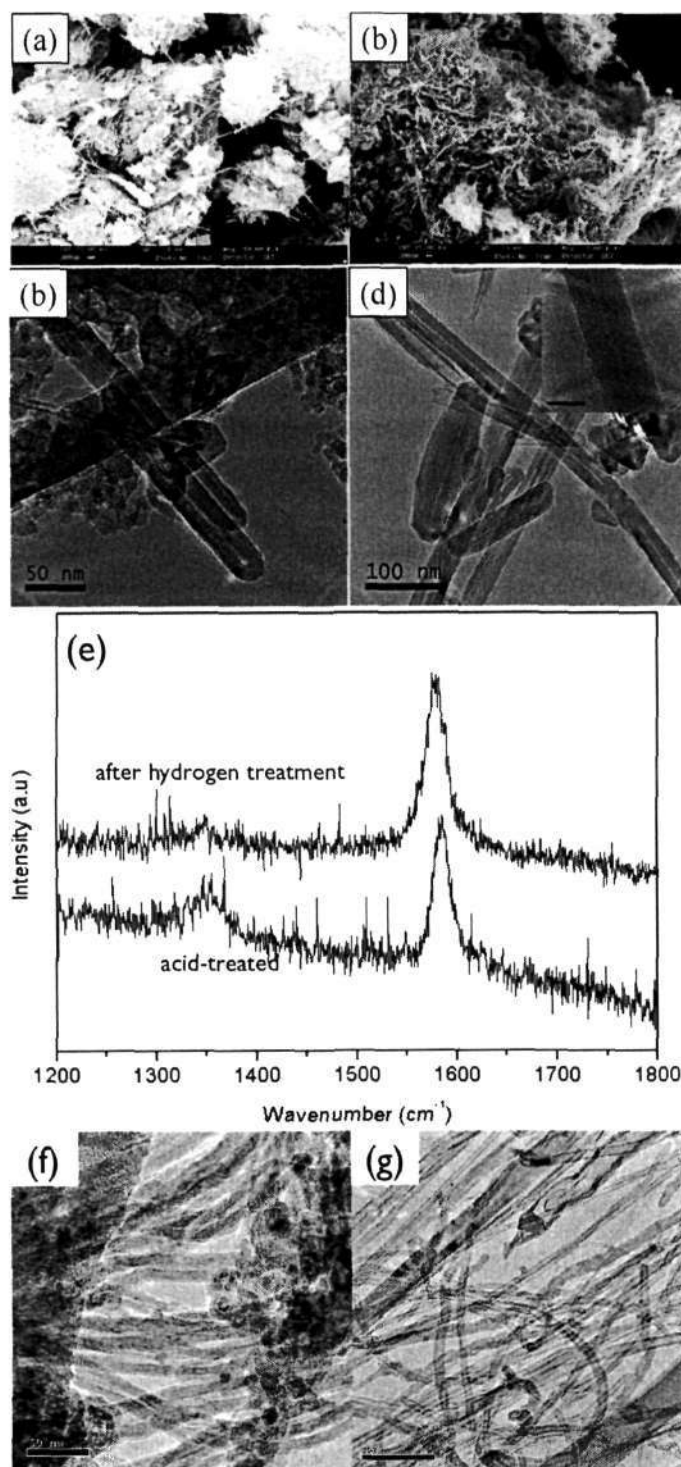


Figure 3.6: (a) SEM image of acid refluxed arc discharge MWNTs, (b) SEM image after hydrogen treatment at 1100 °C. (c) and (d) are the respective TEM images. (e) Raman spectra of acid-treated arc discharge MWNTs and after hydrogen treatment at 1100 °C. (f) and (g) TEM images of acid-treated ferrocene pyrolysis MWNTs before and after hydrogen treatment respectively.

3-fold after purification and radial breathing modes are visible after purification. From the radial breathing modes, we estimate the average diameter of the laser SWNTs to be 1.36 nm. The visible-NIR spectra of laser SWNTs at each stage of purification are very similar to that of the arc SWNTs as their diameters are comparable (Figure 3.5 (b)). HiPco SWNTs have a average diameter of 0.9 nm and we were able to purify HiPco SWNTs using our new method.

We have examined the efficacy of the high temperature hydrogen treatment procedure for MWNTs. Acid treated MWNTs contain a large amount of amorphous carbon as seen in the SEM and TEM images in Figures 3.6 (a) and (b). The amorphous carbon is removed by the high temperature hydrogen treatment (Figures 3.6 (c) and (d)). The high resolution electron microscope (HREM) image shown as an inset in Figure 3.6 (d) indicates that the crystalline nature of the MWNTs is well-preserved after the acid and hydrogen treatment. The Raman spectra confirm the high purity of the MWNTs subjected to these treatments (Figure 3.6 (e)). The G/D band intensity improves significantly after hydrogen treatment. We find that aligned carbon nanotubes prepared by ferrocene pyrolysis (see Chapter 2) are also effectively purified by high temperature hydrogen treatment as revealed by the TEM images in Figures 3.6 (f) and (g).

3.4 Protocol for the purification of SWNTs

One of the problems in the purification of nanotubes is the evaluation of the purity of the purified sample. Several techniques such as electron microscopy, thermogravimetric analysis (TGA), Raman spectroscopy and visible-NIR spectroscopy have been employed for the determination for the purity of SWNTs. Itkis *et al.* [18] have pointed out the incapability of electron microscopy in the quantitative evaluation of purity of the bulk SWNTs. This is

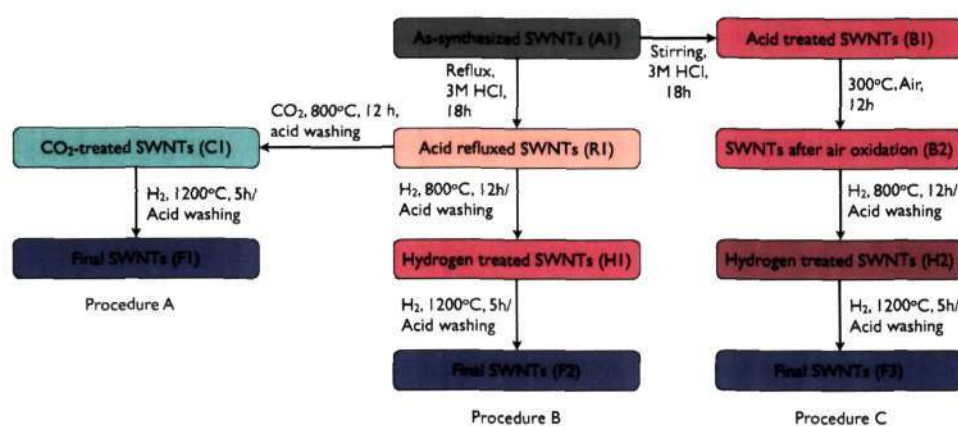


Figure 3.7: Schematic diagram of the three procedures investigated for developing a protocol for the purification of SWNTs prepared by the arc-discharge method.

due to the small volume of the sample analyzed and the absence of algorithms to convert the images into numerical data. The use of solution-phase Raman spectroscopy and NIR spectroscopy for the quantitative evaluation of bulk purity has been strongly recommended. Clearly, any procedure or protocol for the purification of SWNTs should not only take into account the various steps referred to earlier, but also the sensitivity of the methods of evaluation of purity as pointed out by Itkis *et al.* [18]. Such an evaluation has been carried out on SWNTs treated with gases such as O_2 , CO_2 and H_2 followed by acid cleaning. Noting that a procedure based on acid washing followed by air-oxidation at $300^\circ C$, hydrogen treatment at $800^\circ C$ and ending again by acid washing yielded only near-pure SWNTs containing some residue due to the metal particles (12%), three procedures (schematically represented in Figure 3.7) have been examined for the purification of SWNTs synthesized by the arc-discharge. At each step, the product was examined by transmission electron microscopy, thermogravimetric analysis, Raman spectroscopy and visible-NIR spectroscopy. The results obtained are instructive and illustrate the nature of the challenge faced in the purification of SWNTs and the relative efficiencies of the various steps and procedures. As-synthesized SWNTs

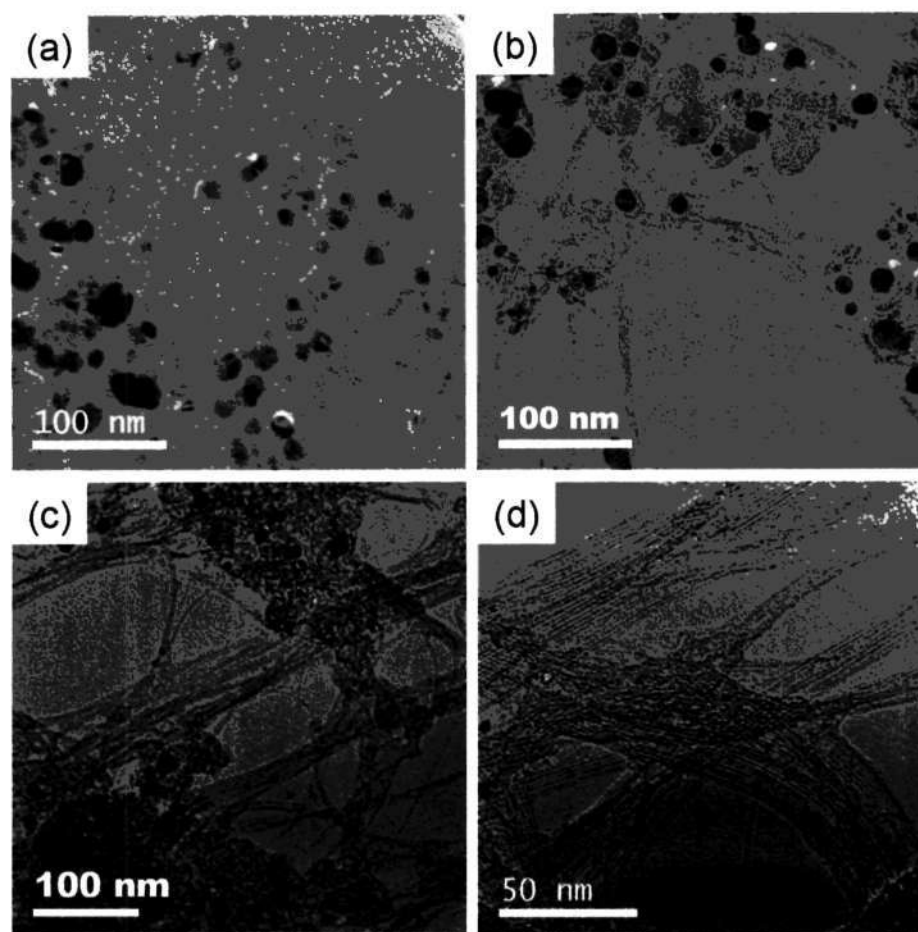


Figure 3.8: TEM images of (a) as-synthesized SWNTs, (b) acid-refluxed SWNTs, (c) SWNTs after CO₂ treatment followed by acid washing (procedure A), d) SWNTs after final H₂ treatment at 1200 °C followed by acid washing (procedure A).

contain a large proportion of amorphous carbon and metal nanoparticles as can be seen in the TEM image in Figure 3.8 (a). Even after acid washing or refluxing, a considerable proportion of the metal nanoparticles remains as evident from the TEM image in Figure 3.8 (b). TGA shows little difference between the as-synthesized and acid-treated SWNTs with a residual weight percentage of 30% (curves a-c in Figure 3.9). As-synthesized SWNTs get oxidized at a relatively low temperature of 320 °C and there is only a small increase in the oxidation temperature on acid treatment. Treatment with air (at 300 °C), CO₂ (at 800 °C) or H₂ (at 800 °C) followed by acid washing

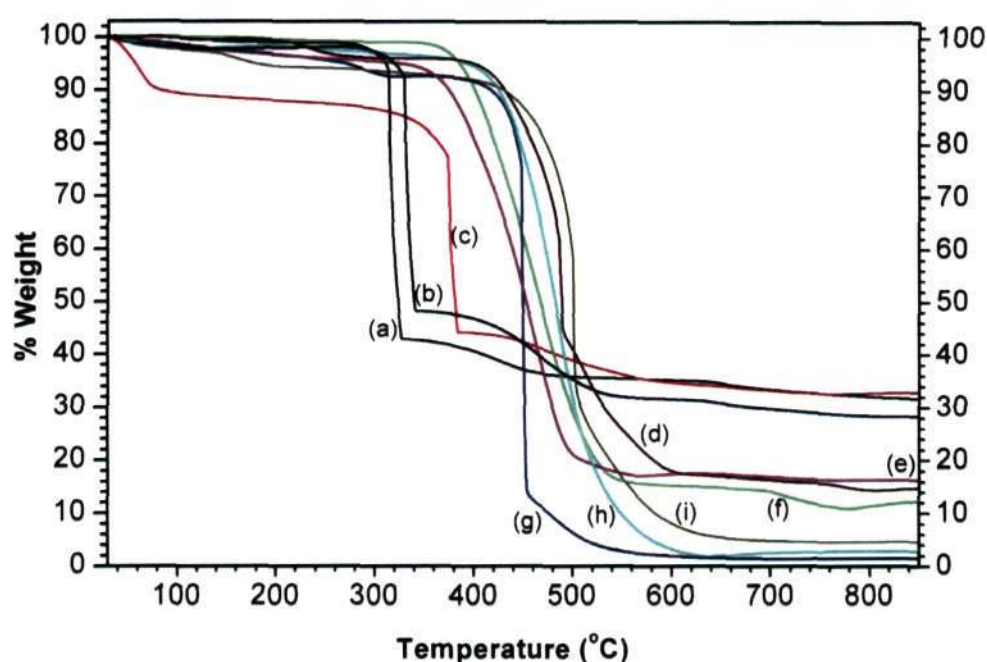


Figure 3.9: TGA curves of (a) as-synthesized SWNTs, (b) acid-stirred SWNTs, (c) acid-refluxed SWNTs, d) SWNTs after air oxidation followed by acid washing (procedure C), (e) H₂-treated SWNTs at 800 °C followed by acid washing (procedure B), (f) CO₂-treated SWNTs at 800 °C followed by acid washing (procedure A), (g) the final product in procedure A, (h) the final product in procedure B, (i) the final product in procedure C. TGA were carried out in an O₂ atmosphere and the samples were heated at 5 °C min⁻¹.

removes a good proportion of the metal particles as evident by the increase in the oxidation temperature of the SWNTs to 450 °C and a large decrease in the wt % of the residue (15%). It can be seen from the TEM image in Figure 3.8 (c) that after CO₂-treatment at 800 °C followed by acid washing, the metal nanoparticles are not completely eliminated. It is only after the final hydrogen treatment at 1200 °C followed by acid washing that amorphous carbon and metal nanoparticles are eliminated almost entirely in all the three procedures. The oxidation temperatures of the final products obtained by the procedures A, B and C are 460, 480 and 510 °C respectively, the wt% of the residues being 2, 2 and 4 respectively. A TEM image of SWNTs obtained after the final H₂-treatment at 1200 °C and acid washing is shown in Figure 3.8 (d). The quality of the products obtained by procedures A, B and C has been

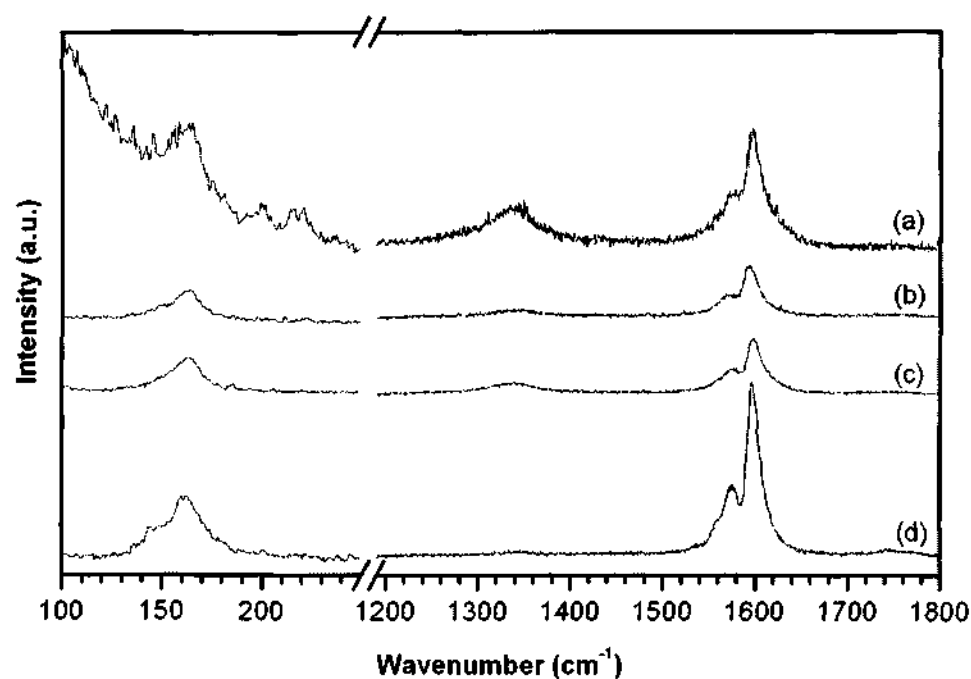


Figure 3.10: Raman spectra at different stages in procedure B: (a) as-synthesized SWNTs, (b) acid-refluxed SWNTs, (c) H_2 -treated SWNTs at 800°C followed by acid washing, (d) final product after H_2 treatment at 1200°C followed by acid washing.

examined by Raman and visible-NIR spectroscopy. The Raman spectrum of the products after every step in procedure B is as shown in Figure 3.10. The presence of amorphous carbon in the as-synthesized SWNTs (spectrum a) is indicated by the presence of an intense D-band (1340 cm^{-1}). Furthermore, the low-frequency radial breathing mode is not clearly observed. On acid refluxing, the intensities of the radial breathing band and the G-band (1595 cm^{-1}) improve, but the D-band is eliminated only after the H_2 -treatment at 1200°C as seen in spectrum (d). Similar results are obtained in the samples in the other procedures as well, the near absence of the D-band, increase in the intensity of the G-band and the appearance of sharp radial breathing modes all occurring only after the final H_2 -treatment at 1200°C followed by acid washing. Taking the ratio of the intensities of the D and G bands as a measure of purity, we see a progressive decrease in the D/G intensity ratio

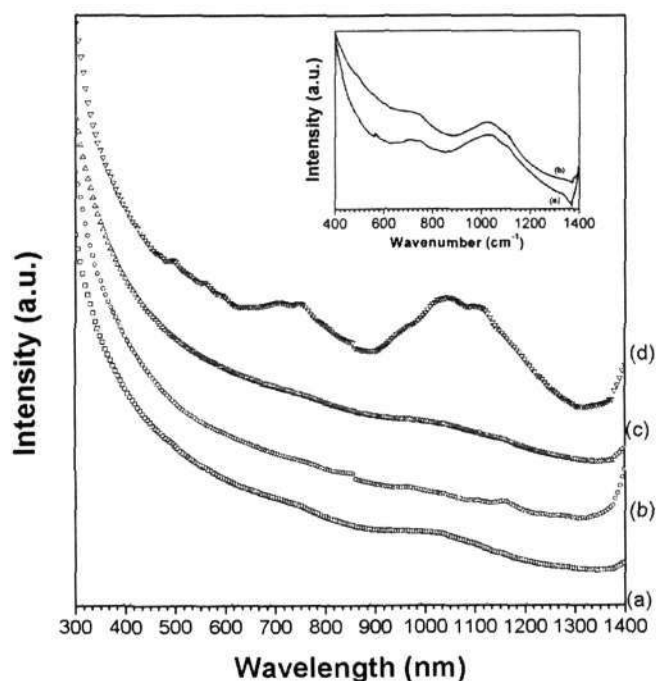


Figure 3.11: Visible-NIR spectra at different stages in procedure B: (a) as-synthesized SWNTs, (b) acid-refluxed SWNTs, (c) H-treated SWNTs at 800 °C followed by acid washing, (d) final product after H₂ treatment at 1200 °C followed by acid washing. The inset shows the visible-NIR spectra of the final products from procedures A and C (labeled accordingly).

through the various steps, until the ratio becomes negligible after the final step in procedure B (Figure 3.10). The visible-NIR spectra of the products at the various stages of purification in procedure B are shown in Figure 3.11. The absorption bands due to the van Hove singularities are observed only after the final H₂-treatment at 1200 °C, the behavior being similar in procedures A and C as well. Since we observe a good electronic spectrum only after attaining the highest purity, it would seem that NIR spectroscopy is relatively more sensitive to impurities. While procedure B, involving high-temperature hydrogen treatment, seems to be the best and simplest amongst the protocols discussed above, it should be noted that absolute purity cannot be guaranteed for the SWNTs produced by the catalyst-mediated methods. It would be most desirable if one can find a catalyst-free method of production of the SWNTs which would only require the removal of the carbonaceous

impurities. As far as ascertaining the purity is concerned, clearly one has to employ all the techniques (TGA, TEM and Raman). The variation of the intensity ratio of the D and G bands in the Raman spectrum gives a good quantitative measure of purity, although a negligible D/G intensity ratio may not indicate 100% purity. It is noteworthy that the near absence of the D band is accompanied by clean absorption bands in the NIR spectrum. In this sense, the NIR spectrum provides a crucial test of purity [18].

3.5 Conclusions

In conclusion, we have developed a new and effective method for the purification of SWNTs and MWNTs. The method involves acid washing followed by the high-temperature hydrogen treatment repeated twice. Excellent SWNTs containing little or no amorphous carbon and metal particles are obtained by this means, as verified by microscopy, XRD and spectroscopic techniques. It should be noted that hydrogen treatment not only removes amorphous carbon but also helps in dissolution of metal nanoparticles on acid washing by discasing and embrittling the carbon coating on the particles.

3.6 References

1. T. W. Ebbesen, P. M. Ajayan, H. Hiura, and K. Tanigaki, *Nature* **367**, 519 (1994).
2. S. Bandow, A. M. Rao, K. A. Williams, A. Thess, R. E. Smalley, and P. C. Eklund, *J. Phys. Chem. B* **101**, 8839 (1997).
3. E. Dujardin, T. W. Ebbesen, A. Krishnan, and M. M. J. Treacy, *Adv. Mater.* **10**, 611 (1998).
4. E. Dujardin, C. Meny, P. Panissod, J. Kintzinger, N. Yao, and T. W. Ebbesen, *Sol. Stat. Commun.* **114**, 543 (2000).
5. A. G. Rinzler, J. Liu, H. Dai, P. Nikolaev, C. B. Huffman, F. J. Rodriguez-Macias, P. J. Boul, A. H. Lu, D. Heymann, D. T. Colbert, R. S. Lee, J. E. Fischer, A. M. Rao, P. C. Eklund, and R. E. Smalley, *Appl. Phys. A* **67**, 29 (1998).
6. A. C. Dillon, T. Gennett, K. M. Jones, J. L. Alleman, P. A. Parilla, and M. J. Heben, *Adv. Mater.* **11**, 1354 (1999).
7. K. Tohji, T. Goto, H. Takahashi, Y. Shinoda, N. Shimizu, B. Jeyadevan, I. Matsuoka, Y. Saito, A. Kasuya, T. Ohsuna, K. Hiraga, and Y. Nishina, *Nature* **383**, 679 (1996).
8. K. Tohji, H. Takahashi, Y. Shinoda, N. Shimizu, B. Jeyadevan, I. Matsuoka, Y. Saito, A. Kasuya, S. Ito, and Y. Nishina, *J. Phys. Chem. B* **101**, 1974 (1997).
9. I. W. Chiang, B. E. Brinson, A. Y. Huang, P. A. Willis, M. J. Bronikowski, J. L. Margrave, R. E. Smalley, and R. H. Hauge, *J. Phys. Chem. B* **105**, 8297 (2001).
10. I. W. Chiang, B. E. Brinson, R. E. Smalley, J. L. Margrave, and R. H. Hauge, *J. Phys. Chem. B* **105**, 1157 (2001).
11. M. T. Martinez, M. A. Callejas, A. M. Benito, W. K. Maser, M. Cochet, J. M. Andrés, J. Schreiber, O. Chauvet, and J. L. G. Fierro, *Chem. Commun.* 1000 (2002).
12. R. Sen, S. M. Rickard, M. E. Itkis, and R. C. Haddon, *Chem. Mater.* **15**, 4273 (2003).
13. K. E. H. Gilbert, *Purification, Separation and Characterization of Single-walled Carbon Nanotubes (SWNTs)*, 227th ACS National Meeting (2004).
14. Y. Xu, H. Peng, R. H. Hauge, and R. E. Smalley, *Nano Lett.* **5**, 163 (2005).

15. C. Journet, W. K. Maser, P. Bernier, A. Loiseau, M. Lamy de la Chapelle, S. Lefrant, P. Deniard, R. Lee, and J. E. Fischer, *Nature* **388**, 756 (1997).
16. M. J. O'Connell, S. H. Bachilo, C. B. Huffman, V. C. Moore, M. S. Strano, E. H. Haroz, K. L. Rialon, P. J. Boul, W. H. Noon, C. Kittrell, J. Ma, R. H. Hauge, R. B. Weisman, and R. E. Smalley, *Science* **297**, 593 (2002).
17. A. Thess, R. Lee, P. Nikolaev, H. Dai, P. Petit, J. Robert, C. Xu, Y. H. Lee, S. G. Kim, A. G. Rinzler, D. T. Colbert, G. E. Scuseria, D. Tománek, J. E. Fischer, and R. E. Smalley, *Science* **273**, 483 (1996).
18. M. E. Itkis, D. E. Perea, R. Jung, S. Niyogi, and R. C. Haddon, *J. Am. Chem. Soc.* **127**, 3439 (2005).

Chapter 4

CHEMICALLY-BONDED CERAMIC COATINGS ON CARBON NANOTUBES AND INORGANIC NANOWIRES

Summary¹

Reacting acid-treated carbon nanotubes with metal halides such as TiCl_4 , followed by reaction with water and calcination, yields nanotubes with a chemically-bonded oxide layer, the thickness being controlled by the number of cycles of the reaction with the metal halide and H_2O . Chemically-bonded oxide layers have been similarly generated on nanowires of Al_2O_3 and silicon by the reaction of the metal halides with the surface hydroxyl groups present on the nanowire surfaces. Typical of the ceramic oxide coated nanostructures prepared by this method are, TiO_2 -coated MWNTs and SWNTs, SiO_2 -coated MWNTs as well as TiO_2 -coated Al_2O_3 nanowires and Si nanowires. The methodology described here may be of value in preparing useful composites involving oxide layers and nanostructures.

4.1 Introduction

Ceramic oxide coated nanotubes and nanowires have potential application in sensors, field effect transistors and composites. Thus, several workers have prepared composites of these materials and studied their properties [1, 2]. Rao and co-workers have employed carbon nanotubes (CNTs) as templates for the preparation of nanotubes and nanowires of inorganic materials, specially of metal oxides [3–5]. For this purpose, the CNTs were covered with

¹A paper based on this study has appeared in *Adv. Mater.* (2005).

an oxide precursor or a gel and the nanotubes burnt off in air. Han *et al.* [6] coated SWNTs by a simple solution based chemical route. While Fu *et al.* [7] used a high pressure method to coat the nanotubes with layers of rare-earth oxides. Ruthenium oxide nanotubes have been obtained by Min *et al.* [8] by the oxidation of Ru-coated carbon nanotubes prepared by atomic layer deposition. It was our view that it would be of considerable importance if we were able to prepare composite structures of CNTs and inorganic nanowires, wherein a layer of a ceramic oxide is chemically bonded to the surface of the nanostructures. Knowing that Si-O or metal-oxygen bonds can be formed with substrates by the reaction of appropriate chloro-compound with the hydroxyl groups present on the substrate, we have explored whether ceramic oxide-coated nanostructures can be obtained by the reaction of reactive metal chlorides with acid-treated CNTs and metal oxide nanowires. This seemed entirely feasible since the CNTs on acid treatment get functionalized with surface hydroxyl and carboxyl groups, and the metal oxide nanowires would necessarily possess hydroxyl groups on the surface. The surface functional groups have been made use for the solubilization of CNTs and other purposes. On reaction with the vapor of a metal halide such as TiCl_4 , the surface hydroxyl groups on the nanostructures can form metal-oxygen bonds by eliminating HCl leaving extra metal-chlorine bonds. The metal-chlorine bonds can be hydrolyzed by treatment with water vapor and the hydroxide layer again reacted with the metal chloride. On repeating the process several times followed by calcination, we have obtained a CNT or a metal oxide nanowire with a chemically-bonded ceramic coating of the desired thickness. We illustrate the process schematically in Figure 4.1.

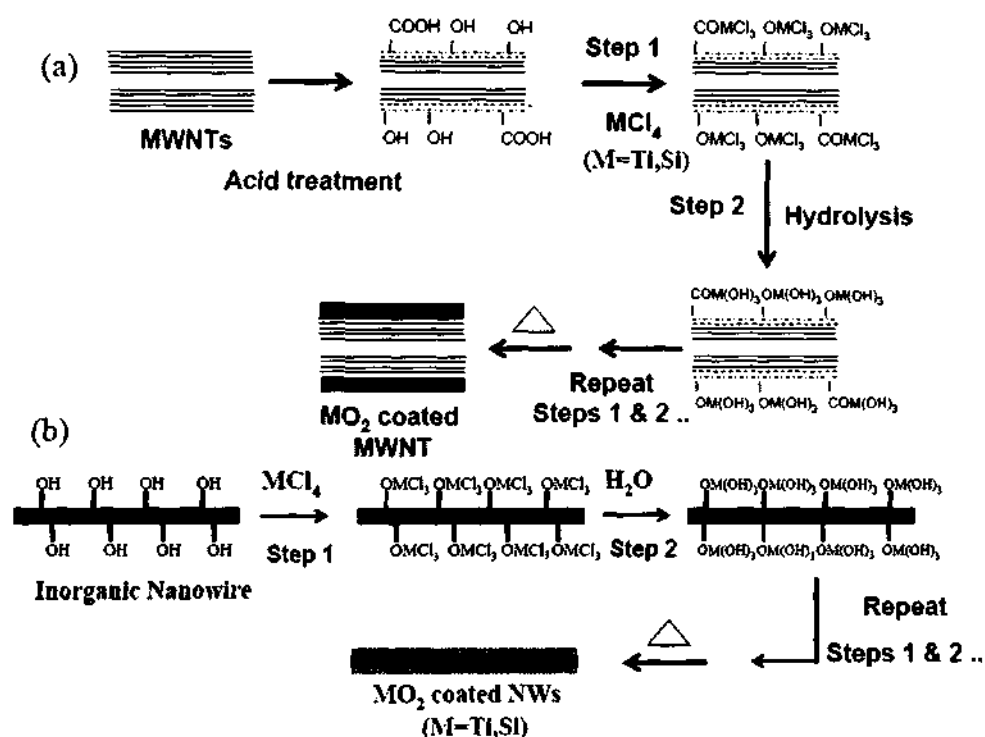


Figure 4.1: The ceramic coating process for (a) carbon nanotubes and (b) nanowires.

4.2 Experimental details

The metal halides used in the reaction were obtained from Sigma-Aldrich and were used without further purification. Arc-discharge MWNTs were prepared and functionalized using nitric acid treatment as reported in the literature [4]. The SWNTs were synthesized by the arc-discharge process using Ni-Y as catalyst [9]. The SWNTs were functionalized by refluxing them in dilute HNO_3 for 12 h. Al_2O_3 and Si nanowires were synthesized by carbothermal reduction [10,11]. The surface of the nanowires were activated treating the nanowires with dilute HCl. The functionalized CNTs and oxide nanowires were dried under dynamic vacuum for 8-10 h at 80°C before the reaction. The schematic diagram of the experimental set-up used for the coating of metal oxides on carbon nanotubes as well as inorganic nanowires is as shown in Figure 4.2. The set-up consists of three glass chambers, for

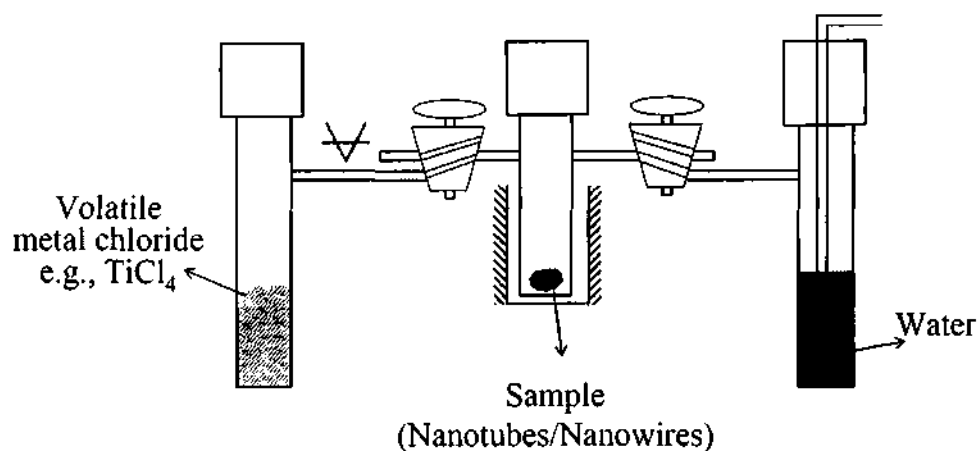


Figure 4.2: Schematic diagram of the experimental set-up.

the metal halide, reaction sample and water respectively. The chambers were inter-connected using high vacuum stopcocks. A diaphragm pump was used for the evacuation of the chamber. The sample chamber was maintained at 80 or 150 °C. In a typical reaction, the sample chamber was evacuated for 15 minutes and then metal halide was allowed into the sample chamber. After 5 minutes, the chamber was evacuated to remove the unreacted metal halide. The hydrolysis step was carried out by passing water vapor into the sample chamber for 5 minutes. The excess water vapor was removed by evacuation before proceeding to the next step. After a desired number of cycles, the product was calcined at 350 °C and subjected to analysis. It should be noted that by carrying out the reaction at 80/150 °C, the coating obtained on the nanotube or nanowire would not be of the oxide, but of the same oxidic/hydroxidic species. It is only after the calcination that an oxide coating gets formed. For purpose of brevity, we have called the products obtained at 80/ 150 °C as oxide-coated nanostructures.

Energy Dispersive Analysis of X-rays (EDX) spectra were obtained with a Leica S-440I microscope fitted with an EDX spectrometer and Link ISIS detector. TEM images were recorded with a JEOL JEM 3010 instrument operating at an accelerating voltage of 300 kV fitted with a Gatan CCD

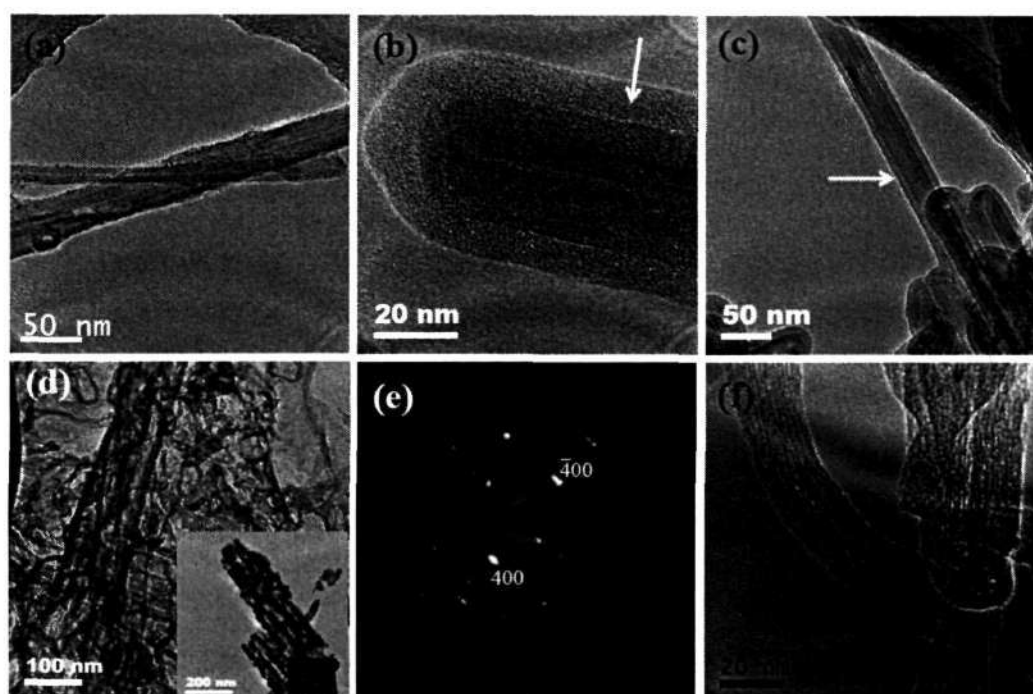


Figure 4.3: (a) TEM image of TiO₂-coated nanotube prepared at 80 °C, (b) and (c) TEM image of the same sample after calcination at 350 °C, (d) TEM image of the titania nanotubes and nanowires after the removal of carbon nanotubes, (e) SAED pattern (corresponding to inset in (d)) and (f) TEM image of TiO₂-coated SWNTs after calcination at 350 °C. Arrow shows the oxide coating.

camera. Powder X-ray diffraction (XRD) patterns were recorded using a Seifert XRD 3000 TT instrument. Thermogravimetric analysis of the samples were carried out on a Mettler-Toledo-TG-850 apparatus.

4.3 Results and Discussion

In Figure 4.3 (a), we show a TEM image of TiO₂-coated MWNTs obtained after 10 cycles at 80 °C. The color of the MWNTs changed from black to gray after the reaction. The EDX spectrum in Figure 4.4 (a) shows the presence of Ti and Cl after the reaction, the latter arising from the incomplete hydrolysis of TiCl₄. On calcination, at 350 °C for 12 h, the chlorine is eliminated as

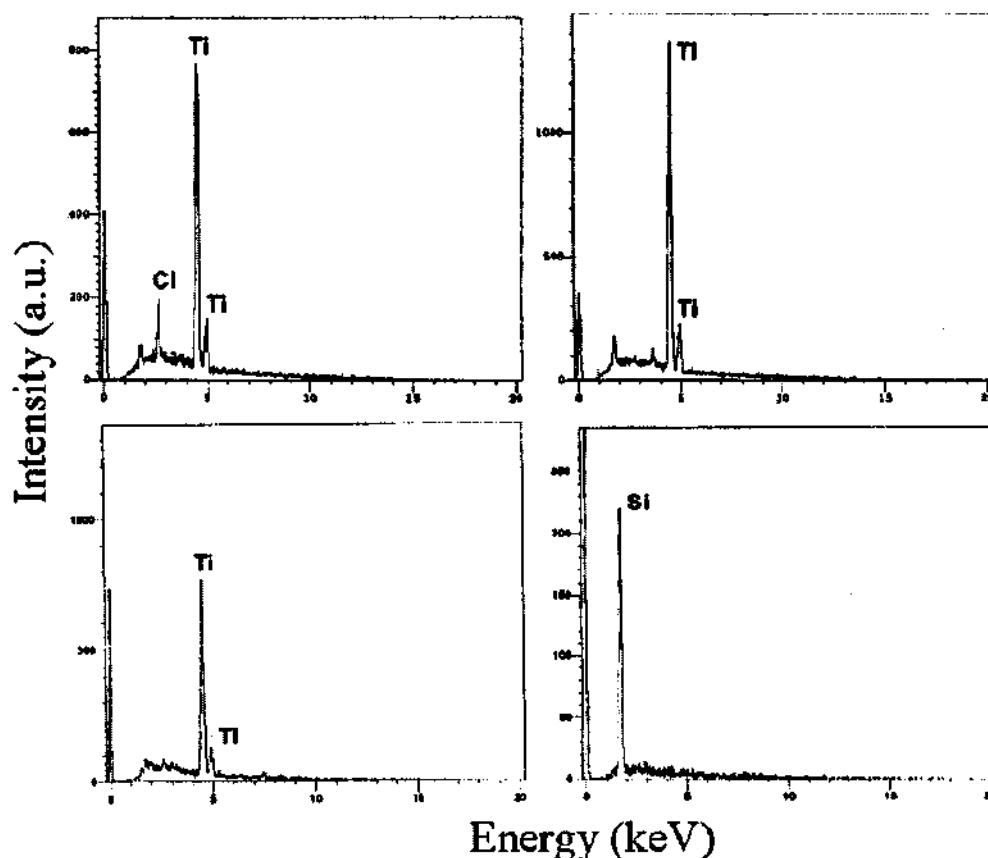


Figure 4.4: EDX of (a) TiO_2 -coated MWNTs prepared at 80°C corresponding to the TEM image in Figure 4.3 (a), (b) after calcination at 350°C , (c) TiO_2 -coated SWNTs prepared at 80°C after calcination) and (d) SiO_2 -coated MWNTs.

revealed by the EDX spectrum in Figure 4.4 (b). The TEM images of the calcined product are shown in Figures 4.3 (b) and (c). The thickness of the oxide layer is 8-10 nm range. The amorphous nature of the oxide coating was revealed by x-ray diffraction pattern. Carrying out the reaction at a higher temperature such as at 150°C did not bring about any significant changes in the oxide coating. Thermogravimetric analysis revealed that the nanotubes were completely oxidized at 630°C leaving a residue of 9-wt%. On heating the TiO_2 -coated MWNTs at 700°C , the nanotubes got oxidized, yielding the TiO_2 nanostructures shown in the TEM image in Figure 4.3 (d). The selected area electron diffraction (SAED) pattern of the nanorods in

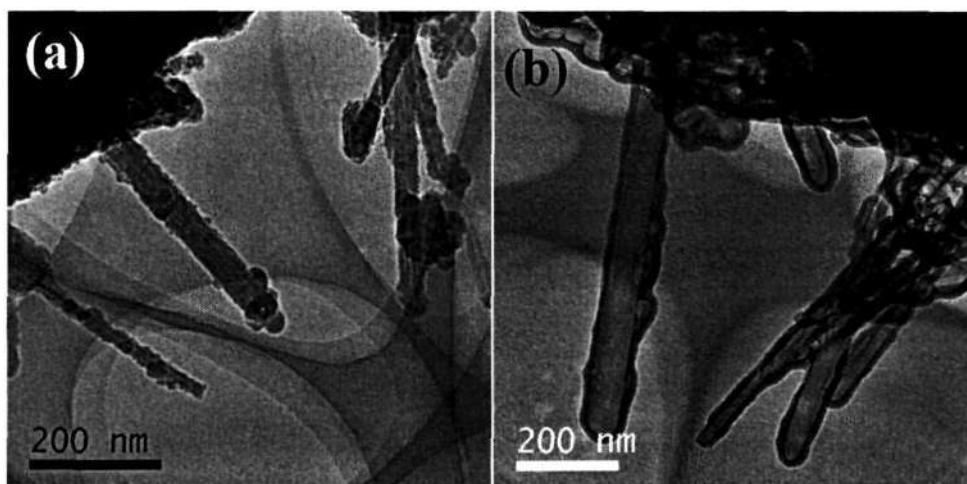


Figure 4.5: TEM image of (a) SiO₂-coated MWNTs prepared at 80 °C after calcination and (b) silica nanotubes obtained on heating the SiO₂-coated MWNTs at 700 °C.

Figure 4.3 (e) reveals that the structure corresponds to a metastable layered phase, TiO₂ (B). We could also cover SWNTs with a layer of TiO₂ following a similar procedure to that of MWNTs. A TEM image of TiO₂-covered SWNT bundles obtained after 10 cycles at 80 °C is shown in Figure 4.3 (f). The EDX spectrum in Figure 4.4 (c), shows the presence of Ti. TiO₂ nanostructures were obtained on heating the TiO₂-covered SWNTs at 700 °C.

Encouraged by the success in preparing TiO₂-covered CNTs, we carried out experiments with SiCl₄. In Figure 4.5 (a), we show a TEM image of the SiO₂-covered MWNTs (coating thickness in the 10-15 nm range) prepared after 10 cycles at 80 °C and calcined at 350 °C. The EDX spectrum shows the presence of Si (Figure 4.4 (d)). SiO₂ nanotubes were obtained on heating the SiO₂ covered MWNTs at 700 °C as can be seen from the TEM image in Figure 4.5 (b).

We have carried out several experiments on the preparation of Al₂O₃ nanowires coated with other metal oxides. In Figure 4.6 (a), we show a scanning electron microscope (SEM) image of the single-crystalline Al₂O₃ nanowires coated with TiO₂ obtained after 10 cycles at 150 °C. The EDX

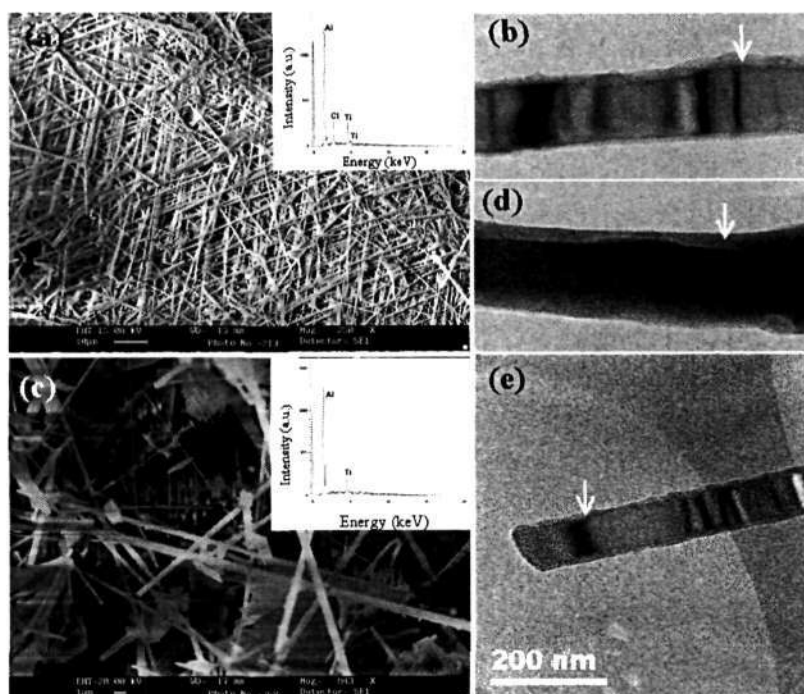


Figure 4.6: (a) SEM image of TiO_2 -coated Al_2O_3 nanowires prepared at 150°C (Inset shows EDX spectrum), (b) TEM image of a as-prepared TiO_2 -coated alumina nanowire, (c) SEM image of the above product after calcination (Inset shows EDX spectrum) and (d) TEM image of TiO_2 -coated Al_2O_3 nanowire after calcination and (e) TEM image of a SiO_2 -coated Al_2O_3 nanowire after calcination. Arrow indicate oxide coating.

spectrum in the inset reveals the presence of Ti and Cl. The TEM image in Figure 4.6 (b) shows the presence of a thin layer of TiO_2 . Figure 4.6 (c) shows the SEM image of the nanowires after calcination. As in the case of CNTs, chlorine was eliminated on calcination (see inset in Figure 4.6 (c) for the EDX spectrum). A TEM image of a TiO_2 -coated Al_2O_3 nanowire after calcination is shown in Figure 4.6 (d). The Al_2O_3 nanowires remained single-crystalline after the coating reaction. We were able to coat the Al_2O_3 nanowires with a layer of SiO_2 by using SiCl_4 . The TEM image in Figure 4.6 (e) shows SiO_2 -coated Al_2O_3 nanowires obtained after 10 cycles at 150°C . Preliminary experiments showed that Al_2O_3 nanowires could be coated chromic oxide using chromyl chloride. We have been able to coat silicon nanowires with a ceramic layer, by the reaction with metal halides.

The hydroxyl groups present on the surface oxide in Si nanowires participate in the reaction.

4.4 Conclusions

We have developed a new and versatile method for obtaining chemically bonded ceramic oxide coatings on carbon nanotubes (CNTs) and inorganic nanowires. We believe that the methodology described here can be used for controlled layer by layer coatings of various metal oxides over CNTs as well as one-dimensional structures of metal oxides. A good case in point is SnO₂-coated CNTs for possible use in sensor applications [12]. The method described here can also be used for the electrical insulation of nanotubes and nanowires in nanocircuits and potential synthesis of ceramic composites with higher toughness.

4.5 References

1. P. F. J. Harris, *Inter. Mater. Rev.* **49**, 31 (2004).
2. J. Goldberger, R. He, Y. Zhang, S. Lee, H. Yan, H. Choi, and P. Yang, *Nature* **422**, 599 (2003).
3. C. N. R. Rao, B. C. Satishkumar, and A. Govindaraj, *Chem. Commun.* 1581 (1997).
4. B. C. Satishkumar, A. Govindaraj, E. M. Vogl, L. Basumallick, and C. N. R. Rao, *J. Mater. Res.* **12**, 604 (1997).
5. B. C. Satishkumar, A. Govindaraj, M. Nath, and C. N. R. Rao, *J. Mater. Chem.* **10**, 2115 (2000).
6. W. Han and A. Zettl, *Nano Lett.* **3**, 681 (2003).
7. L. Fu, Z. Liu, Y. Liu, B. Han, J. Wang, P. Hu, L. Cao, and D. Zhu, *Adv. Mater.* **16**, 350 (2004).
8. Y. Min, E. J. Bae, K. S. Jeong, Y. J. Cho, J. Lee, W. B. Choi, and G. Park, *Adv. Mater.* **15**, 1019 (2003).
9. C. Journet, W. K. Maser, P. Bernier, A. Loiseau, M. Lamy de la Chapelle, S. Lefrant, P. Deniard, R. Lee, and J. E. Fischer, *Nature* **388**, 756 (1997).
10. G. Gundiah, F. L. Deepak, A. Govindaraj, and C. N. R. Rao, *Top. in Catal.* **24**, 137 (2003).
11. G. Gundiah, F. L. Deepak, A. Govindaraj, and C. N. R. Rao, *Chem. Phys. Lett.* **381**, 579 (2003).
12. Y. X. Liang, Y. J. Chen, and J. H. Wang, *Appl. Phys. Lett.* **85**, 666 (2004).

Chapter 5

FUNCTIONALIZATION AND SOLUBILIZATION OF INORGANIC NANOWIRES AND BORON NITRIDE NANOTUBES

Summary¹

Dispersions of the nanowires of Al₂O₃, ZnO and MgO in dimethylformamide (DMF), dimethylsulfoxide (DMSO) and acetonitrile have been studied by electron microscopy and photoluminescence spectroscopy, and by examining their sedimentation behavior. Stable nanowire dispersions were best obtained in DMF. The best photoluminescence spectra of the nanowires were generally obtained with DMF dispersions.

By interaction with a Lewis base (trialkylamine or trialkylphosphine), BN nanotubes have been dispersed in a hydrocarbon medium, with retention of the nanotube structure.

5.1 Introduction

Obtaining solutions or dispersions of nanomaterials in suitable solvents is essential for a wide variety of applications. There has been tremendous interest in obtaining dispersion of carbon nanotubes. The area of functionalization and solubilization of inorganic nanowires and nanotubes remained fairly unexplored. The solubility of the Mo₆S_{4.5}I_{4.5} nanowires in common solvents

¹Papers based on this study have appeared in *Chem. Phys. Lett.* (2006) and *J. Mater. Chem.* (2007)

has been investigated recently [1–4]. Boron nitride (BN) is an important ceramic material with a wide range of applications. During the last year, much interest has been evinced in the functionalization and solubilization of BN nanotubes [5–9]. For example, poly(*m*-phenylenevinylene-co-(2,5-dioctoxy-*p*-phenylenevinylene)) has been used to solubilize BN nanotubes in organic solvents, wherein the polymer wraps around the BN nanotubes leading to its solubilization [5]. Water-soluble BN nanotubes have been prepared by using amine-terminated poly-(ethylene glycol) [6]. BN nanotubes have been covalently functionalized using stearoyl chloride and subsequently dissolved in organic solvents [7]. Cycloaddition of dimethyl sulfoxide to BN nanotubes is suggested to weaken the B-N bond and helps in the peeling of the nanotubes [8]. BN nanotubes have also been fluorinated [9].

In this context, it has to be noted that oxide nanostructures are generally dispersed in polar solvents such as dimethylformamide (DMF) and dimethylsulfoxide (DMSO) in optical tweezing and other experiments [10]. We have examined the dispersions of Al_2O_3 , ZnO and MgO nanowires in DMF, DMSO and acetonitrile. For this purpose, we have examined the sedimentation behavior of the oxide nanowires in the polar solvents, and studied the photoluminescence spectra of the dispersions. The literature procedures for the functionalization and solubilization of BN nanotubes appear somewhat difficult and we, therefore, felt that there should be a simpler way to accomplish the desired results. We, therefore, considered it desirable to exploit the inherent electron deficiency of boron compounds. If we consider the boron site in BN nanotubes to act as a Lewis acid, it should be possible to form adducts with Lewis bases such as alkyl amines and phosphines, which should then enable one to disperse them in suitable solvents. In Figure 5.1, we show a schematic sketch of the same.

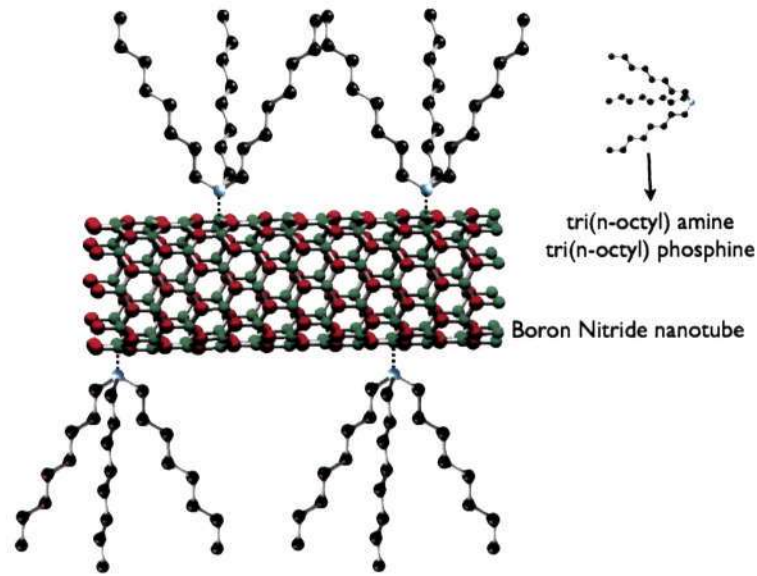


Figure 5.1: Schematic diagram of BN nanotube functionalization and solubilization using Lewis bases such as tri(n-octyl) amine, tri(n-octyl) phosphine and tri(n-butyl) amine.

5.2 Experimental Details

The synthesis of the oxide nanowires was carried out by the carbothermal procedure [11]. Nanowires of Al_2O_3 have been obtained starting from a mixture of Al powder and graphite or activated carbon in flowing Ar gas at a temperature of 1300°C [12]. ZnO nanowires on the other hand were prepared synthesized by heating a mixture of zinc oxide/zinc oxalate and MWNTs or active carbon in Ar atmosphere along with O_2 at 900°C [12]. MgO nanowires have been obtained by a variety of procedures starting from a mixture of MgO/Mg along with MWNTs, activated carbon or graphite in Ar atmosphere [13]. The dispersions of the various oxide nanowires were obtained as follows. A known quantity of the nanowires (32 mg of Al_2O_3 or ZnO nanowires) was dispersed in DMF, DMSO or acetonitrile (30 ml of the solvent individually) and sonicated for 1 h. The dispersion was allowed to stand for about 12 h after which the sediment (sediment-1) that settled down was weighed and collected for scanning electron microscopy (SEM).

The remaining dispersion was re-sonicated and allowed to sediment for 60 h. Thereafter, the remaining sediment (sediment-2) was again weighed and collected for SEM. Similarly a drop of the dispersion was taken and deposited on a glass slide and observed under the microscope. SEM observations of the dispersions were carried out at regular intervals of time to monitor the presence of nanowires in each case (for example 12, 24, 36, 48 and 60 h). The dispersions of the MgO nanowires were obtained as follows. A known quantity of the nanowire (7 mg) was dispersed in DMF (15 ml) and sonicated for 1 h. This dispersion was allowed to stand during the course of which a drop of the dispersion taken at various intervals of time was deposited onto a copper grid for transmission electron microscopy (TEM). The TEM observations of the dispersions were carried out at regular intervals of time (3, 6, 12, 24, 96 h). Apart from this the sediment that was obtained at the end of 96 h was also observed by TEM. The dispersions of the oxide nanowires in DMF, DMSO and acetonitrile were characterized by photoluminescence spectroscopy. SEM images were obtained with a LEICA S440i scanning electron microscope. Samples for SEM were prepared by adding a drop of the dispersion on to a glass slide. In the case of the sediments the powder that was collected was dried followed by microscopy.

BN nanotubes were prepared by a standard literature procedure [14]. BN nanotubes were prepared by the reaction of B_2O_3 with multi-walled carbon nanotubes (MWNTs) in the presence of ammonia at $1250^\circ C$ for 3 h. A grey spongy product was obtained after the reaction indicating the presence of unreacted MWNTs along with BN nanotubes. The product was washed with hot water to remove excess B_2O_3 . The excess carbon present in the product was removed by oxidation at $800^\circ C$ in low-pressure air (20 mPa). In a typical functionalization/solubilization experiment, 2 ml of trialkylamine or trialkylphosphine were added to 5 mg of purified BN nanotubes. The

mixture was warmed at 70 °C for 12 h and subsequently sonicated for a few minutes. The functionalized BN nanotubes were then dispersed in toluene (8 ml) or other hydrocarbons such as benzene, at room temperature. The dispersions were stable over long periods of time. It is not essential to interact the nanotubes with an amine or a phosphine at 70 °C. Interaction at room temperature for a long period yielded the same result. TEM images were obtained with a JEOL JEM 3010 operating with an accelerating voltage of 300 kV. Samples for TEM studies were prepared by adding a drop of the dispersion onto a holey carbon coated Cu grid followed by slow evaporation. Photoluminescence measurements were carried out at room temperature with a Perkin-Elmer model LS50B luminescence spectrometer. Raman spectra of the BN nanotubes were recorded using a JobinYvonHoriba HR800 Raman spectrometer using a He-Ne laser (633 nm).

5.3 Results and Discussion

5.3.1 Metal oxide nanowires

The dispersions of the various oxide nanowires in the polar solvents showed interesting features as found from electron microscopy and photoluminescence spectroscopy. Dispersions of Al₂O₃ nanowires in DMF were stable up to 24 h in contrast to those in DMSO and acetonitrile which were not stable, with the sedimentation starting much earlier. In the case of acetonitrile, the sedimentation started just after it is allowed to stand. MgO nanowires dispersed in DMF are more stable up-to 12 h in comparison to DMSO and acetonitrile. Starting with a known amount of Al₂O₃ nanowires dispersed in the various solvents, we measured the proportion of solute in the solvent at the end of 60 h and found that DMF and DMSO have about 6% of the solute remaining in solution, whereas in the case of acetonitrile it was 3% or less.

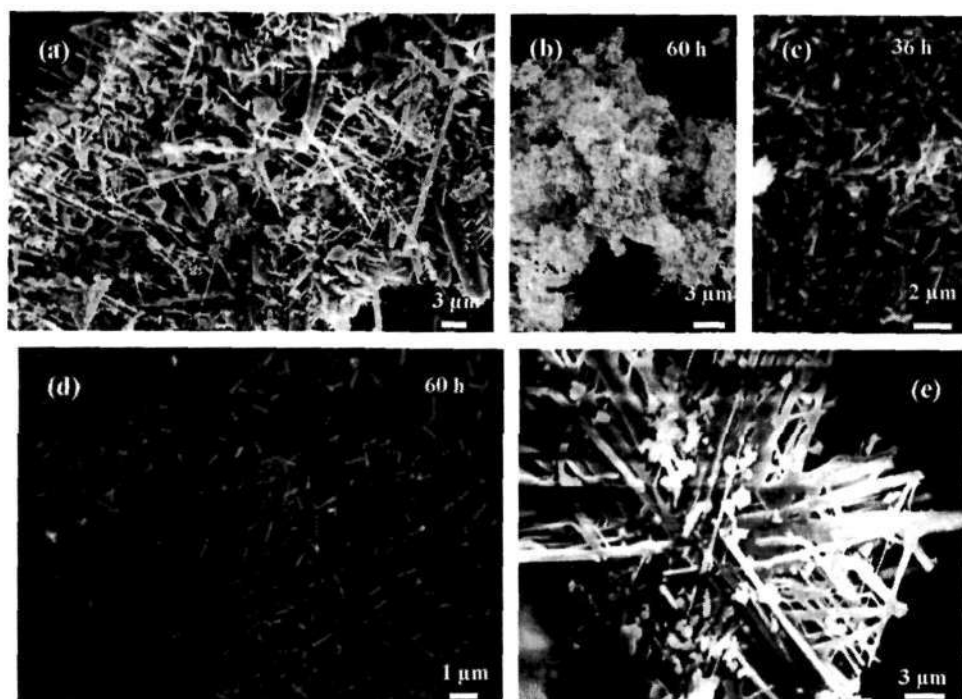


Figure 5.2: SEM images of (a) starting Al₂O₃ nanowires, (b-d) dispersions of Al₂O₃ nanowires in DMF, DMSO and acetonitrile respectively, (e) Sediment obtained from acetonitrile.

Visual observations indicated that DMF forms the best dispersions in comparison to DMSO and acetonitrile. In the case of ZnO nanowires dispersed in DMF, the proportion of solute remaining in the solvent was about 9%. Such a high percentage of solute stably dispersed in the solvent is useful for several measurements and applications, which cannot otherwise be achieved in the solid state. In Figure 5.2 (a), we show the SEM image of the starting Al₂O₃ nanowires. The nanowires occur individually and in large bundles. In Figure 5.2 (b), we show the SEM image of the nanowire dispersion in DMF obtained after 60 h. The presence of large bundles of the nanowires can be seen, indicating the stability of the bundles of nanowires in the dispersion.

The SEM image in Figure 5.2 (c) shows the Al₂O₃ nanowires dispersed in DMSO after a period of 36 h. The image reveals smaller bundles and isolated nanowires, in contrast to that in DMF. The SEM image of the dispersion of the Al₂O₃ nanowires in acetonitrile obtained after 60 h is shown in Figure

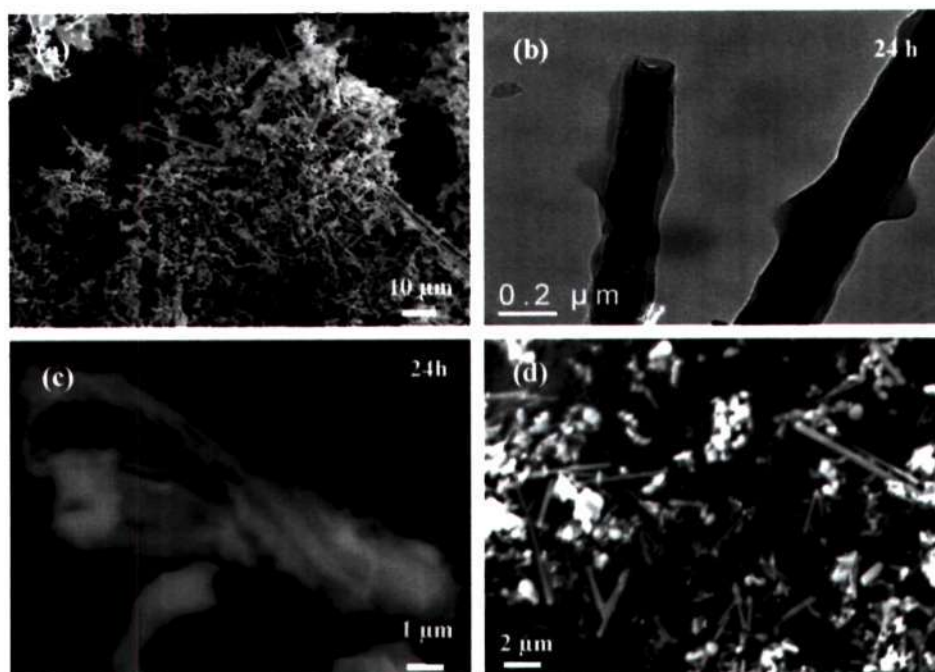


Figure 5.3: SEM images of (a) raw MgO nanowires, (b) TEM image of MgO nanowire dispersion in DMF, (c) ZnO nanowire dispersion in DMF and (d) SEM image of the sediment of ZnO nanowires.

5.2 (d), revealing isolated individual nanowires in large numbers. The SEM image of the sediment obtained from acetonitrile after 12 h is shown in Figure 5.2 (e). Large bundles of nanowires are seen in the sediment in contrast to the dispersion. The SEM image in Figure 5.3 (a) shows the raw MgO nanowires used for the study. The nanowires extend to several microns in length. The TEM image of the MgO nanowires in DMF shown in Figure 5.3 (b) reveals nanowires of uniform diameter of 150-200 nm obtained in the dispersion at a time period of 24 h. The dispersion of the ZnO nanowires obtained in DMF after a time period of 24 h and the sediment after 12 h are shown in SEM image of Figures 5.3 (c) and (d), respectively. The SEM image reveals in Figure 5.3 (c) the presence of bundles of nanowires, whereas the image of the sediment in Figure 5.3 (d) reveals the presence of a few isolated nanowires (along with other types of particles) that seem to have been excluded from the dispersion during the course of time. Thus,

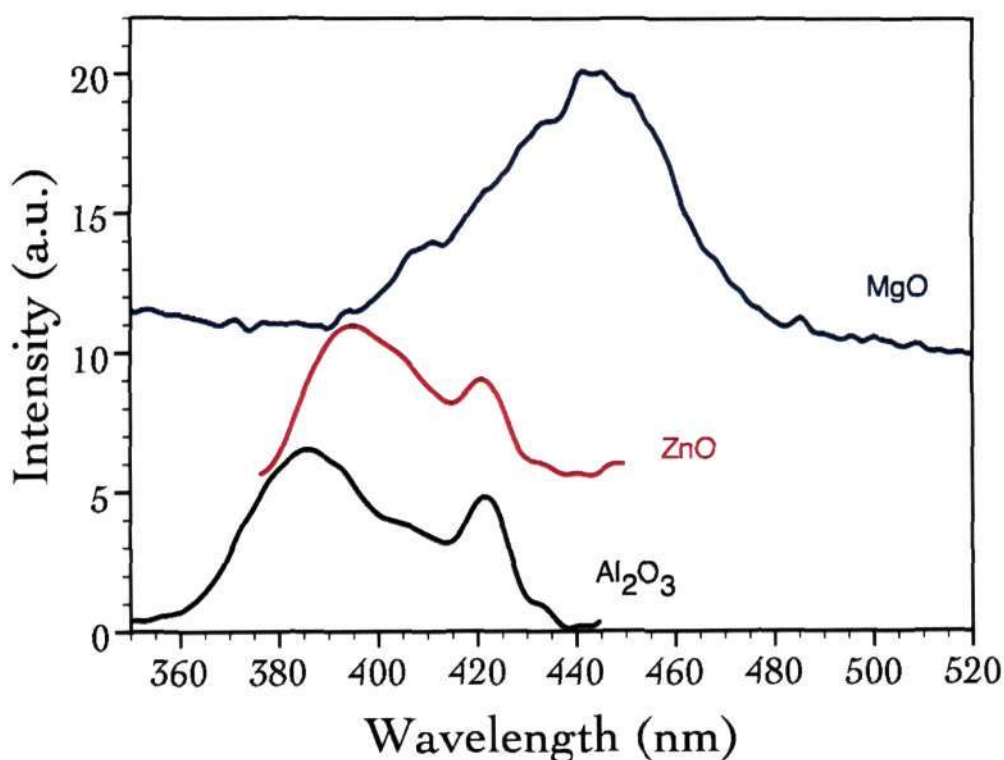


Figure 5.4: Photoluminescence spectra of the various starting materials.

sedimentation studies have shown that in general DMF is a good solvent for obtaining stable dispersions of the nanowires. In comparison, DMSO and acetonitrile may not be as suitable, acetonitrile being the poorest solvent of the three. The photoluminescence spectra of as-synthesized Al₂O₃, ZnO and MgO nanowires are shown in Figure 5.4. The photoluminescence spectra of the dispersions of Al₂O₃ nanowires excited at 300 nm are shown in Figure 5.5 (a). The spectrum in the solid state reveals two bands at 380 and 420 nm, which are generally known to arise from oxygen-related defects [?, 15]. The nanowire dispersion in DMF shows two sharp and clear bands at 408 and 430 nm, slightly red-shifted from the spectrum of solid Al₂O₃. The spectrum of the dispersion in DMSO shows weak features which are slightly red-shifted relative to the bands in DMF. Thus, the peak positions in DMSO are 410 and 435 nm. The spectrum of the dispersion in acetonitrile shows several bands between 400 and 450 nm in the region extending up-to 475 nm which may

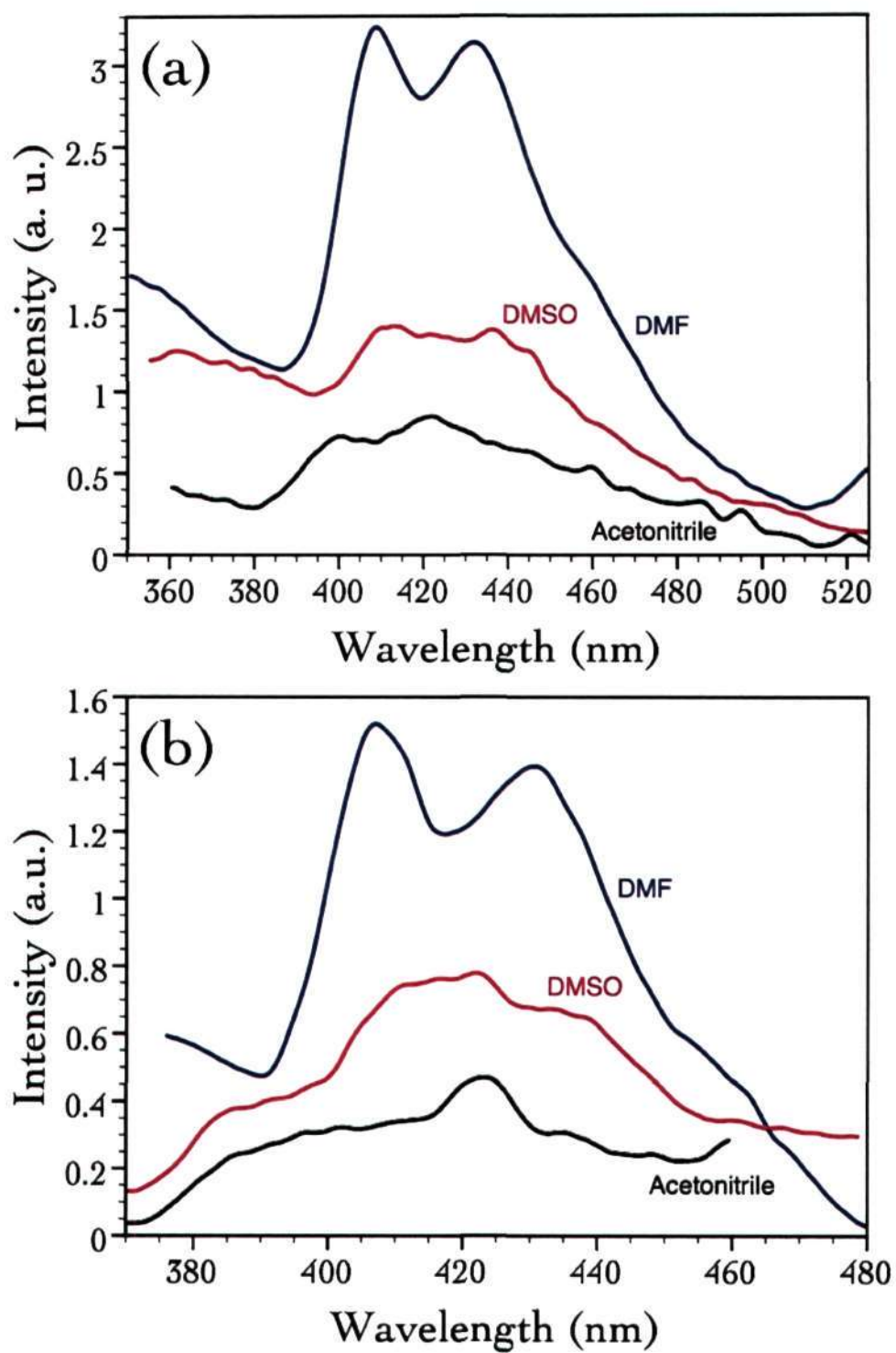


Figure 5.5: Photoluminescence spectra of (a) Al_2O_3 and (b) ZnO nanowire dispersions in the various polar solvents.

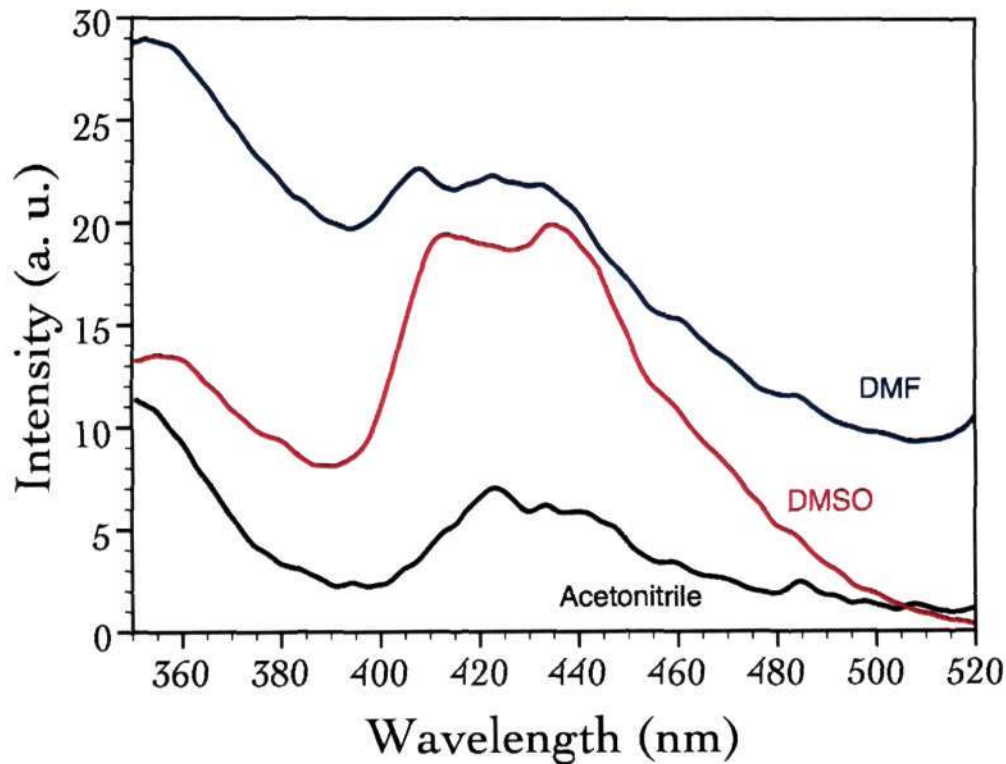


Figure 5.6: Photoluminescence spectra of MgO nanowire dispersions in the various polar solvents.

arise from isolated nanowires. The photoluminescence spectra of the ZnO nanowire dispersions (Figure 5.5 (b)) show interesting features (excitation wavelength, 280 nm). The solid spectrum in Figure 5.4 shows a peak at 395 nm and a shoulder around 420 nm the emission corresponding to near-band edge emission in the case of ZnO. The photoluminescence spectrum of the nanowires in DMF shows slight redshifts with the peak positions at 406 and 429 nm. The presence of clear and intense bands in this case is noteworthy. In the case of the nanowire dispersions in DMSO, there is a band centered at 420 nm and a shoulder at 435 nm. The acetonitrile dispersion shows only a small feature centered at 420 nm. The photoluminescence spectrum of solid MgO in Figure 5.4 shows a peak at 443 nm, (excitation wavelength, 300 nm), the emission corresponding to oxygen vacancies [13,16]. The photoluminescence spectrum of the nanowires in DMF shows two peaks around 406 and 430

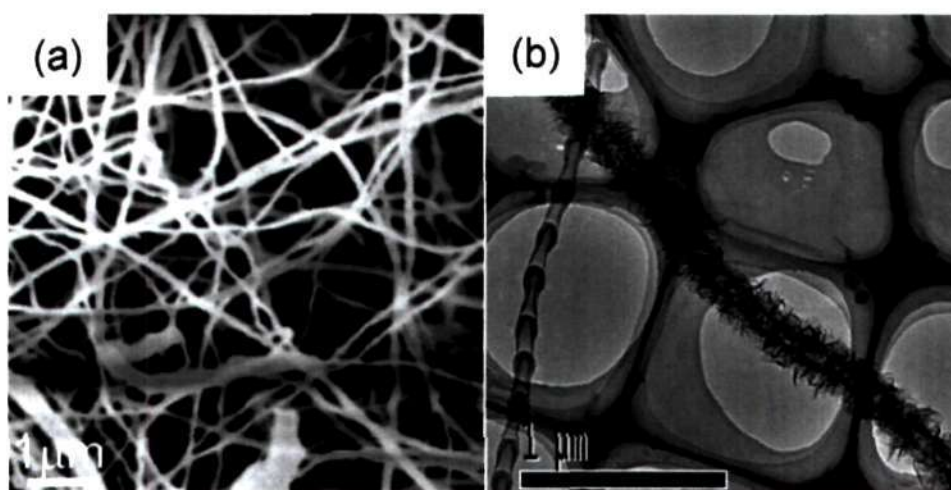


Figure 5.7: (a) SEM image of purified BN nanotubes. (b) TEM image of BN nanotubes.

nm. In addition, there is a band around 535 nm. These emission bands have been reported previously in the case of bulk MgO by Rosenblatt and co-workers [16]. In the case of DMSO dispersions, there is a slight red shift with peaks appearing at 411 and at 435 nm. The dispersion of the nanowires in acetonitrile shows several features centered around 430 nm (Figure 5.6).

5.3.2 Boron Nitride nanotubes

In Figure 5.7 (a), we show a representative SEM image of the BN nanotubes prepared by us. The nanotubes have diameters in the 80-200 nm range with lengths of tens of microns. BN nanotubes have either bamboo-like or worm-like structures as revealed by the TEM image shown in Figure 5.7 (b). The Raman spectrum of purified BN nanotubes did not show the D-band (1340 cm^{-1}) or the G-band (1600 cm^{-1}) of carbon nanotubes. The nanotubes exhibit a Raman band centered at 1370 cm^{-1} as shown in Figure 5.8, this band is assigned to the E_{2g} tangential mode [17, 18]. In Figure 5.9 (a), we show a photograph of a toluene dispersion of BN nanotubes treated with trioctylamine. In Figure 5.10 (a), we show a TEM image of the

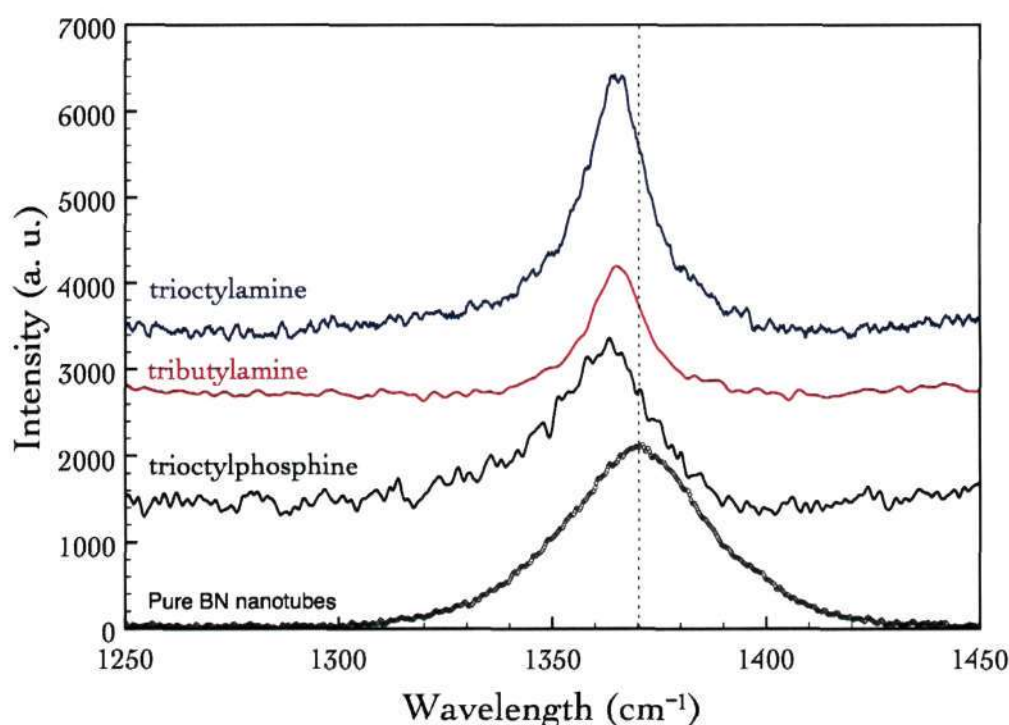


Figure 5.8: Raman spectra of pristine BN nanotubes and those functionalized with tri(n-octyl) amine, tri(n-octyl) phosphine and tri(n-butyl) amine.

BN nanotubes obtained by taking a drop of the dispersion on the electron microscopy grid. Evidence for the interaction between tributylamine and BN nanotubes has been obtained by nuclear magnetic resonance spectroscopy and Raman spectroscopy. We have studied the ^1H and ^{13}C NMR spectra of tributylamine functionalized BN nanotubes in comparison with the spectra of tributylamine. We observe a small increase in the ^1H chemical shift by ~ 0.02 ppm in the amine-BN adduct. In the case of ^{13}C NMR spectra, we observe a significant increase in the chemical shifts of the 'c' and 'd' carbons by ~ 0.4 ppm and a decrease in the chemical shift of the 'b' carbon atom by ~ 0.3 ppm. The chemical shift of the 'a' carbon is also higher in the amine-BN adduct by ~ 0.1 ppm. The changes in the ^1H and ^{13}C spectra of tributylamine found on interaction with BN are comparable to those reported in the literature for similar complexes [19, 20].

We have also carried out solubilization experiments using the as-prepared

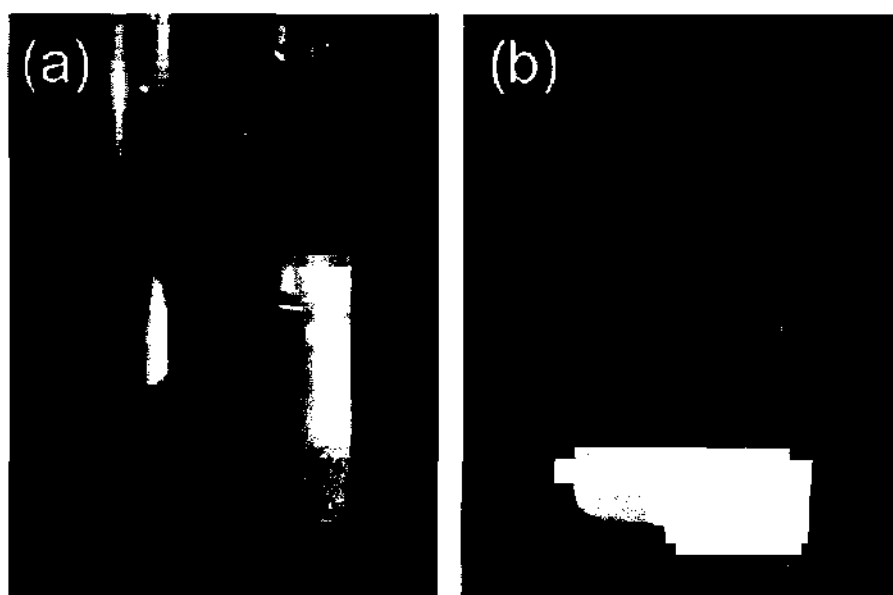


Figure 5.9: Photographs of dispersions of BN nanotubes obtained after interaction with (a) trioctylamine and (b) trioctylphosphine.

BN nanotubes containing carbon nanotubes as impurity. Initially, a grey dispersion containing both carbon and BN nanotubes was obtained, but the carbon nanotubes settled to the bottom within a few hours leaving the BN nanotubes in the solution. This indicates that there is no significant interaction between the Lewis base and the carbon nanotubes. Encouraged by the results obtained with the two trialkylamines, we interacted the BN nanotubes with trioctylphosphine at 70 °C for 12 h or at 30 °C for a longer period. We could disperse the product in toluene as can be seen in the photograph in Figure 5.9 (b). A TEM image of the nanotubes from the dispersion is shown in Figure 5.10 (c). Raman spectra of the dispersions of BN nanotubes were recorded after interacting them with an amine or a phosphine. For this purpose, a drop of the dispersion was placed on a glass slide and the spectrum recorded. In Figure 5.8, we show Raman spectrum of BN nanotubes treated with trioctylphosphine. We observe a band due to the tangential mode at 1361 cm^{-1} , similar to the starting material. Raman spectra of the toluene dispersions of BN nanotubes treated with tributylamine

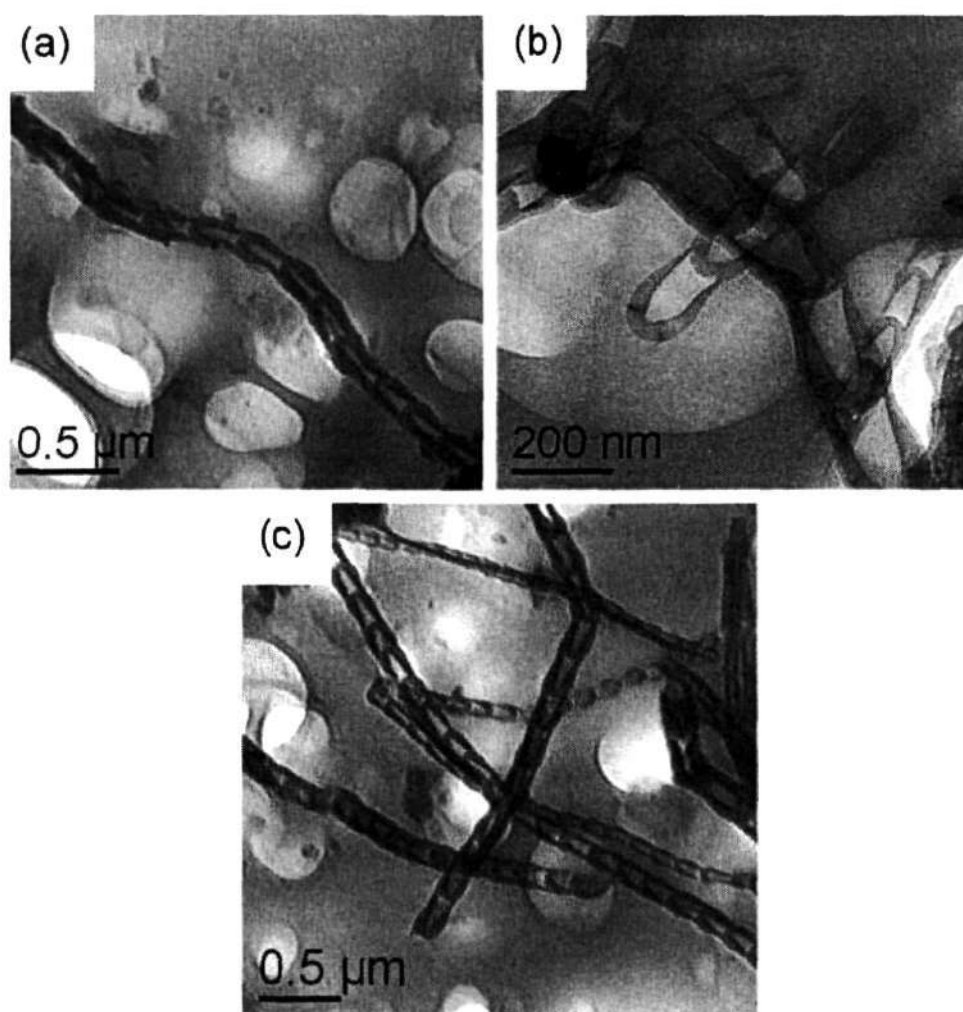


Figure 5.10: TEM images of the dispersions of BN nanotubes functionalized with (a) trioctylamine, (b) tributylamine and (c) trioctylphosphine.

and trioctylamine showed a band due to the tangential mode around 1365 cm^{-1} . The E_{2g} tangential mode of BN nanotube (1370 cm^{-1}) shifts to lower wavenumbers after the interaction of the amine or the phosphine indicating the donation of electron from the amine or phosphine group to the BN nanotube. These results suffice to demonstrate that the interaction of BN nanotubes with Lewis bases helps to solubilize them in nonpolar solvents. We should note that in the absence of interaction with an amine or a phosphine, BN nanotubes could not be dispersed in toluene and the nanotubes settled to the bottom within a short period.

5.4 Conclusions

In summary, we have investigated dispersions of Al_2O_3 , ZnO and MgO nanowires in polar solvents by electron microscopy and photoluminescence spectroscopy. Of the solvents that have been examined, DMF seems to be the best for obtaining stable nanowire dispersions, although acetonitrile dispersions in the case of Al_2O_3 nanowires may represent features of isolated nanowires. Stable oxide nanowire dispersions in DMF should be useful to investigate properties and in some applications. We have successfully demonstrated that the Lewis acid nature of boron in BN nanotubes can be exploited to functionalize and solubilize their nanostructures through interaction with Lewis bases such as trioctylamine and trioctylphosphine. The solubilized nanotubes retain the nanotube features and the hydrocarbon dispersions are stable up to a few days. It is noteworthy that the interaction of the BN nanotubes with the Lewis bases at room temperature suffices to provide good dispersions of the BN nanotubes in hydrocarbon solvents. Any carbon impurity, such as the unreacted carbon nanotubes used as templates in the preparation of the BN nanotubes, settles to the bottom after interaction of the BN nanotubes with a Lewis base, thereby providing a means of separation of carbon and BN nanotubes.

5.5 References

1. V. Nicolosi, D. Vrbanic, A. Mrzel, J. McCauley, S. O'Flaherty, D. Mihailovic, W. J. Blau, and J. N. Coleman, *Chem. Phys. Lett.* **401**, 13 (2005).
2. V. Nicolosi, D. Vrbanic, A. Mrzel, J. McCauley, S. O'Flaherty, C. McGuinness, G. Compagnini, D. Mihailovic, W. J. Blau, and J. N. Coleman, *J. Phys. Chem. B* **109**, 7124 (2005).
3. V. Nicolosi, D. Vengust, D. Mihailovic, W. J. Blau, and J. N. Coleman, *Chem. Phys. Lett.* **425**, 89 (2006).
4. V. Nicolosi, P. D. Nellist, S. Sanvito, E. C. Cosgriff, S. Krishnamurthy, W. J. Blau, M. L. H. Green, D. Vengust, D. Dvorsek, D. Mihailovic, G. Compagnini, J. Sloan, V. Stolojan, J. D. Carey, S. J. Pennycook, and J. N. Coleman, *Adv. Mater.* **19**, 543 (2007).
5. C. Zhi, Y. Bando, C. Tang, R. Xie, T. Sekiguchi, and D. Goldberg, *J. Am. Chem. Soc.* **127**, 15996 (2005).
6. S. Xie, W. Wang, K. A. S. Fernando, X. Wang, Y. Lin, and Y. Sun, *Chem. Commun.* 3670 (2005).
7. C. Zhi, Y. Bando, C. Tang, S. Honda, K. Sato, H. Kuwahara, and D. Goldberg, *Angew. Chem. Inter. Ed.* **44**, 7932 (2005).
8. Q. Huang, Y. Bando, C. Zhi, D. Goldberg, K. Kurashima, F. Xu, and L. Gao, *Angew. Chem. Inter. Ed.* **45**, 2044 (2006).
9. C. Tang, Y. Bando, Y. Huang, S. Yue, C. Gu, F. Xu, and D. Goldberg, *J. Am. Chem. Soc.* **127**, 6552 (2005).
10. A. van der Horst, D. L. J. Vossen, K. Visscher, M. Dogterom, and A. von Blaaderen, *Micros. Anal.* **44**, 15 (2005).
11. C. N. R. Rao, G. Gundiah, F. L. Deepak, A. Govindaraj, and A. K. Cheetham, *J. Mater. Chem.* **14**, 440 (2004).
12. G. Gundiah, F. L. Deepak, A. Govindaraj, and C. N. R. Rao, *Top. in Catal.* **24**, 137 (2003).
13. K. P. Kalyanikutty, F. L. Deepak, C. Edem, A. Govindaraj, and C. N. R. Rao, *Mater. Res. Bull.* **40**, 831 (2005).
14. F. L. Deepak, C. P. Vinod, K. Mukhopadhyay, A. Govindaraj, and C. N. R. Rao, *Chem. Phys. Lett.* **353**, 345 (2002).
15. X. S. Peng, L. D. Zhang, G. W. Meng, X. F. Wang, Y. W. Wang, C. Z. Wang, and G. S. Wu, *J. Phys. Chem. B* **106**, 11163 (2002).

16. G. H. Rosenblatt, M. W. Rowe, G. P. Williams Jr., R. T. Williams, and Y. Chen, *Phys. Rev. B* **39**, 10309 (1989).
17. J. Wu, W. Q. Han, W. Walukiewicz, J. W. Ager, W. Shan, E. E. Haller, and A. Zettl, *Nano Lett.* **4**, 647 (2004).
18. S. Saha, D. V. S. Muthu, D. Goldberg, C. Tang, C. Zhi, Y. Bando, and A. K. Sood, *Chem. Phys. Lett.* **421**, 86 (2006).
19. T. D. Coyle and F. G. A. Stone, *J. Am. Chem. Soc.* **83**, 4138 (1961).
20. M. Ilczyszyn, Z. Latajka, and H. Ratajczak, *Org. Magn. Reson.* **22**, 419 (1984).

Chapter 6

ELECTRICAL PROPERTIES OF NANOCOMPOSITES OF CARBON NANOTUBES AND INORGANIC NANOWIRES WITH CONDUCTING POLYMERS

Summary¹

Composites of polyaniline (PANI) have been prepared with pristine multi-walled and single-walled carbon nanotubes as well as carbon nanotubes subjected to acid treatment and subsequent reaction with thionyl chloride. For this purpose, *in-situ* polymerization of aniline was carried out in the presence of nanotubes. The composites have been characterized by X-ray diffraction, electron microscopy as well as infrared and Raman spectroscopy. Electrical resistivities of the PANI-nanotube composites have been measured and compared with those of the nanotubes and PANI.

Composites of nanowires (NW) of ZnO, RuO₂ and Ag with polyaniline (PANI) as well as polypyrrole (PPy) have been prepared, for the first time, by an *in-situ* process, in order to investigate their electrical properties. Characterization by electron microscopy and IR spectroscopy indicated considerable interaction between the oxide nanowires and the polymer. The room-temperature resistivity of the composites prepared *in-situ* varies in the 0.01-400 Ω cm range depending on the composition. While the resistivities of the PANI-ZnONW and PPy-ZnONW composites prepared by the *in-situ* process are generally higher than that of PANI/PPy, those of PANI-RuO₂NW and PANI-AgNW are lower. Composites of ZnONW with polyaniline prepared

¹Papers based on this study have appeared in *J. Nanosci. Nanotech.* (2002) and *J. Mater. Chem.* (2005)

by an ex-situ process exhibit a resistivity close to that of polyaniline.

6.1 Introduction

There has been a surge of interest in nanostructured materials as part of the effort towards device miniaturization and understanding of novel quantum phenomena at the nanometer scale. Some of the properties have been exploited by incorporating the nanomaterials into some form of matrix such as polymers. Following the first report of the preparation of carbon nanotube-polymer composites by Ajayan *et al.* [1], there have been efforts to combine carbon nanotubes and polymers to produce functional composite materials with desirable electrical and mechanical properties [2–5]. These composites can have potential applications in photovoltaic devices and electrostatic as well as conductive coatings in optical devices. Carbon nanotubes have been incorporated in insulating as well as conducting polymers such as polyaniline (PANI) and polypyrrole (PPy). PANI and PPy are attractive polymers for preparing such composites in view of the low-cost, environmental stability and easy processibility. Aniline has been polymerized on multi-walled carbon nanotube (MWNTs) electrodes by Downs *et al.* [6] to obtain PANI films with novel surface characteristics and high current densities. Composites of PANI with MWNTs, with an order of magnitude lower resistivity than that of pure PANI at room temperature have been prepared by Cochet *et al.* [7] by *in-situ* polymerization. Blanchet *et al.* [8] have shown that the high aspect ratio of the single-walled carbon nanotubes (SWNTs) enables percolation into the PANI network at low concentrations and that the PANI-SWNT composites can be used as printable conductors for organic electronics devices. Zengin *et al.* [9] prepared films of PANI-MWNT composite by *in-situ* as well as ex-situ methods with electrical conductivities higher than that of the pristine

nanotubes. Well-aligned PANI-MWNTs composite films with electrical resistivities in between those of PANI and MWNTs have also been prepared by Feng *et al.* [10]. The change in the sign of the magnetoresistance at low-temperatures has been used by Long *et al.* [11] as the basis to reveal the strong coupling between the carbon nanotubes and polyaniline in the composites. PPy-MWNT nanocables prepared by the *in-situ* oxidation polymerization in the presence of different surfactants and exhibit a negative temperature coefficient of resistance are shown to negative magnetoresistance [12]. Jurewicz *et al.* [13] have shown that PPy-MWNT composites exhibit a higher specific capacitance than that of pristine MWNT. Incorporation of MWNTs into semiconducting polymers such as poly(m-phenylenevinylene-co-2,5-dioctoxy-p-phenylenevinylene) enhances the electrical conductivity without any degradation in electroluminescent properties [14].

We were interested in studying PANI composites with carbon nanotubes as well as inorganic nanowires. For this purpose, we have prepared PANI-carbon nanotubes composites by *in-situ* polymerization of aniline in the presence of MWNTs and acid treated MWNTs. We have characterized these composites along with the PANI composites prepared with acid treated MWNTs subjected to treatment with thionyl chloride. We have carried out similar studies with SWNTs. We have measured electrical resistivities of the various PANI-nanotube composites. Inorganic nanowires is important class of one-dimensional nanomaterials and a wide range of nanowires of functional inorganic materials is now available, opening up the possibility of a new class of nanocomposites with polymers. This prompted us to investigate the composites of inorganic nanowires with conducting polymers for the electrical properties. For this purpose, we have chosen nanowires of zinc oxide (ZnONW), ruthenium dioxide (RuO₂NW) and silver (AgNW). ZnO is a wide bandgap semiconductor with a bandgap of 3.37 eV while RuO₂ and silver are

metallic. RuO_2 also exhibits a large specific capacitance and is used as an electrode material in supercapacitors [15]. We have prepared composites with different molar ratios of the monomer (aniline or pyrrole) and the inorganic nanowires and studied their electrical properties. While most of the composites were prepared by the *in-situ* polymerization of aniline or pyrrole in the presence of the nanowires, we have also prepared a few PANI-ZnONW composites by an ex-situ process, for purpose of comparison. The ZnONW were also functionalized with thionyl chloride in an effort to enhance the interfacial bonding between the nanowires and the polymer in the composites prepared by the *in-situ* process.

6.2 Experimental Details

MWNTs for the study were prepared by the arc evaporation of graphite at 10 V and 50 A dc [16]. The acid treated MWNTs were prepared by refluxing the MWNTs in a mixture of conc. H_2SO_4 and conc. HNO_3 (2:1 ratio by volume) for 1 h. The resulting mixture was then allowed to cool and diluted with distilled water. The acid treated MWNTs were then filtered and washed thoroughly with distilled water to remove any traces of the acid. Such nanotubes are always open and contain acidic sites on the surface [17, 18]. The chlorination of the acid treated MWNTs was carried out by stirring acid treated MWNTs in thionyl chloride at 100°C for a day in an argon atmosphere. The sample was then washed with distilled water and filtered. Similar samples were prepared with MWNTs generated from the pyrolysis of acetylene over iron nanoparticles that were well dispersed over silica [19]. The SWNTs for the experiments were prepared by the method as reported by Journet *et al.* [20]. The Acid treated SWNTs were prepared by sonicating the nanotubes in a mixture of conc. H_2SO_4 and conc. HNO_3 (2:1 ratio by volume) for 20 min. The chlorination of the SWNTs was also carried out in

the same manner as described earlier for multi-walled nanotubes.

HCl doped polyaniline (PANI) was prepared by the method similar to that of Fite *et al.* [21]. Ammonium persulfate (5.6 g) was dissolved in 100 ml of 1 M aqueous HCl solution and was cooled to 0 °C. Aniline (5 ml) was taken in a round bottom flask containing 100 ml of 1 M aqueous HCl solution and was cooled to 0 °C. The oxidizing agent was slowly added to the aniline solution under sonication at 0 °C. The sonication was carried out for another 2 h after the addition of the oxidizing agent. The product was filtered and washed thoroughly with distilled water first and later with methanol to remove the oligomers. The filtered sample was dried under a dynamic vacuum at room temperature for 24 h to ensure the absence of moisture, which affects the conductivity of polyaniline [22]. We have prepared composites of unfunctionalized, acid treated and chlorinated MWNTs and SWNTs with polyaniline. The nanotube-PANI composites were prepared as follows. The nanotubes were added to aniline and sonicated for 15 min and later 1.0M aqueous HCl solution was added. The compositions of the composites of MWNTs are 2:1 and 1:2 by weight of aniline and MWNTs. The PANI-SWNT composites were prepared with a 1:1 ratio of aniline and SWNTs.

Zinc oxide nanowires were prepared by the carbon-assisted route using zinc oxalate and MWNTs in the absence of any catalyst [23]. ZnONWs were functionalized by treating them with SOCl_2 followed by thorough washing with distilled water. We designate these nanowires as Cl-ZnONW. Nanowires of silver were obtained using the solution-based approach as reported by Xia and co-workers [24]. RuO_2 NWs were obtained by the method reported in the literature [25]. We have prepared composites of inorganic nanowires with polyaniline as well as polypyrrole by *in-situ* and *ex-situ* methods.

In the *in-situ* method of preparation of the PANI-inorganic nanowire

composites, the nanowires were dispersed in distilled aniline, followed by polymerization. In a typical synthesis of the PANI-ZnONW (2:1) composite, an ammonium persulfate solution (0.6867 g dissolved in 13.7 ml of 1 M aqueous HCl solution) was slowly added to a mixture of aniline (0.67 g, 7.3 mmol) and ZnONWs (0.303 g, 3.65 mmol) taken in a round bottom flask containing 13.7 ml of 1M aqueous HCl solution under sonication at 0 °C. Sonication was carried out for another two hours after the addition of the ammonium persulfate solution. The product was filtered and washed thoroughly with distilled water (to remove the unreacted ammonium persulfate and excess of HCl) and then with methanol (to remove the oligomers). The filtered sample was dried under a dynamic vacuum at room temperature for 24 h to ensure the absence of moisture, which affects the conductivity of polyaniline. [22] The various compositions of the PANI-ZnONW composites prepared by us are: 6:1, 2:1 and 1:2 (molar ratios). The 6:1 and 2:1 PANI-RuO₂NW composites and 6:1 PANI-AgNW composites were prepared by a procedure similar to that described above.

The polypyrrole-nanowire composites were prepared by a method similar to that outlined in the literature using camphor sulfonic acid (CSA) as the dopant. [26] For the synthesis of PPy-ZnONW (2:1), 0.5 ml distilled pyrrole was added to 0.303 g ZnONW with 26 ml water containing 0.587 g CSA. (NH₄)₂S₂O₈ (1.7 g) was dissolved in 26 ml water was later added dropwise in to previous solution while under sonication. All the solutions are pre-cooled to 0 °C before the two solutions were added together. The composite thus prepared was washed thoroughly with distilled water and methanol and dried in vacuum for 24 h. The compositions of the PPy-ZnONW composites prepared by us are: 6:1 and 2:1 (molar ratio of pyrrole and ZnONW).

In the ex-situ synthesis of PANI-ZnONW composites, a camphor sulfonic acid (CSA)-doped polyaniline solution was prepared in m-cresol as described

by Reghu *et al* [27]. The ZnONWs were then dispersed in different volumes of CSA-doped polyaniline solution by ultrasonication and the solvent was removed by drying at 50 °C for 24 h to yield the composite of polyaniline and ZnONW. The compositions of the PANI-ZnONWs prepared by the ex-situ process are: 2:1, 1:2 and 1:4 (molar ratios).

A polyvinyl alcohol (PVA)-AgNW composite (0.065 volume fraction of AgNWs) was prepared by adding AgNWs (50 mg) to a hot aqueous solution of PVA (0.95g). This mixture was sonicated for 2 h and the water removed by evaporation at 60 °C. The composites and the parent nanotubes were characterized by X-ray powder diffraction (XRD), scanning electron microscopy (SEM), transmission electron microscopy(TEM), infrared spectroscopy and Raman spectroscopy. The electric properties were measured by the 4-probe technique between 30 °C and –258 °C. The powder X-ray diffraction patterns was recorded using a Seifert XRD 3000 TT instrument. All the SEM images were obtained with a Leica S-440I microscope and TEM images with a JEOL JEM 3010 instrument operating at an accelerating voltage of 300 kV. The IR measurements were done on Bruker FT-IR spectrometer. The Raman measurements were performed in a 90 degrees geometry using a Jobin Yvon TRIAX 550 triple grating spectrometer equipped with a cryogenic charge-coupled device camera, using diode-pumped frequency doubled solid state Nd:YAG laser of 532 nm (Model DPSS 532-400, Coherent Inc. USA).

6.3 Results and Discussion

6.3.1 Carbon Nanotubes

In Figure 6.1, we show the TEM images of pyrolysis MWNTs and SWNTs to illustrate the quality of the nanotubes employed for the preparation of the composites with PANI. In Figure 6.2 (a), we show the TEM image of

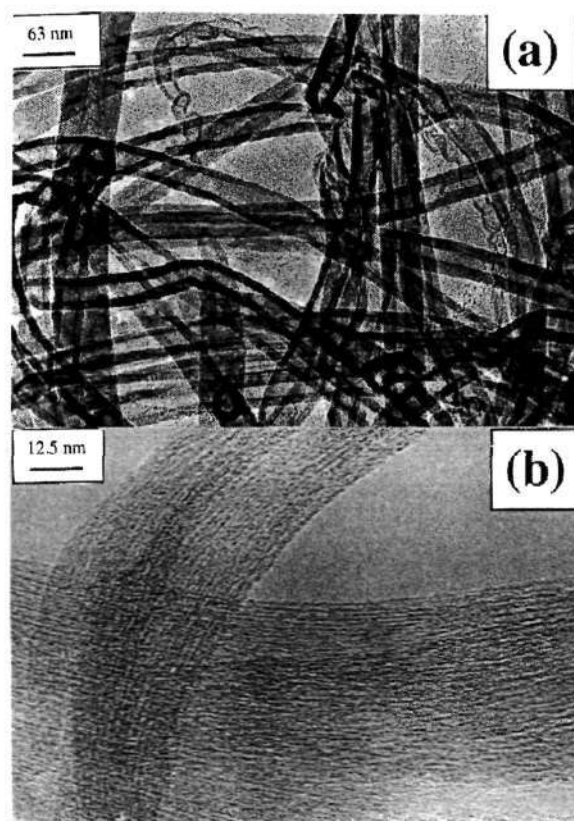


Figure 6.1: Representative TEM images of the nanotubes as synthesized for the preparation of PANI-nanotube composites- (a) pyrolysis MWNTs and (b) arc-discharge SWNTs.

a MWNT covered by polyaniline. The TEM image in Figure 6.2 (6) corresponds to the composite of PANI with acid treated MWNTs (2:1). Figure 6.2 (c) shows the TEM image of the PANI-chlorinated MWNTs (2:1) composite.

In Figure 6.3, we show the XRD pattern for MWNTs and polyaniline nanotube composites. The multi-walled carbon nanotube show only (hk0) and (00l) reflections. The diffraction pattern of multi-walled nanotubes exhibit four major reflections: (002) reflections at 3.435 Å (which corresponds to the interplanar spacing between the graphene sheets in the nanotubes), (001) reflections at 2.132 Å with squared Lorentzian line shape, (004) reflection at 1.705 Å and (110) reflections at 1.231 Å. In Figure 6.4, we compare the infrared spectrum of PANI with spectra of the composites of PANI with

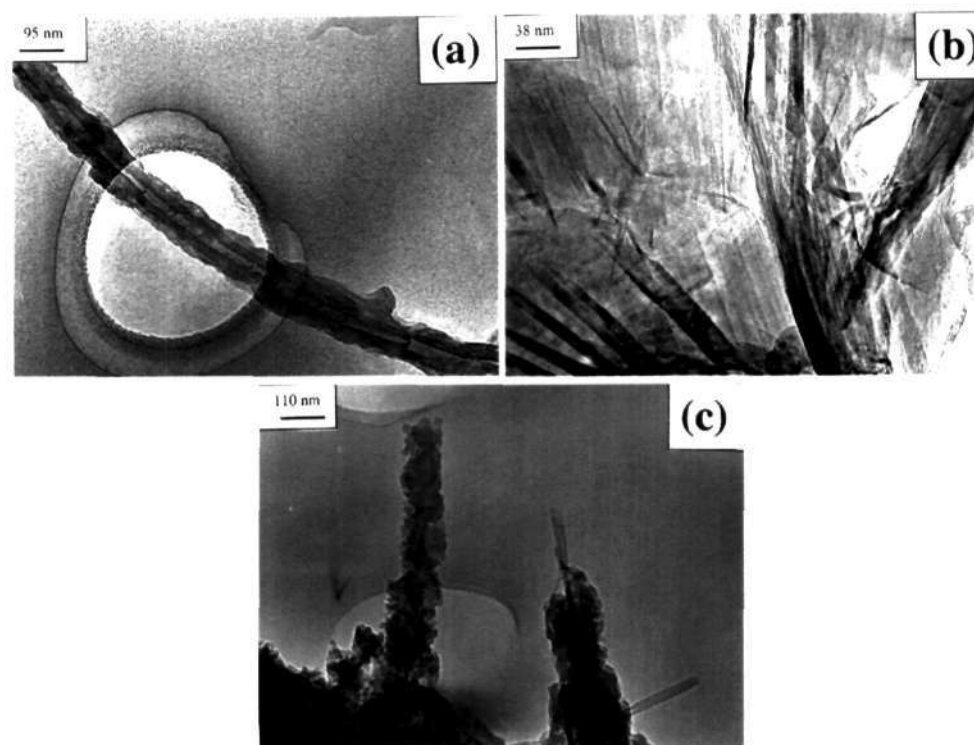


Figure 6.2: TEM images of PANI-MWNT (2:1) composites with: (a) as-prepared MWNTs, (b) acid treated MWNTs and (c) chlorinated MWNTs.

MWNTs. We do not see any significant changes in the N-H stretching or the -N=quinoid=N- bands in the PANI composite with the as prepared MWNTs. Interestingly, the band positions in the IR spectra of the PANI composite with acid treated MWNTs (2:1) and chlorinated MWNTs (2:1) show negligible changes as can be seen from Figures 6.4. The relative intensities of the -N=quinoid=N- band, however, are slightly different specially in the spectra the composites of PANI with acid treated and chlorinated MWNTs. We also see an additional band at 1700 cm^{-1} in the spectrum of the PANI-chlorinated MWNT (1:2) composite.

In Figure 6.5, the Raman spectra of the as prepared MWNTs, acid treated MWNTs and chlorinated MWNTs illustrates how the nanotube character is retained eve after various treatments. We observe the E_{2g} in-plane stretching vibration at 1590 cm^{-1} , a shoulder around 1615 cm^{-1} corresponding to the

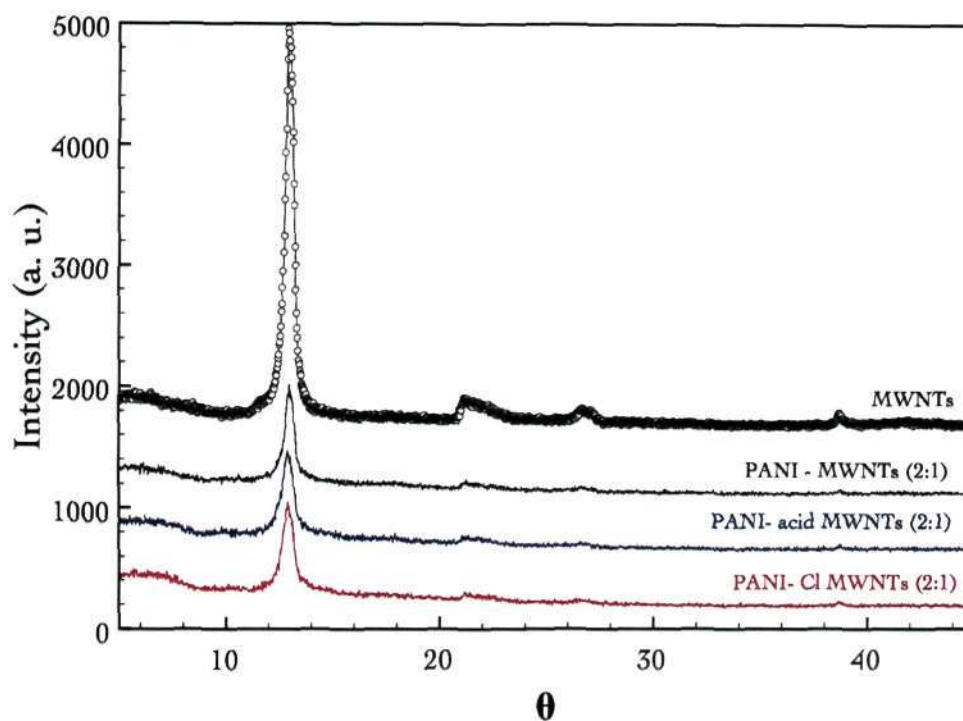


Figure 6.3: XRD patterns of MWNTs and (2:1) PANI nanocomposites with different MWNTs.

D-line and the 1360 cm^{-1} mode due to the D-line (from sp^3 carbons). In the acid treated MWNTs, the intensity of the 1360 cm^{-1} increases slightly indicating an increase in the number of sp^3 carbons after acid treatment. The Raman spectra of the PANI-nanotube composites shown in Figure 6, we see characteristic bands due to polyaniline along with the nanotube bands. The in-plane deformation (600 cm^{-1}), which is characteristic of the para-disubstituted benzene unit is hardly observed in the composites. There is a significant change in the intensity of the band at 1486 cm^{-1} compared to the band at 1180 cm^{-1} in all the composites. The band at 1180 cm^{-1} is due to the C-H in-plane bending which is characteristic of the para-disubstituted benzene unit and the band at 1486 cm^{-1} corresponds to the C=N stretching of the quinone diimine structure [28]. There appears to be an increase in the quinone diimine units in the PANI composite compared to PANI. In the PANI-MWNT (1:2) composite we observe the expected decrease in the

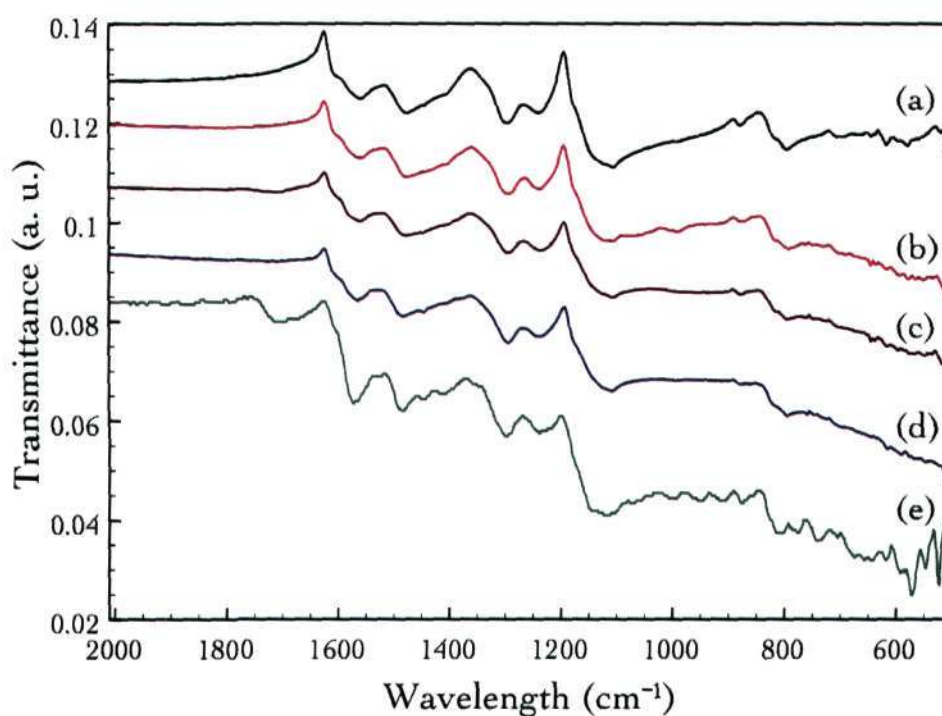


Figure 6.4: IR spectra of PANI-nanotube composites with - (a) PANI, (b) PANI-MWNT (2:1), (c) PANI-acid treated MWNT (2:1), (d) PANI-chlorinated MWNT (2:1) and (e) PANI-chlorinated MWNT (1:2).

intensities of the parent bands due to PANI.

In Figure 6.6 (a), we compare electrical resistivities of the parent nanotubes with that PANI and the composites of PANI with multi-walled nanotubes. The resistivities of the MWNTs are low and nearly temperature independent. Polyaniline shows insulating type behavior with a strong temperature dependence of resistivity. The resistivity of the MWNTs decreases slightly on acid treatment but the resistivity of the chlorinated MWNTs is similar to that of the pristine MWNTs. The resistivities of the 1:2 PANI-MWNT composites fall in between the resistivities of PANI and MWNTs. The resistivities of the 2:1 composites show a similar behavior. In Figure 6.6 (b), we show the electrical resistivities of the 1:1 PANI-SWNT composites. The PANI-SWNT (1:1) composite shows a slightly higher resistivity

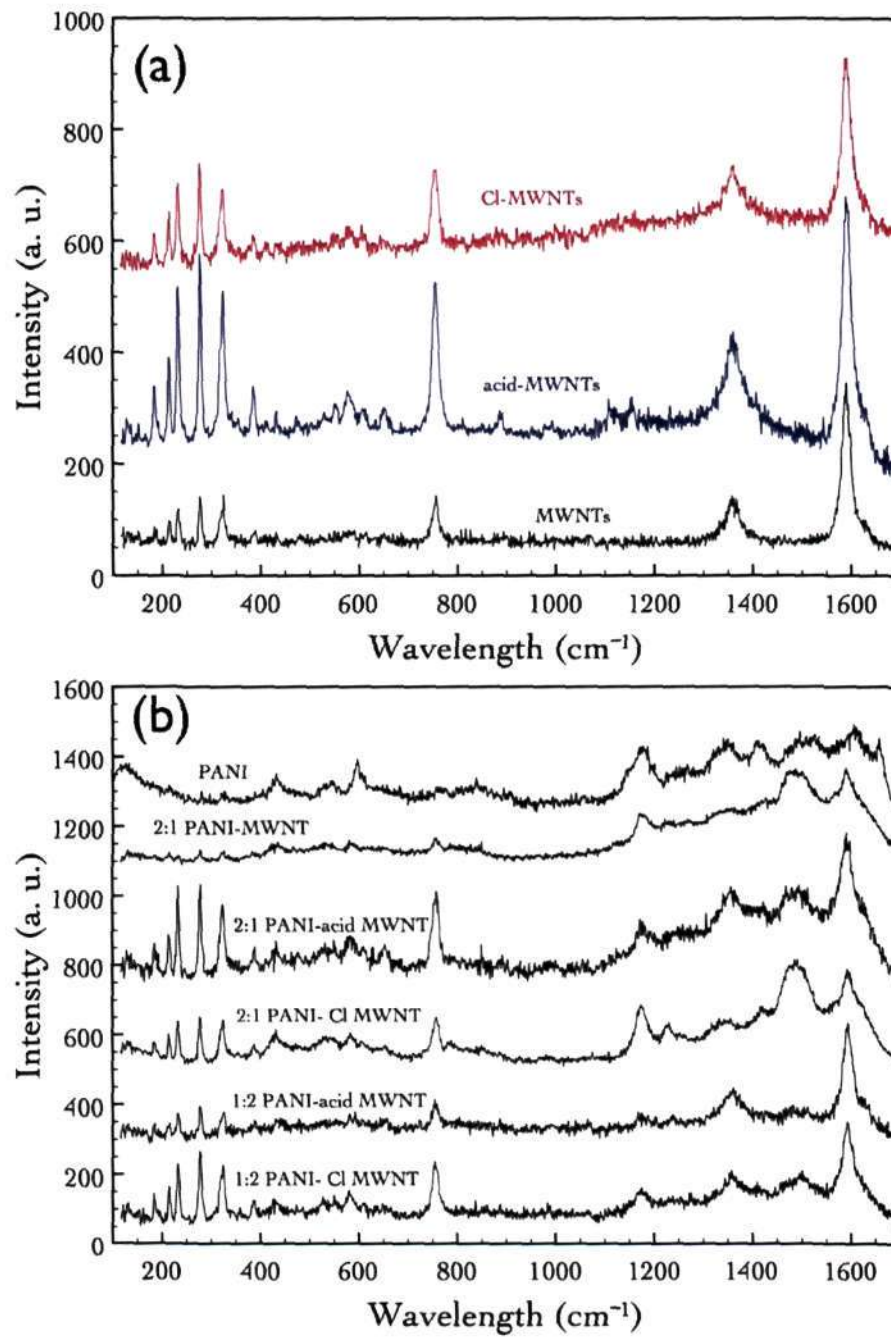


Figure 6.5: Raman spectra of (a) different types of MWNTs and (b) PANI and PANI-MWNTs nanocomposites.

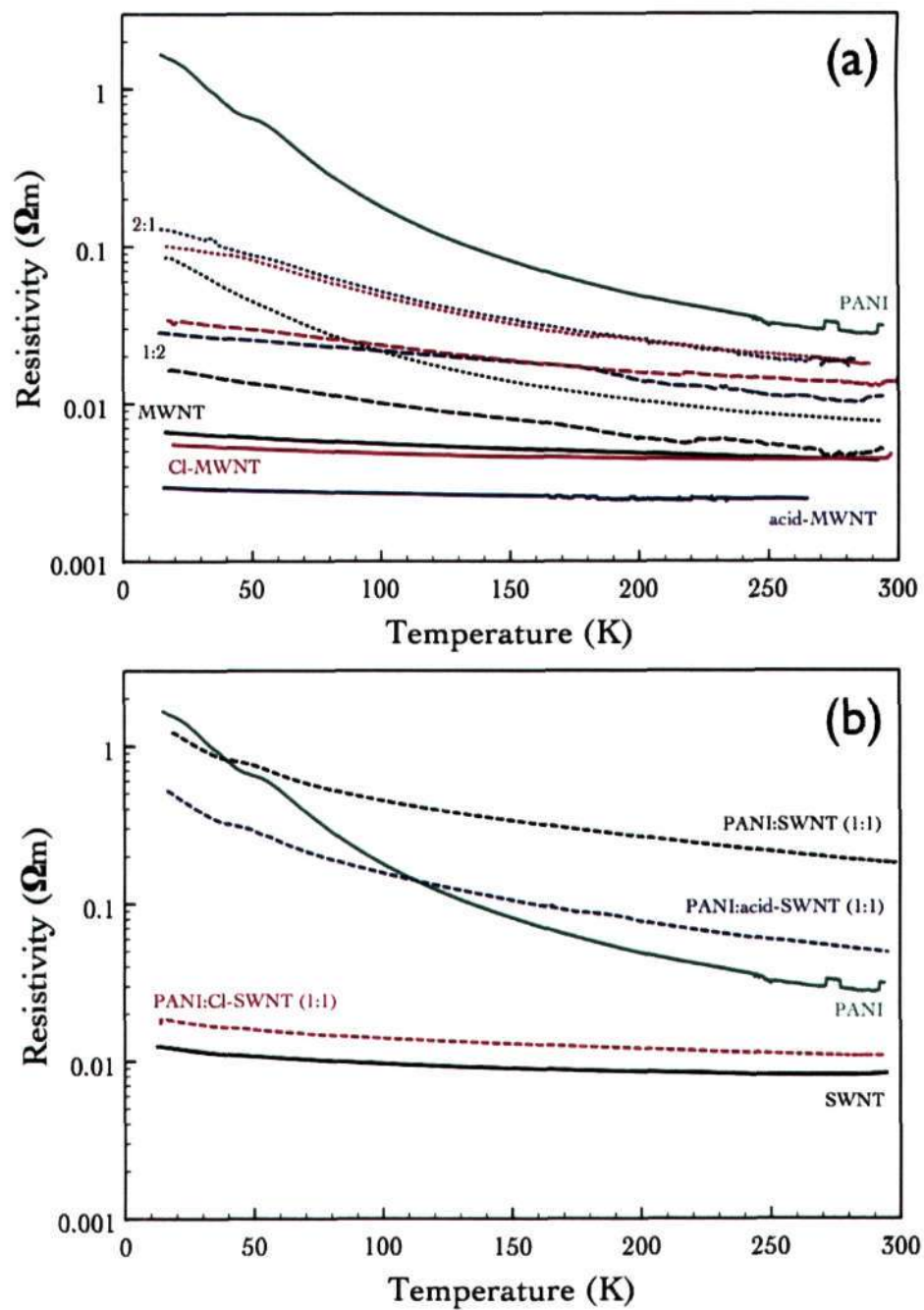


Figure 6.6: Electrical resistivities of (a) MWNTs and PANI-MWNTs nanocomposites and (b) SWNTs and PANI-SWNTs nanocomposites.

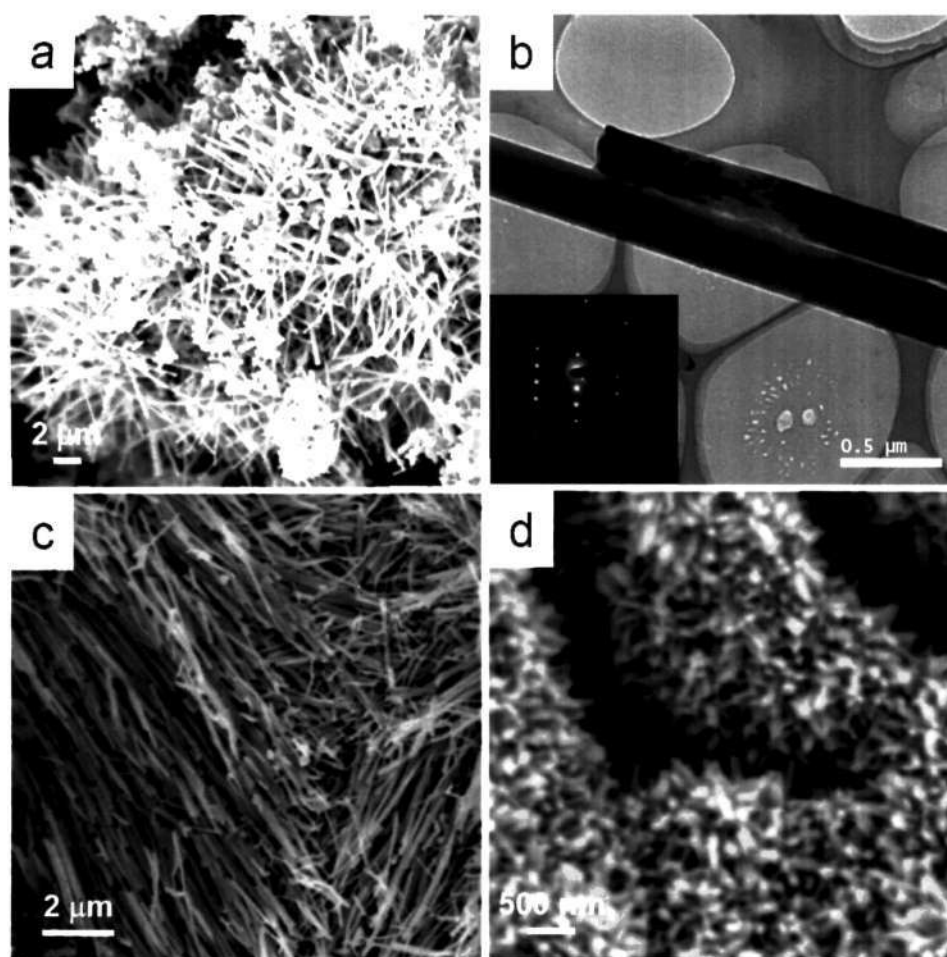


Figure 6.7: (a) SEM image of as-synthesized ZnO nanowires, (b) corresponding TEM image with SAED of a ZnO nanowire as inset, (c) SEM image of silver nanowires and (d) SEM image of the RuO₂ nanowires.

than PANI while the PANI-acid treated SWNT composite shows a resistivity close to that of PANI. The resistivity of the PANI-chlorinated SWNT composite is close to that of the SWNTs.

6.3.2 Inorganic nanowires

In Figure 6.7, we show electron micrographs of the as-synthesized nanowires used for the preparation of the composites. The ZnONWs are crystalline and show the characteristic hexagonal structure (JCPDS File: 36-1451). Figure 6.7 (a) shows a SEM image of the ZnO nanowires with diameters ranging

between 100 and 300 nm and lengths extending to several microns. A TEM image of the ZnONWs is shown in Figure 6.7 (b) and its corresponding selected area electron diffraction (SAED) pattern (shown in the inset) confirms the single-crystalline nature of the nanowires. Figure 6.7 (c) shows a SEM image of silver nanowires with diameters ranging between 100 to 200 nm and lengths extending to several microns. The RuO₂NWs had diameters in the 50-100 nm range with lengths of few hundred nanometers as shown in Figure 6.7 (d). The RuO₂NWs are crystalline and show the characteristic rutile structure (JCPDS File: 43-1027).

In order to verify that the nanowires were homogeneously distributed in the polymer composites, we carried out an electron microscopic examination of the composites. A SEM image of the PANI-ZnONW (2:1) composite prepared by the *in-situ* procedure is shown in Figure 6.8 (a). The nanowires are seen along the edges and are randomly dispersed. The presence of the nanowires is also confirmed by EDAX. We show a SEM image of the PANI-CI-ZnONW (2:1) composite in Figure 6.8 (b). A SEM image of the PANI-RuO₂NW (6:1) composite is shown in Figure 6.8 (c). The nanowires are embedded in the polymer matrix as clearly evident from the TEM image of PANI-AgNW(6:1) shown in Figure 6.8 (d). The XRD patterns of the PANI-ZnONW composites prepared by the *in-situ* procedure were characteristic of ZnO with the hexagonal structure, showing that the crystallinity of ZnONW is not affected in the composite. PANI exhibits the characteristic stretching bands of the quinoid and benzenoid rings [28] at 1560 cm⁻¹ and 1475 cm⁻¹ respectively in the infrared spectrum (Figure 6.9 (a)), indicating the oxidation state of emeraldine salt. The quinoid band is less intense than the benzenoid band in PANI. The C-N stretching bands of the quinoid and benzenoid rings are seen at 1291 cm⁻¹ and 1236 cm⁻¹ and the in-plane C-H stretching band at 1110 cm⁻¹. The Zn-O stretching mode of the ZnONW appears as a broad

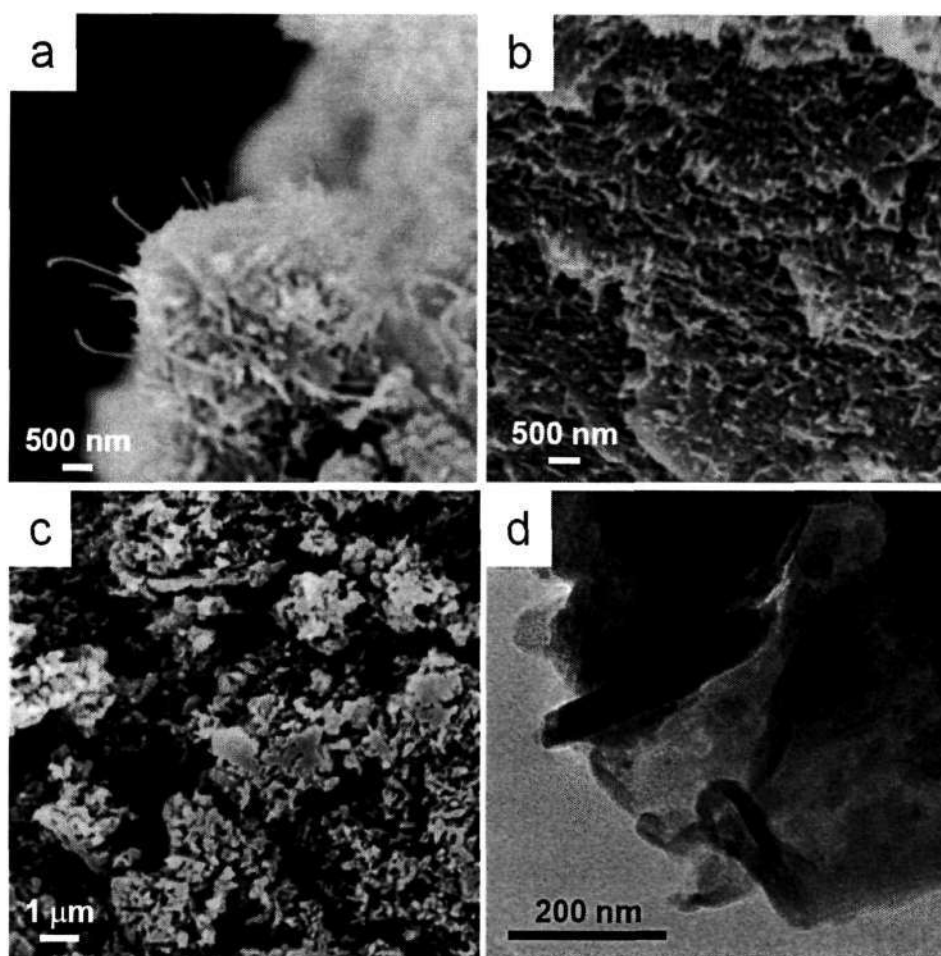


Figure 6.8: SEM images of (a) PANI-ZnONW (2:1), (b) PANI-Cl- ZnONW (2:1), (c) PANI-RuO₂NWs (6:1) and (d) TEM image of PANI-AgNWs (6:1). All the composites were prepared by the *in-situ* polymerization of aniline.

band around 450 cm^{-1} (Figure 6.9 (e)) [29]. The PANI-ZnONW composites prepared by the *in-situ* method show a significant shift of the quinoid band to 1563 cm^{-1} in the PANI-Cl-ZnONW (2:1) composite and to 1580 cm^{-1} in the PANI- ZnONW (1:2) composite (Figure 6.9). The benzenoid band is also shifted to higher wavenumbers with the increasing proportion of ZnONW, 1479 cm^{-1} in the PANI-Cl-ZnONW (2:1) composite and 1489 cm^{-1} in the PANI- ZnONW (1:2) composite. There is also an increase in the intensity of the quinoid band with the addition of ZnONW, suggesting that the nanowires promote and/or stabilize the quinoid form to a greater extent.

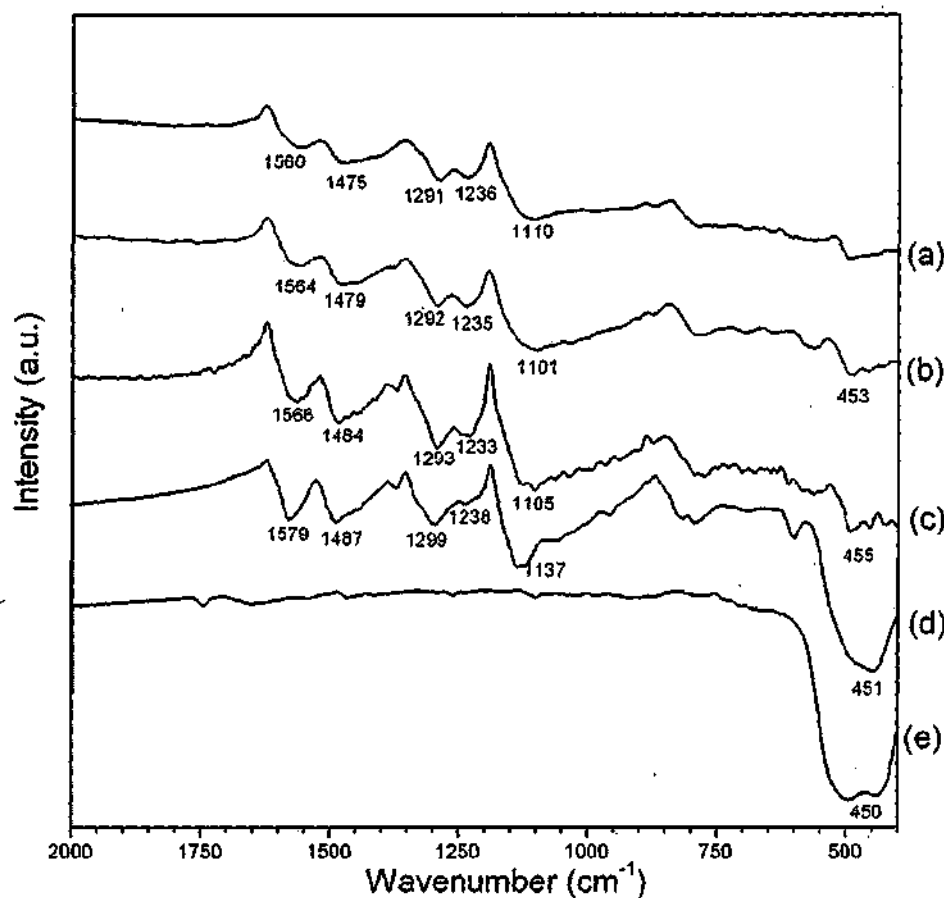


Figure 6.9: Infrared spectra of (a) PANI, (b) PANI-Cl-ZnONW (2:1), (c) PANI-ZnONW (2:1), (d) PANI-ZnONW (1:2) composites prepared by the *in-situ* method and (e) ZnONW.

Similar observations are reported in the case of PANI-MWNT composites. [9] The intensity of the Zn-O stretching band in the composites increases with the increase in the proportion of ZnONWs as expected. PPy shows characteristic C=C stretching, C=N stretching, C-N stretching and C-H stretching at 1551, 1477, 1300 and 1045 cm^{-1} respectively in the infrared spectrum [30]. In the PPy-ZnONW composites, shifts in the C=C, C=N, C-N and C-H stretching bands to 1564, 1485, 1285 and 1046 cm^{-1} are observed. The increase in the C=C, C=N and C-H stretching frequencies are attributed to a decrease in the doping level of the polymer, which in turn can lead to a higher resistivity. In Figure 6.10 (a), we show the electrical resistivity data of the

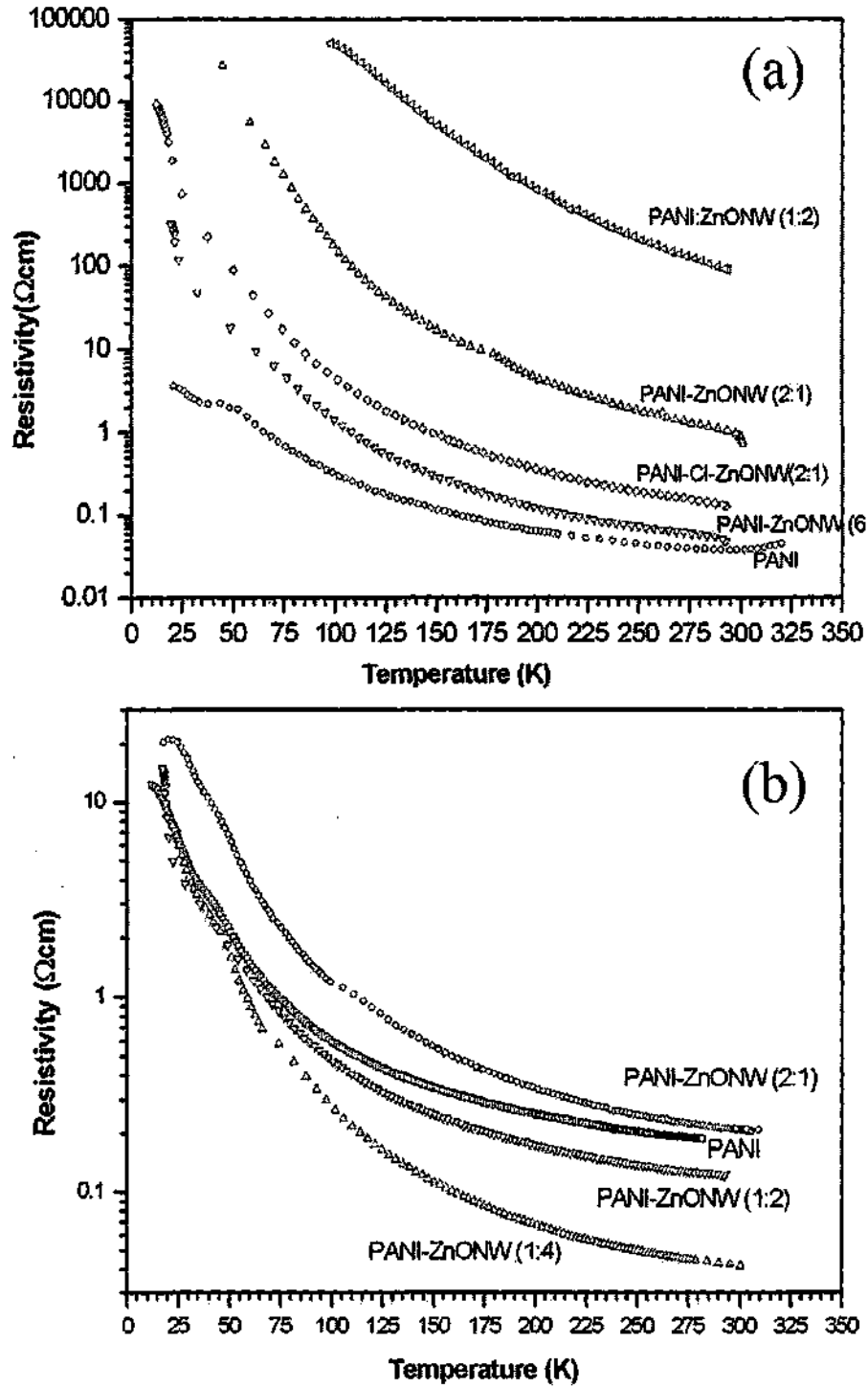


Figure 6.10: (a) Electrical resistivity of PANI-ZnONW composites prepared by the *in-situ* method and (b) electrical resistivity of PANI-ZnONW composites prepared by the *ex-situ* method.

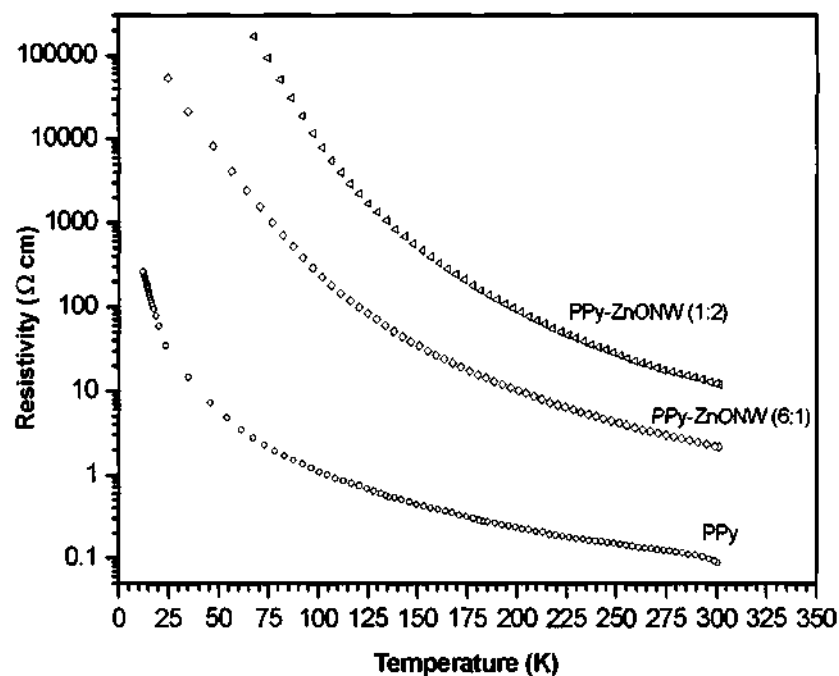


Figure 6.11: Electrical resistivities of PPy-ZnONW composites prepared by the *in-situ* method.

PANI-ZnONW composites. The ZnO nanowires exhibit a room-temperature resistivity of 27600 Ωcm , which is higher than that of single crystals [31]. Polyaniline exhibits semiconducting behavior with a room temperature resistivity of 0.03 Ωcm , in accordance with the value reported in literature [22]. The PANI-ZnONW composites are also semiconducting and exhibit room-temperature resistivities intermediate between those of PANI and ZnONW. There is an increase in the temperature dependence of the nanowires with the increase in the proportion of ZnONWs. It is possible that an increase in the ZnONW concentration leads to an increase in the pH of the reactant mixture, resulting in a different doping level of the conducting polymer. The PANI-Cl-ZnONW (2:1) composite shows a slightly lower room-temperature resistivity compared to that without functionalization by an order of magnitude. It may be noted that in PANI-Cl-ZnONW(2:1), the NH groups of the polymer can undergo a chemical reaction with the chlorines on the nanowire surface. The electrical resistivity data of the PPy-ZnONW composites are

shown in Figure 6.11. The room-temperature resistivity of PPy is $0.088 \Omega\text{cm}$. The electrical properties of these composites are similar to those with PANI, and we see an increase in the resistivity with the increasing proportion of ZnONWs. The temperature-dependence of resistivity of the composites is similar to that of PANI-ZnONWs. The electrical resistivity data of the nanowires composites in Figures 6.10 (a) and 6.11 demonstrate that we can manipulate the resistivity behavior of the composites over a large range by varying the composition.

In the PANI-ZnONW composites prepared by the *ex-situ* method, the nanowires are embedded in a matrix of polyaniline as evident from the SEM and TEM images. The presence of ZnONWs is also confirmed by the EDAX spectrum. The crystallinity of the ZnONWs is preserved in the composite as revealed by the XRD patterns. In Figure 6.10 (b), we show the electrical resistivity data of PANI-ZnONW composites prepared by the *ex-situ* method. The resistivity of the PANI sample used here is different from that in Figure 6.10 (a) because of the different method employed for the synthesis. There is a decrease in the room temperature resistivity and an increase in the temperature-dependence of resistivity after the incorporation of a large proportion of ZnONW in PANI. The slightly lower resistivity of the PANI-ZnONW *ex-situ* composites in comparison with the *in-situ* composites may be due to the chemical modification of the nanowire surfaces that may occur in the *in-situ* process and due to the chemical interaction between the NH groups of the PANI and surface Zn^{2+} of the nanowire. [32] Infrared spectroscopic evidence for the interaction of the oxide nanowires with the polymer matrix was provided earlier. Electrical resistivity of the composites of PANI with RuO_2NWs and AgNWs are shown in Figure 6.12. RuO_2NW is metallic and the resistivity increases with increase in temperature. The electrical resistivity of the PANI- RuO_2NW composites lies in between that

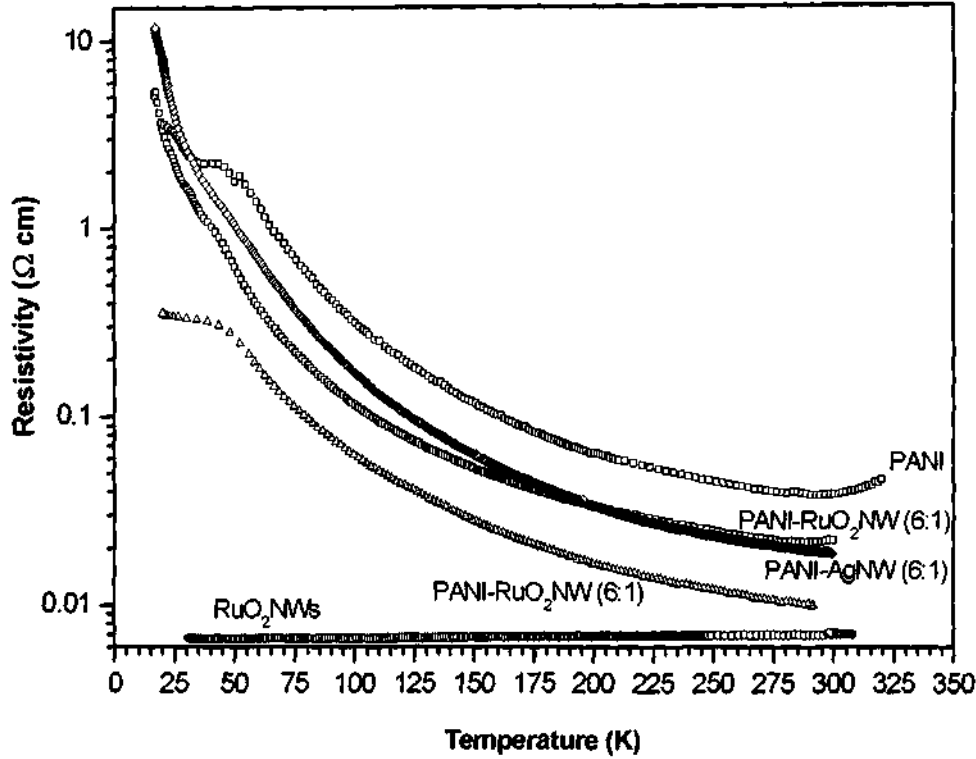


Figure 6.12: Electrical resistivity of PANI composites with RuO₂NW and AgNW prepared by the *in-situ* method.

of PANI and RuO₂, the resistivity decreasing with increase in the proportion of RuO₂NWs. The temperature dependence of these composites is similar to that of PANI. The resistivity of the 6:1 PANI-AgNW composite is lower than that of pristine PANI. It is noteworthy that the resistivity of 6:1 PANI-AgNW is comparable to that of 6:1 PANI-RuO₂NWs. In order to understand the electrical behavior of the polymer-nanowire composites, it is important to know whether the nanowires provide a percolation path. We have therefore estimated the minimum molar ratio of PANI to metallic nanowires to form a connected network. In the case of metallic RuO₂ and AgNWs, the required molar ratios are 3:1 and 2.4:1 respectively [33, 34].

The minimum volume fraction of rods needed to form a connected network is given by

$$\phi = 3D_{eff}^2/2L^2, \quad (6.1)$$

where D_{eff} and L are the effective diameter and length of the rod respectively. In the case of RuO₂NWs $D_{eff} = 80$ nm and $L = 300$ nm and for AgNWs, $D_{eff} = 150$ nm and $L = 1$ μ m. The diameters of the nanowires were estimated from transmission electron micrographs while the lengths of the nanowires were determined by SEM. Due to the intense sonication involved during the preparation of the polymer composites, the average length of the AgNWs decreases to 1 μ m. In terms of volume fractions, the volume fraction of RuO₂NWs and AgNWs needed are 0.0711 and 0.0459 respectively.

These values are much larger than the ratios reported for polymer-SWNTs composites. This is due to the larger diameter, smaller aspect ratio and higher density of the metallic nanowires in comparison with the SWNTs. It therefore becomes clear that there is no percolation network in the polymer-metal nanowire composites giving rise to the metallic behavior. In order to convince ourselves of this conclusion, we prepared PVA-AgNWs composite with a composition close to that required for percolation, but the composite failed to show high conductivity.

A comment on the conduction process in the polymer-inorganic nanowire composite would be in order: The electrical conductivity of a conducting polymer arises due to the introduction of charge carriers by doping, the doped form being more conducting than the undoped form. In the inorganic nanowire composites, the nanowires are embedded in a conducting matrix and the conductivity of the composite would be a function of both the matrix and the nanowires. In the case of ZnONW composites, the electrical conductivity is mainly due to the polymer matrix as the conductivity of the ZnONWs is far lower than that of the polymer. The nanowires and the polymer contribute in the electrical conductivity in the case of the RuO₂NW and AgNW composites. Since the nanowires do not form a connected network, the obtained increase in the conductivity can arise due to the participation

of the nanowires in the conduction process in some way. The resistivity of the PANI composite therefore lies in between that of PANI and metallic nanowires.

6.4 Conclusions

Composites of polyaniline with the pristine multi-walled carbon nanotubes as well as acid treated and chlorinated nanotubes can be prepared by the *in-situ* polymerization of aniline by ammonium persulfate as an oxidizing agent. The PANI-nanotube composites could be characterized satisfactorily by Raman spectroscopy and electron microscopy. The electrical resistivities of the nanocomposite differ from those of the parent nanotubes or that of PANI. The results show that the electrical resistivity of the PANI-nanotube composites can be manipulated through the variation of the composition as well as by the prior treatment of the nanotubes.

It has been possible to prepare composites of ZnO, RuO₂ and Ag nanowires (NW) with polyaniline and polypyrrole by the *in-situ* procedure. The ZnONW composites show a wide range of resistivities between those of the nanowire and that of the polymer. Polyaniline composites with chlorinated ZnONWs show lower resistivity than the unfunctionalized nanowires. Composites of ZnONWs with PANI prepared by the *ex-situ* process show slightly lower resistivities than that of the polymer. The PANI composites with RuO₂NWs and AgNWs exhibit lower resistivities than PANI. The range of composites prepared by us with room temperature resistivity (0.01-400 cm) indicates that the composites could be useful in some applications. For example, the PANI-RuO₂NW composites may be used as electrode materials in supercapacitors. The present work constitutes the first study of the electrical properties of inorganic nanowire-polymer composites. There is clearly great room for further studies on these materials.

6.5 References

1. P. M. Ajayan, O. Stephan, C. Colliex, and D. Trauth, *Science* **265**, 1212 (1994).
2. E. T. Thostenson, Z. Ren, and T. W. Choua, *Compos. Sci. Technol.* **61**, 1899 (2001).
3. P. F. J. Harris, *Inter. Mater. Rev.* **49**, 31 (2004).
4. R. Andrews and M. C. Weisenberger, *Current Opinion in Solid State and Materials Science* **8**, 31 (2004).
5. R. H. Baughman, A. A. Zakhidov, and W. A. De Heer, *Science* **297**, 787 (2002).
6. C. Downs, J. Nugent, P. M. Ajayan, D. J. Duquette, and K. S. V. Santhanam, *Adv. Mater.* **11**, 1028 (1999).
7. M. Cochet, W. K. Maser, A. M. Benito, M. A. Callejas, M. T. Martínez, J. Benoit, J. Schreiber, and O. Chauvet, *Chem. Commun.* 1450 (2001).
8. G. B. Blanchet, C. R. Fincher, and F. Gao, *Appl. Phys. Lett.* **82**, 1290 (2003).
9. H. Zengin, W. Zhou, J. Jin, R. Czerw, D. W. Smith Jr., L. Echegoyen, D. L. Carroll, S. H. Foulger, and J. Ballato, *Adv. Mater.* **14**, 1480 (2002).
10. W. Feng, X. D. Bai, Y. Q. Lian, J. Liang, X. G. Wang, and K. Yoshino, *Carbon* **41**, 1551 (2003).
11. Y. Long, Z. Chen, X. Zhang, J. Zhang, and Z. Liu, *Appl. Phys. Lett.* **85**, 1796 (2004).
12. X. Zhang, J. Zhang, R. Wang, T. Zhu, and Z. Liu, *ChemPhysChem* **5**, 998 (2004).
13. K. Jurewicz, S. Delpeux, V. Bertagna, F. Béguin, and E. Frackowiak, *Chem. Phys. Lett.* **347**, 36 (2001).
14. S. A. Curran, P. M. Ajayan, W. J. Blau, D. L. Carroll, J. N. Coleman, A. B. Dalton, A. P. Davey, A. Drury, B. McCarthy, S. Maier, and A. Strevens, *Adv. Mater.* **10**, 1091 (1998).

15. R. Kötz and M. Carlen, *Electrochim. Acta* **45**, 2483 (2000).
16. C. N. R. Rao, R. Seshadri, A. Govindaraj, and R. Sen, *Mater. Sci. Eng. R.* **15**, 209 (1995).
17. B. C. Satishkumar, A. Govindaraj, J. Mofokeng, G. N. Subbanna, and C. N. R. Rao, *J. Phys. B* **29**, 4925 (1996).
18. S. C. Tsang, P. J. F. Harris, and M. L. H. Green, *Nature* **362**, 520 (1993).
19. M. Nath, B. C. Satishkumar, A. Govindaraj, C. P. Vinod, and C. N. R. Rao, *Chem. Phys. Lett.* **322**, 333 (2000).
20. C. Journet, W. K. Maser, P. Bernier, A. Loiseau, M. Lamy de la Chapelle, S. Lefrant, P. Deniard, R. Lee, and J. E. Fischer, *Nature* **388**, 756 (1997).
21. C. Fite, Y. Cao, and A. J. Heeger, *Solid Stat. Commun.* **70**, 245 (1989).
22. A. G. MacDiarmid and A. J. Epstein, *Faraday Discuss. Chem. Soc.* **88**, 317 (1989).
23. G. Gundiah, F. L. Deepak, A. Govindaraj, and C. N. R. Rao, *Top. in Catal.* **24**, 137 (2003).
24. Y. Sun, B. Gates, B. Mayers, and Y. Xia, *Nano Lett.* **2**, 165 (2002).
25. B. C. Satishkumar, A. Govindaraj, M. Nath, and C. N. R. Rao, *J. Mater. Chem.* **10**, 2115 (2000).
26. S. Maeda and S. P. Armes, *J. Mater. Chem.* **4**, 935 (1994).
27. M. Reghu, Y. Cao, D. Moses, and A. J. Heeger, *Phys. Rev. B* **47**, 1758 (1993).
28. Y. Furukawa, F. Ueda, Y. Hyodo, I. Harada, T. Nakajima, and T. Kawagoe, *Macromolecules* **21**, 1297 (1988).
29. A. E. J. Gonzalez, J. A. S. Urueta, and R. S. Parra, *J. Cryst. Growth* **192**, 430 (1998).
30. B. Tian and G. Zerbi, *J. Chem. Phys.* **92**, 3886 (1990).
31. A. R. Hutson, *Phys. Rev. Lett.* **4**, 505 (1960).

-
32. Z. X. Zheng, Y. Y. Xi, P. Dong, H. G. Huang, J. Z. Zhou, L. L. Wu, and Z. H. Lin, *PhysChemComm* **5**, 63 (2002).
 33. M. Doi and S. F. Edwards, *The Theory of Polymer Dynamics* (Oxford University Press, Clarendon, 1992).
 34. M. B. Bryning, M. F. Islam, J. M. Kikkawa, and A. G. Yodh, *Adv. Mater.* **17**, 1186 (2005).

Chapter 7

MECHANICAL PROPERTIES OF NANOCOMPOSITES OF INORGANIC NANOWIRES WITH POLYMERS

Summary¹

Mechanical properties of poly(vinyl alcohol) matrix composites incorporating SiC and Al₂O₃ nanowires (NWs) have been investigated. A marked increase in the elastic modulus (up to 90%) has been observed even with a small addition (0.8 vol.%) of the nanowires. This observation cannot be explained by iso-stress analysis, which is appropriate for describing the variation of properties with the reinforcement volume fraction in discontinuously reinforced composites. A significant increase in the strength of the composite with the addition of NWs is also observed. This is due to the significant pull-out of the NWs and the corresponding stretching of the matrix due to the complete wetting of the NW surface by the polymer. The increase in tensile strength is found to saturate at higher vol.% of NW addition, due to the reduced propensity for shear-band induced plastic deformation.

7.1 Introduction

Synthesis and characterization of one-dimensional nanostructures constitute an area of great interest. Of the various one-dimensional materials, single-walled carbon nanotubes (SWNTs) have been studied extensively. In particular, electrical and mechanical properties of SWNT-polymer composites

¹A paper based on this study has been published in *Nanotechnology* (2006)

have been examined in great detail. Incorporation of SWNTs in the polymers generally enhances the stiffness and strength. Although the electrical properties, sensor characteristics and other aspects of inorganic nanowires have been reported [1, 2], there has been no systematic study of the mechanical properties of the nanowire composites with polymers. Mechanical properties of individual SiC nanowires (NWs) have been examined by atomic force microscopy. While the elastic modulus, E , is close to the theoretical limit, the fracture strength is larger than that of the fiber [3]. Wang *et al.* [4] have studied the mechanical properties of SiC-SiO₂ biaxial nanowires using electric field induced dynamic phenomena, while Yang *et al.* [5] have used carbon-coated SiC nanowires for preparing ceramic composites with high toughness. We have investigated the mechanical properties of composites of SiC and Al₂O₃ nanowires with polyvinyl alcohol (PVA). PVA was chosen for the study in view of practical applications and also because earlier studies of carbon nanotube composites were with PVA [6–9]. For the purpose of the present study, we prepared the PVA-NW composites as a function of the nanowire volume fraction and characterized them by electron microscopy, infrared spectroscopy, and differential scanning calorimetry. Dynamic mechanical analysis (DMA) was conducted to measure the elastic modulus and tensile testing to measure the strength of the polymer composites. To our knowledge, this is the first report on the mechanical properties of inorganic nanowire-reinforced polymer matrix composites.

7.2 Experimental details

Nanowires of SiC and Al₂O₃ were synthesized using methods reported earlier in the literature [10, 11]. In a typical preparation of the PVA-SiC NW (0.8 vol%) composite, PVA (1.95 g) and SiC NW (0.05 g) were added to warm

water (50 ml), and mixture heated at 70 °C till the polymer dissolved forming a dispersion of the nanowires. The dispersion was dried in Petri dishes at 50 °C over a period of 3 days [12]. As the mechanical properties of PVA are sensitive to the water content, the polymer films were stored in a vacuum desiccator with anhydrous CaCl₂ for at least a week before mechanical testing. Composites with PVA were prepared with 0.2, 0.4 and 0.8 vol.% of SiC NW and 0.4 vol.% of Al₂O₃NW. Visual as well as optical microscopic examination of the composite strips indicated uniform distribution of the nanowires throughout the matrix.

The composites as well as the nanowires were characterized by several techniques. Scanning electron microscopy (SEM) images and energy dispersive analysis of X-rays (EDAX) were obtained with a Leica S-440I microscope fitted with a Link ISIS spectrometer. Infrared (IR) spectra were recorded on small pieces of the samples embedded in KBr pellets using Bruker FT-IR spectrometer. Differential scanning calorimetry (DSC) was carried on the samples (7 mg) with a scanning rate of 20 K/min between 120 – 260 °C using a Mettler-Toledo DSC.

Mechanical testing was conducted on samples of 25 mm in length, 10 mm in width and 0.1 mm in thickness. Because of the high compliance of the films, it was difficult to mount an extensometer on the samples to measure E. A dynamic mechanical analyzer (DMA) was therefore, used to assess the elastic properties of the composite samples in tensile mode of loading. A 5N static tensile load and displacement amplitude of 16 μm at a frequency of 1 Hz were applied. Nine measurements for each sample were made and the average values are reported here. Tensile stress-strain curves were generated using an electro-mechanical universal testing machine with specially designed flat-ended fixtures were machined in order the grip the specimens

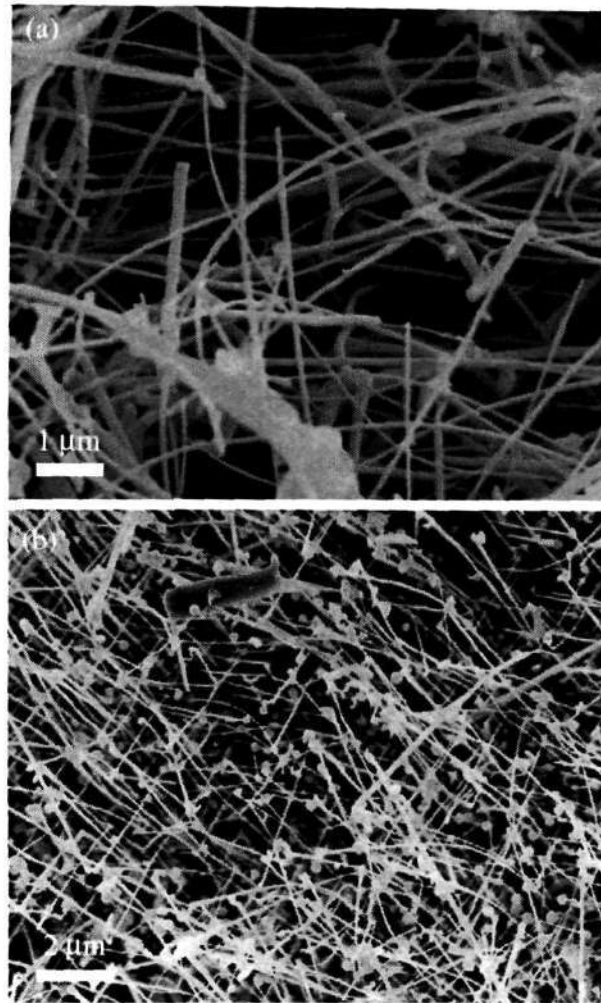


Figure 7.1: SEM images of (a) SiC and (b) Al₂O₃ NWs that were used for producing the PVA-matrix composites.

carefully. All the samples were tested for failure under displacement control with a prescribed displacement rate of 1.5 mm min^{-1} . Fractography of the tested samples were carried out using SIRION field emission scanning electron microscope.

7.3 Results and Discussion

Representative SEM images of the SiC and Al₂O₃ NWs used for producing the composites are shown in Figure 7.1. The nanowires have diameters in the

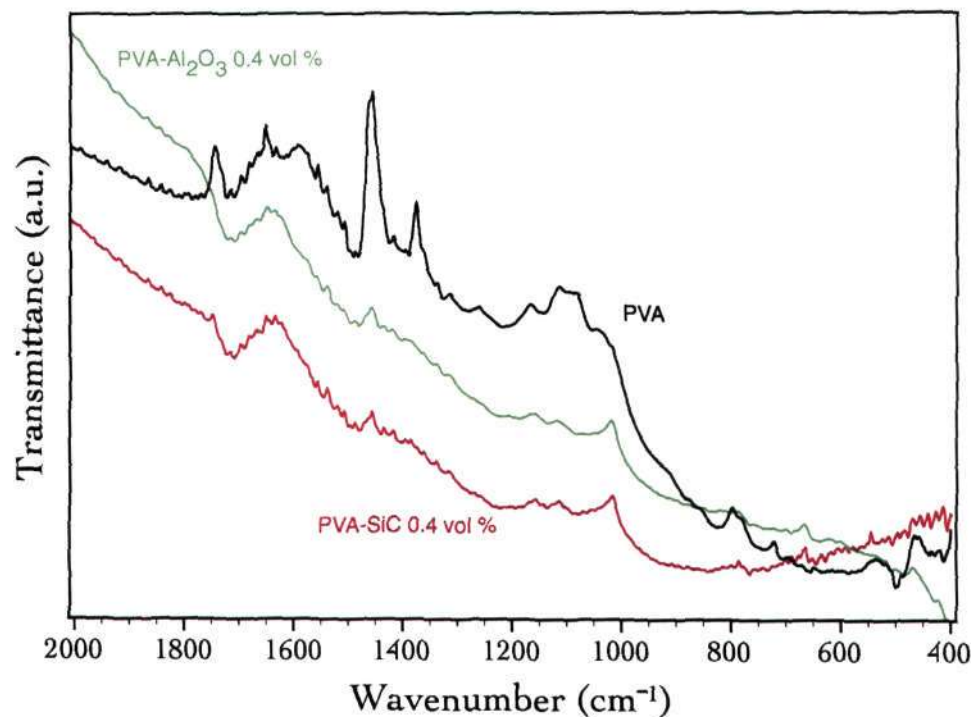


Figure 7.2: Infrared spectra of PVA and NW composites. Notice the variation in intensity of the 1140 cm^{-1} band relative to that of the 1425 cm^{-1} band.

90-150 nm range with lengths extending to tens of microns. The nanowires were single-crystalline, the growth direction of SiC NWs being $\langle 111 \rangle$ and that of Al₂O₃ NWs forming a 35° acute angle with $\langle 104 \rangle$ [10, 11].

The 1140 cm^{-1} band of PVA in the infrared spectrum is known to be sensitive to the crystallinity [13, 14]. Figure 7.2 shows the IR spectra of PVA and 0.4 vol.% NW reinforced PVA composites. The spectrum of PVA agrees with that reported in the literature [13, 14]. In the NW composites, we observe an increase in the relative intensity of the 1140 cm^{-1} band with respect to the 1425 cm^{-1} band. The observation suggests an increase in the degree of crystallinity of PVA on addition of the NWs.

Quantitative information about the change in polymer crystallinity, χ , due the addition of nanowires was obtained through DSC. Figure 7.3 (a) shows the thermograms of PVA as well as those of the composites, focusing on the broad endothermic peak due to melting centered around 225°C . The

Sample	Degree of crystallinity (%)	Elastic modulus, E (GPa) (% increase)	Lower and upper bounds for E (GPa)	Tensile strength, σ_U (MPa) (% increase)
PVA	33.9	3.2 ± 0.21	-	72.7 ± 3.4
+ SiC	34.5	3.76 ± 0.21 (17.5)	3.2-4.39	110.6 ± 4.9 (52.1)
NW (0.2)	34.8	4.58 ± 0.07 (43.1)	3.2-5.59	119.2 ± 3.2 (64.0)
+ SiC	35.0	6.08 ± 0.21 (90.0)	3.2-7.97	123.1 ± 4.0 (69.3)
NW (0.8)	38.4	5.06 ± 0.29 (58.1)	3.2-4.94	123.8 ± 6.7 (70.3)
+ Al ₂ O ₃				
NW (0.4)				

Table 7.1: Summary of the various properties of the nanocomposites

peak becomes narrower as the concentration of nanowires in the composite increases. From these scans, χ was calculated as equal to $(\Delta H/\Delta H_C)$, where ΔH is the heat required to melt 1g of dry sample (obtained by integrating the area under the endothermic peak between 190 and 240 °C) and ΔH_C is the standard enthalpy for 100% crystalline PVA ($\Delta H_C = 138.6 \text{ Jg}^{-1}$ [14]). The χ values, normalized with respect to the actual PVA content in the samples, are listed in Table 7.1. Figure 7.3 (b) shows the variation of χ with the volume fraction of the NWs, V_f . For the SiC NW composite, χ appears to vary linearly with V_f . However, the variation is small (a maximum of 1.1% for the 0.8 vol.% SiC NW composite) and can be considered negligible. For the Al₂O₃ NW composite, on the other hand, 0.4 vol.% addition of the nanowires leads to a 4.5% increase in χ , which is significant. Experimental results obtained from the dynamical mechanical analysis (DMA) and tensile testing is summarized in Table 7.1. There is a significant increase in E (up to 90%) even with a relatively small addition (0.8 vol.%) of NWs. In the case of SiC NWs, the variation of E with V_f is linear (Figure 7.4). The Al₂O₃ NW composite exhibits a 10% higher E than the SiC NW composite with the same amount of reinforcement (0.4 vol.%).

Figure 7.5 (a) shows representative tensile stress vs. strain (σ vs ϵ),

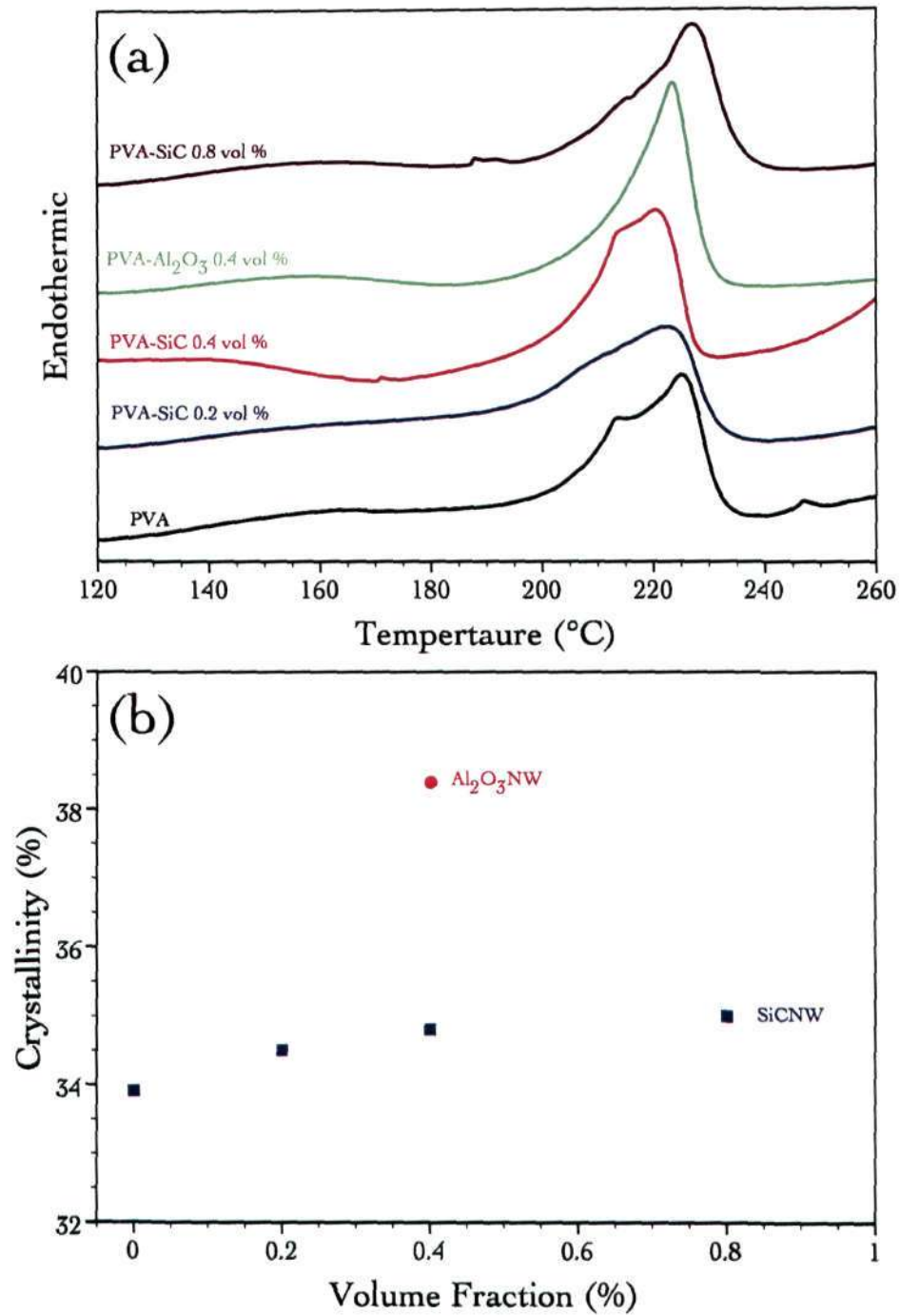


Figure 7.3: (a) DSC scans of PVA and NW composites showing the crystallization peak in the temperature range of 200 – 240 °C. (b) Variation of the degree of crystallinity of PVA, as a function of the NW volume fraction.

curves obtained with blank PVA as well as the composites with various V_f . With increasing V_f , a significant increase in the yield strength occurs. However, an estimation of the yield strengths from these plots is difficult due to lack of accurate strain measurement (which needs either mounting of an extensometer or a strain gauge on the sample, both of which are difficult due to the thin and highly compliant samples). Since the peak in the load appears immediately after yielding, the ultimate tensile strength, σ_U , was used as the metric that captures the strengthening changes due to the addition of the NWs. It is seen from Figure 7.5 (a) that for PVA alone, yielding and maximum load occurs almost simultaneously, with the material sustaining the same stress level for prolonged straining. Essentially, blank PVA behaves like an elastic-perfectly plastic solid. While the composites exhibit higher strengths, a significant strain softening is seen immediately after the peak in the load. Localization also sets in rather quickly, vis-a-vis blank PVA, and hence the composites exhibit much lower ductility. Thus the 0.4 vol.% Al_2O_3 and the 0.8 vol.% SiC NW composites show near-zero ductility, fracturing immediately after yielding.

The variation of σ_U with V_f shown in Figure 7.5 (b) reveals that σ_U reaches a plateau after an initial steep rise, in the case of SiC NW reinforced composite. For the same amount of V_f (0.4 vol.%), the Al_2O_3 NW composite has a similar strength (within experimental scatter) as that of the SiC NW composite. This is in contrast to that observed in E, where a clear 10% difference was noted. An equation of the type,

$$\sigma_U = \sigma_1 - \sigma_2 \exp[-V_f/V_0] \quad (7.1)$$

describes the SiC NW data exceptionally well with an R value (that indicates the goodness of fit) of 0.9998. The fit gives 122.96 ± 0.69 MPa, 50.22 ± 0.98 MPa and $0.145 \pm 0.008\%$ for σ_1 , σ_2 and V_0 , respectively. We discuss the

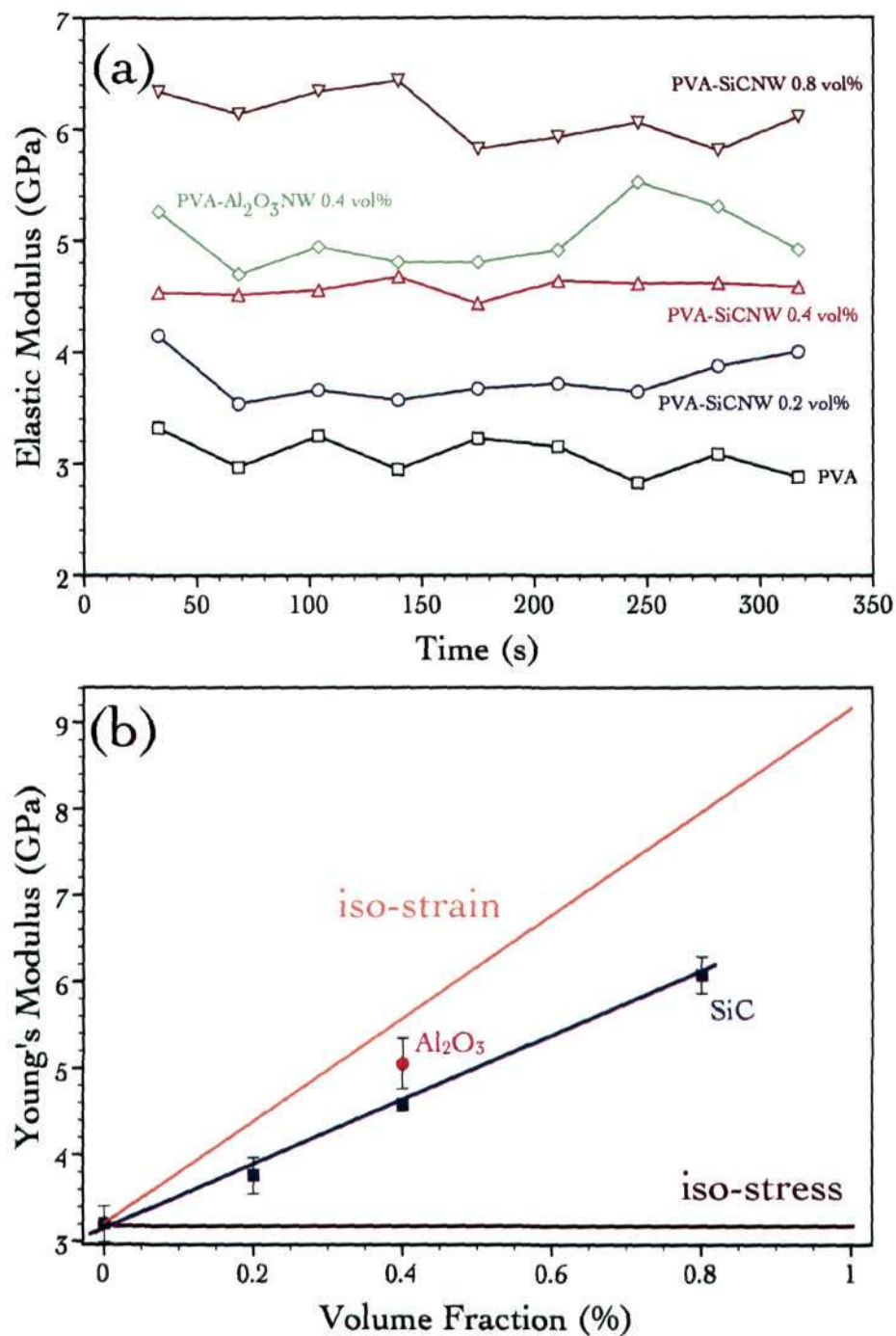


Figure 7.4: (a) Young's modulus as a function of time, a total of 9 measurements were made for each sample and (b) Variation of elastic modulus, E (measured with the DMA technique), as a function of the NW volume fraction, V_f . The upper- and lower-bound predictions are also plotted.

implications of this fit later in this section.

Typical SEM images obtained from the fracture surfaces of tensile-tested samples are shown in Figures 7.6 and 7.7 for the SiC and Al₂O₃ NW composites, respectively. Fracture surfaces of the matrix (PVA) are generally featureless (even at high resolution), as typified by the backgrounds in Figures 7.6 (a) and 7.7 (a). These figures also show extensive pull-out of the NWs from the matrix, with pull-out lengths reaching several micrometers (going up to 10 μm in certain cases).

Furthermore, good adhesion between the NWs and the matrix is illustrated by the pulling of the base of the matrix revealed in Figures 7.6 (b) and 7.7 (b). In the case of the SiC NW composites, the debonding appears to occur at the NW/matrix interface as reflected by the rather clean appearance of the SiC NWs as shown in Figure 7.6 (b). In contrast, the pulled-out Al₂O₃ NWs appear to be coated with the polymer. This can be seen in the inset in Figure 7.7 (a) as well as from the corrugated nature of the pulled-out NW (Figure 7.7 (b)). In SiC and Al₂O₃ NW composites, holes in the matrix surrounding the broken NWs are seen (see the base of the NW in Figure 7.6 (a) and also the inset in Figure 7.7 (b)). Qualitatively, these holes are much more pronounced in the case of Al₂O₃ NW composites. It is likely that these holes are due to the recession of the stretched matrix (due to the pull-out of the NWs) that eventually debonds after reaching a critical shear strain. Visual observations of the tensile-tested samples show a square pattern, corresponding to shear banding of the PVA. Such a shear-band pattern obtained from the 0.4 vol% SiC NW reinforced composite is shown in Figure 7.8. The shear-band morphology is found generally to diminish with increasing V_f . In the case of 0.8 vol% SiC and 0.4 vol% Al₂O₃ NW composites, with near-zero ductility, the shear-band pattern is absent.

A significant observation in the present study is the marked increase in

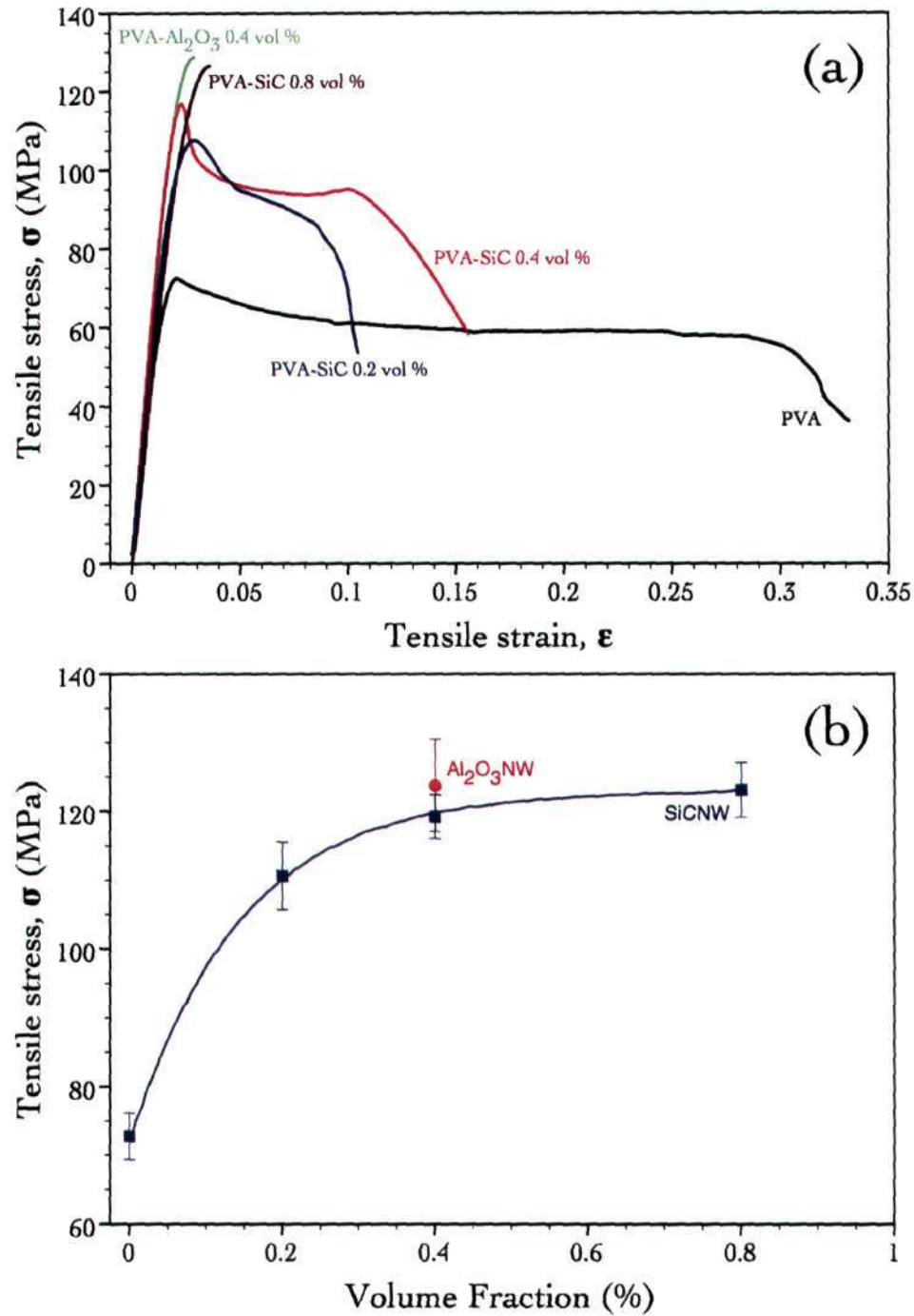


Figure 7.5: (a) Tensile stress-strain curves of PVA and NW composites, showing an increase in the ultimate tensile strength and reduction in ductility with increasing NW volume fraction. (b) Variation of tensile stress as function of nanowire volume fraction. The solid line represents the least-square fit to the equation (7.1).

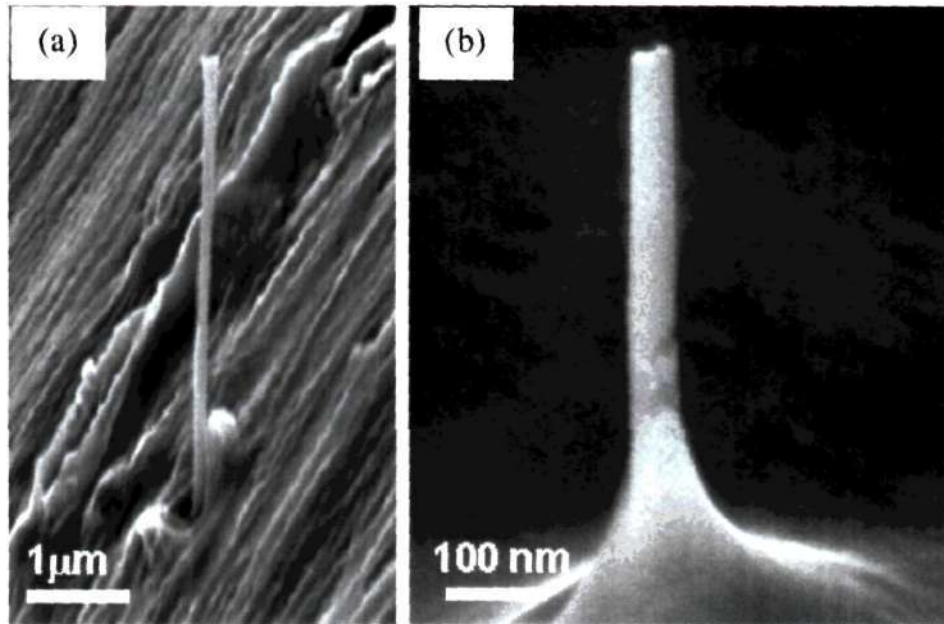


Figure 7.6: Field emission ESEM images obtained from the fractured PVA-SiC NW (0.8 vol%) composite showing pull-out of the nanowires as well as stretching of the matrix along with the nanowire.

the E value, even with relatively small additions of the inorganic NWs. This is to be compared with the report of Zhang *et al.* [9] who find that the elastic modulus of the PVA/PVP/SDS polymer increases from 2.5 to 4.0 GPa upon the addition of 5 wt% SWNTs. With the multi-walled carbon nanotubes (MWNTs), a linear increase in E with V_f of the MWNTs has been reported by Coleman *et al.* [6]. With a 0.6 vol% addition of MWNTs, the PVA (nearly noncrystalline) modulus was reported to increase from 1.92 to 7.04 GPa. Clearly, the inorganic NWs are significantly better than the SWNTs and are comparable to the MWNTs in their stiffening effect. The upper and lower bounds of the elastic moduli of the composites, E , can be written in terms of a simple rule-of mixtures given below (derived by imposing iso-strain and iso-stress conditions, respectively):

$$E = V_f E_f + (1 - V_f) E_m \quad (7.2)$$

$$E = E_f E_m / (V_f E_f + (1 - V_f) E_m) \quad (7.3)$$

Here, E_f and E_m are the moduli of the NW and matrix, respectively. Equation (7.2) is applicable when the NWs are aligned perpendicular to the loading direction whereas equation (7.3) is for NWs parallel to the loading direction. The above equations can predict E only for the case where the NWs are continuous throughout the composite. By taking E_f to be 600 GPa for the SiC NWs, corresponding to the bulk single-crystalline modulus of SiC [185] and 3.2 GPa for unreinforced PVA, the upper and lower bounds derived from equations (7.1) and (7.2) are plotted in Figure 7.4 (b). We see that the E data of the composites are closer to the upper bound. In the case of the Al_2O_3 NW composite, the measured E is higher (see table 1) than the upper bound predicted using 440 GPa for the elastic modulus of Al_2O_3 [15]. This could be due to the relatively large increase in χ in this case.

Considering that the concentration of the reinforcement phase is small (0.8 vol% at the maximum) and that the NWs are randomly dispersed through the matrix one would expect the E values of the composites to be closer to the lower bound, as the matrix deformation dominates the overall response of the composite. In contrast, a near doubling of E with only 0.8% loading of SiC NWs is observed. There can be several possible reasons for this large increase as detailed below.

- Large aspect ratio: Because the reinforcements are nanosized, the large aspect ratio (length/diameter) could make the composite behave like a continuous fibre composite. This scenario is unlikely as the aspect ratios of the NWs used are ~ 100 -200, which are lower than the value of ~ 1000 or so for a transition between short fibre reinforced composite behavior and the long-fibre reinforced one [15]. The specimen dimensions are also much larger than the NW dimensions. The anomalous increase from the relatively smaller sized specimens is ruled out.

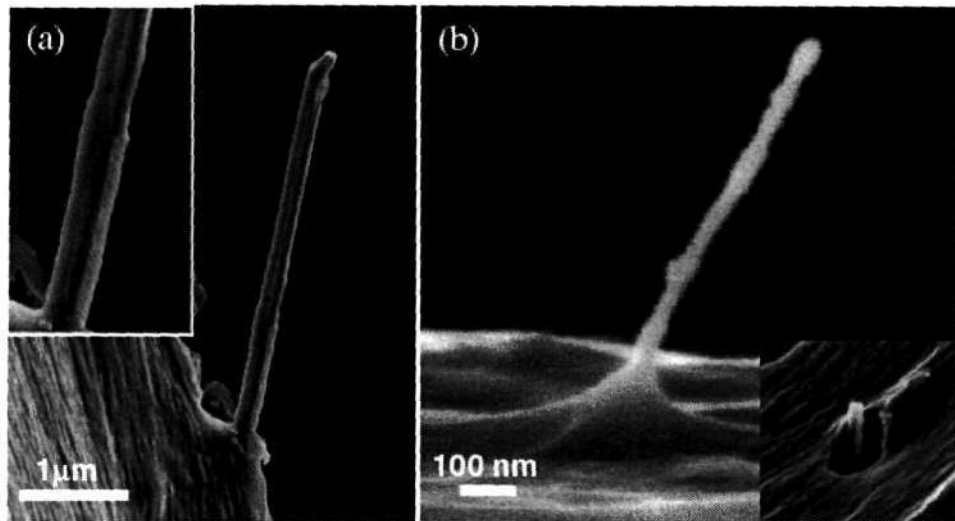


Figure 7.7: Field emission SEM images obtained from the fractured PVA- Al_2O_3 NW (0.4 vol%) composite showing pulled-out nanowires. The inset in (b) shows the formation of a hole around the nanowire, indicating retraction of the stretched and debonded matrix material.

- High surface/volume ratio: Because of their small sizes, nanostructured materials have high surface to volume ratios, which affect not only the functional properties but also the mechanical properties such as Miller and Shenoy [16] have investigated the size-dependent elastic properties of nanosized structural elements through continuum modeling that takes the ratio of surface to volume elastic moduli into consideration. Direct atomistic simulations by them on Al and Si nanostructures suggest that the elastic modulus is sensitive to the size only at very small length scales, typically below 10-15 nm. For sizes larger than this, bulk values are obtained asymptotically. The nanowires used by us are 90-150 nm in diameter. Therefore, the surface to volume ratio is unlikely to enhance the elastic modulus of the nanowires. In fact, the E value extracted by fitting equation (7.1) through the SiC NW data in Figure 7.4 (b), with E_f as an independent variable, gives E_f as 378.5 GPa, which is close to the E value reported for bulk sintered SiC [185].

- **In-plane alignment of the fibres:** Due to the very nature of the technique used for processing the NW composites, in-plane alignment of the NWs is a realistic possibility. From the Krenchel theory of short-fibre reinforcements [17], the orientation and length effects can be incorporated using an efficiency factor to evaluate E ,

$$E = KV_f E_f + (1 - V_f)E_m \quad (7.4)$$

where K is the Krenchel efficiency factor, which is equal to $3/8$ for a random planar arrangement of short fibres. The elastic modulus of the SiC NWs determined by fitting the above equation to the experimental data is ~ 1 TPa, which is significantly higher than that of theoretical modulus of 600 GPa for (111) oriented SiC NWs [185]. It is interesting to note that similar physically inadmissible values have been obtained by Coleman *et al.* [6] in the case of MWNT reinforced composites.

- **Inducement of crystallization of the matrix by the NWs:** The NWs act as nucleation sites for the growth of polymer crystals. For the SiC NW composites, the increase in χ is very small and hence NW induced crystallization is ruled out as accounting for the marked changes in E values of the SiC NW composites. For the Al_2O_3 NW reinforced composite, on the other hand, the oxide surface seems to be more favorable for nucleation and growth of the polymer crystals, as a large increase in χ was observed in this case. This, in turn, can be attributed to the E value that is higher than the upper-bound value (predicted using the iso-strain analysis) of E in this composite (see table 1). It therefore appears that surface functionalization can be used to improve the interaction between the polymer and the nanowires and hence the mechanical properties.

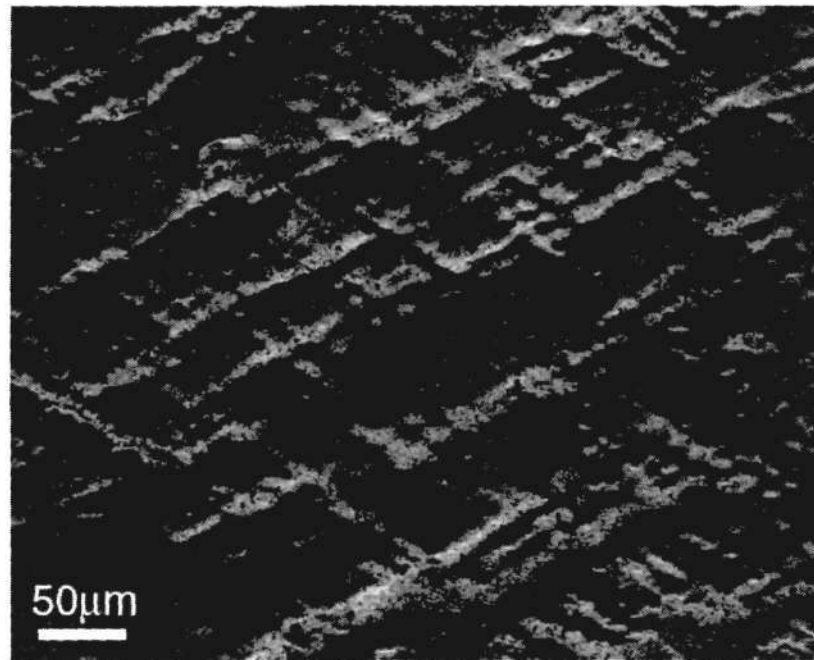


Figure 7.8: Optical micrograph of the deformed PVA-SiC NWs (0.4 vol%) showing shear-band induced deformation.

From the preceding discussion, it can be summarized that none of the above factors considered cannot can alone account for the marked increase in the stiffness of the semi-crystalline PVA. It may be that an optimum combination of these factors results in the high values of E in the composites. It is also possible that there are other possible causes, which we have not taken into account.

Strength enhancement with the addition of NWs to PVA is also marked. Similar to the stiffness, SWNTs do not appear to cause such a significant strengthening rate (see Zhang *et al.* [9] for example) whereas MWNTs do indeed have a similar strengthening effect [6] as that of the inorganic NWs. Small changes in the crystallinity of the polymer can have pronounced effects on the strength. If the interface debonds relatively easily, efficient load transfer cannot take place and hence composites tend to have a low strength. In contrast, high shear strength of the interface means that the reinforcement

phase carries considerably more load, leading to superior strength of the composites. The NW surface induced crystallization means a strong matrix/NW interface (in agreement with the stretching of the matrix by the NWs, shown in Figures 7 (b) and 8 (b)). Effective load transfer across the interface leads to considerable strengthening of the composite. Clearly, MWNTs and inorganic NWs (employed in this study) appear to favor load transfer.

An important observation made in the present study is that σ_U appears to attain a plateau, after an initial steep rise (Figure 7.5 (b)), with equation (7.1) capturing the experimental trends well. In the limit, $V_f = 0$, equation (7.1) gives $\sigma_U = (\sigma_1 - \sigma_2)$, the strength of the blank PVA. Differentiation of equation (7.1) with respect to V_f gives the rate of strengthening. The highest rate of strengthening is obtained in the limit $V_f \rightarrow 0$ and is equal to σ_2/V_0 . From the extracted values (by fitting equation (7.1) into the σ_U versus V_f data), $\sigma_2/V_0 \sim 34.6$ GPa. This should, in principle, scale with the strength of the SiC NWs. Wong *et al.* [185] reported 53.4 GPa as the strength of SiC NWs (of diameter 23 nm) measured in bending. The value obtained in our work reflects the strength of NW bundles, which tends to be lower than that a single NW [18]. Furthermore, size also plays a role in determining the strength of ceramics: increasing size typically means a lower strength [18]. Given these differences, the agreement between the strength of SiCNWs obtained in this work and that of Wong *et al.* [185] seems reasonable. Coleman *et al.* [6] report the rate of strengthening in the MWNT reinforced PVA to be 6.8 GPa, which is considerably lower than that found with the NWs. This could be due to the relatively smooth surfaces of MWNTs, which facilitate easy debonding whereas stress transfer is substantial in the case of inorganic NW reinforced composites. The flattening out of the σ_U versus V_f curve at higher V_f values implies that it may not be possible to increase the strength

of the polymer ad infinitum by adding more and more NWs. The micromechanical origin of this can be understood with the aid of equation (7.1) as well as Figure 7.8. The former suggests that some type of exhaustion process occurs with increasing V_f . Plastic deformation in glassy polymers can occur by crazing, which is common in glassy polymers such as PS, PMMA and PSF wherein polymer chains align perpendicular to the maximum principal stress. It can also occur by shear localization, wherein shear bands originate and propagate along the direction of maximum shear stress [19]. While crazing is considered as a brittle deformation mode, shear banding is considered to be ductile mode of deformation. In the semi-crystalline PVA polymer matrix examined in this study, it is apparent that shear localization is the predominant mode of deformation. The addition of NWs to the polymer appears to suppress the shear localization, with the NWs acting as obstacles for shear-band propagation, eventually exhausting it. In order to design NW reinforced composites that accommodate a higher vol% of NWs and hence higher strengths, it would be necessary to expose the effects of changing the matrix material and tailoring the interface properties.

7.4 Conclusions

In conclusion, the present study establishes the occurrence of a significant enhancement in the stiffness and the strength of semi-crystalline PVA due to the incorporation of SiC and Al₂O₃ nanowires. Experimental results show the enhancement of the mechanical properties to occur, even with a small vol.% addition of NWs. Thus, the elastic modulus E of the composites increases linearly with the volume fraction V_f , in accordance with the iso-strain rule-of-mixtures for predicting the composite E . The strength of the composites increases markedly initially and reaches a plateau. The initial hardening rate is commensurate with the strength of the SiC NWs. Shear localization

within the matrix and pull-out of the NWs are important micromechanisms of deformation and fracture. With increasing V_f , there is a reduced propensity for shear band mediated plastic deformation (possibly because of the NWs arresting the shear propagation), which leads to the loss in ductility.

7.5 References

1. Y. Huang and C. M. Lieber, *Pur. Appl. Chem.* **76**, 2051 (2004).
2. Q. Wan, Q. H. Li, Y. J. Chen, T. H. Wang, X. L. He, J. P. Li, and C. L. Lin, *Appl. Phys. Lett.* **84**, 3654 (2004).
3. E. W. Wong, P. E. Sheehan, and C. M. Lieber, *Science* **277**, 1971 (1997).
4. Z. L. Wang, Z. R. Dai, R. P. Gao, Z. G. Bai, and J. L. Gole, *Appl. Phys. Lett.* **77**, 3349 (2000).
5. W. Yang, H. Araki, C. Tang, S. Thaveethavorn, A. Kohyama, H. Suzuki, and T. Noda, *Adv. Mater.* **17**, 1519 (2005).
6. J. N. Coleman, M. Cadek, R. Blake, V. Nicolosi, K. P. Ryan, C. Belton, A. Fonseca, J. B. Nagy, Y. K. Gun'ko, and W. J. Blau, *Adv. Funct. Mater.* **14**, 791 (2004).
7. J. N. Coleman, U. Khan, and Y. K. Gun'ko, *Adv. Mater.* **18**, 689 (2006).
8. M. S. P. Shaffer and A. H. Windle, *Adv. Mater.* **11**, 937 (1999).
9. X. Zhang, T. Liu, T. V. Sreekumar, S. Kumar, V. C. Moore, R. H. Hauge, and R. E. Smalley, *Nano Lett.* **3**, 1285 (2003).
10. G. Gundiah, G. V. Madhav, A. Govindaraj, M. M. Seikh, and C. N. R. Rao, *J. Mater. Chem.* **12**, 1606 (2002).
11. G. Gundiah, F. L. Deepak, A. Govindaraj, and C. N. R. Rao, *Top. in Catal.* **24**, 137 (2003).
12. H. Tadokoro, J. Nagai, S. Seki, and I. Nitta, *Bull. Chem. Soc. Japan* **34**, 1504 (1961).
13. N. A. Pappas, *Makromol. Chem.* **176**, 3433 (1977).
14. N. A. Pappas and P. J. Hansen, *J. Appl. Polym. Sci.* **27**, 4787 (1982).
15. A. Kelly and N. H. MacMillan, *Strong Solids* (Clarendon, Oxford, 1986).
16. R. E. Miller and V. B. Shenoy, *Nanotechnology* **11**, 139 (2000).
17. H. Krenchel, *Fiber Reinforcement* (Akademisk Forlag, Copenhagen, Denmark, 1964).
18. C. Zweben and B. W. Rosen, *J. Mech. Phys. Solids* **18**, 189 (1970).
19. E. J. Kramer, *Adv. Polym. Sci.* **52-53**, 1 (1983).

Chapter 8

ELECTROCHEMICAL SUPERCAPACITORS BASED ON CARBON NANOSTRUCTURES

Summary¹

Carbon nanotubes, graphenes and polyaniline-SWNT nanocomposites have been investigated as electrode materials in electrochemical supercapacitors. Polyaniline-SWNT nanocomposites exhibit specific capacitance in between that of polyaniline and SWNTs. The graphene samples prepared by exfoliation of graphitic oxide and by the transformation of nanodiamond exhibit high specific capacitance in aq. H₂SO₄, the value reaching up to 117 F/g. By using an ionic liquid, the operating voltage has been extended to 3.5 V (instead of 1 V in the case of aq. H₂SO₄), the specific capacitance and energy density being 75 F/g and 31.9 WhKg⁻¹ respectively. This value of the energy density is one of the highest reported to date. The performance characteristics of graphenes are directly related to the surface area and are superior to those of carbon nanotubes.

8.1 Introduction

Electrochemical supercapacitors are passive and static electrical energy storage devices for applications requiring high power density such as energy back-up systems, consumer portable devices and electrical/hybrid automobiles [1,2]. In a electrochemical supercapacitor, electrical energy is stored by means of the charge held in the interfacial double layer at a porous carbon

¹A paper based on this study has been published in *J. Chem. Sci.* (2008)

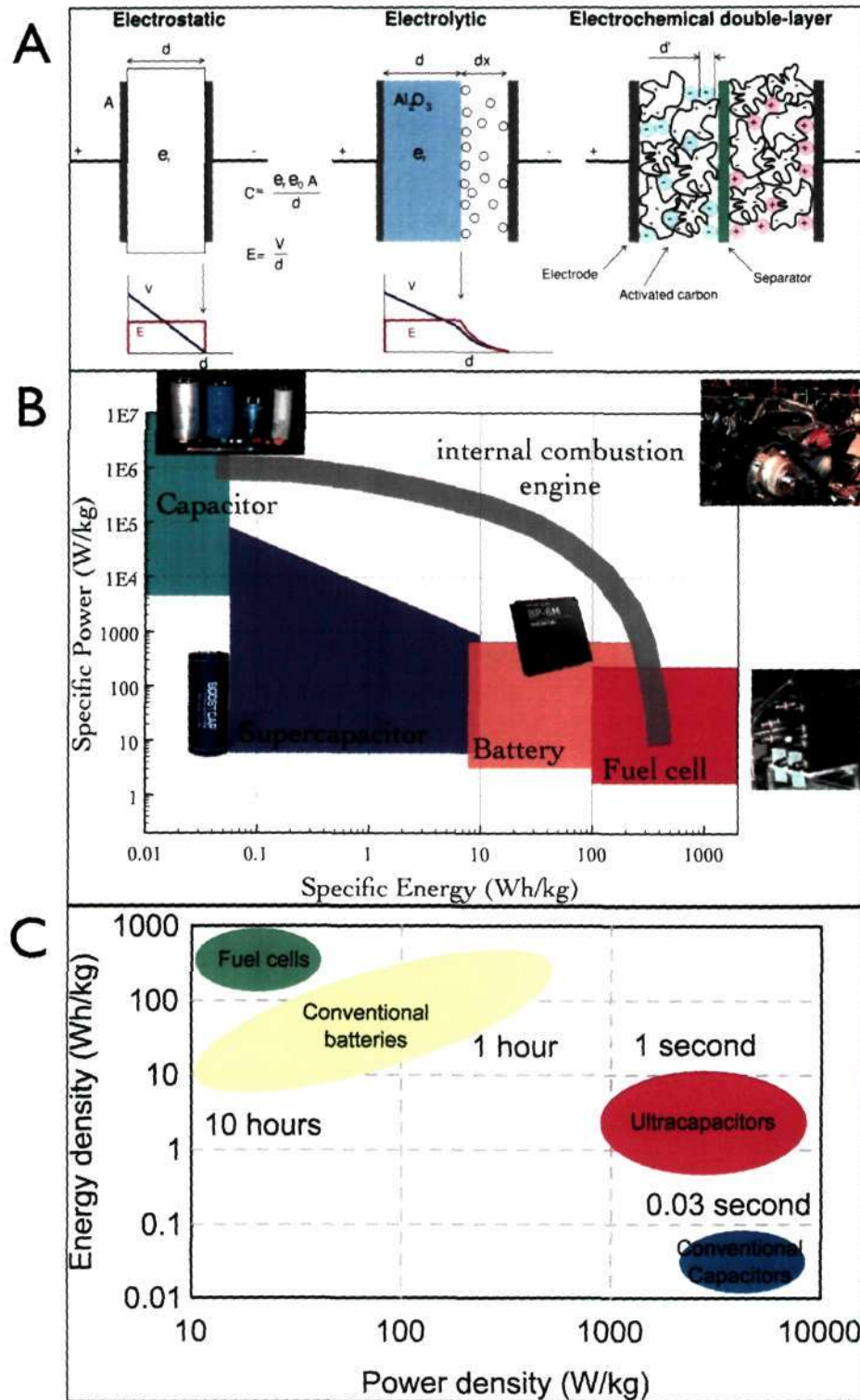


Figure 8.1: (A) Schematic diagram of electrostatic capacitors, electrolytic capacitors and electrochemical supercapacitors. (B) and (C) Sketch of Ragone plot for various energy storage and conversion devices. The indicated areas are rough guide lines.

material perfused with an aqueous electrolyte (as seen in Figure 8.1 (A)). A DOE ultracapacitor development program was initiated in 1989, and short term as well as long term goals were defined for 1998-2003 and after 2003, respectively. The EC was supposed to boost the battery or the fuel cell in the hybrid electric vehicle to provide the necessary power for acceleration, and additionally allow for recuperation of brake energy. The applications envisaged are principally boost components supporting batteries or replacing batteries primarily in electric vehicles. Electrochemical capacitors fill in the gap between batteries and conventional capacitors such as electrolytic capacitors or metallized film capacitors (see Figures 8.1 (B) and (C)). In terms of specific energy as well as in terms of specific power this gap covers several orders of magnitude. Batteries and low temperature fuel cells are typical low power devices whereas conventional capacitors may have a power density of $>10^6$ watts per dm^3 at very low energy density. Thus, electrochemical capacitors may improve battery performance in terms of power density or may improve capacitor performance in terms of energy density when combined with the respective device. In addition, electrochemical capacitors are expected to have a much longer cycle life than batteries because no or negligibly small chemical charge transfer reactions are involved. In Figure 8.2, the differences between electrochemical supercapacitors and batteries are outlined.

Carbon is a unique element almost suited for fabrication of electrochemical supercapacitors of the double-layer type. From an electrochemical point of view, carbon is relatively, though not entirely, unreactive and thus has a potential voltage range of 1.0 V in aqueous solution and 3.5 V in non-aqueous media. These supercapacitors are known as electrochemical double layer capacitors (EDLCs). In EDLCs, there is no electron transfer from the solution to the electrode. Electrochemical capacitors store the electric energy in an electrochemical double layer (Helmholtz Layer) formed at a solid/electrolyte

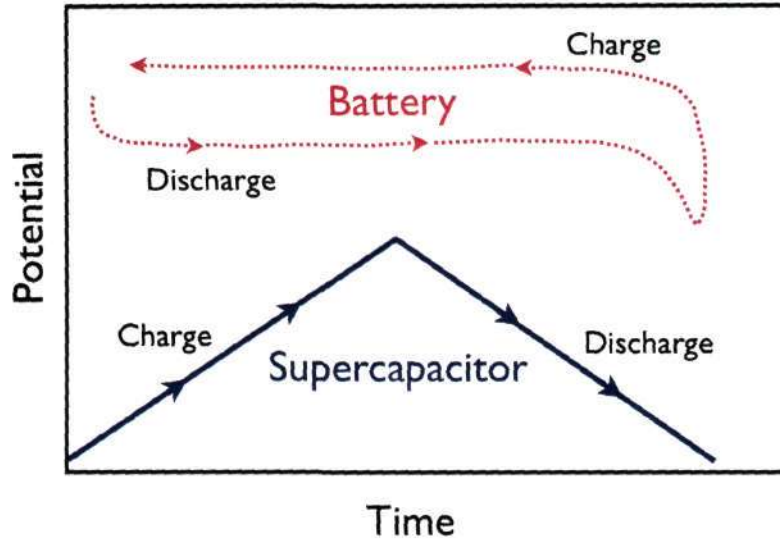


Figure 8.2: Differences between a battery and a supercapacitor: top panel shows the charge and discharge cycles of the two storage systems and table in the bottom outlines the primary differences.

interface. Positive and negative ionic charges within the electrolyte accumulate at the surface of the solid electrode and compensate for the electronic charge at the electrode surface. The thickness of the double layer depends on the concentration of the electrolyte and on the size of the ions and is in the order of 5-10 Å, for concentrated electrolytes. The double layer capacitance is about 10-20 $\mu\text{F}/\text{cm}^2$ for a smooth electrode in concentrated electrolyte solution and can be estimated according to equation:

$$C/A = \epsilon_0 \epsilon_r / d \quad (8.1)$$

assuming a relative dielectric constant of 10 for water in the double layer. d being the thickness of the double-layer with surface area A . The corresponding electric field in the electrochemical double layer is very high and assumes values of up to 10^6 V/cm easily. Compared to conventional capacitors where a total capacitance of pF and μ F is typical, the capacitance of and the energy density stored in the electrochemical double layer is rather high per se. In order to achieve a higher capacitance the electrode surface area is additionally increased by using porous electrodes with an extremely large internal effective surface. Combination of two such electrodes gives an electrochemical capacitor of rather high capacitance. Figure 8.1 (A) shows a schematic diagram of an electrochemical supercapacitor consisting of two high surface-area electrodes separated by a porous separator. The electrodes along with the separator is soaked with a suitable electrolyte.

The capacitance of a single electrode can be estimated by assuming a high surface area carbon with $1000 \text{ m}^2/\text{g}$ and a double layer capacitance of $10 \mu\text{F}/\text{cm}^2$. This leads to a specific capacitance of $100 \text{ F}/\text{g}$ for one electrode. For a capacitor two electrodes are needed with doubled weight and half the total capacitance ($1/C = 1/C_1 + 1/C_2$) resulting in $25 \text{ F}/\text{g}$ of active capacitor mass for this example. The difference between single electrode values and specifications given for the complete capacitor is of significant importance. Whenever specifications of an electrochemical supercapacitor are given, one should indicate whether the values correspond to single electrode measurement or are calculated for a complete capacitor. The difference between these two situations is a factor of four and therefore of significant importance. The maximum energy stored in such a capacitor is given by

$$W = CU_0^2/2 \quad (8.2)$$

With a cell voltage U_0 of 1 V (aqueous electrolyte) one obtains a specific

energy of about 3.5 Wh/kg of active mass. Using an organic electrolyte with a typical cell voltage of 2.3 V one obtains about 18 Wh/kg of active mass. These values are considerably lower than those obtained for available batteries but much higher than for conventional capacitors. It should be mentioned that the above values depend on the double layer capacitance, the specific surface area of the respective electrode material, the wetting behavior of the pores, and on the nominal cell voltage.

Supercapacitors have also been built using a different principle, wherein there is electron transfer between the electrode and the electrolyte, this capacitance is known as pseudocapacitance. Pseudocapacitance arises whenever, for thermodynamic reasons, there is some continuous dependence of charge, q , passed Faradiacally in oxidation or reduction, upon the electrode potential, Craig and co-workers have developed supercapacitors by adsorbing H or monolayers of the base metals like Pb, Bi, Cu at Pt or Au surfaces. Solid oxide redox systems like RuO_2 can also exhibit pseudocapacitance.

Porous carbon materials such as activated carbon [3, 4], xerogels [5], carbon nanotubes [6–9], mesoporous carbon [10] and carbide-derived carbons [11] have been investigated for use as electrodes in EDLCs. In the last few years, there has been great interest in graphene, which constitutes an entirely new class of carbon. Electrical characterization of single-layer graphene has been reported. [12, 13] We have investigated the use of graphene as electrode material in electrochemical supercapacitors. For this purpose, we have employed graphene prepared by three independent methods and compared their supercapacitor behaviour with aq. H_2SO_4 as the electrolyte. We have compared the performance of the graphene samples with that of single-walled carbon nanotubes (SWNTs), double-walled carbon nanotubes (DWNTs) and multi-walled carbon nanotubes (MWNTs). Furthermore, we have explored

the use of ionic liquids as electrolytes. Thus, by employing the ionic liquid, N-butyl-N-methylpyrrolidinium bis(trifluoromethanesulfonyl)imide (PYR₁₄TFSI), we have been able to extend the operating voltage up to 3.5 V compared to 1 V normally obtained with aq. H₂SO₄ [14]. The present study reveals that graphenes attain a specific capacitance as high as 117 F/g in aq. H₂SO₄. In the ionic liquid, a specific capacitance of 75 F/g is attained with an energy density of 31.9 WhKg⁻¹. We have also studied the electrochemical supercapacitors using polyaniline-SWNT nanocomposites as active layers.

8.2 Experimental Details

We have prepared graphene by three methods, which yield samples with different porosities and other characteristics. The first method involved thermal exfoliation of graphitic oxide [15]. In this method, graphitic oxide was prepared by reacting graphite (Aldrich, 15 μm) with concentrated nitric acid and sulphuric acid with potassium chlorate at room temperature for 5 days. Thermal exfoliation of graphitic oxide was carried out in a long quartz tube at 1050 °C. In the second method, graphene was obtained by heating nanodiamond at 1650 °C in a helium atmosphere [16]. The last method involved the decomposition of camphor over nickel nanoparticles [17]. The reaction was carried out in a two-stage furnace and the camphor was slowly sublimed from the first furnace to the second furnace held at 770 °C where the micron sized nickel particles were placed. MWNTs were synthesized using the arc discharge process and were purified by heating in air at 700 °C for one hour. SWNTs were prepared by the arc evaporation of Ni-Y catalyst impregnated graphite rods and were purified using hydrogen treatment (see Chapter 3). MWNTs were also prepared by ferrocene pyrolysis (see Chapter 2). Double-walled carbon nanotubes (DWNTs) were prepared by the pyrolysis of hydrocarbons over Co/Mo-MgO catalyst. Polyaniline-SWNTs

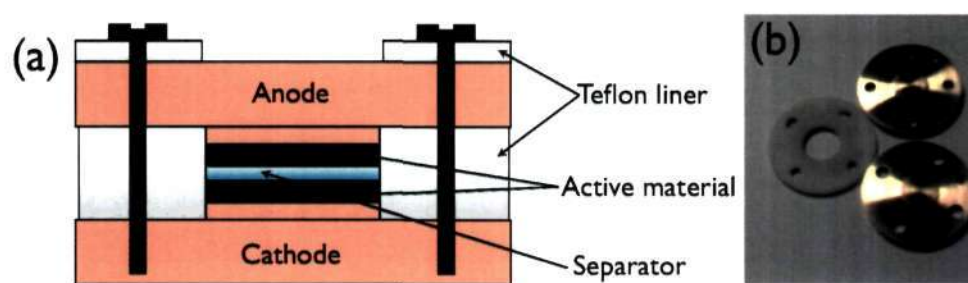


Figure 8.3: (a) Schematic diagram and (b) photograph of the electrochemical cell used for testing.

nanocomposites were prepared by the in-situ polymerization of aniline in the presence of SWNTs. Nanocomposites with different molar ratios of aniline and SWNTs have been prepared for the study.

The graphene samples were characterized using transmission electron microscopy (TEM), atomic force microscopy (AFM), X-ray diffraction (XRD) and Raman spectroscopy. TEM images were obtained with a JEOL JEM 3010 instrument fitted with a Gatan CCD camera operating at an accelerating voltage of 300 kV. AFM measurements were performed using CP 2 atomic force microscope and Raman spectroscopic characterization was carried out using JobinYvon LabRam HR spectrometer with 632 nm HeNe laser. Surface area measurements were carried out in a QuantaChrome Autosorb-1 instrument. The graphene electrodes and supercapacitor cells were fabricated following Conway [2] and the measurements were carried out with a two-electrode configuration (see Figure 8.3), the mass of each electrode being 5 mg in the case of SWNT, MWNT, DG and CG while it was 3 mg for EG. Electrochemical measurements were performed using a PG262A potentiostat/galvanostat, (Technoscience Ltd, Bangalore, India). Experiments with $\text{PYR}_{14}\text{TFSI}$ -based supercapacitors were carried out at 60 °C in a mBraun glove box keeping the oxygen and water levels at less than 0.1 ppm. The ionic liquid was dried at 80 °C under vacuum for a day prior to the experiment. We have performed cyclic voltammetry as well as constant current

charging and discharging to characterize the two-electrode supercapacitor cells with the different graphenes and electrolytes. Specific capacitance was calculated using the following formulae: In cyclic voltammetry, $C_{CV} = 2(i_+ - i_-)/(m \times \text{scan rate})$, where i_+ and i_- are maximum current in the positive scan and negative scan respectively and m is the mass of electrode. In constant current charging and discharging, $C_{CD} = 2(i)/(s \times m)$, i is the constant current applied and s is the slope of the discharge curve. The energy density is given as $E = CV^2$, where C is the capacitance taking into account both the electrode masses and V is the operational voltage.

8.3 Results and Discussion

8.3.1 Carbon Nanotubes and Graphenes

In Figure 8.4 (a) and (b), we show the TEM images of graphene samples prepared by exfoliation of graphitic oxide (EG) and transformation of nanodiamond (DG) respectively. There is some disorder in the graphene sheets of EG while there are nanoparticle-like features in the case of DG. The AFM image profiles of EG and DG show that they consist of 3-6 graphene layers (see Figure 8.4 (c) and (d)). The graphene prepared from camphor (CG) comprises a considerably large number of layers accounting for the sharp graphitic reflections in powder x-ray diffraction pattern, unlike the EG and DG samples. The Brunauer-Emmett-Teller (BET) surface area of EG and DG were 925 and 520 m^2/g respectively. The average pore size was 3 nm in the case of EG and DG was microporous. CG exhibited type-II adsorption behavior with a BET surface area of m^2/g . The ratio of the intensities of the Raman G and 2D bands varies in the order $\text{CG} > \text{EG} > \text{DG}$ and the in-plane crystallite sizes also varies in the same order (see Table 1). From the data in Table 1, we conclude that EG and DG have good graphene characteristics.

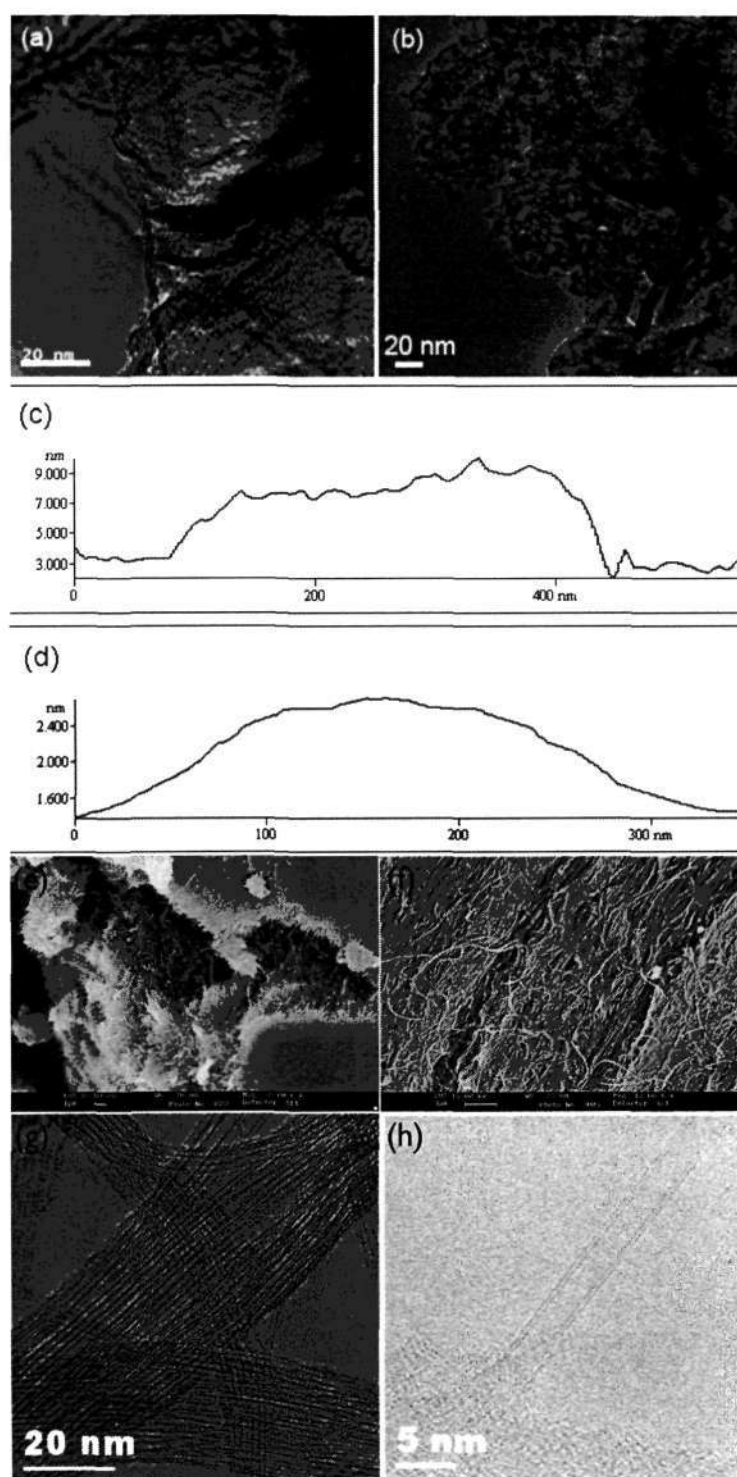


Figure 8.4: TEM images of (a) graphene obtained by the thermal exfoliation of graphitic oxide (EG). (b) thermal conversion of nanodiamond to graphene (DG). (c) and (d) AFM height profiles of EG and DG respectively. (e) and (f) SEM images of arc-discharge MWNTs and ferrocene pyrolysis MWNTs obtained by nebulized spray pyrolysis respectively. (g) and (h) TEM images of SWNTs obtained by the arc-discharge process and DWNTs obtained by CVD.

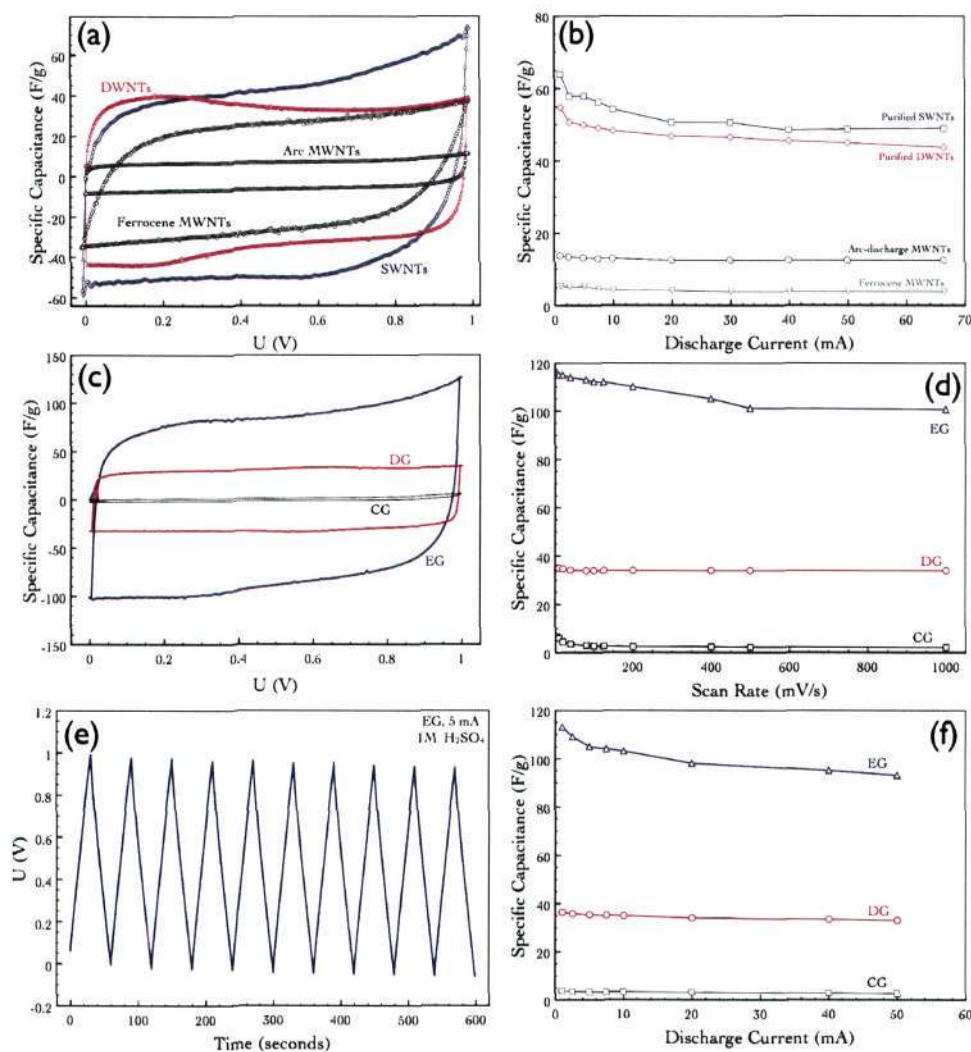


Figure 8.5: Voltammetry characteristics of a capacitor built from carbon nanotube electrodes (5 mg each) at a scan rate of 100 mV/s using (a) aqueous H_2SO_4 (1 M) and (b) specific capacitance as a function of discharge current. Voltammetry characteristics of a capacitor built from graphene electrodes (5 mg each) at a scan rate of 100 mV/s using (c) aqueous H_2SO_4 (1 M) and (d) specific capacitance as a function of scan rate. (e) Typical charging and discharging curves of EG at 5 mA and (f) specific capacitance as a function of discharge current.

Sample	Number of Layers	Crystallite Size (nm)	L_a	Surface (m^2/g)
CG	> 20	6.1	10	46
EG	3-6	4.7	6	925
DG	3-6	5.0	4	520

Table 8.1: Characteristics of the graphene samples - number of layers, crystallite size obtained from X-ray diffraction and in-plane crystallinity (L_a) from Raman spectroscopy and BET surface area

In Figure 8.5 (a), we show cyclic voltamograms (CVs) at a scan rate of 100 mV/s for capacitors built using graphene as electrodes and 1M H_2SO_4 as electrolyte. All the supercapacitors exhibit good box-like CVs with EG exhibiting the highest specific capacitance of 117 F/g. The specific capacitance decreases slightly as the scan rate is increased as shown in Figure 8.5 (b), but the capacitance remains at 100 F/g at a scan rate of 1000 mV/s, retaining the box-like characteristics. DG exhibits a capacitance of 35 F/g in 1M H_2SO_4 with no change in the specific capacitance even at higher scan rates or discharge currents as seen in Figure 8.5 (d). CG exhibits a very low specific capacitance of 6 F/g.

The results obtained from cyclic voltammetry were confirmed by charge-discharge experiments. In Figure 8.5 (c), we show typical charge-discharge curves at 5 mA current for a supercapacitor built using EG. The charging and discharging curves are linear with no loss due to series resistance. The specific capacitance of EG decreases slightly as the discharge current is increased from 1 mA to 50 mA, while the other graphene samples exhibited no such dependence (Figure 8.5 (d)). There is a significant correlation between the electrochemical results and the AFM or the Raman observations. As the number of layers in the graphene decreases, the value of the surface area and specific capacitance increases. The graphene prepared by exfoliation exhibits a capacitance of $12.4 \text{ F}/\text{cm}^2$ while the graphene prepared by the nanodiamond route exhibits a capacitance of $6.7 \text{ F}/\text{cm}^2$. The presence of surface functional groups in the EG sample is likely to give rise to some

psuedocapacitance.

We have carried out measurements on different types of carbon nanotubes for comparison. MWNTs as well as SWNTs produced by the arc-discharge process, MWNTs prepared by the nebulized spray pyrolysis of mesitylene and ferrocene and DWNTs prepared by chemical vapor deposition have been used for this purpose. In Figure 8.5 (e), we show typical cyclic voltammograms of supercapacitors fabricated using different carbon nanotubes as active material in aq. H_2SO_4 . The specific capacitance of SWNTs and MWNTs are 64 and 14 F/g respectively and are independent of the scan rate or discharge current as seen in Figure 8.5 (f). Ferrocene MWNTs exhibit a low specific capacitance of 5 F/g while DWNTs exhibit a capacitance of 55 F/g. Thus, EG exhibits the largest specific capacitance of 117 F/g in aq. H_2SO_4 , significantly greater than that observed with carbon nanotubes.

Encouraged by the results obtained using 1M H_2SO_4 as electrolyte we fabricated cells using the ionic liquid, N-butyl-N-methylpyrrolidinium bis(trifluoromethanesulfonyl)imide $\text{PYR}_{14}\text{TFSI}$ as the electrolyte. $\text{PYR}_{14}\text{TFSI}$ has a large electrochemical window (6.5 V) and typically yields an operating voltage of 3.5. We have investigated the EG and DG samples with this electrolyte as they showed promising results in our experiments with aq. H_2SO_4 . In Figure 8.6 (a), we show typical CVs of graphene- $\text{PYR}_{14}\text{TFSI}$ supercapacitors obtained at a scan rate of 100 mV/s. In $\text{PYR}_{14}\text{TFSI}$, specific capacitance values of 75 F/g and 40 F/g were obtained with EG and DG respectively. The specific capacitance depends significantly on the scan rate as the ionic liquid is highly viscous (Figure 8.6 (b)). The value of the maximum energy density stored using these capacitors are 31.9 and 17.0 WhKg^{-1} respectively for EG and DG. These are some of the highest values reported to date and are comparable to those of microporous carbons reported by Balducci *et al.* [18].

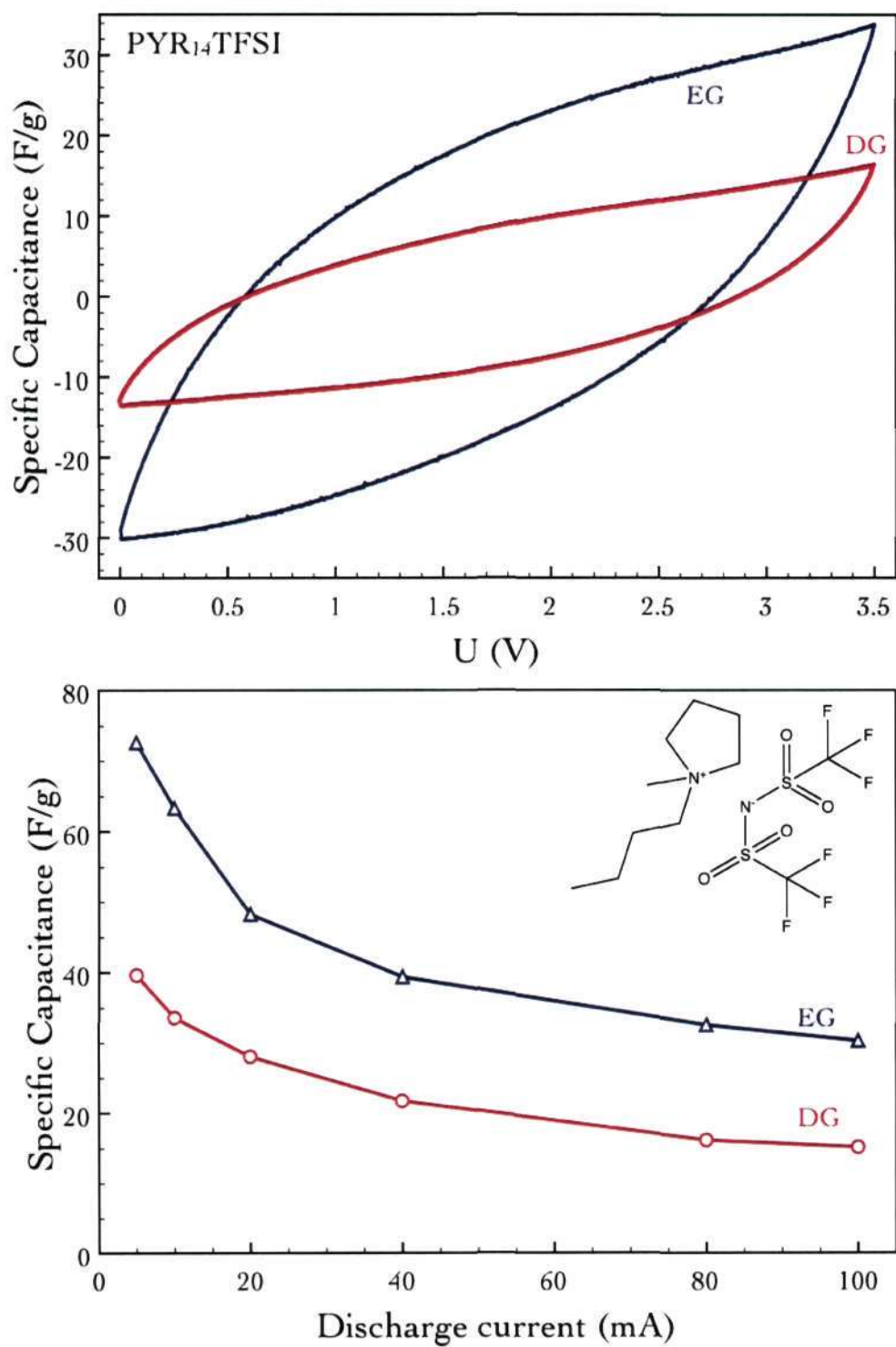


Figure 8.6: (a) Voltammetry characteristics of a capacitor built from graphene electrodes (5 mg each) at a scan rate of 100 mV/s using ionic liquid. (b) Specific capacitance as a function of scan rate using PYR₁₄TFSI. Inset in (b) shows the molecular structure of PYR₁₄TFSI.

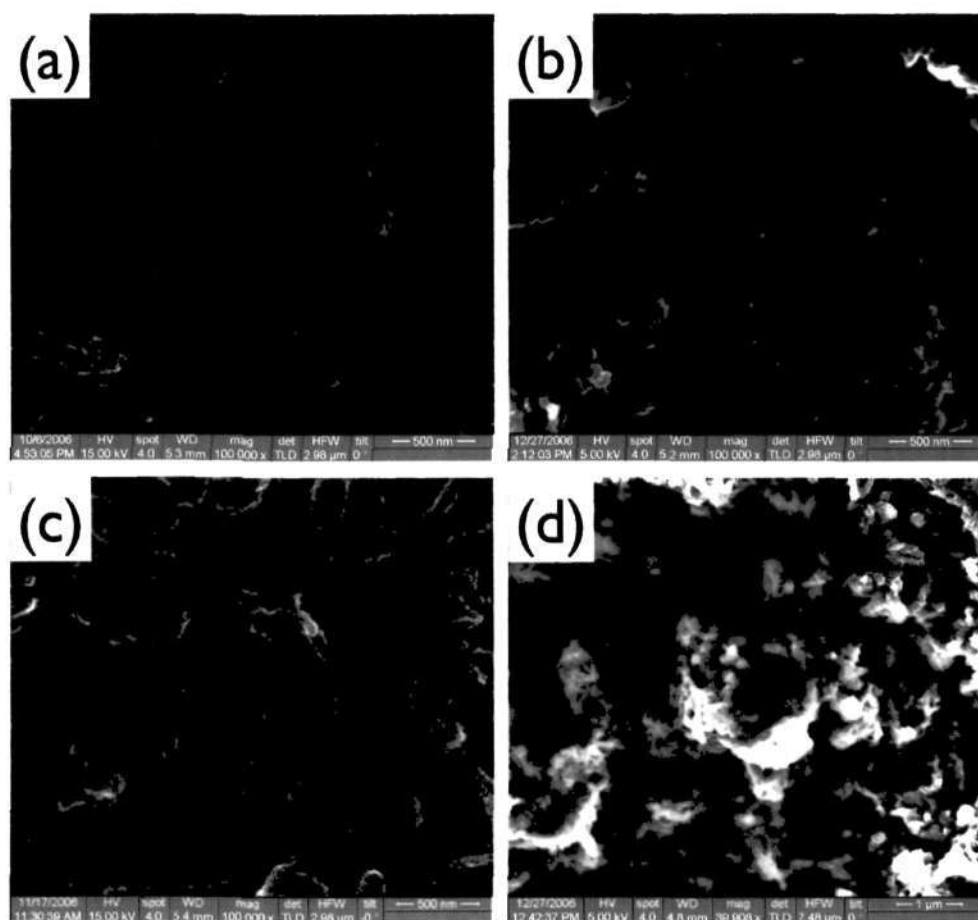


Figure 8.7: FESEM image of (a) SWNTs, (b) polyaniline-SWNT (2:1), (c) polyaniline-SWNT (1:2) and (d) polyaniline.

8.3.2 Polyaniline-SWNT nanocomposites

In Figure 8.7, we show the FESEM image of purified SWNTs, polyaniline-SWNT nanocomposites and pure polyaniline. The SWNTs are pure and contain negligible traces of impurities. The SWNTs are uniformly covered with polyaniline in the nanocomposites and pure polyaniline show fibrillar structure. In Figure 8.8, we show the electrochemical characteristics of supercapacitors based on polyaniline, polyaniline-SWNT nanocomposites and SWNTs with 1M H_2SO_4 electrolyte. Polyaniline has exhibits a large specific capacitance of 400 F/g with a lower operating voltage of 0.6 V. The specific capacitance of the nanocomposites lies in between that of polyaniline

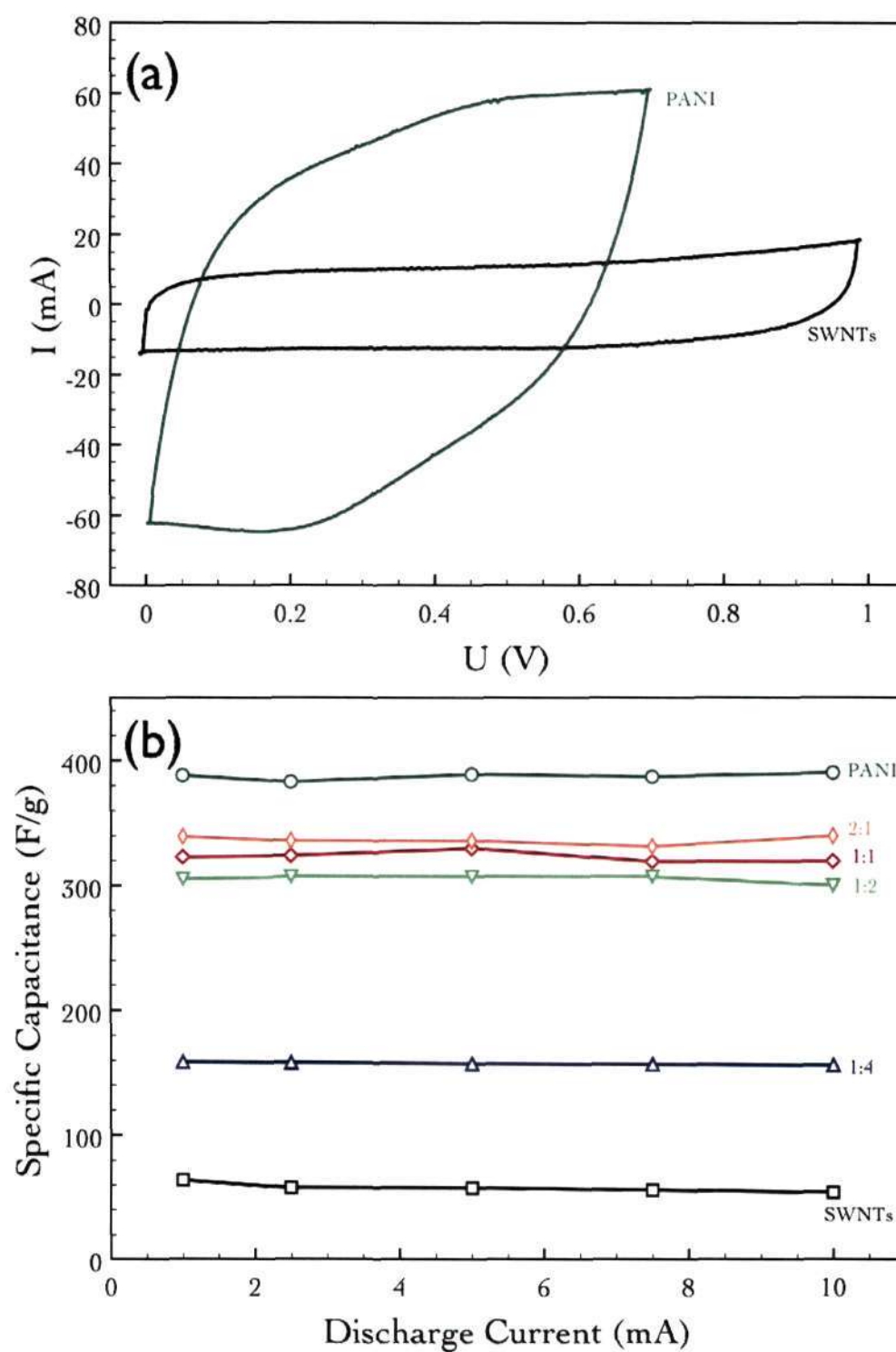


Figure 8.8: (a) Voltammetry characteristics of a capacitor built from PANI and SWNT electrodes at a scan rate of 100 mV/s using H_2SO_4 electrolyte. (b) Specific capacitance as a function of discharge current for different nanocomposites, PANI and SWNTs.

and SWNTs. There is a rapid increase in the specific capacitance and it saturates at molar ratio of 1:1.

8.4 Conclusions

In conclusion, polyaniline-SWNT nanocomposites exhibit specific capacitance in between that of polyaniline and SWNTs, when used as electrode materials in electrochemical supercapacitors. Graphenes act as good electrode materials for application in supercapacitors. The specific capacitance of the exfoliated graphene in the aqueous electrolyte is comparable to that obtained with activated carbons and superior to that of carbon nanotubes while value of the energy density of the graphene capacitors is one of the highest known to date. The supercapacitor characteristics are directly related to the number of layers and the associated surface area. It should be possible to improve the performance characteristics of graphene by modifying or improving the quality of the samples.

8.5 References

1. R. Kötz and M. Carlen, *Electrochim. Acta* **45**, 2483 (2000).
2. B. E. Conway, *Electrochemical Supercapacitors* (Kluwer Academic, Plenum, New York, 1999).
3. E. Frackowiak and F. Beguin, *Carbon* **39**, 937 (2001).
4. D. Qu and H. Shi, *J. Power Sources* **74**, 99 (1998).
5. S. T. Meyer, R. W. Pekala, and J. L. Kaschmitter, *J. Electrochem. Soc.* **140**, 446 (1993).
6. C. Niu, E. K. Sichel, R. Hoch, D. Moy, and H. Tennent, *Appl. Phys. Lett.* **70**, 1480 (1997).
7. E. Frackowiak, K. Metenier, V. Bartagna, and V. Beguin, *Appl. Phys. Lett.* **70**, 2421 (1997).
8. K. H. An, W. S. Kim, Y. S. Park, J. Moon, D. J. Bae, S. C. Lim, Y. S. Lee, and Y. H. Lee, *Adv. Funt. Mater.* **11**, 387 (2001).
9. C. Du, J. Yeh, and N. Pan, *Nanotechnology* **16**, 350 (2005).
10. S. Yoon, J. Lee, T. Hyeon, and S. M. Oh, *J. Electrochem. Soc.* **147**, 2507 (2000).
11. J. Chimola, G. Yushin, Y. Gogotsi, C. Portet, P. Simon, and P. L. Taberna, *Science* **313**, 1760 (2006).
12. K. S. Novoselov, A. K. Geim, S. V. Morozov, D. Jiang, Y. Zhang, S. V. Dubonos, I. V. Grigorieva, and A. A. Firsov, *Science* **306**, 666 (2004).
13. A. K. Geim and K. S. Novoselov, *Nat. Mater.* **6**, 183 (2007).
14. A. Balducci, W. A. Henderson, M. Mastragostino, S. Passerini, P. Simon, and F. Soavi, *Electrochim. Acta* **50**, 2233 (2005).
15. H. C. Sniepp, J. L. Li, M. J. McAllister, H. Sai, M. H. Alonso, D. H. Adamson, R. K. Prud'homme, R. Car, D. A. Saville, and I. A. Aksay, *J. Phys. Chem. B* **110**, 8535 (2006).
16. O. Andersson, B. L. V. Prasad, H. Sato, T. Enoki, Y. Hishiyama, Y. Kaburagi, M. Yoshikawa, and S. Bandow, *Phys. Rev. B* **58**, 16387 (1998).
17. P. R. Somani, S. P. Somani, and M. Umeno, *Chem. Phys. Lett.* **430**, 56 (2006).
18. A. Balducci, R. Dugas, P. L. Taberna, P. Simon, D. Plee, M. Mastragostino, and S. Passerini, *J. Power Sources* **165**, 922 (2007).

Other publications of the author

- B. Chitara, S. V. Bhat, S. R. C. Vivekchand, A. Gomathi and C. N. R. Rao, "White light sources based on composites of GaN nanocrystals with conducting polymers and nanophosphors", *Solid Stat. Commun.*, **147**, 409-413 (2008).
- K. S. Subrahmanyam, S. R. C. Vivekchand, A. Govindaraj and C. N. R. Rao, "A comparative study of graphenes prepared by different methods: Characterization, Properties and Solubilization", *J. Mater. Chem.*, **18**, 1517 (2008).
- N. Varghese, S. R. C. Vivekchand, A. Govindaraj and C. N. R. Rao, "A calorimetric investigation of the assembly of gold nanorods to form necklaces", *Chem. Phys. Lett.*, **450**, 340-344 (2008).
- S. V. Bhat and S. R. C. Vivekchand, "Optical spectroscopic studies of composites conducting PANI with CdSe and ZnO nanocrystals", *Chem. Phys. Lett.*, **433**, 154-158 (2006).
- C. N. R. Rao, V. V. Agrawal, K. Biswas, U. K. Gautam, M. Ghosh, A. Govindaraj, G. U. Kulkarni, K. P. Kalyanikutty, K. Sardar and S. R. C. Vivekchand "Soft-chemical approaches to inorganic nanostructures", *Pur. Appl. Chem.*, **78**, 1619-1650 (2006).
- C. S. Rout, S. H. Krishna, S. R. C. Vivekchand, A. Govindaraj and C. N. R. Rao, "Hydrogen and ethanol sensors based on ZnO nanorods, nanowires and nanotubes", *Chem. Phys. Lett.*, **418**, 582-586 (2006).
- U. K. Gautam, S. R. C. Vivekchand, A. Govindaraj and C. N. R. Rao, GaS and GaSe nanowalls and their transformation to Ga₂O₃ and GaN nanowalls", *Chem. Commun.*, 3995-3997 (2005).

- U. K. Gautam, S. R. C. Vivekchand, A. Govindaraj, G. U. Kulkarni, N. R. Selvi and C. N. R. Rao, "Generation of onions and nanotubes of GaS and GaSe through laser and thermally induced exfoliation", *J. Am. Chem. Soc.*, **127**, 3658-3659 (2005).

Reviews and Chapters in books

- C. N. R. Rao, S. R. C. Vivekchand, K. Biswas and A. Govindaraj, "Synthesis of Inorganic nanomaterials", *Dalton Transactions*, 3728-3749 (2007).
- S. R. C. Vivekchand, A. Govindaraj and C. N. R. Rao, "Nanotubes and Nanowires: Recent Developments", in *Nanomaterials Chemistry: Recent Developments*, edited by C. N. R. Rao, A. Muller and A. K. Cheetham, Wiley-VCH, July (2007).
- C. N. R. Rao, A. Govindaraj and S. R. C. Vivekchand, "Inorganic Nanomaterials: Current status and future prospects", *Ann. Rep. Prog. Chem. A*, **102**, 20-45 (2006).